

AD-A266 464



WL-TR-93-2004

DISSOCIATION RATES OF DIATOMIC
MOLECULES



PHILIP C. COSBY
HANSPETER HELM

SRI INTERNATIONAL
333 RAVENSWOOD AVENUE
MENLO PARK, CA 94025-3493

DTIC
ELECTE
JUL 07 1993
S A D

DEC 1992

FINAL REPORT FOR 09/15/85-05/15/92

APPROVED FOR PUBLIC RELEASE; DISTRIBUTION IS UNLIMITED

AERO PROPULSION AND POWER DIRECTORATE
WRIGHT LABORATORY
AIR FORCE MATERIEL COMMAND
WRIGHT PATTERSON AFB OH 45433-7650

93-15322



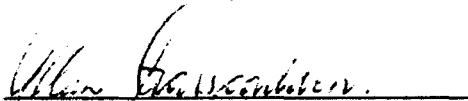
93 7 06 05 0

NOTICE

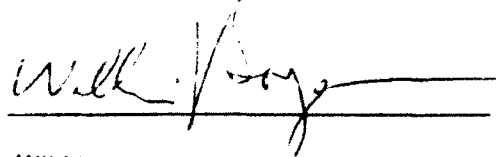
When Government drawings, specifications, or other data are used for any purpose other than in connection with a definitely Government-related procurement, the United States Government incurs no responsibility or any obligation whatsoever. The fact that the government may have formulated or in any way supplied the said drawings, specifications, or other data, is not to be regarded by implication, or otherwise in any manner construed, as licensing the holder, or any other person or corporation; or as conveying any rights or permission to manufacture, use, or sell any patented invention that may in any way be related thereto.

This report is releasable to the National Technical Information Service (NTIS). At NTIS, it will be available to the general public, including foreign nations.

This technical report has been reviewed and is approved for publication.



Power Components Branch
Aerospace Power Division
Aero Propulsion and Power Directorate



WILLIAM U. BORGER
Chief, Aerospace Power Division
Aero Propulsion & Power Directorate

If your address has changed, if you wish to be removed from our mailing list, or if the addressee is no longer employed by your organization please notify WL/POOC-3, WPAFB, OH 45433-7919 to help us maintain a current mailing list.

Copies of this report should not be returned unless return is required by security considerations, contractual obligations, or notice on a specific document.

REPORT DOCUMENTATION PAGE			Form Approved OMB No. 0704-0188	
<small>Estimated burden for this collection of information is estimated to average 1 hour per response, including the time for reviewing instructions, searching existing data sources, gathering and maintaining the data needed, and completing and reviewing the collection of information. Send comments regarding this burden estimate or any other aspect of this collection of information, including suggestions for reducing this burden, to Washington Headquarters Services, Directorate for Information Operations and Reports, 1215 Jefferson Davis Highway, Suite 1204, Arlington, VA 22202-4302, and to the Office of Management and Budget, Paperwork Reduction Project (0704-0188), Washington, DC 20503.</small>				
1. AGENCY USE ONLY (Leave blank)		2. REPORT DATE December 1992	3. REPORT TYPE AND DATES COVERED Final - 15 Sep. 85 to 15 May 92	
4. TITLE AND SUBTITLE Dissociation Rates of Diatomic Molecules			5. FUNDING NUMBERS Contract No. CF33615-85-C-2560 PE-61102 PR-2301 TA-S2 NU-36	
6. AUTHOR(S) Philip C. Cosby and Hanspeter Helm				
7. PERFORMING ORGANIZATION NAME(S) AND ADDRESS(ES) SRI International 333 Ravenswood Avenue Menlo Park, CA 94025-3493			8. PERFORMING ORGANIZATION REPORT NUMBER PYU 1147/MP 92-280	
9. SPONSORING/MONITORING AGENCY NAME(S) AND ADDRESS(ES) Aero Propulsion and Power Directorate Wright Laboratory Air Force Materiel Command Wright-Patterson AFB, OH 45433-6563 WL/POOC, Attn: Garscadden (513) 255-2923			10. SPONSORING/MONITORING AGENCY REPORT NUMBER WL-TR-93-2004	
11. SUPPLEMENTARY NOTES				
12a. DISTRIBUTION / AVAILABILITY STATEMENT Approved for public release; distribution is unlimited			12b. DISTRIBUTION CODE	
13. ABSTRACT (Maximum 200 words) Absolute cross sections were measured for the electron-impact dissociation of simple molecules using a novel fast beam technique with multicoincident detection of the dissociation fragments. Translational energy released in the dissociation and product mass ratios were explicitly measured, allowing a detailed understanding of the dissociation mechanisms. The technique was applied to the molecules of nitrogen, oxygen, carbon monoxide, carbon dioxide, nitrogen dioxide, chlorine, and other molecules. A detailed description of the measurement technique is presented together with the measured data.				
14. SUBJECT TERMS Dissociation, electron impact, cross sections, nitrogen, oxygen, carbon monoxide, carbon dioxide, nitrogen dioxide, chlorine			15. NUMBER OF PAGES 233	
			16. PRICE CODE	
17. SECURITY CLASSIFICATION OF REPORT Unclassified	18. SECURITY CLASSIFICATION OF THIS PAGE Unclassified	19. SECURITY CLASSIFICATION OF ABSTRACT Unclassified	20. LIMITATION OF ABSTRACT UL	

CONTENTS

1. INTRODUCTION	1
2. EXPERIMENTAL TECHNIQUE	3
Ion Beam Production	3
Neutral Beam Production	5
Neutral Flux Measurement	6
State Composition of the Neutral Beam	6
Species Composition of the Neutral Beam	11
Electron Impact	13
Fragment Detection	18
Collection Efficiency	21
Coincidence Efficiency	24
Dissociation Cross Section Determination	25
3. RESULTS AND DISCUSSION	29
Carbon Monoxide	29
Nitrogen	29
Oxygen	29
Chlorine	30
Carbon Dioxide	35
Nitrogen Dioxide	39
Other Molecules	41
REFERENCES	45
APPENDICES	
A Photofragment Spectroscopy of O ₂ : Excitation of the Schumann-Runge Band System	47
B Observations of New Metastable States of N ₂	54
C Unimolecular Dissociation of NO	86
D Electron-Impact Dissociation of Carbon Monoxide	96
E Photodissociation Measurement of Rovibrational Energies and Populations of Molecules in Fast Beams	151
F Electron-Impact Dissociation of Nitrogen	162
G Electron-Impact Dissociation of Oxygen	195

DTIC QUALITY INSPECTED 8

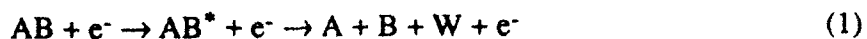
Distribution/	
Availability Codes	
Dist	Avail and/or Special
A-1	

FIGURES

1	Diagram of the electron-impact dissociation apparatus.....	4
2	Fragment translational energy releases observed for the prompt dissociation products of O_2 following charge-transfer neutralization of O_2^+ in NO gas (top) and in O_2 gas (bottom)	9
3	Photofragment ($O + O$) yield in the photodissociation of O_2	10
4	Composition of the CO beam	12
5	Distribution of the ratio of radial distances at the detector for the correlated neutral products of 38.5-eV electron impact on CO.....	14
6	Schematic diagram of the electron gun	15
7	Characteristics of the electron beam.....	17
8	Newton velocity diagram showing the mapping of the CO center-of-mass energy release onto the position-sensitive detector as a radial (R) and temporal (Δt) separation of the C and O fragments.	20
9	Diagram of the electron-impact dissociation apparatus.....	23
10	Accumulation of C + O electron-impact dissociation products (N^*) as the electron gun is translated across the CO beam at a constant velocity	28
11	Fragment translational energy releases observed in the electron-impact dissociation of Cl_2 at three electron energies.....	31
12	Potential energy curves of selected electronic states of Cl_2 and the ground electronic state of Cl_2^+	32
13	Total cross section for the electron-impact dissociation of Cl_2 as a function of electron energy	34
14	Fragment energy releases observed in the dissociation of CO_2	36
15	Total cross section for the electron-impact dissociation of CO_2 as a function of electron energy	38
16	Fragment energy releases observed in the dissociation of NO_2 following 50-eV electron impact	40
17	Distribution of the mass ratios of the NO_2 dissociation products following 50-eV electron impact.	42
18	Total cross section for the electron-impact dissociation of NO_2 as a function of electron energy	43

1. INTRODUCTION

From an experimental point of view, electron-impact dissociation of molecules is clearly the least understood of the basic collision processes. Yet this interaction can play a critical role in the chemistry of gas phase systems involving electrons with energies above several electron volts. In this range, the electrons can induce transitions to excited states in a molecule, which dissociate to produce fragments having high translational energies:



Apart from destroying the original molecule, the dissociation provides an efficient mechanism for the conversion of electron kinetic energy into the translational energy (W) of heavier species. In many cases the dissociation fragments are highly reactive and generate new chemical species in the gas. These effects are of particular concern for the control of plasma processes and in various pulsed power systems.

Progress in measuring reaction (1) for various molecules has been reviewed by Zipf¹ and by Compton and Bardsley.² Virtually all measurements have been of partial cross sections for the production of highly excited products that can be detected by spontaneous fluorescence, field ionization, or secondary emission at a surface. Ground state atomic or molecular fragments, which constitute the lowest energy and generally the most probable dissociation products, are not accessible with these techniques. Nevertheless, several important electron-impact dissociation measurements have been made that give access to ground state fragments. Corrigan³ derived the cross section for the dissociation of H_2 from observations of the pressure rise in a closed volume of this gas subjected to electron bombardment. Winters obtained the dissociation cross sections of N_2 ,⁴ CH_4 ,⁵ and several fluoroalkane compounds⁶ by measuring the pumping speed produced by the gettering of their dissociation fragments by metal surfaces. Niehaus⁷ obtained relative dissociation cross sections of N_2 and several organic compounds using a dual-filament mass spectrometer ion source. This concept of using two adjacent ionization volumes and mass spectrometer detection was recently used by Nakano, Toyoda, and Sugai⁸ to measure absolute cross sections for the electron-impact dissociation of CH_3 and CH_2 radicals.

The purpose of the research described here was to develop a new and generally applicable technique for the quantitative observation of electron dissociation reactions. In our approach, the reactant molecules are present as a fast neutral beam that is intersected by an electron beam. Because of the high beam velocity, the dissociation products are constrained to a narrow cone

and can be detected through secondary emission at an electron multiplier. At keV energies, the secondary emission efficiency of the multiplier is relatively insensitive to electronic excitation in the fragments, allowing near-uniform detection sensitivity to both ground and excited state products. Position and time-sensitive detection at the multiplier of the two correlated products from a single dissociating molecule permits accurate definition of the center-of-mass translational energy release (W) in the dissociation and the angular distribution of the fragments. Charged particles produced by the electron interaction are collected by an electric field such that dissociative ionization cannot contribute to the correlated product signal.

2. EXPERIMENTAL TECHNIQUE

Our technique consists of four distinct steps that must operate in concert to quantitatively observe electron-impact dissociation. These steps are (1) production of a molecular ion beam, (2) charge-transfer neutralization of this beam to produce the fast molecular beam, (3) intersection of the molecular beam by an electron beam, and (4) detection of the dissociation fragments using an unique position-sensitive detector for correlated fragments (PSD-C). Each of these steps is delineated in Figure 1, which gives an overall diagram of the experimental apparatus.

ION BEAM PRODUCTION

An ion beam, accelerated to several keV energy, provides the base for production of the fast neutral beam. Molecular ions are produced in an ion source, accelerated to a selected energy of 3000 to 5000 eV, focused, mass selected by a Wien filter or magnetic sector, and collimated into a beam of low angular divergence in preparation for its neutralization. The stability, intensity, purity, collimation, and internal state distribution in the ion beam intimately affect the quality of the neutral beam that is produced. These qualities are determined primarily by the ion source used to create the ions from a precursor gas.

During this research, three ion sources were used. Initially, a hot filament discharge ion source⁹ was used. This source allowed the preparation of intense ion beams of simple molecular ions such as H_2^+ and N_2^+ . However, the tungsten filament of this source was contained within the high pressure region of the discharge. Hence, the source could not be used with oxidizing or reactive gases. Furthermore, we found that the rovibrational energy distribution of the ions produced by this source was extremely hot (>1000 K) and that excited electronic states of the ions were generally not quenched within the discharge. The use of this ion source was discontinued in favor of two other ion sources: a Nier-type electron impact ion source and a hollow-cathode discharge ion source.

The electron-impact ion source is a relatively simple design that we have used extensively in earlier research; its characteristics were recently described in detail.¹⁰ This source is by far the most flexible in its ability to produce any given ion species. However, this flexibility stems from the relatively low pressure of the gas present in the source ($<5 \times 10^{-2}$ Torr), which makes the

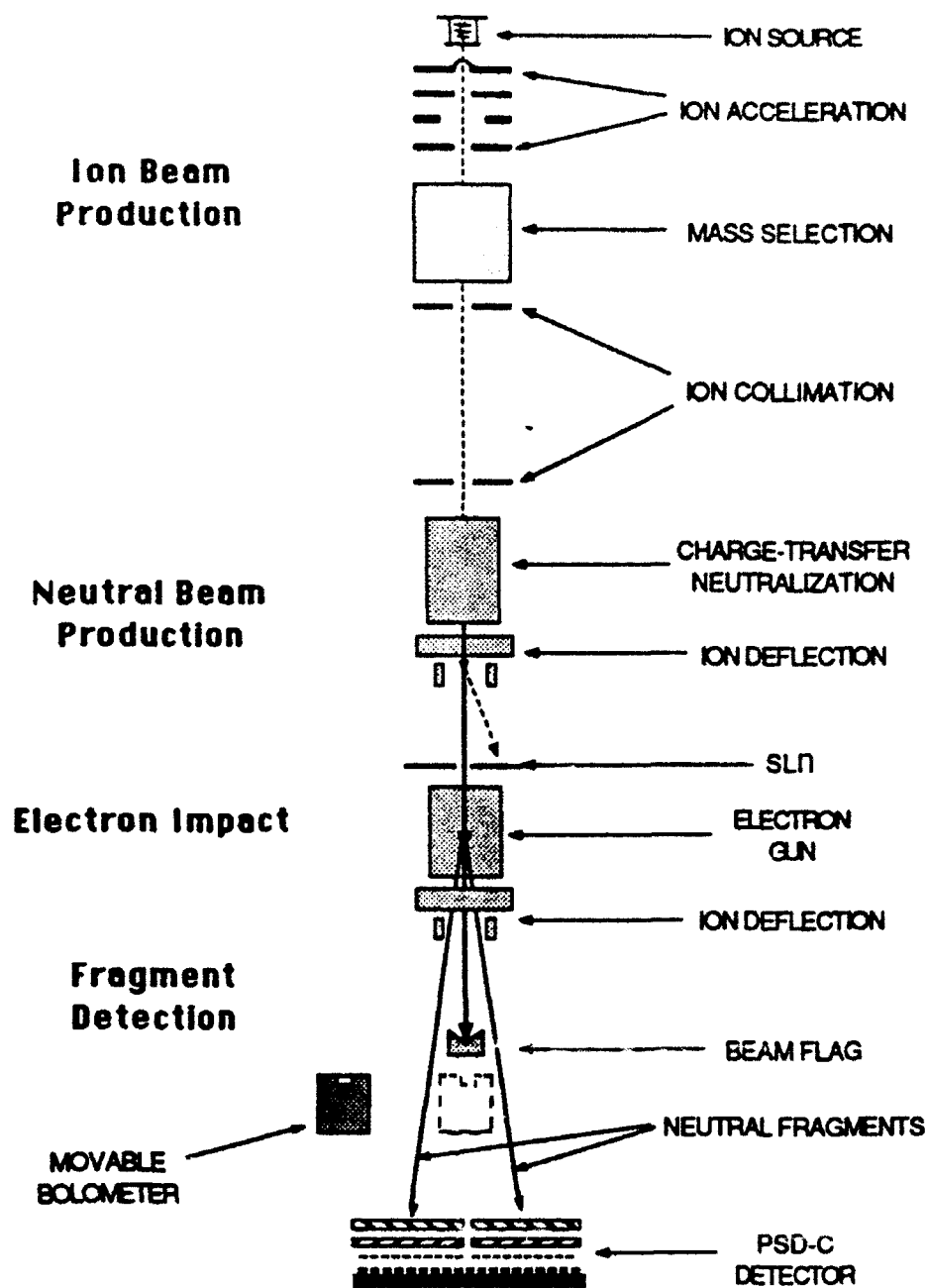


Figure 1. Diagram of the electron-impact dissociation apparatus.
The four functional regions of the apparatus are labelled in bold type.

ion production insensitive to small impurities in the gas sample. However, this low pressure also allows little opportunity to relax electronic or vibrational excitation created in the ionization process.

The third ion source is a water-cooled hollow-cathode discharge source¹¹ operated at pressures of 0.2 to 1 Torr. The high pressure within the source volume allows a very effective quenching of the internal energy produced during ion production. Intense, relaxed beams of such species as CO^+ , O_2^+ , N_2^+ , and H_3^+ have been produced with this source. However, the discharge operation is erratic when corrosive gases such as NO are used, and production of a desired ion species is highly susceptible to competing ion-molecule reactions within the source.

The internal state composition of an ion beam can be inferred indirectly from known radiative properties of the molecular ions, photodissociation of the ion beam, or photodissociation of the neutral beam. In addition, we have found that translational spectroscopy of the products of dissociative charge transfer (DCT) is especially useful. We recently applied DCT of O_2^+ in Cs vapor to obtain detailed distributions of both the electronic and rovibrational distributions of O_2^+ produced in our electron impact ion source under various conditions.¹⁰ Initial tests showed this technique to be applicable also to N_2^+ , CO^+ , and NO^+ , and it is probably generally applicable to most diatomic molecular ions. However, a detailed correlation between ion state and dissociation channel has thus far been completed only for O_2^+ .

NEUTRAL BEAM PRODUCTION

The collimated ion beam is passed through a 10-cm-long cell containing the charge transfer gas. The pressure in this cell is adjusted such that attenuation of the ion beam by the gas is <10%. Ions that pass through the cell are deflected by an electrostatic field at its exit and collected. Fast neutrals created in the cell are collimated by a 0.5×3 mm slit positioned typically 39-cm downstream of the cell. The function of the slit is to (1) produce a well-defined neutral beam with an angular divergence of 1.2 mrad, (2) in combination with the beam flag, mask the PSD-C from observing both fragments from a dissociation event occurring upstream of the slit, and (3) preferentially pass the products of near-resonant charge transfer, which are predominantly forward-scattered with little angular divergence, while greatly attenuating contributions from other scattering processes, such as collision-induced dissociation and dissociative charge transfer.

Neutral Flux Measurement

The neutral beam flux passing through the slit is monitored by measuring the apparent current generated by the neutral beam in a Faraday cup centered on the PSD-C. The Faraday cup consists of a stainless steel tube terminated by an insulated stainless steel collector. A potential difference of 80 V DC between the collector and the tube and a length/diameter ratio of 40 for the tube facilitates the consistent removal from the collector of the secondary electrons that are produced by the impact of the fast neutral beam. The neutral beam flux N is related to the measured current at the Faraday cup I_{fc} by the relation:

$$N = \frac{I_{fc}}{\eta}, \quad (2)$$

where η is the effective secondary emission coefficient.

Absolute calibration of the neutral beam flux was made with a pyroelectric bolometer^{12,13} constructed from a 0.5-in.-diameter \times 0.1-inch disk of lead zirconate-titanate with silver electrodes deposited on the circular surfaces.¹⁴ The neutral beam was modulated at 5 Hz (by modulating the ion beam before charge transfer neutralization), and the pyroelectric signal, which is proportional to the power deposited by the fast beam, was detected by a lock-in amplifier. The absolute neutral beam flux was determined by comparison with the pyroelectric signal produced by an ion beam, whose flux was known from measurement of its current with a calibrated electrometer:

$$N = \frac{IV_n}{eV_i}, \quad (3)$$

where N is the neutral beam flux, I is the current of the ion beam of equal energy, e is the electron charge, and V_n and V_i are the bolometer outputs produced by the neutral and ion beam, respectively. Comparison of these two measurements of the neutral beam flux provides a direct measurement of the effective secondary emission coefficient η at the Faraday cup for routine beam monitoring, with an accuracy of approximately 6%. This coefficient was found to be stable to within this calibration accuracy over extended periods (months). Maintaining the entire detector region under a clean (ion-pumped) high vacuum ($<1 \times 10^{-8}$ Torr) probably contributed to this stability.

State Composition of the Neutral Beam

The molecular ion beam is converted to the neutral beam by near-resonant charge transfer:

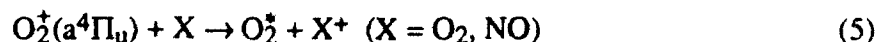


where A^+ represents the fast ion species and B represents the thermal neutralizing gas. The cross sections for reaction (4) are largest when the product A is formed in a single electron transfer and when there is no net transfer of energy between the reactants and products, i.e., when the recombination energy of A^+ equals the ionization potential of B . In addition to the initial state distribution in the reactant ion beam A^+ , the vibrational overlap integrals in both the recombination ($A^+ \rightarrow A$) and ionization ($B \rightarrow B^+$) channels also play a significant role in determining the vibrational distribution of fast neutral A .¹⁵

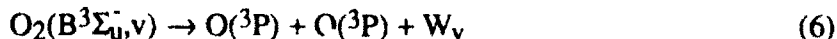
Besides theoretical calculations, there have been very few experimental measurements of the actual state distributions of the fast neutral products formed by molecular charge transfer at keV energies. Yet the state distribution in this beam is important for understanding its electron dissociation reaction. Ding and Richter¹⁶ observed the products of the N_2^+/N_2 reaction using laser-induced fluorescence, but could probe only a few vibrational levels in the ground electronic state. Detailed studies of the products of H_2^+ charge transfer in alkali metal vapor have also been made,¹⁷ but the products there are Rydberg states of the ion, so vibrational overlap in the recombination is diagonal, a situation rarely found in the production of ground state molecules.

We made two studies during the present work to probe the final states formed in the charge transfer. In the first of these, Cl_2 molecules produced by the charge transfer of Cl_2^+ in Cl_2 were photodissociated at 11 laser wavelengths between 7993 Å and 3507 Å, exciting $D^1\Pi_u \leftarrow X^1\Sigma_g^+$ transitions at the blue wavelengths and $1^3\Pi_g \leftarrow B^3\Pi_u$ transitions at the red wavelengths. By measuring the discrete vibrational contributions to the translational energy spectrum of the photofragments, we obtained a detailed vibrational distribution and relative populations for both the X and B states.¹⁸

In the second study, we detected the fast neutral product O_2^* in the charge transfer reactions:



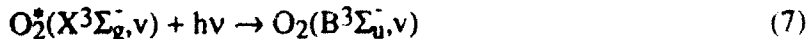
Here we specifically use an electronically excited reactant ion so that products can be observed with dissociation techniques. For both the O_2 and NO neutralizing gases, a significant fraction of the product O_2^* populates vibrational levels in the $B^3\Sigma_u^-$ state, which predissociates:



to atoms with discrete releases of translational energy, which were measured with the PSD-C detector.

The product translational energy spectra observed for O₂ and NO targets are shown in Figure 2 where the discrete energy releases associated with reaction (6) appear as structure in the two spectra with an intensity proportional to vibrational population. The spectra are appreciably different for the two target gases, with B(v = 0-6) populated with charge transfer in O₂ and B(v = 0-22) populated by charge transfer in NO. Since the Franck-Condon factors for ionization are essentially the same in both these molecules, the essential difference in the product distributions arises from their different ionization potentials, 12.06 eV for O₂ and 9.25 eV for NO. Considering the initial vibrational distribution in the reactant O₂⁺ a⁴Π_u state, which is independently measured, and the Franck-Condon factors for the a⁴Π_u → B³Σ_u⁻ recombination, we found that the charge transfer produces a Gaussian distribution of final states centered on the resonant energy and with a full-width-at-half-maximum of ~1 eV. This same propensity also described the products of the Cl₂⁺/Cl₂ reaction.

Resonant capture in the O₂⁺(a)/NO reaction should also produce high vibrational levels in the O₂ ground electronic state X³Σ_g⁻, which of course do not dissociate. We probed these by photodissociation of the O₂⁺ beam:



which is followed immediately by dissociation (6). Initial measurements using fixed-frequency lasers are described in Appendix A. These measurements detected population in the higher vibrational levels, but did not allow a population distribution to be determined. Later measurements using a tunable dye laser yielded the results shown in Figure 3. This figure shows the fragment intensity of reaction (6) dispersed both in ranges of W_v and continuously in exciting photon energy, hν, of reaction (7). Bands appearing in the spectrum can be precisely identified and are labeled by the vibrational quantum numbers (v',v'') of the B state and the X state, respectively. Analysis of the band intensities yielded the relative vibrational populations in X³Σ_g⁻(v = 27-34). These populations are found to be consistent with the Gaussian distribution of product states described above.

In all these studies, the propensity of the neutralization reaction to form near-resonant product channels is found to hold. However, this does not prevent the population of product channels far from resonance to some extent. Although only a tiny fraction of the charge transfer reactions lead to production of nonresonant product states (indeed a negligible fraction from the

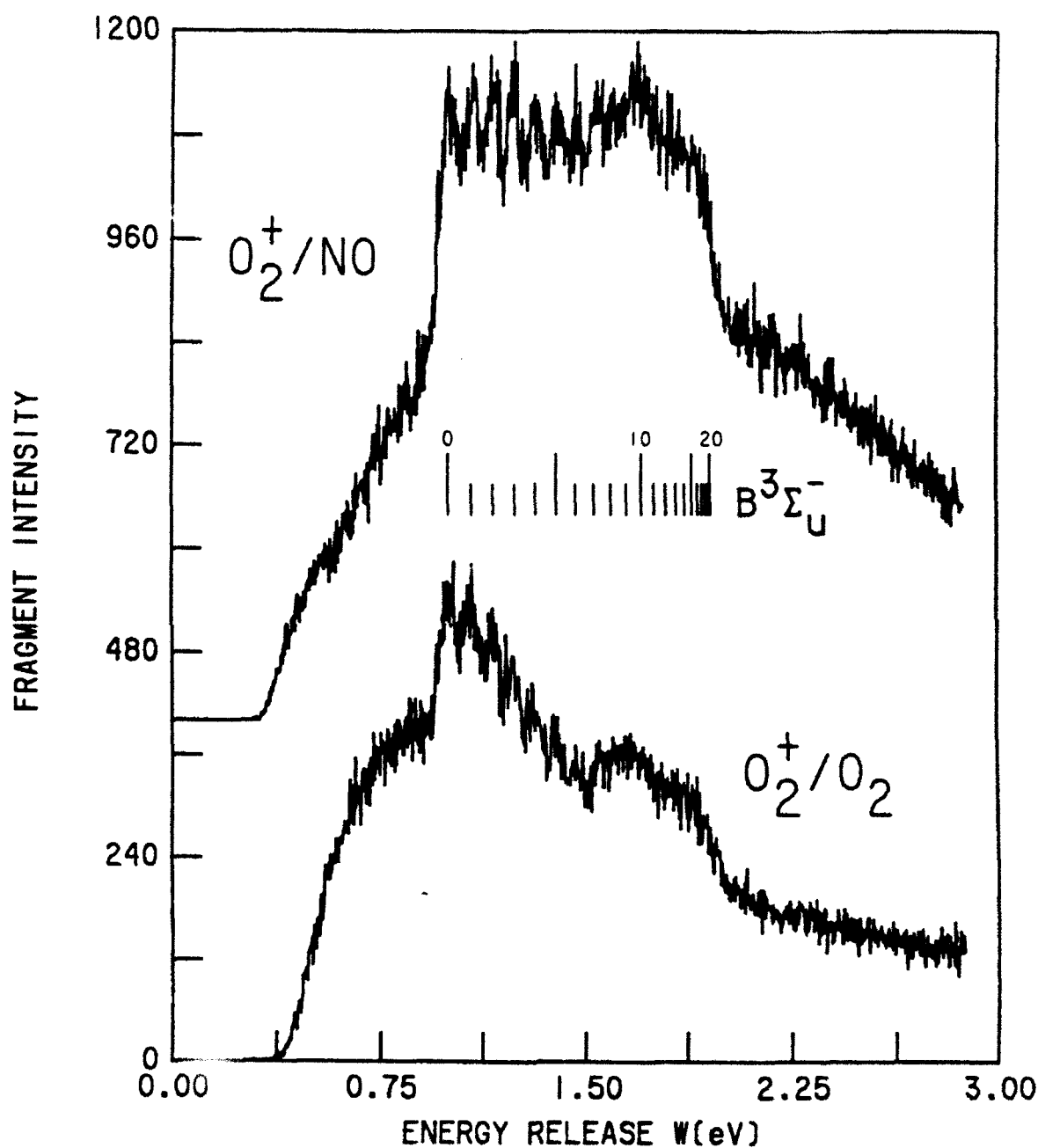


Figure 2. Fragment translational energy releases observed for the prompt dissociation products of O_2 following charge-transfer neutralization of O_2^+ in NO gas (top) and in O_2 gas (bottom). Vibrational levels of the $O_2 B^3\Sigma_u^-$ state are indicated up to its dissociation limit.

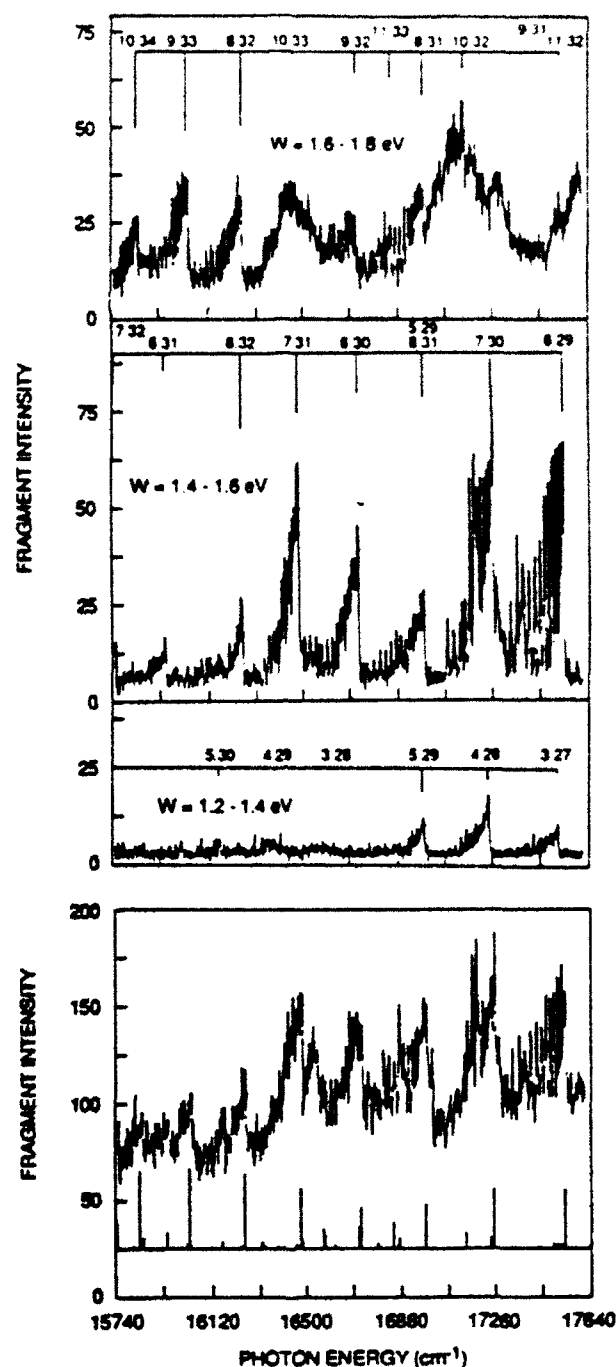


Figure 3. Photofragment (O + O) yield in the photodissociation of O₂.

The lowest spectrum shows the total photofragment flux as a function of the photon energy. In the upper spectra, this flux is dispersed into three translational energy release ranges. Calculated band origins and Franck-Condon factors for the $B^3\Sigma_u^-(v') \leftarrow X^3\Sigma_g^-(v'')$ transitions labelled (v', v'') are shown by the position and length of the vertical bars. Deviations in the observed band intensities from the Franck-Condon factors mainly reflect vibrational populations in the $X^3\Sigma_g^-$ state.

standpoint of neutral beam purity), those molecules produced in long-lived dissociative states that survive the transit time between the charge transfer cell and the electron beam interaction region are found to produce the dominant dissociation background when observing electron-impact dissociation products. This background constitutes the single greatest impediment to the present measurements. For N_2 and NO beams, identification of the spontaneously dissociating states has been considered in some detail, as discussed in Appendices B and C, respectively.

Species Composition of the Neutral Beam

Contamination of the desired neutral beam by other atomic or molecular species can arise either in the ion source or in the charge transfer cell. Mass selection of the ion beam with unit mass resolution excludes the products of dissociative ionization or of ion-molecule reactions in the ion source from entering the charge transfer cell. The second source of contamination is collisional dissociation or dissociative charge transfer of the CO^+ beam in the charge transfer cell. In general, these contributions will be small, reflecting the size of their cross sections ($<1 \text{ \AA}^2$) in comparison with that for symmetric resonance exchange (20 \AA^2). In addition, significant scattering accompanies these processes with small cross sections, so many of these fragments are excluded by the slit entrance to the interaction region, with an acceptance of 1.3 mrad vertical and 5.1 mrad horizontal. By comparison, a dissociation occurring in the charge transfer cell with an energy release of $W = 1 \text{ eV}$ will produce the fragments dispersed over 21 mrad in the laboratory frame. Nevertheless, it is important to confirm the beam purity.

We have two techniques for determining beam purity. The first is to use the electron beam to ionize the molecular beam and observe the ionization products. Fragments produced in the charge transfer cell will arrive at the electron interaction region with very nearly the same laboratory velocity as the molecular ion precursor and with an angular divergence established by the entrance slit. If we position a pair of vertical electrostatic deflector plates in the region between the electron beam and the beam flag (see Figure 1), fast charged species produced by direct ionization of the molecular beam will be deflected by an amount inversely proportional to their mass. This deflection, projected over a distance of approximately 94 cm , is observed on one of the position-sensitive anodes of the PSD-C.

Figure 4 shows the integrated counts observed on the anode for one deflection voltage (175 V) following 50-eV electron impact on the CO beam. The abscissa in this figure gives the distance of ion impact vertically with respect to the projected point of impact of the neutral beam on the detector. The large peak is produced by CO^+ , formed by direct ionization of CO . Fragments due to dissociative ionization are distributed over a range of distances on the detector

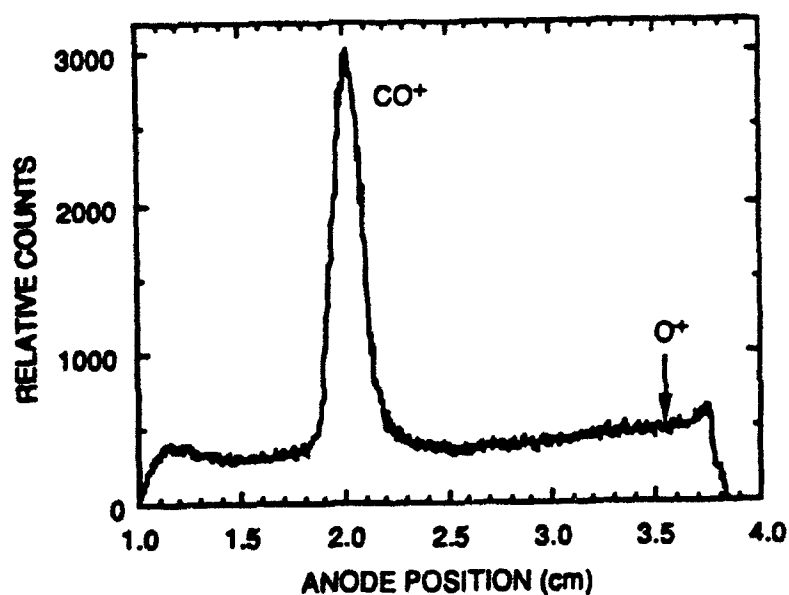


Figure 4. Composition of the CO beam. The relative flux of noncoincident events detected on one anode of the PSD-C is shown as a function of radial distance from the CO beam following 50-eV electron impact and deflection of the charged fragments. The expected location of O^+ produced from the ionization of O contaminants in the beam is indicated by the arrow. The underlying background in the spectrum is due to slow metastables produced by electron impact on the residual gas in the electron gun that drift unimpeded to the PSD-C.

and do not appear as a discrete peak under these conditions. The width of this peak reflects the angular divergence in the neutral beam (1.2 mrad) and the vertical slit width (0.05 cm).

The position of the peak (2.02 cm) on the detector reflects the specific deflection voltage chosen. If the molecular beam were contaminated by O atoms, for example, a peak of comparable width should be observed near 3.54 cm in this spectrum with a height reflecting the concentration (and relative ionization cross section) of this species. A series of such spectra obtained for a range of deflection voltages and at electron energies up to 200 eV showed no definitive evidence of contamination by either C or O, leading to the conclusion that CO constitutes $\geq 95\%$ of the molecular beam.

The second technique for assaying beam purity is observation of the electron-impact dissociation fragments itself. As discussed in the section on Fragment Detection below, the separation R of the fragments at the detector surface is measured as the sum of the radial distances of the two fragments from the center of the detector: $R = R_a + R_b$. Since the two fragments were necessarily ejected with equal momenta in the center-of-mass frame and the difference in the fragment arrival times at the detector is small relative to their flight time after dissociation:

$$\frac{R_m}{R_M} \sim \frac{M}{m}, \quad (8)$$

where m and M denote the masses of the light and heavy fragments, respectively. That is, the ratio of these distances is inversely proportional to the ratio of the fragment masses. Figure 5 shows the distance ratio observed for the fragments produced by electron-impact dissociation of a fast CO beam by 40-eV electrons. The dashed line in this figure denotes the mass ratio for C + O fragments. Although the distance ratio distribution is rather broad, reflecting both the angular divergence of the CO beam and the approximate nature of Eq. (8), the distribution clearly confirms the expected products and, therefore, the precursor neutral beam.

ELECTRON IMPACT

The rectangular electron beam used for the neutral beam dissociation and ionization measurements is produced in a simple pentode gun from a directly heated thorium-coated (ThO_2) iridium filament of rectangular geometry (0.07×2.8 cm). The structure of this gun is shown in Figure 6. The fourth lens, with an open area of 0.3×2.6 cm, provides the smallest geometric constraint to the electron beam, whose width is otherwise determined by the accelerating voltages applied to the first four lens elements. The fifth lens, with an open area of 0.95×3.8 cm, is maintained at ground potential and is covered with 95% transmission tungsten mesh to

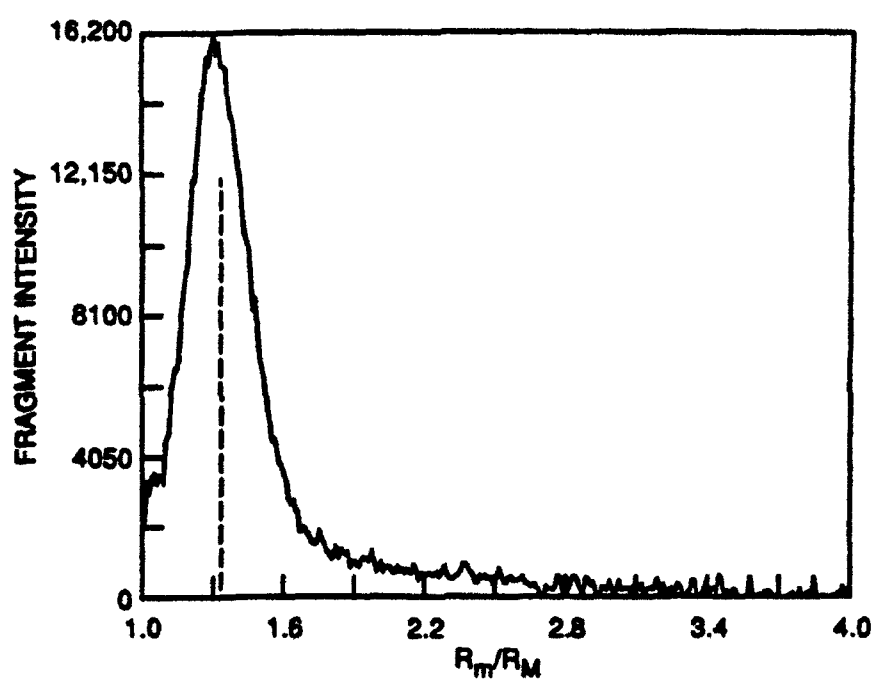


Figure 5. Distribution of the ratio of radial distances at the detector for the correlated neutral products of 38.5 eV electron impact on CO. The mass ratio of C and O fragments is shown by the dashed line.

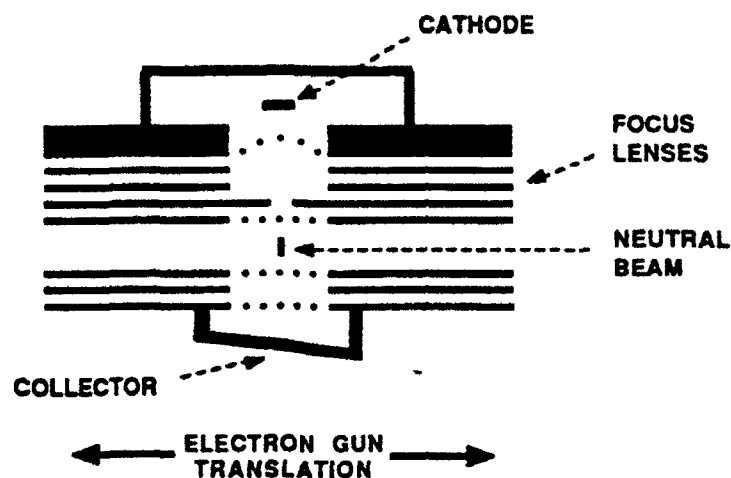


Figure 6. Schematic diagram of the electron gun.
The direction of gun translation relative to the neutral beam is indicated.

minimize field penetration into the region of electron beam-neutral beam interaction. This lens defines one side of the interaction region, with an identical element terminating the 0.89-cm-wide interaction region. A potential of 1.5 V DC is maintained between these two elements to minimize trapping of slow electrons or ions in this region. The nominal electron energy is selected by the potential difference between the filament and the entrance to the interaction region.

The electrons that pass through the interaction region are collected by a two-element, 1-cm-deep Faraday cup. The potential of the cup, typically -20 V DC with respect to the interaction region (lens 5), is adjusted to approximately 2 V above the onset of the plateau for a constant current of collected electrons ($dI/dV = 0$). No magnetic field is used for collimation of the electron beam, to facilitate transmission of an ion beam through the gun to the detector. Electron currents at the Faraday cup range from 0.1 mA for a nominal 10-eV electron beam to 1 mA for nominal beam energies ≥ 50 eV. Retarding potential difference measurements at the Faraday cup show a triangular electron energy spread with a full-width-at-half-maximum of 1.5 eV, independent of beam energy over the range 15-200 eV. This width roughly corresponds

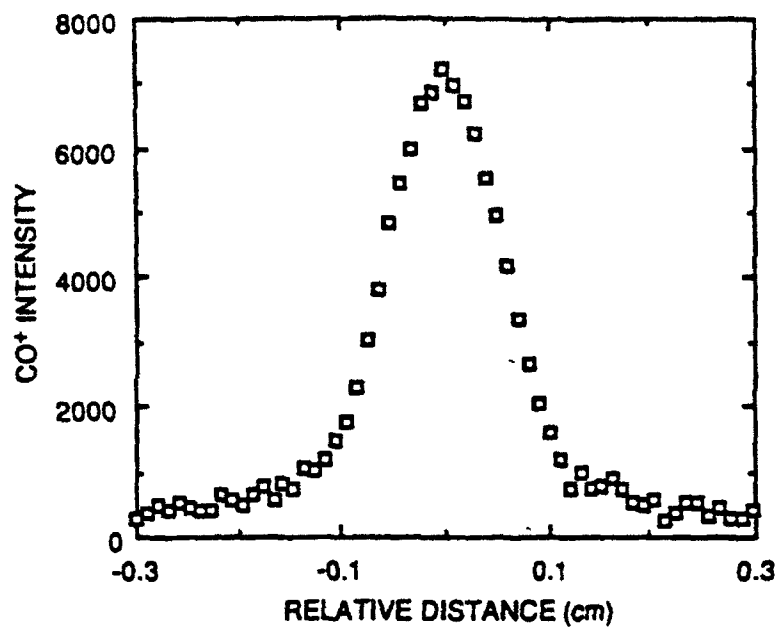
to the voltage drop across the directly heated filament. The gun assembly is maintained at a vacuum of $\leq 3 \times 10^{-8}$ Torr during operation.

The explicit spatial overlap of the electron beam and the fast neutral beam is one of several critical elements required for determining the absolute dissociation cross section. To facilitate the measurement and optimization of this overlap, the entire electron gun assembly is mounted on a micrometer-adjusted translation stage. For reference, consider an orthogonal x,y,z coordinate system with the neutral beam propagating along the y axis with its slit dimensions of 0.05×0.2 cm in the z,x plane. The electron beam propagates along the x axis with its narrow and long dimensions in the z,y plane, and the gun assembly can be translated along the z-axis with a precision and reproducibility of $< 7 \times 10^{-4}$ cm.

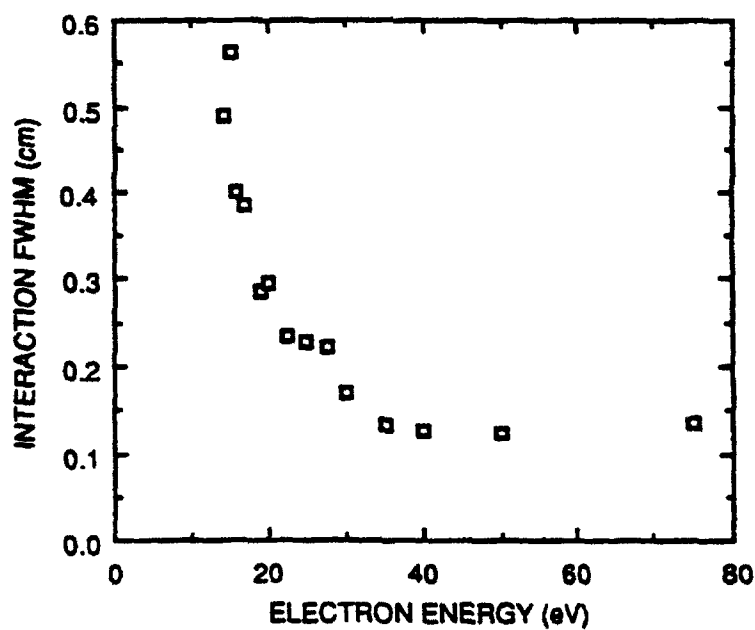
The relative overlap of the two beams is determined by observing the products of the electron impact interaction (dissociation or, more easily, ionization) as a function of electron gun translation. Figure 7a shows the number of CO^+ ions (the summation of the counts in the CO^+ peak in Figure 4) formed by electron-impact ionization of the CO beam at 40 eV as the electron gun position is translated over a distance of 0.6 cm. The 0.128-cm FWHM of the near-Gaussian ionization signal represents the convolution of a 0.07-cm-wide neutral beam (at the electron beam, considering angular divergence) with the spatial distribution of the electron beam at this energy. As mentioned above, the spatial distribution of the electron beam is highly dependent on the accelerating voltage.

Figure 7b shows the variation in the FWHM of the ionization products with nominal electron energy. These values are also a good representation of the effective electron beam width; explicit deconvolution of the 0.07-cm neutral beam width decreases these values by ≤ 0.007 cm. The electron beam energy is calibrated with respect to the nominal acceleration voltage by comparing the apparent electron energy dependence of the measured cross sections for ionization of Ar and other species in the first 20 eV above threshold with literature values.

In addition to providing a mechanism for defining the overlap of the electron and neutral beam, translation of the electron gun allows phase-sensitive detection of the electron-impact dissociation signal from various other dissociation processes that can occur in the fast beam. To appreciate how very minor effects can mask the dissociation signal, consider the relative densities of the electron beam and the neutral beam in the interaction region. For typical conditions of a 3000-eV neutral beam flux of $3 \times 10^{10} \text{ s}^{-1}$ and a current of 0.5 mA for 20-eV



(a)



(b)

Figure 7. Characteristics of the electron beam.

(a) The apparent flux of CO⁺ ionization products arriving at the PSD-C as the electron gun is translated a distance of 0.6 cm across the 0.07-cm-wide CO beam. The peak essentially reflects the spatial distribution in the electron beam along the direction of translation. (b) The variation in this spatial distribution with electron beam energy, expressed in terms of its full width at half maximum.

electrons, their respective beam densities amount to only 1.4×10^5 molecules/cm³ and 3.6×10^7 electrons/cm³. These are small in comparison with the density of residual gas of 9.6×10^8 cm⁻³ in the interaction region at a pressure of 3×10^{-8} Torr.

Thus the main product of electron impact will be the ionization and excitation of the residual gas. These products are easily distinguished because they are translationally slow; however, the impact of slow metastables that drift from the electron beam region contribute a significant, but noncoincident, background at the PSD-C. Similarly, collisions of the fast neutral beam with the residual gas in the region between the slit and the beam flag can produce fast products. For example, collision-induced dissociation with a cross section of order 1×10^{-18} cm² can produce a product flux comparable to electron-impact dissociation with a cross section of 1×10^{-16} cm².

Our initial approach to distinguishing electron-impact dissociation products from other dissociation events was simple electrical modulation of the electron flux and phase-sensitive detection of the dissociation products. However, this approach was found to have a very serious drawback in that the residual gas rapidly adsorbs on all surfaces in the electron gun in the momentary absence of electron bombardment degassing. The repetitive adsorption/degassing cycle that accompanies modulation of the electron current also modulates the neutral gas density within the electron interaction region (thus producing a collision-induced dissociation background) in phase with the electron beam. Translation of the electron gun assembly, with the electron beam operating at constant current and continuously striking the same surfaces, allows modulation of the electron beam/neutral beam interaction without affecting other variables.¹⁹

Further details of our techniques for electron-impact dissociation are given in Appendix D.

FRAGMENT DETECTION

The single most important element in the measurement of electron-impact dissociation is the unique position-sensitive detector for correlated fragments PSD-C. This detector²⁰ makes use of the fact that, when a molecule dissociates, its fragments are imparted equal, but opposite, momenta with respect to its center of mass, which is traveling at the velocity of the molecule before dissociation. The components of the fragment momenta, both parallel with and perpendicular to the center of mass velocity, produce a spatial separation of the two fragments that is linearly proportional to the distance over which the fragment trajectories are allowed to propagate unimpeded.²¹

This separation is shown by the Newton velocity diagram for the dissociation of CO in Figure 8. The function of the PSD-C, positioned a distance L from the point of dissociation, is to measure this separation of the two fragments resolved into its two components: R , the radial separation of the fragments in the direction perpendicular to the center of mass velocity (the beam direction) and the separation parallel to the beam, as manifested by the difference in the fragment arrival times Δt . The PSD-C detector explicitly measures these two quantities for each pair of fragments, from which we determine both the center-of-mass translational energy release with which the molecule ejected the fragments:

$$W = \frac{E_0}{L^2} \left[\frac{Mm}{(M+m)^2} \right] \left[R^2 + (v\Delta t)^2 \right] \left[1 + \frac{2(m-M)v\Delta t}{(M+m)L} \right] \quad (9)$$

and we calculate the center-of-mass angle (with respect to the beam direction) Θ at which they were ejected:

$$\Theta = \tan^{-1}(R/v\Delta t) \quad (10)$$

In these equations, m and M are the masses of the light and heavy fragments, respectively, produced by the dissociating molecule of mass $m + M$, $E_0 = (M + m)v^2/2$ is the kinetic energy of the molecule (i.e., the kinetic energy of the molecular ion charge transfer precursor), v is its velocity, and L , R , and Δt are defined above.

Although this concept of dissociation product measurement is quite simple, the implementation of a practical detector required considerable care and was one of the major accomplishments under this contract. A detailed description of the physical detector is given in Appendix E. The accuracy of the detector is found to be better than $100 \mu\text{m}$ in the determination of R and better than 1 ns for Δt . The beam energy is specified to within $\pm 5 \text{ eV}$. For cases, such as photodissociation with a well-defined laser beam, where the distance L can be precisely specified to within 0.2 cm for photodissociation events, W can be determined with an absolute accuracy of better than $\pm 0.020 \text{ eV}$. For the present case of electron-impact dissociation, the uncertainty in L , ΔL , is specified by the length of the electron beam, neutral beam interaction ($\Delta L = 2.6 \text{ cm}$), producing a resolution in W of $\Delta W/W = 2\Delta L/L = 0.052$. If a molecule were to dissociate by some mechanism other than electron impact, such as spontaneous dissociation or collision-induced dissociation, ΔL can be even larger, with a maximum value of $\Delta L = 18 \text{ cm}$, as limited by the spacing between the beam defining slit and the beam terminating flag (see Figure 1). The W resolution for such processes is substantially degraded: $\Delta W/W \leq 0.38$.

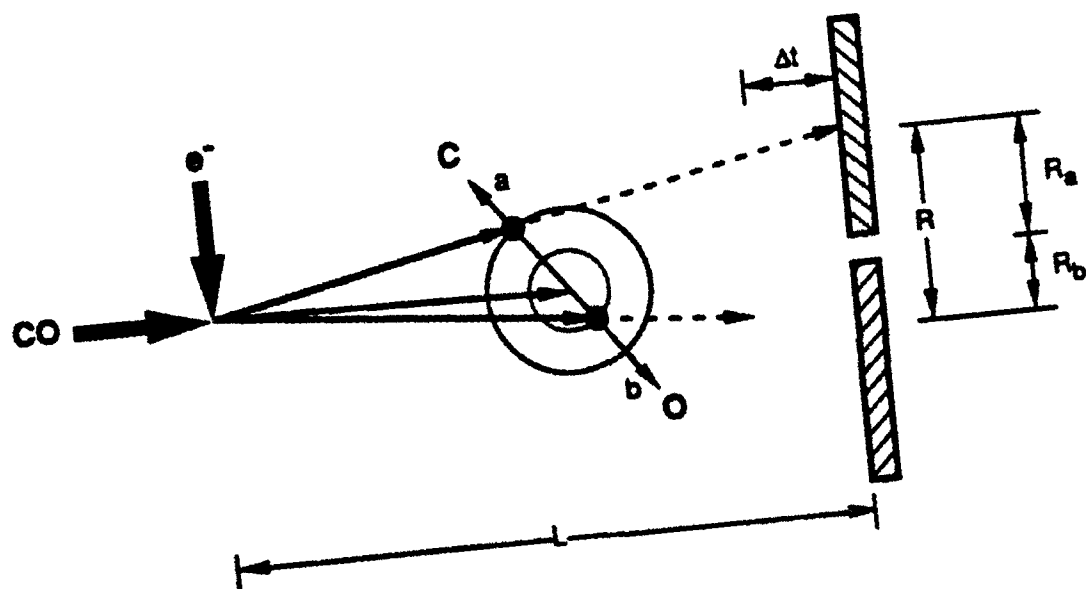


Figure 8. Newton velocity diagram showing the mapping of the CO center-of-mass energy release onto the position-sensitive detector as a radial (R) and temporal (Δt) separation of the C and O fragments.

The correlation between fragment separation and arrival time difference exists only when both fragments arise from a single dissociating molecule. In fact, this constraint is easily satisfied at the detector. For a worst case event, where the fragments from 3000-eV neutral beam are ejected with $W = 4$ eV parallel to the beam, both fragments arrive within $\Delta t = 0.52 \mu\text{s}$. This interval is yet smaller for larger E_0 , smaller W , and other ejection angles. Count rates of several thousand per second on either anode of the detector can be maintained with negligible false coincidence events and negligible dead-time losses for the dissociation fragments. Even when a false coincidence is detected, the lack of correlation between R and Δt produces a constant background that can easily be distinguished. However, this practical count rate limitation becomes a serious impediment to observing the electron-impact dissociation of molecular species for which the charge-transfer neutralization has produced a very high spontaneous dissociation background.

The fact that the two correlated fragments are detected allows effective discrimination against competing electron-impact dissociation processes such as dissociative ionization:



Application of a weak electric field in the region between the beam flag and the detector prevents the charged fragment from arriving at the detector. Of course, the neutral product can impact on one-half of the detector, but is not interpreted as a correlated event.

A critical consideration in the quantitative measurement of electron-impact dissociation is that not all dissociation products can be detected. This loss of fragments arises both in the projection of the fragments onto the active surface of the detector and in the detector's ability to generate a useful electrical signal registering the fragment impact. We account for these two sources of fragment loss by a collection efficiency term χ and a coincidence efficiency term ξ .

Collection Efficiency

The present fragment detection technique has a significant advantage in that the Jacobian for the transformation from the center-of-mass frame of the molecule to the laboratory frame of the detector is unity, provided the active area of the detector is large enough to collect all fragments.²¹ However, a practical implementation of this technique places several geometric constraints on the fragment trajectories that can actually strike the detector. These constraints, which arise from the beam flag and the finite active area of the detector, produce a collection

efficiency that is an explicit function of beam energy E_0 , translational energy release W , and the center-of-mass fragment ejection angles Θ , defined above, and Φ , the radial angle in the plane orthogonal to the beam velocity: $\chi(E_0, W, \Theta, \Phi)$.

Given explicit values for these variables and the physical dimensions of the apparatus, χ can be explicitly calculated for linear trajectories. To realistically reproduce the angular divergence of the fast neutral beam, the extended dimensions of the electron beam/neutral beam overlap region, and the radial asymmetry of the beam flag, we use Monte Carlo sampling to compute χ . For the experiments described here, E_0 is the selected value of the ion beam energy (3000-5000 eV), W is defined by the explicitly observed values for the dissociation fragments, Eq. (9), and Θ, Φ are drawn from the observed center-of-mass angular distribution.

As shown in Eq. (10), the angle of fragment ejection relative to the velocity vector of the beam is given by the ratio of the fragments' spatial and temporal separations. Since the molecules are (presumably) randomly oriented in the beam, spontaneous dissociation of the molecule produces a fragment pair for which Θ can assume any value between 0 and $\pi/2$. The electron beam provides an orientation reference between the center-of-mass distribution of the electron-impact dissociation fragments and the laboratory direction defined by the neutral beam velocity.

More specifically, the momentum transfer vector K , the difference between the momenta of the incident and scattered electron that induced the electronic transition, provides the symmetry axis for the collision.^{22,23} At electron energies substantially above the transition threshold, the direction of K is effectively orthogonal to the incident electron velocity. At threshold energies, K can assume any direction with respect to the incident velocity; the actual distribution of angles is given by the differential cross section,²⁴ such as is measured by electron energy loss spectroscopy. Alignment of the molecular axis of a diatomic molecule with respect to K is well defined by group theory for any pair of initial and final states in the molecule and can be described as either perpendicular ($1.5 \sin^2\theta$) or parallel ($3 \cos^2\theta$) with respect to K and with cylindrical symmetry about K . Presuming axial ejection (along the bond axis), this alignment also describes the molecular fragments.

For the orientation of the electron beam with respect to the active area of the PSD-C shown in Figure 9, observation of the fragment angular distribution with cylindrical symmetry about the neutral beam direction gives little information with regard to fragment alignment with respect to K . Indeed, for an electron-induced perpendicular transition at high electron energies, most of the fragments would actually fall outside the active area of the PSD-C. However, with

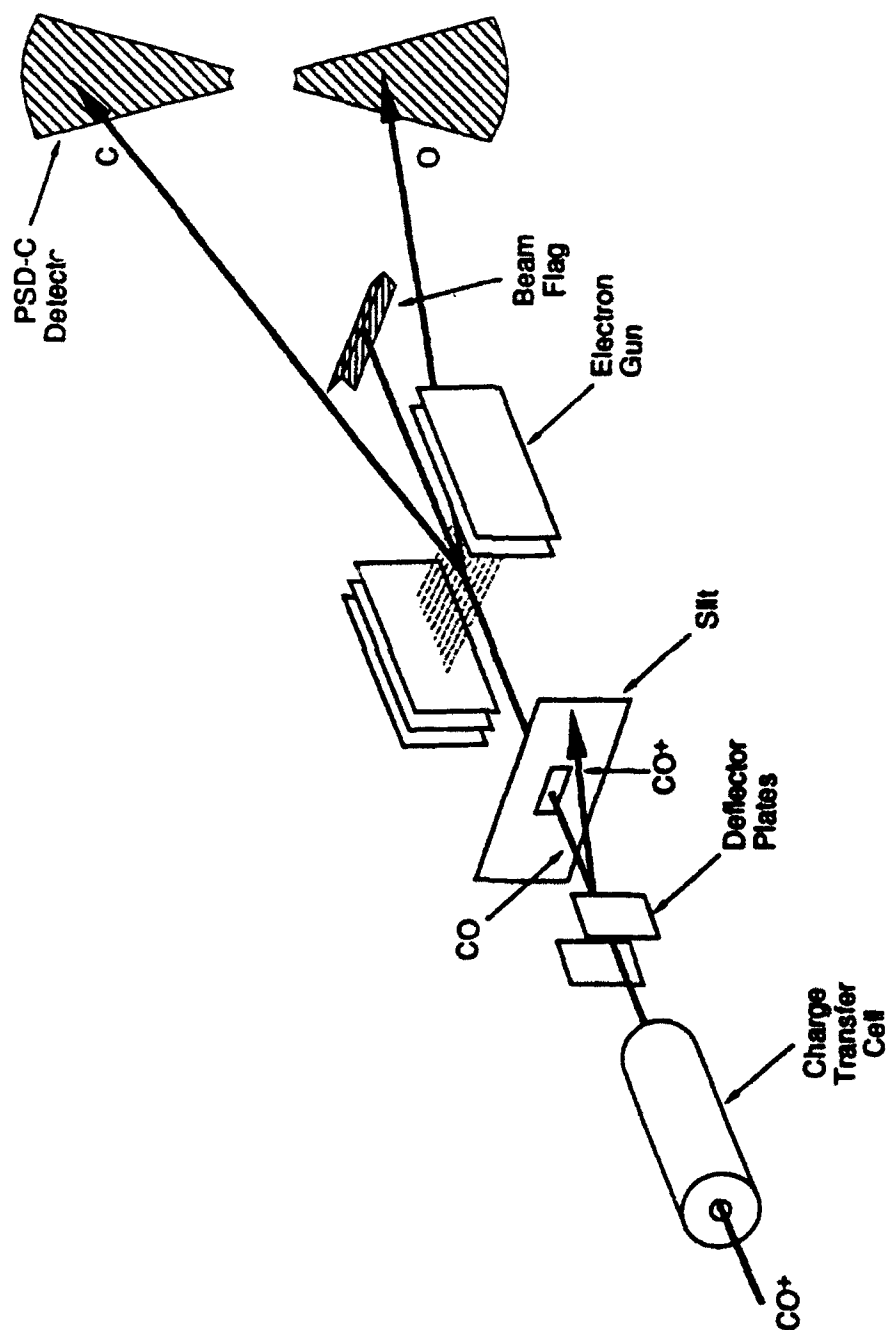


Figure 9. Diagram of the electron-impact dissociation apparatus. A fast (keV) CO beam, produced by charge transfer neutralization of CO^+ , is intersected by an electron beam. The correlated fragments C and O from dissociation of individual CO molecules are spatially and temporally detected at the position-sensitive detector for correlated fragments (PSD-C). Undissociated CO molecules are intercepted by the beam flag. The bolometer, Faraday cup, and charged particle deflection plates in the region downstream of the electron beam are not shown.

the electron beam direction oriented along the direction of the PSD-C active area, a preferential collection of the fragments from this transition is expected. Measurements are made for electron-impact dissociation with both orientations of the electron beam.

An unexpected outcome of the present research has been that, for all molecules thus far studied, the fragments appear with a Θ -distribution characteristic of an isotropic distribution in the center-of-mass frame. Furthermore, the total electron dissociation cross sections obtained from the two electron beam orientations are found to be equal to within their nominal accuracy (20%-30%), as would be expected from an isotropic fragment distribution. These results suggest that the electron velocity vectors are not orthogonal to the neutral beam velocity. While there is a geometric constraint along the narrow width of the beam that would limit linear electron trajectories to a maximum deviation from orthogonality of approximately 12° at beam intersection, the very long length of the electron beam along the neutral beam direction (2.6 cm) provides effectively no angular constraint in the plane of the neutral beam. In view of these findings, we interpret the collection of dissociation fragments as arising from an isotropic distribution in the center-of-mass frame of the molecule, but we acknowledge the possibility of undetected anisotropies in assessing the absolute errors in the measurement.

Coincidence Efficiency

Fast neutrals striking an active area of the detector create secondary electrons that are amplified by the microchannel plates and provide both a fast timing signal and a position-dependent signal that must be detected and interpreted. The efficiency in converting a neutral impact into a detected electrical signal is an independent characteristic of each half of the detector.²¹ For the case of a molecular dissociation producing a flux of D fragment pairs striking an active region of the detector, the apparent fluxes of detected fragments on the two detector halves are:

$$\begin{aligned} C_1 &= D \cdot p_1 \\ C_2 &= D \cdot p_2 \end{aligned} \tag{12}$$

where p_1 and p_2 are the efficiencies on each half of the detector for converting fragment impacts to detected events. The apparent coincidence flux, where both fragments from the same molecule have produced detectable signals, is:

$$C = D \cdot p_1 \cdot p_2. \tag{13}$$

Taking the ratio of the apparent coincidence flux to the apparent fragment flux on each half of the detector yields a direct measure of the individual efficiencies:

$$\begin{aligned}\rho_2 &= C/C_1 \\ \rho_1 &= C/C_2.\end{aligned}\tag{14}$$

This measurement can be made with any well-defined source of dissociation events. In practice, we use molecular photodissociation as the source because of the ease with which a substantial flux of fragments can be generated and modulated. The coincidence efficiency $\xi = \rho_1 \rho_2$ is explicitly dependent on fragment velocity (which is effectively the same as that of the parent molecule). However, we operate at sufficiently high velocities that fragment mass, charge, and electronic excitation have little effect on ξ , which can generally be determined to within 5% accuracy.

DISSOCIATION CROSS SECTION DETERMINATION

The cross section σ for electron-impact dissociation occurring in a crossed molecular and ion beam is given²⁵ by the equation:

$$\sigma = \frac{R F}{N_e N_n M},\tag{15}$$

where R , N_e , and N_n are the flux of products, electrons, and neutral molecules, respectively, M is a velocity factor:

$$M = \frac{\sqrt{v_e^2 + v_n^2 - 2v_e v_n \cos\theta}}{v_e v_n \sin\theta},\tag{16}$$

where v_e and v_n are the velocities of the electron and neutral beams and θ is their angle of intersection. For orthogonal beams where $v_e > v_n$, as in the present experiment, $M \sim v_n^{-1}$. The form factor F describing the overlap of the two beams is given by:

$$F = \frac{N_e N_n}{\int_{-\infty}^{\infty} n_e(z) n_n(z) dz},\tag{17}$$

where $n_e(z)$ and $n_n(z)$ are the differential fluxes of the electron and neutral beams along the direction mutually orthogonal to both beams, z . Since the profile of the electron beam can be determined directly, as discussed above, and the neutral beam profile can be accurately calculated from the slit dimensions and measured angular divergence, the cross section could be calculated directly from Eq. (15). However, small changes in the profile of the electron beam can introduce large errors in the cross section through the form factor F . Defrance et al.²⁶ and Müller et al.¹⁹ have shown that the ability to accurately translate the electron beam completely through the region of intersection allows the uncertainties introduced by F to be completely avoided in the cross section measurement. From their derivation, if the total number of dissociation fragments N is accumulated as the position of the electron beam is moved at a constant velocity u along the z direction through the region of intersection of the two beams, then the dissociation cross section is given by:

$$\sigma = \frac{N u}{M N_e N_n} \sim \frac{N u v_n}{N_e N_n}, \quad (18)$$

provided the starting and ending positions of the electron beam are totally beyond the range of overlap. In terms of the experimental observables, i.e., the number of detected dissociation fragment pairs (N^*), the neutral current at the Faraday cup I_{fc} , and the electron beam current I_e , the cross section σ is:

$$\sigma = \frac{N^* u v_n \eta e}{\xi \chi I_e I_{fc}}, \quad (19)$$

where e is the electron charge and the other symbols have been defined above. In practice, the electron beam position is scanned in a series of m discrete steps, with the N^* dissociation products accumulated for a selected time interval τ at each position z . To exclude electron-independent dissociation products from the accumulated total fragments, the (position independent) background dissociation flux N_{bkg} is accumulated during the scan for a period of 5τ with the electron beam positioned at the scan starting position z_0 , ending position z_m , or alternately at z_0 and z_m after each five steps of the electron gun:

$$N^* = \sum_{k=0}^{m/5} \left[\sum_{i=5k}^{5k+4} N^*(z_k, \tau) - N^*_{bkg}(z_0, 5\tau) \right]. \quad (20)$$

The significance of modulo 5 in the summation is only as a compromise between minimizing the rather significant period of time required to reposition the electron gun to its starting or

ending location with the micrometer drive (1-2 s) and maintaining an accurate sample of the dissociation background flux throughout the scan. Typically, $500 \leq m \leq 3000$, $1s \leq t \leq 3s$, $|z_m - z_0| \geq 0.48$ cm and $u = |z_m - z_0|/m\tau \leq 9.8 \times 10^{-4}$ cm/s.

A typical accumulation of N^* as a function of electron gun position is shown in Figure 10 for CO interacting with 48.5 eV electrons. The data points in this figure are the values of the argument of the summation over k in Eq. (20), i.e., after each background subtraction. Error bars associated with the data points in Figure 10 represent the statistical error arising from the background subtraction, and they increase in both relative and absolute value with increasing scan distance after the electron beam has completely passed through the neutral beam. The value of N^* for the cross section calculation is determined from the onset of the linear region after the electron beam has passed completely through the neutral beam.

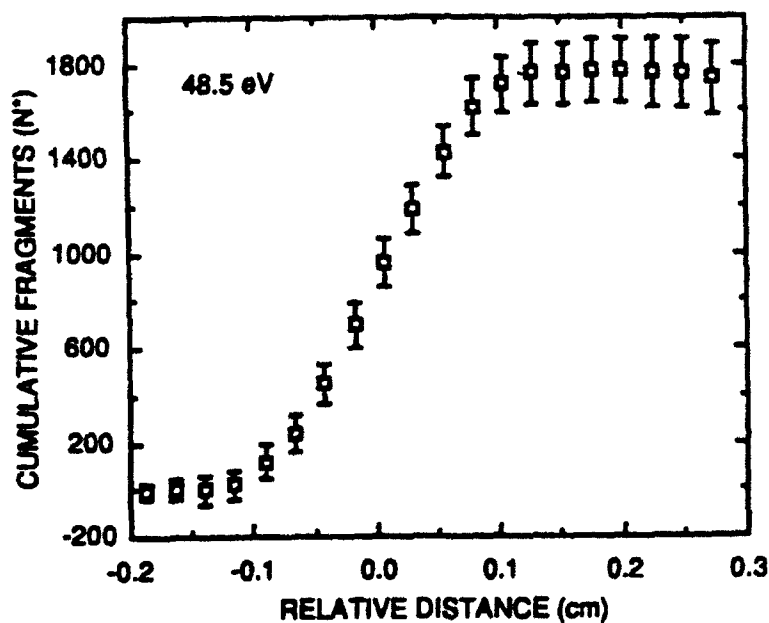


Figure 10. Accumulation of C + O electron-impact dissociation products (N^*) as the electron gun is translated across the CO beam at a constant velocity. The data points refer to N^* evaluated after 5 successive positions of the electron gun. The electron beam energy is 48.5 eV. The error bars refer to the statistical error in N^* .

3. RESULTS AND DISCUSSION

CARBON MONOXIDE

The electron-impact dissociation of CO to form C and O atoms was observed at electron energies between the dissociation threshold (14 eV) and 198.5 eV. The center-of-mass energy released in the dissociation of individual molecules was explicitly measured. The observed energy release distribution was found to be highly structured, reflecting electron-impact excitation to Rydberg states converging to $\text{CO}^+(\text{X}^2\Sigma^+)$, which predissociate to ground state atoms. Little or no dissociation is observed from states above the first ionization limit or from continuum states. We measured total-electron impact dissociation cross sections, exclusive of dissociative ionization contributions, and partial cross sections for the dissociative excitation of specific CO electronic states.

These results are discussed in detail in the manuscript attached to this report as Appendix D, which has been accepted for publication in *The Journal of Chemical Physics*.

NITROGEN

The electron-impact dissociation of N_2 to form two nitrogen atoms was observed at electron energies between 18.5 eV and 148.5 eV. The observed translational energy releases in the N_2 dissociation are consistent with predissociation to $\text{N}(^2\text{D}) + \text{N}(^4\text{S})$ fragments as the primary dissociation mechanism. Little or no dissociation is observed from states above the first dissociation limit or from continuum states. This was also found to be the case for the isoelectronic CO molecule. Absolute cross sections for the electron-impact dissociation were measured and compared with previous measurements. Recommended values of this cross section are given for electron-impact energies between 10 eV and 200 eV.

These results are presented in the manuscript attached to this report as Appendix F, which has been submitted for publication in *The Journal of Chemical Physics*.

OXYGEN

The electron-impact dissociation of O_2 to form two oxygen atoms was observed at electron energies between 13.5 eV and 198.5 eV. The observed translational energy releases in the O_2 dissociation are consistent with production of $\text{O}(^1\text{D}) + \text{O}(^3\text{P})$ fragments following

electron impact excitation to the $B^3\Sigma_u^-$, $B'^3\Sigma_u^-$, and $2^3\Pi_u$ states and production of $O(^3P) + O(^3P)$ fragments from excitation to the (unresolved) $c^1\Sigma_u^-$, $A'^3\Delta_u$, and $A^3\Sigma_u^+$ states. Absolute cross sections for the electron-impact dissociation of O_2 were measured.

These results are presented in the manuscript attached to this report as Appendix G, which has been submitted for publication in *The Journal of Chemical Physics*.

CHLORINE

Measurements were made for the electron-impact dissociation of Cl_2 molecules. These molecules were produced in a fast beam by the charge-transfer neutralization of Cl_2^+ in Cl_2 gas. Because of the highly reactive nature of Cl_2 gas, use of the hollow-cathode ion source to produce a ground state Cl_2^+ beam was not feasible. Rather, the ions were formed in the electron-impact source, and photofragment spectroscopy was used to assay the composition of the fast Cl_2 beam.

The center-of-mass translational energy (W) distribution of the fragments from the reaction:



is shown in Figure 11 for three electron energies, 12.4 eV, 17.4 eV, and 48 eV. The low energy spectrum is characterized by a broad fragment energy release peaking near $W \sim 1$ eV and extending to approximately $W = 4$ eV. The higher energy spectra yield a similar broad energy release, but also contain substantial additional contributions in the $W = 5-9$ eV region and at $W < 1$ eV.

Interpretation of the energy release spectra is best understood in terms of the electronic states of Cl_2 that are accessible in the electron impact. These are shown schematically in Figure 12, together with the 17.4-eV fragment energy release spectrum. Only the lowest separated atom limit, $Cl(^2P) + Cl(^2P)$, is shown in the figure; higher dissociation limits in the molecule lie above the ionization limit. Figure 12 shows that vertical excitations from the $X^1\Sigma_g^+$ ground electronic state to the dissociative $D^1\Pi_u$ state and to the repulsive wall of the weakly-bound $A, A', B^3\Pi_u$ states give rise to the broad fragment energy release at $0 \leq W \leq 4$ eV that is the principle dissociation mechanism at all electron energies. The fragment energy release from the D state should peak near $W = 1$ eV, while that from the $A, A', B^3\Pi_u$ state should peak near $W \sim 0$, as indicated by the arrows in this figure. Explicit deconvolution of these two contributions finds equal contributions from these two states in the 12.4-eV spectrum, with a substantially smaller contribution from the triplet state in the 17.4-eV spectrum.

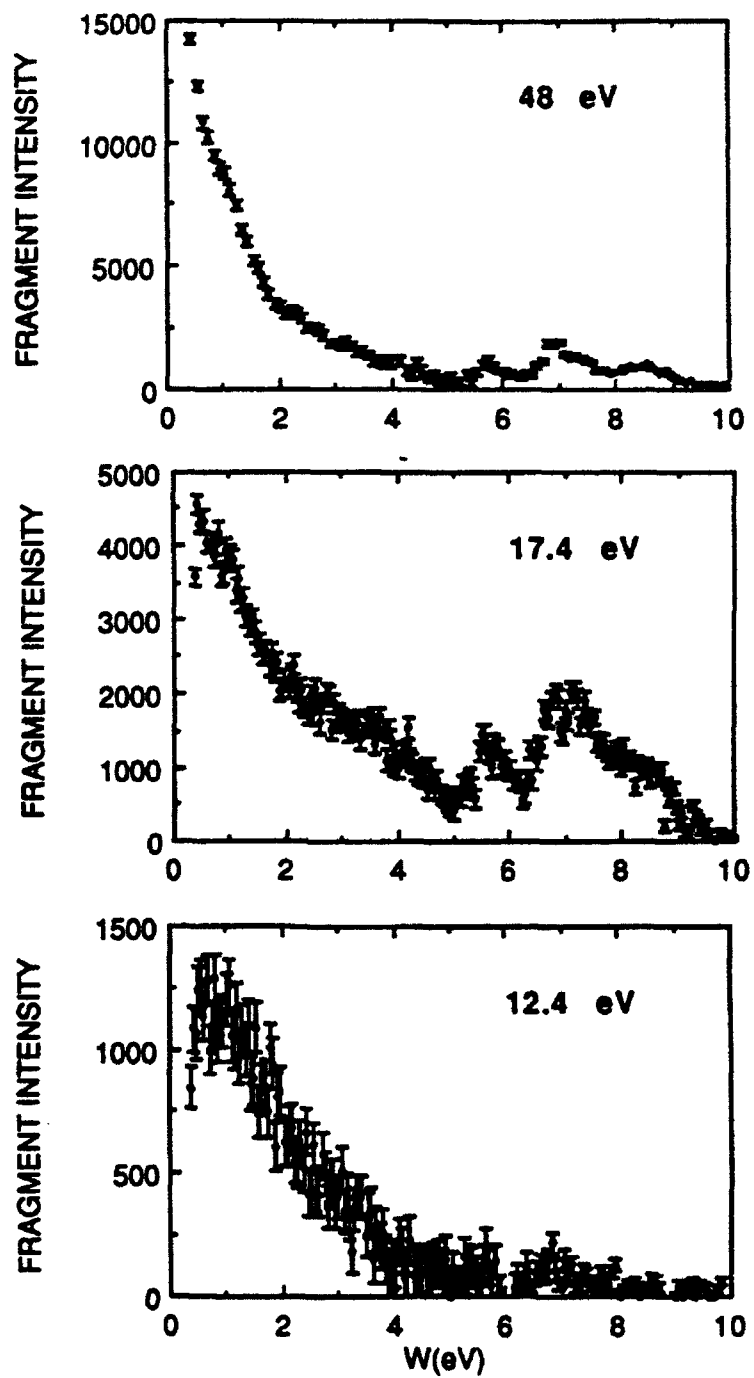


Figure 11. Fragment translational energy releases observed in the electron-impact dissociation of Cl_2 at three electron energies.

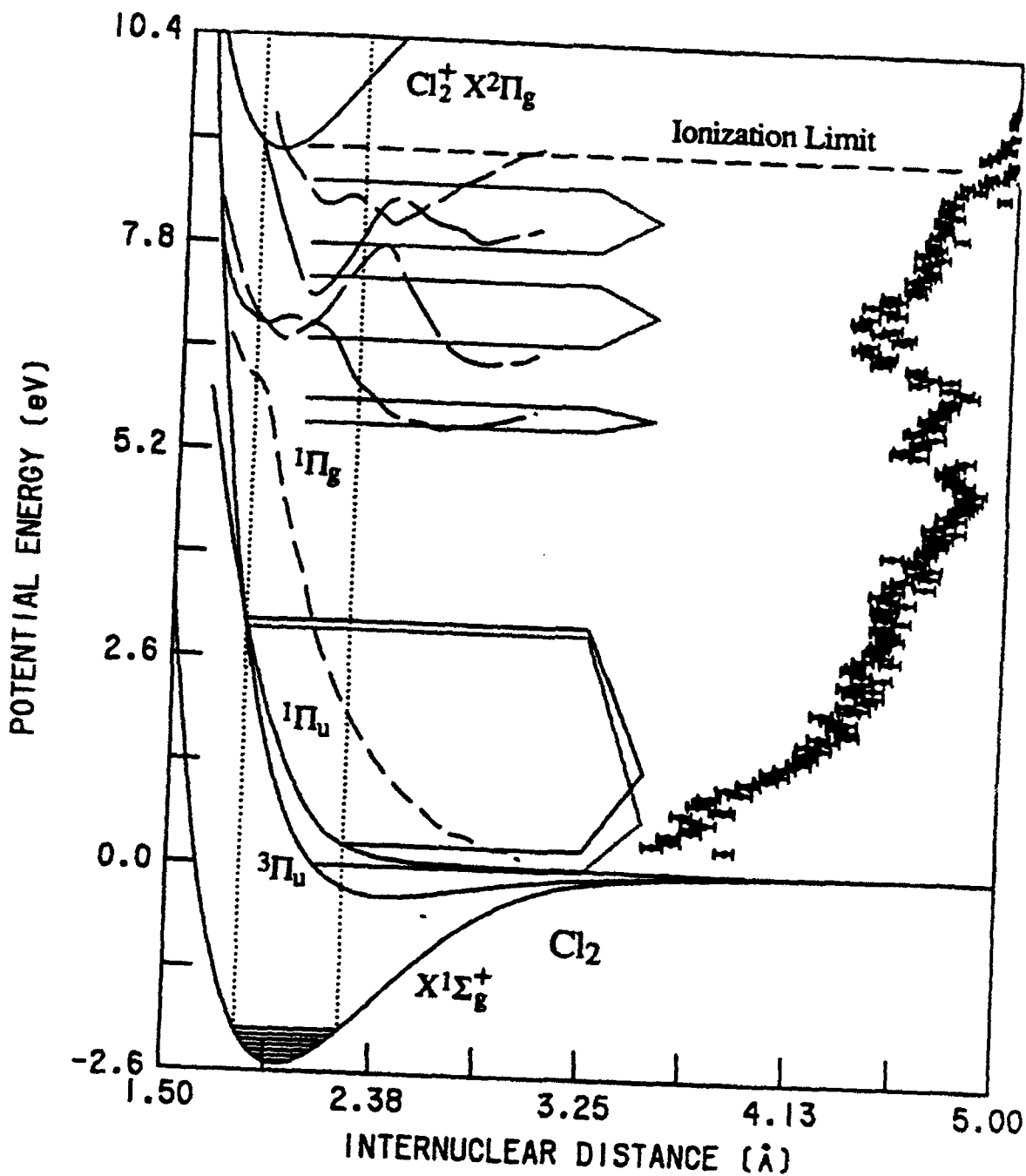


Figure 12. Potential energy curves of selected electronic states of Cl_2 and the ground electronic state of Cl_2^+ . The nearly-degenerate A, A', B $3\Pi_u$ states are represented in the figure by a single potential energy curve labelled $3\Pi_u$. The vertical transition region accessible from the distribution of vibrational levels populated in the Cl_2 beam is indicated, together with several possible dissociation channels. The observed energy release spectrum following dissociation of Cl_2 by 17.4-eV electrons is shown to scale along the energy ordinate.

Significant fragmentation also arises from excitation to higher lying $1\Sigma_u^+$ and $1\Pi_u$ states. These states in Cl_2 are characterized by strong Rydberg-ion pair-valence state interactions. The *ab initio* curves of Peyerimhoff and Buenker²⁷ in this region are shown in Figure 12 for reference. Electron-impact excitation followed by rapid predissociation of two or more states in this region likely accounts for the $W = 7.0$ and 8.2 eV energy releases. No bound states are expected in the region of the $W = 5.7$ eV energy release. However, the $1^1\Sigma_u^+$ state exhibits Condon oscillations in its fluorescence spectrum,²⁸ suggesting radiation into a continuum. The $W = 5.7$ eV energy release could reflect electron-impact excitation of the $1^1\Sigma_u^+$ followed by $1^1\Sigma_u^+ \rightarrow 1^1\Pi_g$ fluorescence. The *ab initio* potential energy curve²⁷ of the dissociative $1^1\Pi_g$ state is given by the dashed curve in the figure.

A comparison of the fragment distributions in Figure 11 for 17.4 eV and 48-eV electron-impact energies shows a relative increase in the number of very low W energy fragments with the higher electron-impact energy. It is unlikely that these arise from direct excitation to the triplet continua, since the cross section for this spin-exchange process should rapidly decrease with increasing electron energy above threshold. More likely, these fragments arise from the radiative decay of electron-excited Rydberg and ion pair states into the lower dissociative continua. This explanation would be consistent with the fact that the increase in low W fragments is roughly proportional to those features in the energy release spectrum that are attributed to predissociated Rydberg states.

Of particular note, negligible fragment energy releases are found from regions above the lowest ionization energy of Cl_2 , which is indicated by the dashed horizontal line in Figure 12. This is also found explicitly in the electron-impact dissociation of CO and of O_2 .²⁹ This suggests that highly excited molecular states, produced by electron impact, autoionize more rapidly than they dissociate. The autoionization products or dissociative autoionization products are specifically excluded from the detector because they are charged.

The absolute cross section for electron-impact dissociation of Cl_2 , Reaction (21), is shown in Figure 13 as a function of electron energy. The error bars in this figure give the total estimated error (absolute and relative) in the cross-section measurements. The electron energy dependence of the cross section is unusual in two respects. First, the cross section remains quite large at very small electron energies. The present measurements could be reliably extended only as low as 8 eV before the width of the electron beam exceeded our ability to fully integrate its form factor. We can state only that the dissociation threshold is below this value. A low dissociation threshold is, of course, consistent with the relatively low dissociation energy of the Cl_2 molecule ($D_0 = 2.48$ eV) relative to other molecules studied. The second unusual feature is

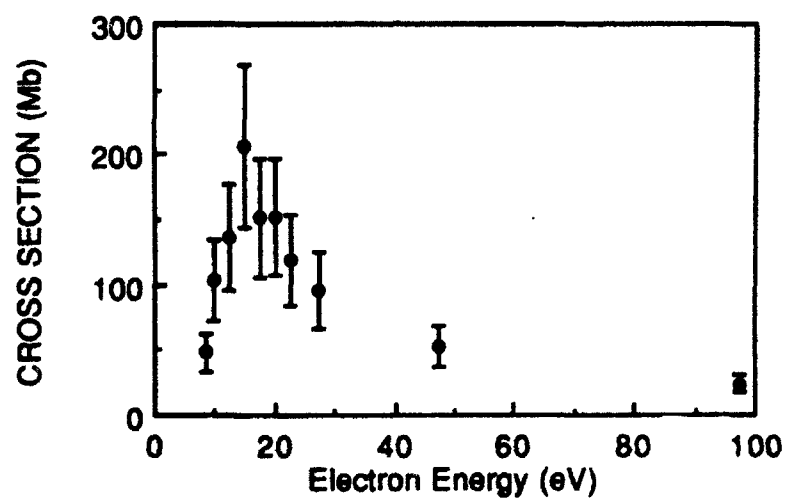


Figure 13. Total cross section for the electron-impact dissociation of Cl_2 as a function of electron energy. The error bars indicate the estimated absolute uncertainty in the measured values. $1 \text{ Mb} = 1 \times 10^{-18} \text{ cm}^2$.

that the cross section peaks abruptly at electron energies near 15 eV, and this behavior is reproducible. Although considerable effort has been made to detect an asymmetry in the fragment angular distribution that might account for such a feature, no such asymmetry has been found.

A manuscript detailing the measurements of photodissociation and electron-impact dissociation of Cl₂ is in preparation.

CARBON DIOXIDE

Electron-impact dissociation of CO₂ was studied over the electron energy range of 12.4 eV to 200 eV. The molecule was formed by charge transfer neutralization of CO₂⁺ ions in CO₂ gas. Production of the CO₂⁺ precursor with the hollow-cathode ion source was found to be too unstable to allow the extended period of beam operation required for the measurements; consequently, all measurements were made with CO₂⁺ formed in the electron-impact ion source. The fast neutral beam produced by charge transfer was probed by electron-impact ionization (see Section 2), demonstrating that the beam consisted of only a single component (CO₂). Observation of the distance ratio of the electron dissociation products, Eq. (8), further demonstrated that the primary (>95%) dissociation reaction is:



The fragment energy release distribution (W) observed for Reaction (22) at 50-eV electron impact is shown at the top of Figure 14. This distribution maximizes below the minimum energy release (W = 0.2 eV) observable by the PSD-C. The dashed line in this figure represents the presumed propagation of the fragment distribution within the unobserved 0 ≤ W ≤ 0.2 eV energy range. With this extrapolation, the mean energy release observed for the CO + O dissociation fragments is W = 0.73 eV and 90% of the fragments are produced with W ≤ 1.71 eV.

The dissociation energy of CO₂ is 5.349 eV, but production of ground state products CO(X¹Σ⁺) + O(³P) is spin-forbidden from the singlet electronic states in this molecule. Although electronic excitation of CO₂ by electron impact has an onset near 7 eV, the strongest excitation channels occur to those excited states lying between 11 eV and the ionization limit at 13.77 eV above the ground electronic state, as evidenced by electron energy loss spectroscopy.^{30,31} States in this region have access to the higher dissociation channels of CO₂: CO(X) + O(¹S) at 9.539 eV and CO(a³Π) + O(³P) at 11.385 eV. Photoexcitation studies indeed find that O(¹S) and CO(a) are the dominant photodissociation products.^{32,33} If the energy-dependent quantum yields for production of these two excited species are folded with the CO₂

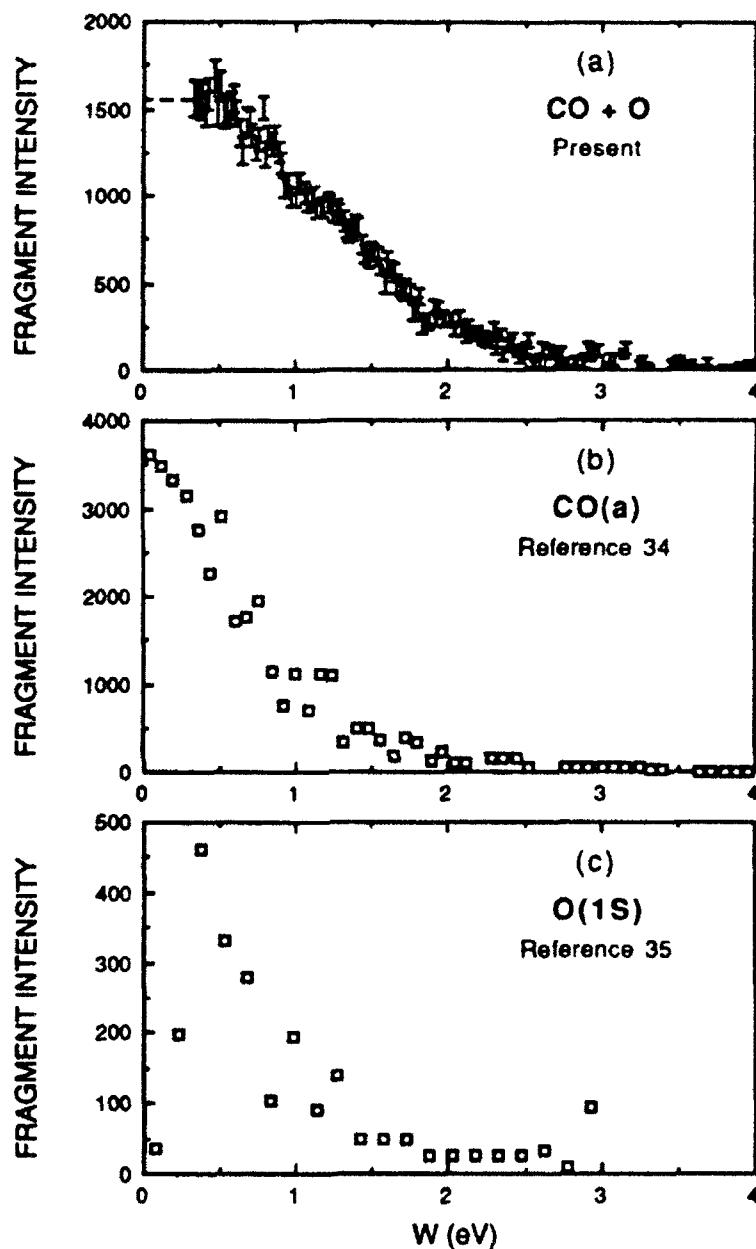
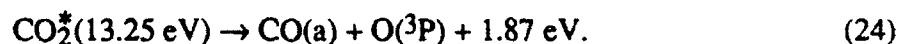
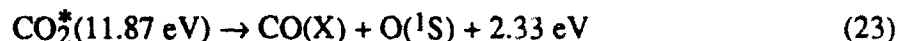


Figure 14. Fragment energy releases observed in the dissociation of CO_2 . The top spectrum is that observed in the present work for the production of $\text{CO} + \text{O}$ fragments following 50-eV electron impact. The center spectrum is that observed by Freund (Ref. 34) for the production of $\text{CO}(a^3\Pi_u)$ following electron impact. The bottom spectrum is that observed for the production of $\text{O}(1\text{S})$ fragments by Welge and Gilpin (Ref. 35) following photon impact.

electron-impact excitation spectrum, $O(^1S)$ and $CO(a)$ are predicted to represent 73% and 27%, respectively, of the dissociation products from CO_2^* electronic states with mean excitation energies of 11.87 eV and 13.25 eV. Subtracting the respective dissociation thresholds from these values yields total average energies for the products:



These average product energies (2.33 eV and 1.87 eV) must be partitioned between translational energy and rovibrational energy of the CO fragment in its respective electronic state. From the fragment translational energy spectrum (top of Figure 14), the average translational energy is 0.73 eV. If the partitioning between translational and rovibrational energy is equal in reactions (23) and (24), this value would suggest that the $CO(X)$ and $CO(a)$ products are produced with average internal energies of 1.6 eV ($X^1\Sigma^+$, $v \sim 5$) and 1.14 eV ($a^3\Pi_u$, $v \sim 4$), respectively.

Freund³⁴ observed the time-of-flight velocity distribution of $CO(a)$ products from the electron-impact dissociation of CO_2 . For comparison, his velocity distribution transformed into a W distribution is shown at the center of Figure 14. This energy release distribution in the $CO(a)$ channel is somewhat narrower than that observed for all product channels (top of Figure 14), with a mean energy release of 0.56 eV and 90% of the products formed with energy releases ≤ 1.63 eV. If we presume that $CO(a)$ does indeed constitute 27% of the dissociation products, as discussed above, and we normalize these two distributions accordingly and subtract them, the resulting " $O(^1S)$ " distribution yields a mean translational energy release of 0.86 eV, with 90% of the fragmentation occurring with $W \leq 1.82$ eV. Welge and Gilpin³⁵ obtained a velocity distribution for an O atom fragment, believed to be $O(^1S)$, produced in the photodissociation of CO_2 at photon energies estimated to lie in the range 10.68-11.80 eV. Their distribution, transformed to W and shown at the bottom of Figure 14, is somewhat narrower than the difference spectrum, with a mean translational energy release of 0.64 eV, but is generally in accord with the above presumptions.

The absolute cross section measured for the dissociation of CO_2 , Reaction (22), is shown by the solid points in Figure 15. The error bars in this figure reflect the statistical uncertainties in the cross section. The total absolute uncertainty is $\pm 30\%$, which includes the presumed error in extrapolating the fragment energy distribution into the unobserved $0 \leq W \leq 0.2$ eV region. The dissociation cross section rises rapidly with electron energy from a threshold near 12.0 ± 0.8 eV to a maximum value of 0.94 \AA^2 near 25 eV. Both the energy dependence of the cross section and its magnitude are considerably different from those derived from early discharge

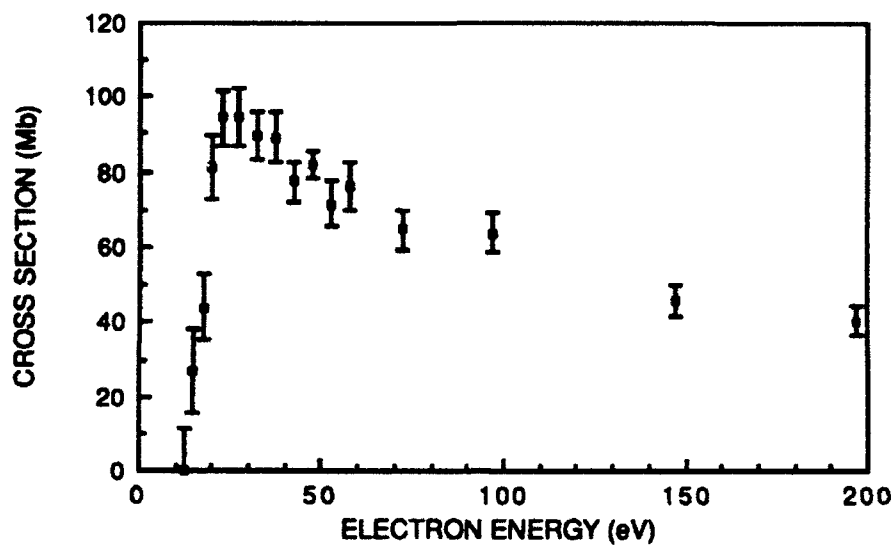


Figure 15. Total cross section for the electron-impact dissociation of CO₂ as a function of electron energy. The error bars indicate the statistical uncertainty in the measured values. 1 Mb = 1×10^{-18} cm².

observations.^{36,37} If we apply the above estimates of 73% and 27% for the partitioning of the CO₂ dissociation between Reactions (23) and (24), then we can derive partial cross sections from the total dissociation cross section given in Figure 15. Using this procedure, we would expect a partial dissociation cross section in the range of 18-33 Mb for the production of CO(*a*³Π) following 27-eV electron impact. This value compares favorably with the *estimated* cross section of 40 Mb reported by Freund³⁴ for the production of CO(*a*) at this electron energy. Thus the presumption that the dissociation dynamics of CO₂ are similar following electron-impact excitation and photoexcitation appears to be largely justified. A paper describing this work is in preparation.

NITROGEN DIOXIDE

Electron-impact dissociation of NO₂ was observed over the electron energy range of 12.5 eV to 100 eV. The NO₂ molecules were created by charge transfer neutralization of NO₂⁺ in NO₂ gas, furan (C₄H₄O) vapor, or mesitylene (1,3,5-trimethylbenzene) vapor. The latter two compounds were found to yield a substantially higher (>3) flux of charge transfer products than the NO₂ gas target. Ionization measurements of the neutral beam indicated that only one species, >95% NO₂, constituted the fast neutral beam. All measurements were made with the NO₂⁺ precursor formed by electron-impact ionization of NO₂ gas. Efforts to produce a stable beam of this ion with the hollow-cathode ion source were unsuccessful.

Figure 16 shows fragment energy release spectrum observed for 48.5-eV electron impact on the NO₂ beam. This distribution is also characteristic of electron impact at other electron energies in the range of 25-100 eV. Although the energy distribution of spontaneous dissociation fragments varied somewhat with the choice of charge-transfer target, the fragment energy distribution was found to be independent of whether the charge transfer neutralization occurred in NO₂, furan, or mesitylene. The fragment distribution maximizes at low energy releases. If we presume that this distribution extrapolates smoothly into the unobserved 0 ≤ W ≤ 0.3 eV region, the average translational energy release is found to be W ~ 0.84 eV.

The electron-impact energy loss spectrum of NO₂ was studied by Rianda et al.³⁸ Their spectrum shows several broad features at excitation energies between approximately 3 eV and the ionization limit at 9.78 eV, which are assigned to various electronic states of NO₂. If we integrate this excitation spectrum over states lying between the lowest dissociation limit of NO₂, production of NO(*X*²Π) + O(³P) at 3.13 eV, and the ionization limit, we obtain an average excitation energy of 7.94 eV for electron impact substantially above threshold. Given this excitation energy, the following dissociation channels of NO₂ are accessible:

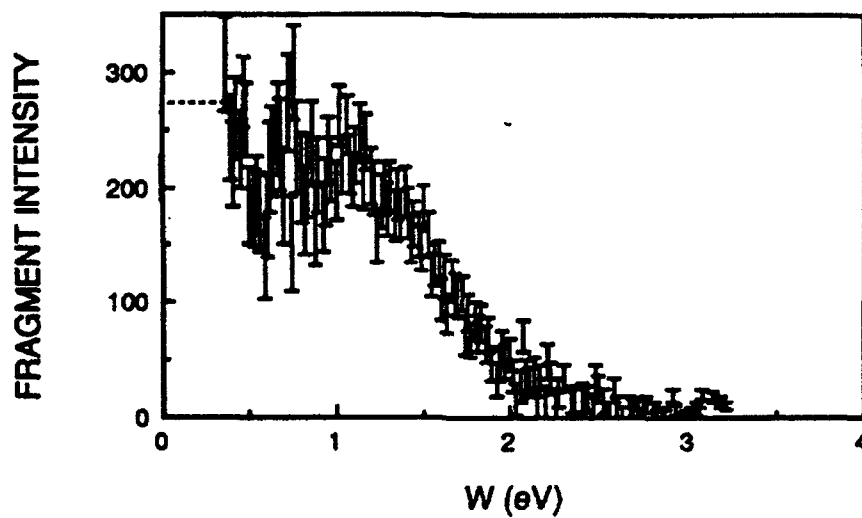


Figure 16. Fragment energy releases observed in the dissociation of NO_2 following 50-eV electron impact.

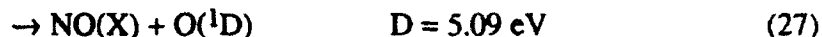
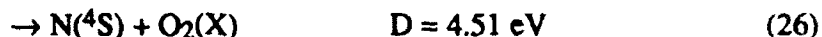


Figure 17 shows the distribution of mass ratios observed in the electron-impact dissociation of NO_2 . The dominant flux of fragments peaks at a ratio near 1.875, corresponding to the production of $\text{NO} + \text{O}$ products. The distribution is broad and overlaps the region in which the ratio of 2.286, corresponding to the production of $\text{N} + \text{O}_2$, would appear. However, there is clearly no explicit contribution to the mass ratio distribution in this region, suggesting that reaction (26), if it occurs at all, will account for <10% of the electron dissociation products.

Neither the mass ratio distribution nor the fragment energy distribution can explicitly identify the electronic states of the dissociation products. However, state-specific photofragment studies³⁹ following excitation of NO_2 by 157-nm (7.87-eV) photons have set limits on the production of $\text{O}({}^1\text{D})$ and $\text{O}({}^1\text{S})$ fragments at $\leq 10\%$ and $\leq 1\%$, respectively. Thus the dominant dissociation channel appears to be reaction (25). Given the mean excitation energy of 7.94 eV and the dissociation energy in reaction (25), the $\text{NO}(\text{X}) + \text{O}({}^3\text{P})$ fragments would be produced with a mean excess energy of 4.81 eV, of which only 0.84 eV is found to appear as translational energy. Thus ~83% of the excess energy, on average, must be accounted for as vibrational and rotational excitation of the $\text{NO}(\text{X}^2\Pi)$ product. This is consistent with the finding in the photodissociation study³⁹ that the $\text{NO X}^2\Pi$ state is strongly populated in vibrational levels up to the thermodynamic limit.

Figure 18 shows the cross section measured for electron-impact dissociation of NO_2 as a function of electron impact energy. The error bars associated with the points in this figure indicate the total absolute error estimated for the measurements.

A manuscript describing this work is in preparation.

OTHER MOLECULES

Measurement of the electron-impact dissociation of H_2 , NO , CF , CF_2 , CF_3 , NF , and NF_2 was attempted during the present studies. However, no useful information was obtained for any of these species. The predominant difficulty in their measurement arises from a very high flux of spontaneous dissociation products that are encountered in the fast beam. Under these conditions, a statistically significant measurement of the electron-impact dissociation products cannot be

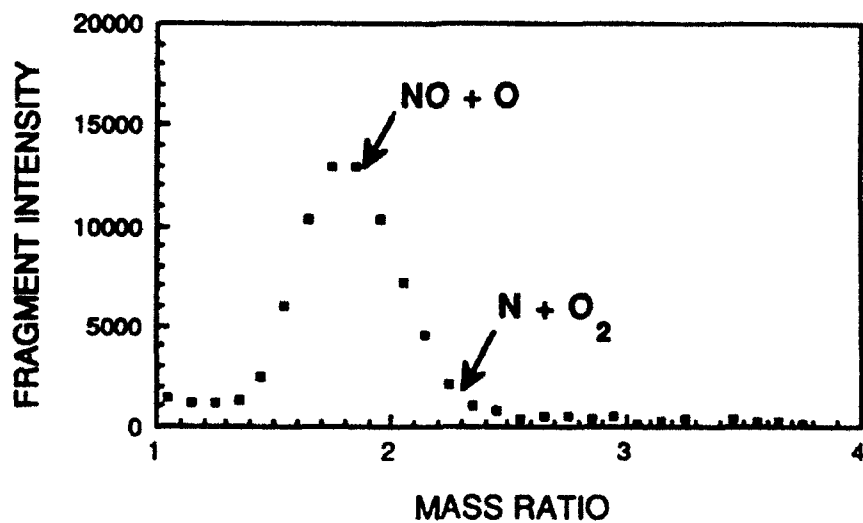


Figure 17. Distribution of the mass ratios of the NO₂ dissociation products following 50 eV electron impact. The expected ratios for two dissociation channels are indicated.

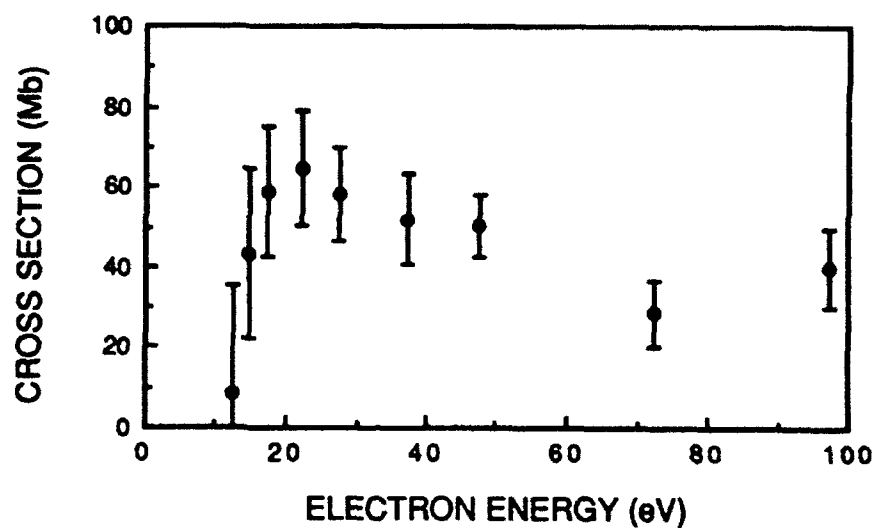


Figure 18. Total cross section for the electron-impact dissociation of NO₂ as a function of electron energy. The error bars indicate the estimated absolute uncertainty in the measured values. 1 Mb = 1×10^{-18} cm².

achieved within a time period (~24 hours) in which other experimental variables, such as neutral beam flux and direction, remain relatively constant.

For the case of H_2 , the spontaneous fragmentation is found to occur from levels of the $c^3\Pi_u$ state that decay with a lifetime in the range of 100 μs to 1 ms by both predissociation⁴⁰ and radiation into dissociative states.⁴¹ Production of this state, which is populated only in trace quantities within the products of H_2^+ charge transfer neutralization, could not be reduced to acceptable levels by varying either the choice of neutralizing gas or the method of H_2^+ production. Furthermore, electrostatic quenching⁴² of the state is not practical for a beam at keV energies. Further measurements with this species would require a highly accurate compensation for detector dead time.

Spontaneous dissociation of NO is discussed briefly in Appendix C. The spontaneous dissociation appears to occur from NO states that would be formed by charge-transfer neutralization of metastable NO^+ states, rather than from the ion ground electronic state. Production of the NO^+ from the high pressure hollow-cathode discharge is, therefore, likely to eliminate much of the spontaneous dissociation. However, we have been unable to produce a stable NO^+ beam with this source. NO^+ was generated with electron impact on NO gas, NO_2 gas, and N_2O gas. In each case, substantially the same spontaneous fragmentation was observed from the neutralized beam. Preliminary investigation of the dissociative charge transfer products from neutralization of these NO^+ beams in Cs vapor, a technique we have applied successfully in the diagnostics of O_2^+ beams,¹⁰ seems to confirm that similar NO^+ state distributions are formed in the ionization of each of these gases. It is probable that modification of the electron impact source for higher pressure operation would allow production of an electronically relaxed NO^+ precursor.

Further studies of CF_n and NF_n are also predicated on the ability to produce the parent ion beams under conditions of minimal electronic excitation.

REFERENCES

1. E. C. Zipf, "Dissociation of Molecules by Electron-Impact," Chapter 4 in *Electron-Molecule Interactions and Their Applications*, Vol. 1, L. G. Christophorou, Ed. (Academic, Orlando, 1984).
2. R. N. Compton and J. N. Bardsley, "Dissociation of Molecules by Slow Electrons," Chapter 4 in *Electron Molecule Collisions*, I. Shimamura and K. Takayanagi, Eds. (Plenum, NY, 1984).
3. S.J.B. Corrigan, J. Chem. Phys. **43**, 4381 (1965).
4. H. F. Winters, J. Chem. Phys. **44**, 1472 (1966).
5. H. F. Winters, J. Chem. Phys. **63**, 3462 (1975).
6. H. F. Winters and M. Inokuti, Phys. Rev. A **25**, 1420 (1982).
7. A. Niehaus, Z. Naturforschung **22a**, 690 (1967).
8. T. Nakano, H. Toyoda, and H. Sugai, Jap. J. Appl. Phys. **30**, 2908; 2912 (1991).
9. Colutron, Model 101Q, Boulder, CO.
10. C. W. Walter, P. C. Cosby, and J. R. Peterson, J. Chem. Phys. **98**, 2860 (1993).
11. H. Helm, Phys. Rev. A **38**, 3425 (1988).
12. K. H. Berkner, B. R. Myers, and R. V. Pyle, Rev. Sci. Instrum. **39**, 1204 (1968).
13. M. W. Geis, K. A. Smith, and R. D. Rundel, J. Phys. E **8**, 1011 (1975).
14. Gulton Industries Type G1512.
15. T. F. Moran, "Electron Transfer Reactions," Chapter 1 in *Electron-Molecule Interactions and Their Applications*, Vol. 2, L. G. Christophorou, Ed. (Academic, Orlando, 1984).
16. A. Ding and K. Richter, Z. Physik A **307**, 31 (1982).
17. D. P. de Bruijn, J. Neuteboom, V. Sidis, and J. Los, Chem. Phys. **85**, 215 (1984).
18. E. Saudrais and P. C. Cosby, "Photofragment Spectroscopy of Cl₂," (in preparation).
19. A. Müller, K. Huber, K. Tinschert, R. Becker, and E. Salzborn, J. Phys. B **18**, 2993 (1985).
20. H. Helm and P. C. Cosby, J. Chem. Phys. **86**, 6813 (1987).
21. D. P. deBruijn and J. Los, Rev. Sci. Instrum. **53**, 1020 (1982).

22. G. H. Dunn, Phys. Rev. Lett. **8**, 62 (1962).
23. R. N. Zare and D. R. Herschbach, Proc. IEEE **51**, 173 (1963).
24. S. Trajmar and D. C. Cartwright, "Excitation of Molecules by Electron Impact," Chapter 2 in *Electron-Molecule Interactions and Their Applications*, Vol. 1, L. G. Christophorou, Ed. (Academic, Orlando, 1984).
25. L. J. Kieffer and G. H. Dunn, Rev. Mod. Phys. **38**, 1 (1966).
26. P. Defrance, F. Brouillard, W. Claeys, and G. Van Wassenhove, J. Phys. B **14**, 103 (1981).
27. S. D. Peyerimhoff and R. J. Buenker, Chem. Phys. **56**, 279 (1981).
28. L. C. Lee, M. Suto, and K. Y. Tang, J. Chem. Phys. **84**, 5277 (1986).
29. The observed cut-off in the dissociation of N₂ occurs at energies somewhat below the ionization limit. This is consistent with a lack of dissociation from states above the ionization limit.
30. R. I. Hall, A. Chutjian, and S. Trajmar, J. Phys. B **6**, L264 (1973).
31. E. N. Lassette, A. Skerbele, M. A. Dillon, and K. J. Ross, J. Chem. Phys. **48**, 5066 (1968).
32. G. M. Lawrence, J. Chem. Phys. **56**, 3435 (1972).
33. G. M. Lawrence, J. Chem. Phys. **57**, 5616 (1972).
34. R. S. Freund, J. Chem. Phys. **55**, 3569 (1971).
35. K. H. Welge and R. Gilpin, J. Chem. Phys. **54**, 4224 (1971).
36. K. K. Corvin and S.J.B. Corrigan, J. Chem. Phys. **50**, 2570 (1969).
37. M. J. Barton and A. Von Engel, Phys. Lett. **32A**, 173 (1970).
38. R. Rianda, R. P. Frueholz, and A. Kuppermann, J. Chem. Phys. **79**, 5914 (1983).
39. M.-R. Taherian, P. C. Cosby, and T. G. Slanger, J. Phys. Chem. **91**, 2304 (1987).
40. L.-Y. C. Chiu, J. Chem. Phys. **40**, 2276 (1964).
41. R. P. Freis and J. R. Hiskes, Phys. Rev. A **2**, 573 (1970).
42. C. E. Johnson, Phys. Rev. A **9**, 576 (1974).

Appendix A

**PHOTOFRAGMENT SPECTROSCOPY OF O₂: EXCITATION OF THE SCHUMANN-
RUNGE BAND SYSTEM**

Photofragment spectroscopy of O₂: Excitation of the Schumann–Runge band system

P. C. Cosby and H. Helm

Molecular Physics Department, SRI International, Menlo Park, California 95025

(Received 9 May 1988; accepted 26 October 1988)

Photodissociation of O₂ is observed by direct detection of coincident neutral photofragments following laser excitation of a fast molecular beam. The O₂ beam was prepared by charge-transfer neutralization of keV energy O₂⁺ and irradiated by a linearly polarized, line selected Kr⁺ ion laser. Kinetic-energy resolved photofragments were observed at eight laser lines between 752.5 and 476.2 nm. Correlation of the observed fragment kinetic energies with laser wavelength shows that the observed photodissociations arise from O₂B³Σ_g⁻ (v' = 1–18) – X³Σ_g⁻ (v'' = 22–37) Schumann–Runge transitions.

INTRODUCTION

The B³Σ_g⁻–X³Σ_g⁻ “Schumann–Runge” (SR) system of O₂ has been the subject of a great many spectroscopic studies over the last 84 years.¹ The importance of this system arises from the fact that it accounts for the effective absorption of solar flux at wavelengths of > 176 nm.² Moreover, the upper state in this system is predissociated, allowing efficient conversion of solar photons into energetic O atoms in the mesosphere and thermosphere.³ Accurate modeling of the O atom production rate requires a precise knowledge of both line positions and linewidths in the SR absorption bands, but the unfortunate combination of poor Franck–Condon factors for absorptions from X(v'' = 0) and rapid predissociation of the B state relative to emission has frustrated the achievement of these goals.

The availability of an intense laboratory source of vibrationally excited O₂ would allow the observation of SR absorptions at visible wavelengths using narrow linewidth lasers and sub-Doppler techniques. This goal was partially achieved in the recent observation⁴ of SR absorption by laser-induced fluorescence in a flame. However, the resolution there was limited by the large Doppler and collisional linewidths associated with an atmospheric pressure flame.

We report here the production of vibrationally excited O₂ in its ground electronic state by the charge transfer of keV energy O₂⁺ in various target gases. The excited O₂ molecules are produced in a highly collimated fast beam allowing⁵ optical excitations with linewidths as narrow as 0.01 cm⁻¹. Photofragment spectroscopy of the coincident O atom dissociation products formed in the predissociation of the B state is used both to detect the absorption and to identify the predissociating B state level. In these initial experiments to demonstrate the feasibility of this technique, only Kr⁺ laser lines are used in the optical excitation step.

EXPERIMENTAL TECHNIQUE

The experiments were performed using the SRI fast neutral beam photofragment spectrometer, which has been recently described.⁶ The O₂⁺ ions were formed by the impact of 180 eV electrons on O₂ gas in a Nier-type electron impact ion source of a design used in earlier studies⁷ of O₂⁺. The ions are accelerated to an energy in the range of 2500 to 4000 eV,

velocity (mass) selected by a Wien filter, and pass through an 8 cm long cell filled with the charge transfer reactant gas, as shown schematically in Fig. 1. A variety of pure reactant gases: O₂, N₂, D₂, Xe, and He, were used in the present experiments. The (unknown) gas pressure in the cell was adjusted to allow a total attenuation of the O₂⁺ beam by approximately 30%.

Fast neutrals are formed by charge transfer with the reactant gas:



where the underline denotes the species with hyperthermal translational energy. Unreacted ions exiting the charge transfer cell are deflected by an electric field and collected. The fast O₂ beam is collimated over a distance of 50 cm and passes through a 0.03 × 0.2 cm slit before being intersected at right angles by the 0.3 cm diameter intracavity beam of a line selected, linearly polarized Kr⁺ laser. For specific lines in the wavelength range of 752.5–476.2 nm, the laser power varied between 20–200 W. Experiments were performed with the electric vector of the laser oriented either perpendicular to the molecular beam velocity vector or collinear with it. The molecular beam flux passing through the laser is estimated to be of order 10⁹ s⁻¹.

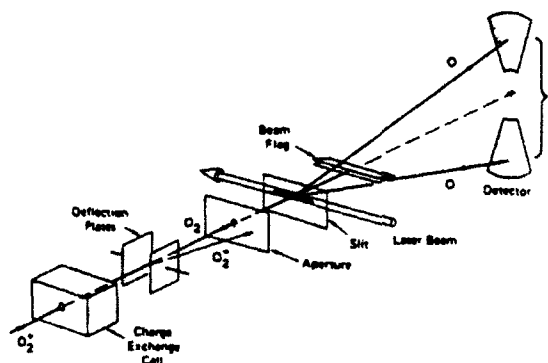


FIG. 1. Schematic diagram of the experimental apparatus. Charge transfer neutralization of a keV O₂⁺ beam produces the fast O₂ beam. Photodissociation of the O₂ by a linearly polarized laser creates correlated pairs of O-atom fragments, whose arrival time difference and separation is explicitly measured by the detector.

The pair of O atoms arising from the dissociation of single O₂ molecules are detected using a position-sensitive detector for correlated particles (PSD-C). This detector, which we have recently described in detail,⁶ explicitly measures both the spatial separation (R) and temporal separation (τ) of the two correlated fragment atoms. From these two measured quantities,⁸ both the center-of-mass kinetic energy of the fragments (W) and the orientation of the dissociating molecule with respect to the molecular beam velocity are completely specified for each dissociation event.

The value of W observed for a given dissociation specifies the energy of the dissociating molecular state E' with respect to the energy of its constituent atoms at infinite separation, i.e., a molecular dissociation limit. Since the photon energy ($h\nu$) used to produce the photodissociation is known, the energy of the absorbing molecular level E^* relative to this same dissociation limit is also specified:

$$E^* = W - h\nu. \quad (2)$$

The absolute accuracy of W (and therefore E' and E^*) measured by the detector is estimated⁶ to be better than 0.02 eV. The angular distribution of fragments which is explicitly measured also for the observed photodissociation provides additional information⁹ on the relative symmetries of the absorbing and dissociating molecular states.

OBSERVED PHOTOFRAGMENT SPECTRA

The O₂ beam was irradiated by eight lines of the Kr⁺ laser over the wavelength range of 752.5–476.2 nm. At each wavelength, discrete releases of kinetic energy in the range $W = 1$ –2 eV were observed to result from the photodissocia-

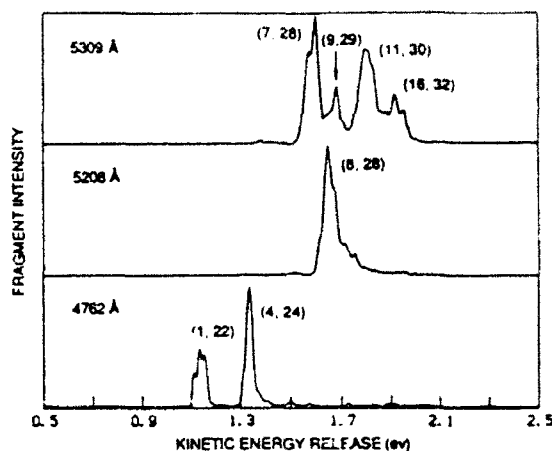


FIG. 2. Kinetic energy spectrum of O-atom photofragments observed at three exciting krypton-ion laser lines. Major peaks are identified by the upper and lower vibrational quantum numbers (v', v'') of the relevant Schumann-Runge absorption band.

tion. The intensity of the fragments varied with energy release and excitation energy over a range of 2 orders of magnitude. The stronger photodissociation rates were generally observed at the shorter wavelengths. Kinetic energy releases less than 1 eV or greater than 2 eV were not produced by photodissociation of O₂ at any of the examined wavelengths. Representative O-atom photofragment energy release spectra obtained at the 476.2, 520.8, and 530.9 nm Kr⁺ laser lines are shown in Fig. 2. The abscissa in this figure is the

TABLE I. Photofragment energy releases observed in the photodissociation of O₂. Assignments are given for absorption in the $B-X$ Schumann-Runge bands.

Excitation wavelength (nm)	Photon energy (eV)	$W_{\text{obs}} = E'$ (eV) ^a	E^* (eV) ^a	Assignment		$W_{\text{obs}} - W_{\text{calc}}$ (eV) ^b
				(v', v'')	N	
752.5	1.6471	1.260	-0.387	(2,31)	30	-0.002
676.4	1.8324	1.439	-0.393	(5,32)	18	0.007
		1.724	-0.108	(10,37)	12	0.002
		1.834	-0.082	(12,37)	22	-0.002
647.1	1.9155	1.834	-0.082	(12,37)	22	-0.002
568.2	2.1815	1.788	-0.394	(11,32)	18	0.004
		1.911	-0.271	(15,34)	12	0.007
530.9	2.3349	1.580	-0.755	(7,28)	22	-0.001
		1.607	-0.728	(7,28)	28	-0.000
		1.681	-0.654	(9,29)	18	-0.004
		1.801	-0.534	(11,30)	24	-0.002
		1.832	-0.503	(11,30)	30	0.006
		1.919	-0.416	(16,32)	6	-0.000
		1.954	-0.381	(18,32)	18	-0.005
		1.654	-0.726	(8,28)	24	0.005
		1.676	-0.704	(8,28)	30	-0.001
		1.184	-1.374	(2,23)	14	-0.008
484.7	2.5575	1.531	-1.027	(7,26)	4	-0.008
		1.919	-0.639	(15,29)	22	-0.005
		1.113	-1.490	(1,22)	16	-0.004
476.2	2.6027	1.137	-1.466	(1,22)	22	-0.003
		1.156	-1.466	(1,22)	26	-0.004
		1.340	-1.263	(4,24)	10	0.002

^a Absolute uncertainty in energy is ± 0.02 eV.

^b Energy calculated relative to $O(^1P_2) + O(^1P_2)$.

fragment kinetic energy W . The fragment intensities are only relative within each spectrum.

A single, discrete energy release is expected to appear in the W spectrum as a peak of approximately Gaussian shape with a width of order 0.010 eV. As can be seen in Fig. 2, some of the observed features appear as nearly discrete energy releases, while others consist of groups of closely spaced energies, some of which are partially resolved. The observed energy releases were found to be invariant with kinetic energy of the O_2 beam and with laser power. Changing the species of target gas to form the O_2 beam by charge transfer also produced no detectable changes in the observed energy releases, although the relative intensities of the subsidiary structure associated with the major peaks could be varied by as much as 50% with choice of charge-transfer reactant. The use of O_2 as the charge-transfer gas produced the highest photodissociation rates.

The kinetic energy releases measured for the prominent peaks in the photofragment spectra are given in Table I. These values of W represent the energy of the dissociating state (E') with respect to the separated atom limit of the fragments. Subtracting the photon energy specifies the energy of the absorbing state (E'') with respect to this same limit. At first glance, the pattern of energy releases appears quite random. For example, an energy release of 1.260 eV is observed at 752.5 nm, whereas increasing the photon energy by nearly 1 eV to 476.2 nm produced a still lower release of 1.113 eV.

The quasidecrete nature of the observed fragment energy releases and their apparent random distribution with exciting photon energy is consistent with photodissociation in a bound-bound absorption, where the upper bound state is a quasi-continuum due to rapid predissociation. In this case, only selected rovibrational levels in the upper state can be pumped at a given laser wavelength, each giving rise to a discrete kinetic energy release. In the following two sections, we discuss the identification of the upper and lower electronic states of O_2 that participate in this process, the $B^3\Sigma_u^-$ and $X^3\Sigma_g^-$ states.

IDENTIFICATION OF THE DISSOCIATING ELECTRONIC STATE

A compelling feature of the photofragment spectra is the restricted range of W over which the quasidecrete energy releases are observed. The lowest energy fragments are observed with $W = 1.113$ eV and the highest with $W \approx 1.954$ eV. This highest value of W corresponds very closely to the energy of $O(^1D)$ above $O(^3P)$, 1.96738 eV. This suggests that the predissociated upper state correlates to an O_2 dissociation limit in which at least one of the atoms is $O(^1D)$, with the dissociation continuum arising from the next lower limit in which one of the atoms is $O(^3P)$.

The lowest vibrational level of the $B^3\Sigma_u^-$ state lies 1.0043 ± 0.0004 eV above the $O(^3P) + O(^3P)$ dissociation limit and this state correlates to the $O(^1D) + O(^3P)$ limit. Predissociation of all levels in this state by the $^3\Sigma_u^-$ and $^{1,3}\Pi_u$ states arising from the $2 O(^3P)$ limit is known to occur, with lifetimes ranging from 1.5–53 ps.¹² Transitions into this state should give rise to photofragments with

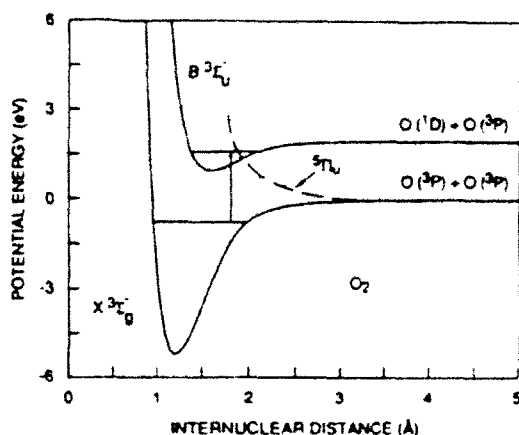


FIG. 3. Potential energy curves for the O_2 states observed in the photodissociation. Photoabsorption occurs from high vibrational levels of the ground electronic state into various rovibrational levels of the $B^3\Sigma_u^-$ state. The B state is predissociated to ground state atoms, whose kinetic energy is measured in the experiment. The B state predissociation is believed to occur by coupling to the repulsive $^1\Sigma_u^-$, $^1\Pi_u$, $^3\Pi_u$, and $^3\Pi_g$ states arising from the lowest dissociation limit. Only the latter state is shown in the figure.

$1.0043 < W < 1.97$ eV. Thus the B state meets all criteria for being the upper electronic state in the observed photodissociation. The energy levels of the B state are rather accurately and completely known.^{13,14} It is shown below that the optical excitation into these levels is fully consistent with the energy releases observed in the photofragment spectra. The potential energy curves of the relevant states of O_2 are shown in Fig. 3.

IDENTIFICATION OF THE ABSORBING ELECTRONIC STATE

The absorbing O_2 state must be formed by charge transfer of O_2^+ , and must survive the 3–5 μ s transit time between the charge-transfer cell and irradiation by the laser. In fact, these constraints are not very restrictive. Fractional populations in the O_2 beam of order 20 ppm would account for the observed photodissociation rate if an allowed transition were pumped by the laser. Furthermore, all of the experimentally known valence and Rydberg states in O_2 can be formed from the addition of a single electron to an $O_2^+ X^2\Pi_g$ or a $^4\Pi_u$ core. These two states are known⁷ to be the major constituents in an O_2^+ ion beam produced by ≈ 200 eV electron impact. However, we must further require that the candidate absorbing state access the predissociated upper state at visible wavelengths. This restriction categorically eliminates all of the known electronic states in O_2 with the exception of the $X^3\Sigma_g^-$ ground electronic state.

The photofragment energy releases require that the absorbing energy levels in the lower state lie at energies between 0.082 and 1.490 ± 0.012 eV below the dissociation limit. For the X state, these energies correspond to highly excited vibrational levels between $v'' = 22$ and the convergence limit. Such levels can indeed be formed in vertical transitions by charge transfer of the $O_2^+ a^4\Pi_u$ state. For the choice of an O_2 target gas, which we found to most efficiently

produce the absorbing levels, the charge transfer into high vibrational levels of the ground state is nearly resonant in energy. Furthermore, the X state is optically connected to the candidate predissociating state $B^3\Sigma_u^-$ via the strongest transitions known in O₂, the Schumann-Runge bands.

Accurate prediction of the energies in the high vibrational levels of O₂ X is problematic. The region above $v'' = 22$ is well beyond the expected range of validity of published Dunham coefficients and RKR potentials are available¹ only in the range below $v = 21$. Vibrational energy levels of X have been calculated for the range $v'' = 0-32$ by Guberman¹⁵ from an *ab initio* potential energy curve. Agreement between the theoretical and experimental values was found to be within 20 cm⁻¹ (1 eV = 8065.479 cm⁻¹) for $v'' < 22$, where comparison could be made. However, this potential energy curve predicts an O₂ dissociation energy^{9,14} nearly 1800 cm⁻¹ smaller than the currently accepted value. Hence, higher vibrational energies computed from the curve will lie increasingly too low in energy.

A considerable volume of spectroscopic data exists on the SR bands that access levels in the X state to $v'' \approx 28$ that allows a more accurate prediction of the requisite vibrational and rotational levels to be made. Early determinations of band origins in the SR system,¹ together with the more recent observations of Creek and Nicholls,¹⁶ Cheung *et al.*,¹³ and Copeland *et al.*⁴ define an interconnected set of vibrational levels of the B and X states extended from $v'' = 0$ to $v'' = 28$. We have performed a correlated least squares fit of these origins following the "term value approach" of Aslund^{17,18} to obtain the relative vibrational energies of the X

state. The precision of the level energies obtained in the fit is found to range from ± 0.02 cm⁻¹ at $v'' = 0$ to ± 0.94 cm⁻¹ at $v'' = 28$. The absolute accuracy of the energies of the higher levels is, of course, unknown. It depends quite critically on the accuracy⁴ of Creek and Nicholls¹⁶ data.

Extrapolation of the vibrational level energies and rotational constants above $v'' = 28$ was accomplished by numerical solution¹⁹ of the Schrödinger equation for a model potential describing the X state. The potential was derived from an RKR²⁰ potential describing the vibrational and rotational constants in the range $v'' = 0-28$ (the data of Ref. 16 provide nearly the sole source of information on rotational constants for $v'' > 2$) and smoothly extended to the dissociation limit by the relation

$$V(R) = D_e - 1.46778 \times 10^5 / R^6 - 1.07679 \times 10^7 / R^{12}, \quad (3)$$

where the units of energy and distance are cm⁻¹ and 10⁻⁸ cm, respectively. The energy levels generated by the potential reproduced the experimental values to within ± 0.5 cm⁻¹ for all vibrational levels and the computed rotational constants were within ± 0.001 cm⁻¹ of those given by Ref. 16 for all levels except $v'' = 28$, where the difference between the calculated and observed constants was -0.0022 cm⁻¹. The calculated energy levels, in eV relative to the dissociation limit, as well as the rotational and first order centrifugal distortion constants for $v'' = 20-26$ are given in Table II. Also provided in this table are the similarly computed vibra-

TABLE II. Computed energies and rotational constants of the O₂ $X^3\Sigma_u^-$ and $B^3\Sigma_u^-$ states. Energies are expressed in eV relative to the O(³P₂) + O(³P₂) separated atom limit.

X state				B state			
v''	$E(v'')$ (eV)	$B(v'')$ (cm ⁻¹)	$D(v'')$ (10 ⁻⁵ cm ⁻¹)	v'	$E(v')$ (eV)	$B(v')$ (cm ⁻¹)	$D(v')$ (10 ⁻⁵ cm ⁻¹)
0	-5.1154			0	1.0043	0.8124	0.4456
20	-1.7981	1.12259	0.5333	1	1.0895	0.80012	0.4622
21	-1.6627	1.10583	0.5448	2	1.1720	0.78564	0.4806
22	-1.5305	1.08873	0.5583	3	1.2515	0.77022	0.4990
23	-1.4015	1.07119	0.5742	4	1.3279	0.75381	0.5253
24	-1.2759	1.05312	0.5928	5	1.4011	0.73668	0.5627
25	-1.1537	1.03438	0.6151	6	1.4709	0.71848	0.6070
26	-1.0352	1.01481	0.6426	7	1.5370	0.69876	0.6636
27	-0.9206	0.99412	0.6806	8	1.5992	0.67708	0.7339
28	-0.8101	0.97169	0.7420	9	1.6570	0.65290	0.8223
29*	-0.7042	0.94628	0.8450	10	1.7102	0.62575	0.9359
30*	-0.6038	0.91627	0.9945	11	1.7583	0.59531	1.0806
31*	-0.5099	0.88075	1.1608	12	1.8011	0.56135	1.2622
32*	-0.4235	0.84082	1.2923	13	1.8383	0.52385	1.4870
33*	-0.3452	0.79767	1.4652	14	1.8699	0.48307	1.7589
34*	-0.2753	0.74964	1.6658	15	1.8960	0.43962	2.0749
35*	-0.2141	0.69848	1.8976	16	1.9169	0.39457	2.4207
36*	-0.1619	0.64321	2.1334	17	1.9332	0.34945	2.7700
37*	-0.1184	0.58492	2.4619	18	1.9457	0.30574	3.1250
38*	-0.0833	0.52443	2.8313				
∞	0.0			∞	1.9674		

* Extrapolated energies and rotational constants (see the text).

tional energies of the B state, referenced to this same dissociation limit, and its rotational constants.

The vibrational wave functions computed from the X state potential energy curve were further used to generate Franck-Condon factors²² for the $B-X$ transitions. Where comparisons could be made ($v' < 20$), the stronger ($> 10^{-3}$) Franck-Condon factors agreed with previous calculations¹ to within 0.5% and weaker ($\approx 10^{-3}$) ones to within 1.4%. The consistent agreement of vibrational energy levels, rotational constants, and Franck-Condon factors with existing experimental data and calculations suggests the model potential used here provides a reasonably accurate description of the ground state potential energy curve over at least a significant portion of the energy regime accessed in the present experiment.

ASSIGNMENT OF THE PHOTOFRAGMENT ENERGY RELEASES

The proposed assignment is based on the direct correspondence of the observed photofragment center-of-mass kinetic energies W to the known predissociated energy levels of the B state relative to the $O(^3P) + O(^3P)$ dissociation limit. In addition, subtraction of the energy of the exciting photons simultaneously yields the energy of the initial X state level from which the photoabsorption was initiated. Despite the fact that only odd rotational levels N'' are populated in the ground state of this homonuclear, zero nuclear spin molecule and only even N' are accessed in the B state, the ≈ 100 cm^{-1} uncertainty of the measured W values rarely allows single v', N' or v'', N'' levels to be uniquely identified solely on the basis of kinetic energy release. However, with the additional restriction $N' = N'' \pm 1$ imposed by the optical transition between these two $^3\Sigma$ states, discrete sets of upper and lower state quantum numbers can generally be established.

The assignments derived for the major photofragment energy releases are given in Table I. In those cases where no unique distinction could be made between assignment to a low rotational level in a given vibrational level and assignment to a high rotational level in a lower vibrational level, the lower rotational assignment was made to be consistent with the expected rotational temperature in the O_2 of < 500 K, unless the Franck-Condon factor computed for the transition was unusually poor.

Given the 0.05 cm^{-1} linewidth of the exciting laser, one would hope to obtain a very precise assignment of the vibrational, rotational, and even fine structure quantum numbers in both the upper and lower electronic states, apart from any consideration of photofragment energy. Several complications frustrate this goal in the present experiment. Since the laser frequencies are fixed, there is no way of knowing *a priori* how far its frequency is removed from the center of an absorption line. The B state is predissociated, hence the $B-X$ absorption lines are characterized by a Lorentzian line shape whose full-width at half-maximum varies over the range of 0.02 – 3.5 cm^{-1} as a function of B state vibrational and rotational quantum number.¹² This Lorentzian line shape can effectively extend over a considerable frequency range. Assuming even a narrow Lorentzian linewidth (0.1 cm^{-1}), a

strong transition whose line center was 20 cm^{-1} removed from the laser frequency would produce a photofragment intensity comparable to that produced by a $120\,000$ times weaker transition coincident with the laser frequency. These considerations are further complicated by the fact that each rotational level of the X and B states can be split by spin-spin and spin-orbit couplings into three fine-structure components. These splittings have been characterized in the B state,^{13,14} but are completely unknown for higher vibrational levels of the ground electronic state. For these reasons, the validity of the assignments made in Table I for $v' > 28$ is intimately dependent on the accuracy of the extrapolated energies and rotational constants for the ground state given in Table II. The fact that consistent assignments can be made for these levels does not confirm the accuracy of the extrapolation.

The rotational structure in several of the $B-X$ vibrational bands encountered here has been explicitly observed,¹⁶ albeit at relatively low resolution. It can be used to verify some of the vibrational assignments in Table I. Two of the previously observed bands, the (1,22) and (8,28) appear as features in the photofragment spectra shown in Fig. 2. We will consider a more detailed assignment of these features in the following.

In the photofragment spectrum excited at 520.8 nm two components corresponding to energy releases of 1.654 and 1.676 eV appear. Comparison of these energies with those of the B state in Table II indicates that the predissociated levels lie 0.055 and 0.077 eV, respectively, above the origin of $v' = 8$. These energies correspond to rotational quantum numbers $N' \approx 24$ and $N' \approx 30$ in $v' = 8$. Subtracting the 2.3799 eV photon energy from the energy releases yields lower state energy levels lying 0.0842 eV and 0.106 eV above $v'' = 28$ in the X state. These correspond to $N'' \approx 25$ and $N'' \approx 29$, respectively. Comparison of the laser frequency ($19\,194.7$ cm^{-1}) with the line positions in the (8,28) emission spectrum observed by Creek and Nicholls¹⁶ finds no transition occurring precisely at this frequency. However, the $P\,25$ ($N' = 24$) is reported 9.36 cm^{-1} to higher frequency and the $R\,31$ ($N' = 32$) line 12.25 cm^{-1} to lower frequency. The next closest line ($R\,29$, $N' = 30$) lies 25 cm^{-1} from the laser frequency. Indeed, excitation of the $P\,25$ and $R\,31$ transitions in the (8,28) band should produce photofragments with energies of 1.646 and 1.676 eV, in agreement with the observed energies. The fact that the lines are excited so far from their line centers suggests that orders of magnitude higher photofragment fluxes will be achieved using a tunable laser for the excitation.

The other band for which a comparison can be made is the (1,22) emission band, also reported by Creek and Nicholls.¹⁶ Transitions in this band are assigned to the lowest energy photofragments observed in the 476.2 nm spectrum. These fragments appear as three discrete, but only partially resolved energy releases of 1.113 , 1.137 , and 1.156 eV, suggesting rotational quantum numbers in B ($v' = 1$) of $N' \approx 16$, 22 , and 26 , respectively. Subtraction of the photon energy (2.6027 eV) from these three W values yields lower state energies corresponding to $X(v'' = 22)$, $N'' \approx 17$, 21 , 25 , respectively. Of the line positions in the (1,22) band report-

ed by Creek and Nicholls, the $P\ 19\ (N' = 18)$ appears nearly coincident ($\sim 0.1\text{ cm}^{-1}$) with the laser frequency of $20\ 991.8\text{ cm}^{-1}$, with two other lines, the $R\ 25\ (N' = 26)$ at -6.3 cm^{-1} and $R\ 23\ (N' = 24)$ at $+18.8\text{ cm}^{-1}$, occurring within an interval of $\pm 20\text{ cm}^{-1}$ about this frequency. The energy releases associated with excitation of these three transitions are consistent with the observed photofragment energies. However, the very near coincidence of the $P\ 19$ line with the laser frequency leads one to expect a photofragment spectrum dominated by a single energy release of 1.123 eV , corresponding to $v' = 1, N' = 18$. This is not consistent with the three or more energy releases observed by experiment.

In viewing this apparent discrepancy, one must consider that the lines reported by Creek and Nicholls were observed in a high pressure, high temperature discharge and exhibited collisional and Doppler broadening of order 1 cm^{-1} . Only lines separated by 2 cm^{-1} or more were resolved sufficiently to report other than a single line position. Below $N' \approx 39$, the components of the P and R branches, which are each expected to consist of three distinct transitions of comparable intensity, are observed as single lines. Thus the apparent coincidence of the laser frequency with the $P\ 19$ line need not occur when the actual frequencies of its P_1, P_2 , and P_3 components are considered. Furthermore, it is possible that one or more lines in the satellite branches associated with the $^3\Sigma_u^- \rightarrow ^3\Sigma_g^-$ transition,¹⁴ with absorption strengths estimated to be $\approx 10^{-3}$ of those in the main branches, are in much closer coincidence with the laser frequency. Considering the properties of a Lorentzian line shape, such an occurrence would more easily give rise to multiple energy releases of comparable intensity.

A final confirmation of the assignment of the photofragment spectra to the Schumann–Runge system are the observed photofragment angular distributions. Such distributions are normally characterized⁹ by a parameter β , which can assume values in the range $-1 < \beta < 2$ to describe molecular dissociations that occur "perpendicular," isotropic, or "parallel" with respect to the laser polarization. With a single exception, the peak labeled (7,28) in the 530.9 nm spectrum, all of the observed features in the photofragment spectra exhibited $\beta > 0.5$. This is consistent⁹ with the dominant transitions in the $\Sigma \rightarrow \Sigma$ absorption arising from the excitation of P or R branch lines with other than very small rotational quantum numbers.

CONCLUSIONS

The present experiment has demonstrated not only that laser photofragment spectroscopy of O_2 is possible, but also that under the proper conditions rotational resolution in the predissociating state can be achieved in the kinetic energy analysis of the dissociation fragments. The observed photodissociation is assigned to photoabsorption from high vibrational levels of the $X^3\Sigma_g^-$ state into the predissociated $B^3\Sigma_u^-$, demonstrating that vibrationally excited O_2 can be produced in observable concentrations by charge transfer of O_2^+ ions.

The present technique offers unique capabilities for a detailed study of absorptions in the Schumann–Runge bands. The complete dispersion of B state vibrational levels

along the photofragment energy coordinate permits individual bands to be observed without interference from other vibrational sequences overlapping the same wavelength range. From the high vibrational levels of the O_2 ground electronic state observed here, it is possible to access *all* levels of the $B^3\Sigma_u^-$ with a tunable laser at visible wavelengths under nearly Doppler-free absorption conditions.

Note added in proof: Since this article was submitted, we have extended the measurements using a tunable dye laser and observed 17 bands of the SR system with rotational resolution. These measurements, which allow complete spectroscopic identification of the photodissociation, accurately locate $O_2\ X^3\Sigma_g^-$ levels in the $v'' = 27\text{--}34$ region. The measured vibrational term energies confirm the accuracy of Table II up to $v'' = 28$, but reveal a divergence, increasing with v'' , between the calculated term energies in the extrapolated region of the ground state potential energy curve and the measured values. At $v'' = 34$, the measured term energy lies 0.0207 eV higher than the extrapolated value in Table II. This reemphasizes the fact that the detailed transition assignments of Table I are only suggestive.

ACKNOWLEDGMENTS

We gratefully acknowledge helpful discussions during the course of this work with Dr. T. G. Slinger and our other co-workers at SRI International. This research was supported by NSF Grant No. ATM-8504152.

- ¹P. H. Krupenie, *J. Phys. Chem. Ref. Data* **1**, 423 (1972).
- ²R. D. Hudson and S. H. Mahle, *J. Geophys. Res.* **77**, 2902 (1972).
- ³R. D. Hudson, V. L. Carter, and E. L. Breig, *J. Geophys. Res.* **74**, 4079 (1969).
- ⁴R. A. Copeland, P. C. Cosby, D. R. Crosley, J. B. Jeffries, and T. G. Slinger, *J. Chem. Phys.* **86**, 2500 (1987).
- ⁵S. L. Kaufman, *Opt. Commun.* **17**, 309 (1976).
- ⁶H. Helm and P. C. Cosby, *J. Chem. Phys.* **86**, 6813 (1987).
- ⁷F. J. Grieman, J. T. Moseley, R. P. Saxon, and P. C. Cosby, *Chem. Phys.* **51**, 169 (1980).
- ⁸D. P. de Bruijn and J. Los, *Rev. Sci. Instrum.* **53**, 1020 (1982).
- ⁹C. Pernot, J. Durup, J.-B. Ozenne, J. A. Beswick, P. C. Cosby, and J. T. Moseley, *J. Chem. Phys.* **71**, 2387 (1979).
- ¹⁰J. T. Moseley, R. P. Saxon, B. A. Huber, P. C. Cosby, R. Abouaf, and M. Tadjeddine, *J. Chem. Phys.* **67**, 1659 (1977); R. Abouaf, B. A. Huber, P. C. Cosby, R. P. Saxon, and J. T. Moseley, *ibid.* **68**, 2406 (1978).
- ¹¹H. Helm, D. P. de Bruijn, and J. Los, *Chem. Phys.* **85**, 233 (1984).
- ¹²P. S. Julienne and M. Krauss, *J. Mol. Spectrosc.* **56**, 270 (1975); B. R. Lewis, L. Berzins, J. H. Carver, and S. T. Gibson, *J. Quant. Spectrosc. Radiat. Transfer* **36**, 187 (1986).
- ¹³A. S.-C. Cheung, K. Yoshino, W. H. Parkinson, and D. E. Freeman, *J. Mol. Spectrosc.* **119**, 1 (1986).
- ¹⁴P. Brix and G. Herzberg, *Can. J. Phys.* **32**, 110 (1953).
- ¹⁵S. L. Guberman, *J. Chem. Phys.* **67**, 1125 (1977).
- ¹⁶D. M. Creek and R. W. Nicholls, *Proc. R. Soc. London Ser. A* **341**, 517 (1975).
- ¹⁷N. Aslund, *Ark. Fys.* **30**, 377 (1965).
- ¹⁸D. L. Albritton, W. J. Harrop, A. L. Schmeltekopf, R. N. Zare, and E. L. Crow, *J. Mol. Spectrosc.* **46**, 67 (1973).
- ¹⁹J. Hutson, *J. Phys. B* **14**, 851 (1981). A copy of the computer program COIST was provided by this author.
- ²⁰R. N. Zare, *J. Chem. Phys.* **40**, 1934 (1964); E. W. Kaiser, *ibid.* **53**, 1686 (1970).
- ²¹A copy of the computer program FCF was provided by D. L. Albritton and R. N. Zare.

Appendix B

OBSERVATIONS OF NEW METASTABLE STATES OF N₂

OBSERVATIONS OF NEW METASTABLE STATES OF N_2

H. Helm and P. C. Cosby

Molecular Physics Department

SRI International, Menlo Park Ca 94025

ABSTRACT

We have used a position sensitive detector for correlated fragments to determine absolute energies of very-slowly predissociating states of molecular nitrogen. At lifetimes in the μs range a number of new Rydberg states are observed with dissociation channels which efficiently compete with radiative decay into bound states of N_2 . An assignment of the observed states to triplet $ns\sigma_g$ Rydberg series converging to vibrational limits of $N_2^+ X^2\Sigma_g^+$ and $N_2^+ A^2\Pi_u$ is given.

Submitted to: The Journal of
Chemical Physics

MP 87-167
July 17, 1987

INTRODUCTION

Spectroscopically, nitrogen is one of the most thoroughly studied diatomic molecules.^{1,2} While the complexity of electronic states in this molecule is now basically well understood and the absolute bond energies of both the neutral and ion are determined with a reasonable degree of certainty, numerous details remain to be worked out. Specifically the complex energy level patterns in the energy region near the first ionization limit have yet to be mapped out in detail.¹ The complexity of states in this region arises from the interaction of Rydberg series with quantum numbers $n \geq 3$ which converge to the ground and first excited state of the ion in both singlet and triplet manifolds. Previous studies of Rydberg states have involved the excitation of valence states of the N_2 molecule. Our present approach is unique in that we form the Rydberg states by adding an electron to the N_2^+ core using charge transfer reactions.

We have recently begun a study of this region by forming excited nitrogen in charge-exchange collisions of mass selected N_2^+ ions in cesium.³ When charge transfer occurs in cesium the dominant populations of N_2 are in the $E^3\Sigma_g^+$ and $a'^1\Sigma_g^+$ states. Photoionizing these molecules we have observed the triplet np and nf Rydberg series converging to $v = 1$ of $N_2^+ X^2\Sigma_g^+$ and measured the lifetime of the $v = 1$ level of the E state. The population of the high-lying E and a'' states (respectively 11.875 eV and 12.255 eV above the ground state) in charge transfer with cesium is not unexpected since near-resonance is favoured in electron transfer collisions.

In order to populate lower-lying metastable states of the nitrogen molecule as well as the ground state we investigated charge transfer gases with

higher ionization potential, namely NO, Xe, H₂ and N₂. The charge transfer reactions of some of these gases are known and expected to favor transitions to the lower-lying states in the electronic manifold of the nitrogen molecule.^{4,5} Surprisingly we found that also in these cases high-lying states of the N₂ molecule were populated, albeit with very small abundance. The experiment which we describe below is sensitive to fractional populations in the neutral beam as low as 1 part in 10⁷. At this level, not unexpectedly, practically all excited states of N₂ which can be formed by addition of an electron to N₂⁺ are conceivably formed. A series of experimental tricks is then used to select from the large variety of states those molecules which decay by unimolecular dissociation on the μ s time scale and the absolute molecular energy of each dissociating state is measured with respect to its dissociation limit. A tentative assignment of the new levels is attempted by monitoring the populations as a function of time after formation, nature of the charge transfer gas and ion source conditions.

EXPERIMENTAL

The parent ions for the charge transfer reaction are extracted from a discharge ion source⁶ at energies between 1.4 and 3.6 keV. The source is either operated in pure nitrogen or in a mixture of nitrogen and argon. The mass-selected ion beam can be charge-exchanged in either an 8-cm long cell operated at a pressure of typically 10⁻³ Torr or at the intersection of the ion beam with a supersonic gas beam. A schematic drawing of the experimental setup is given in Figure 1. All but one of the experimental results given in this paper were obtained with neutral molecules formed in the gas cell. In

this case residual ions are purged from the neutral beam emerging from the cell using deflection plates. The neutral beam then enters the UHV section of the apparatus which is kept at 10^{-8} Torr, through an aperture. After a flight distance of 58 cm from the exit of the cell, the beam is spatially selected by a 250 μ m high and 3 mm wide slit formed by razor blades. Seven cm downstream from the slit the neutral beam is collected in interchangeable 20 mm wide, V-shaped flags which are 1.2 and 1.6 mm high respectively.

Fragment atoms formed by unimolecular dissociation in the region between the slit and the flag can reach a position sensitive detector⁷ which is located 90 cm from the slit, provided they clear the flag dimensions. This requirement restricts the range of dissociation energies and angles of fragments detected. The effective path length from which spontaneous dissociation in the beam is detected by the PSD-C is a function of beam energy, center-of-mass energy release, W , ejection angle, θ , and the flag size used. For example, at 3 keV beam energy and $W = 1$ eV, fragments emerging perpendicular to the parent flight path are detected from the first 15 (20) mm past the slit when the large (small) flag is inserted. The remaining path to the flag is effectively shadowed by the flags. Correspondingly smaller dissociation lengths are permitted for fragments appearing at center-of-mass angles less than 90° .

The position sensitive detector has been described in detail in a previous publication.⁷ It is operated to detect only coincident fragments from single dissociation events. In most of the work reported here we restrict detection to fragment pairs emerging perpendicular to the parent beam direction. These fragments arrive coincident in time at the detector surface and the spatial separation between the fragments at the detector surface, R , is

related to the center-of-mass energy release ,W , by the relation

$$W = E_0 R^2 / 4L^2, \quad (1)$$

where L is the flight distance from the dissociation region to the detector surface, and R is the sum of separations of individual fragments from the detector center, $R = R_A + R_B$. Due to the finite length, ΔL , of the dissociation region in our case (which is a complex function of E_0 , W, and flag height) the resolution in W (when monitoring the effective distance R) is diminished by an amount ΔW :

$$\Delta W = W.2\Delta L/L. \quad (2)$$

Since the dissociation length is of the order of 1 to 3% of the length L, discrete energy releases will appear broadened at the level of 2 to 6% of W. At 1 eV energy release this broadening is only slightly above the best energy resolution we obtained so far with our PSD-C (18 meV) using crossed-beam photodissociation. In these experiments a spatially well defined dissociation length (the width of the laser beam) could be established.

The slit, flags, and the detector assembly are all mounted on individual translation stages to facilitate alignment of the beam. Under typical operating conditions a parent beam current of 10^{-8} to 10^{-7} A of N_2^+ is used and aligned to propagate into a 2.5 mm diameter Faraday cup at the center of the detector (with the slit and flag removed from the beam). The cell is then filled with gas to neutralize up to a few percent of the parent beam. At this level of charge transfer with the permanent gases mentioned above up to 80% of

the parent beam may be attenuated following elastic and inelastic collisions in the cell. During this alignment the neutral beam formed in the parent beam direction is monitored by secondary emission at the Faraday cup, residual ions being deflected and monitored at the aperture. Upon insertion of the slit the current arising from neutrals hitting the Faraday cup drops by a factor of about 10 due to the spatial confinement of the beam. The flag is then inserted. It efficiently blocks all the parent neutral beam from the drift region and the detector.

Under these conditions we find typically 10 to 10^3 coincidences per second at the PSD-C, this count rate being a sensitive function of ion source conditions, parent beam energy and the type of charge transfer gas used. The absolute position of each fragment with respect to the detector center, R_A and R_B , is measured, and the arrival time difference between fragments is monitored using a dedicated computer system. The total separation between correlated fragments, $R = R_A + R_B$ is computed and used in equation (1) to determine the energy release W . The precision in the R measurement is of the order of 50 μm , the precision of the measured arrival time difference is better than 1 ns. Spectra are accumulated while operating the beam continuously for times ranging from 10 minutes to two hours, depending on the signal level.

Due to the very low pressure in the dissociation region and the spatial confinement of the neutral beam by the slit and the flag, the observed dissociation events arise solely from spontaneous decay of excited N_2 states within a few centimeters from the slit. This implies that the states involved had already had ample time (58 cm from the cell to the slit) to dissociate. Any species remaining in appreciable quantity beyond the slit must therefore have

lifetimes in the range of the flight time from the cell to the slit or longer. This time is 5 μ s at 1400 eV decreasing to 3 μ s at 3600 eV.

The role of collisional dissociation was checked by deliberately raising the pressure in the region past the slit. While an increase in the rate of fragment production was observed we also found that collision induced dissociation did not, due to the inherent momentum transfer to the molecule, give rise to well defined correlated fragment positions ($R_A/R_B = 1$). It remains to discuss the role of the slit in the observed dissociation processes. We expect that dissociation induced by grazing incidence on the slit would also severely affect the position ratio R_A/R_B . More importantly, slit induced dissociation can hardly be expected to be sensitive to the conditions used in the ion source and charge exchange cell, and certainly not depend on the size of the flag used as will be shown below. We therefore confidently assign the observed dissociation features to spontaneous dissociation at times of 3 to 5 μ s after the neutral species were formed. The dependence of specific fragment intensities in the flight time between the cell and the slit allows an estimate of the spontaneous dissociation lifetimes.

RESULTS

In Figures 2 through 5 we show typical spectra selected from over 50 spectra recorded for the nitrogen system. All energy distributions, except those shown in Figure 2, were obtained by restricting the accumulated coincidence counts to those from dissociation events which lead to fragments falling within about 1^0 perpendicular to the parent beam flight path. Similar

spectra with higher count rate are obtained using all fragment pairs, and computing both the angle of ejection and energy release [using the full transformation equation (4) of Reference (7)]. However these spectra were of slightly lower resolution, due to errors in our precise knowledge of the absolute neutral beam energy and its velocity component along the beam axis. The relatively high degree of resolution in the spectra shown in Figure 2 to 5 is introduced by the fact that the geometrical arrangement of slit and flag relative to the charge-transfer cell preselects from all dissociative charge transfer⁸ events



only those N_2^* intermediates with a long predissociation lifetime. When dissociative charge exchange of N_2^+ was accomplished using the neutral supersonic beam at a position just past the slit (with the advantage of having a well defined dissociation region) such a dense population of predissociating states was observed that resolution of band-like structure in the fragment energies was impossible.⁹ Hence, all spectra shown here were obtained using N_2^* formed in the charge-transfer cell.

In this configuration the slit, in conjunction with the exit aperture of the charge transfer cell and the flag beam, selects only those neutral molecules that are formed within a 4 mrad forward cone during the charge exchange process (3). This is significant because all the charge transfer gases used here (NO, Xe, H_2 and N_2) have ionization potentials very much

larger than the ionization potential of the dissociating neutrals that we observe in dissociation (see below). Consequently the slowly predissociating N_2^* we observe in (4) must constitute highly nonresonant product channels of reaction (3). It is likely that the dominant charge transfer channels in (3) (with near resonance) remain undetected (since bound) in the present experiment. Indeed the count rates observed in Figures 2-5 suggest that we are dealing here with a total population of $\sim 10^{-5}$ of all neutrals (N_2 and N) emerging from the charge-transfer cell.

The top trace in Figure 2 is obtained using N_2^+ ions produced in a pure nitrogen discharge. The spectrum reveals at least eight discrete energy releases which are identified by the letters A-H at the top of the figure. When adding argon to the discharge, the spectrum is significantly modified. The lower trace is obtained with a nitrogen-argon mixture of about 1:2. The spectra are normalized to the neutral beam current and hence the absolute variation of the level population of dissociating N_2^* states is revealed. We see that while peak F remains approximately constant in height, all other peaks decrease in intensity by a factor of about 2 when argon is added to the discharge. We conclude from this that different N_2^+ precursors are involved in the formation of peak F and the remaining peaks, and that the precursor concentration is severely modified by the presence of argon in the discharge source.

The gas pressure in a pure nitrogen discharge was found to have only little effect on the observed distributions. Increasing the N_2 pressure from 0.8 to 1.6 Torr we observed a minor decrease in intensity of fragments at energies higher than those marked by a peak H in Figure 2, and no detectable changes in the other peaks.

Figure 3 depicts the effect of the charge transfer gas on the population

of N_2^+ dissociating states. The gases from which electron transfer occurs have increasing ionization potential ranging from 9.5 eV in the top (NO) spectrum to 15.5 eV in the bottom spectrum of this figure. While the basic features marked in Figure 2 are again all present for each charge-transfer gas, their population varies significantly. The most notable effects are the increased relative contributions of fragments with energies near 0.6 and 2.4 eV as the ionization potential of the transfer gas is increased and the prominence of feature F near 1.4 eV as the ionization potential is lowered. The spectra in Figure 3 are approximately normalized to the parent ion beam current. The top two spectra (NO, Xe) are shown with their actual relative intensities, but the intensity in the lower two traces (H_2 , N_2) has been multiplied by a factor of three.

Figure 4 shows the effect of the size of the flag on the energy resolution. It is evident that as the size of the flag is increased the resolution increases. This is associated with the concomitant decrease in the effective length of the dissociation path that is monitored (see equation 2 and associated discussion).

Finally Figure 5 gives the dependence of the observed populations on beam energy. All spectra in Figure 5 were obtained from N_2^+ charge exchanged in NO. Similar observations were made using N_2 as charge transfer gas. It is evident from this figure that a number of electronic states participate in the spontaneous dissociation and that their lifetimes are significantly different. The significantly poorer signal observed at 1400 eV reflects in part the decreased efficiency of the channel multiplier plates for detecting low energy neutral fragments.

In the following we attempt to condense the diverse pieces of information obtained from these spectra, and associate the observed features with a pattern of high-lying, long-lived states of N_2 for which predissociation dominates over radiation into lower lying bound states.

DISCUSSION

Approximately one hundred bound vibrational states are known¹ in the region above the first dissociation limit of the nitrogen molecule, $N(^4S)+N(^4S)$. A large number of these are described in terms of Rydbergs converging to the ground and excited states of N_2^+ . In our experiment the time of flight from the ion source to the charge transfer cell (10 μs), restricts the candidate parent ions which can participate in the charge exchange process to ions in the ground state, $X^2\Sigma_g^+$, and in the lowest excited state, $A^2\Pi_u$. The lifetime of the A-state is 14 μs for $v = 1$, long enough for a significant fraction of A state ions to survive passage from the ion source to the charge exchange cell. Hence, we should first of all seek to identify the observed states as electronic states of N_2 that can be formed by simple addition of a Rydberg electron to the X or A state ionic core. The process of one-electron-transfer without concurrent core excitation, restricts the choice of N_2 states accessible to the singlet and triplet manifolds. Of those only long-lived levels have to be considered here, since we observe them in predissociation, microseconds after they were formed. This requirement practically excludes the singlet Rydberg series converging to $N_2^+ X$ of the type $np\sigma$, $np\pi$ (the members of the Worley-Jenkins series) which will efficiently radiate to the ground electronic state of N_2 . By similar reasoning the triplet $np\sigma$

and $n\pi$ series converging to $N_2^+ X$ can also be excluded, since these connect in dipole-allowed transitions to the $B^3\Pi_g$ state.

No rapid radiative channels exist however for most of the states formed by addition of an $n\sigma_g$ electron to either $N_2^+ X$ and $N_2^+ A$:

The lowest members of the singlet and triplet states formed by addition of an $n\sigma_g$ electron to the ionic ground state core have been observed to be metastable.¹ These are $a'^1\Sigma_g^+$ and $E^3\Sigma_g^+$. For the latter, lifetimes of 190 μs have been found for $v = 0$ (Reference 1) and 6 μs for $v = 1$ (Reference 3). The long lifetime of the E-state is due to the necessity of a two-electron rearrangement for it to connect in optical dipole radiation to the allowed lower state $A^3\Sigma_u^+$. The lifetime for the a' state has not yet been measured, but is expected to be at least in the μs range to permit observation in our previous photoionization experiment³ The transition moment for the allowed transition $a' \rightarrow c'^1\Sigma_u^+$ has been calculated to be large, but this transition lies in the far infrared and is therefore consistent with a long radiative lifetime of the a' state. It appears unlikely that fast radiative channels would open for the higher members of the $n\sigma_g$ series hence they are potential candidates for the observed predissociations.

A second group of candidate levels are members of the fine structure manifold of Rydberg levels which appear by addition of an $n\sigma_g$ electron to $N_2^+ A^2\Pi_u$. Two members of this manifold ($o_3^1\Pi_u$ and $F^3\Pi_u$ for $n = 3$) and correspondingly higher members in the series up to $n = 45$ have been identified as part of Worley's Rydberg series converging to the $A^2\Pi_u$ ($\Omega = 1/2$) and ($\Omega = 3/2$) cores respectively. The total manifold that arises from addition of the $n\sigma_g$ electron is shown schematically in Figure 6 for a low and a high value of the principal quantum number n . At high principal quantum numbers, where the singlet-triplet splitting is small or comparable to the spin-orbit coupling of

the A-state core (-80 cm^{-1}), the series members may be labelled by a total electronic angular momentum quantum number that is the sum of the core Ω^+ and the Rydberg electron angular momentum, $\Omega = \Omega^+ \pm 1/2$. This arrangement leads to two groups of Rydberg states separated roughly by the fine structure splitting of the ionic core. Of these, the states with $\Omega = 0^+$, 0^- , and 2 are pure triplet in character and they are of the type $^3\Pi_{u0}$ and $^3\Pi_{u2}$. By contrast, the two states of $\Omega = 1$ mix by spin-orbit interaction and end up as mixture of $^1\Pi_{u1}$ and $^3\Pi_{u1}$. This mixing between the $\Omega = 1$ states makes both components accessible from the ground state of N_2 . These are the members observed¹ in the two Worley series from the ground state. On the other hand, at low principal quantum numbers the singlet-triplet splitting will dominate the distribution within the manifold, the $^1\Pi_u$ member being isolated from the familiar $^3\Pi_u$ components which in turn display fine-structure splitting at the level of the A-state core.

From the above considerations, we expect that the nitrogen molecule exhibits, in addition to the $^3\Pi_{u1}$ component previously observed in absorption from the ground state, Rydberg members with quantum numbers $\Omega = 0^+$, 0^- , and 2 , which at high n lie within about 80 cm^{-1} of the $^3\Pi_{u1}$ levels, and are long-lived. At low n values these levels will group around the previously observed $^3\Pi_{u1}$ levels. The longevity is implied from the fact that the allowed optical transitions from these states must connect in a core transition to the $E^3\Sigma_g^+$ state and to correspondingly higher members of the series ($n\sigma_g + \text{N}_2^+ X^2\Sigma_g^+$). Their lifetime will hence be comparable to the A state of N_2^+ , which is in the microsecond range.

The list of possibly long-lived Rydberg states could be extended to include members built from higher angular momentum electrons. Little is known about these and since our observations, with exception of one, can be

consistently explained in terms of the $ns\sigma_g$ states and their expected quantum defects we conclude that higher angular momentum states do not strongly participate in our observations.

A first assignment of the observed predissociations proceeded quite independent of the above orbital considerations and was based on the measured values of W and the dependence of the corresponding fragment intensity on experimental parameters. We briefly discuss part of this assignment to demonstrate the consistency of the energy levels derived thereby with the expected location of long-lived $ns\sigma_g$ states.

The assignment of the general features of the spectra proceeds most easily from low resolution spectra such as shown in Figure 2. At least eight distinct groups of energy releases can be identified which we have labeled A-H at the top of the figures. The breadth of each group is primarily given by the range of rotational levels that participate in the predissociation, and each group reflects primarily a single vibrational Rydberg level. In Table 1 we have ordered these eight groups according to their W value. A key in the assignment is the observation that the energy releases for groups A and G, and for groups C and H, are each separated by about 1.20 eV. The significance here is that this energy is similar to the energy separation between the nitrogen dissociation limits $4S+2D^0$ and $4S+2P^0$ (1.193 eV) and $4S+2P^0$ and $2D^0+2D^0$ (1.191 eV). Since the four groups observed in dissociation show common response to variables in our experiment (such as addition of argon to the discharge, variation of flight-time, etc.) we conclude that two separate molecular states are involved here which branch in dissociation among two separated atom limits to produce features A and G, and C and H respectively.

The experimental precision does not permit us to decide which of the two pairs of dissociation limits are involved. However another piece of

information allows this decision: The observation that all four groups are quenched when argon is added to the ion source (measured relative to the height of peak F) suggests that the parent levels involved in the formation of these N_2 states lie higher in energy than the lowest vibrational state of $N_2^+X^2\Sigma_g^+$, the only ionic nitrogen level with energy less than the ionization potential of argon. This, and the fact that the energy spacings between A and C and between G and H are each about 240 meV, suggests that the dissociating N_2 states which give rise to the four groups of energy releases are two adjacent vibrational levels of a Rydberg state belonging to the $A^2\Pi_u$ core (which has a vibrational spacing of 232 meV). Adding the measured value of W to the respective dissociation limits the absolute molecular energy of these Rydberg states can be calculated. The resulting level energies are so well separated from the series limit (N_2^+A) that a unique identification can be made for the dissociating N_2 levels of the groups AC, GH. They belong to the two lowest vibrational levels of $n = 4$ in the $^3\Pi_u$ series and they branch during dissociation into the $^4S+^2P^0$ and $^2D^0+^2D^0$ separated atom limits respectively. We indicate in Figure 7 the absolute energy location of these levels as well as their measured energy releases.

By a similar reasoning, peak F can be assigned. Its refusal to respond to addition of argon in the source suggests that its parent derives from charge exchange of the lowest vibrational state of the ground state ion. Only an assignment to $n = 4$ and dissociation to $^4S+^2D^0$ produces a meaningful quantum defect for this dissociating state. Similar reasons apply to the assignment of the dissociation limits of the remaining features, B, and D.

On the left hand side of Figure 7 we show the expected pattern of Rydberg states formed with $ns\sigma_g$ orbitals. Previously observed energy levels are shown by full lines, theoretical predictions are represented by dashed lines in this

figure. For the ${}^3\Pi_{u0,2}$ case we "expect" energies close to those of the observed ${}^3\Pi_{u1}$ levels, which are the energy levels marked in the series converging to the N_2 (A) state in Figure 7. The association with our observed energy levels is obvious, and the respective assignments are included in Table 1.

The rather intense feature E does not appear to fall into the pattern of $ns\sigma_g$ levels. We suggest that these fragments may arise from a level about 1 eV above the lowest dissociation limit as indicated in Figure 7 and in Table 1. At this energy two long-lived states are predicted: the $G^3\Delta_g$ and ${}^1\Sigma_g^+$ state shown in Figure 3 of Reference 1.

It remains to discuss observed flight time effects as well as the origin of the oscillatory features observed in the higher resolution spectra (Figures 3-5).

Three effects can interplay to change the relative state populations of dissociating N_2^* when the energy of the parent N_2^+ beam is varied. Firstly, the flight time of the N_2^+ ions from the source to the charge transfer cell decreases as the acceleration voltage increases. Changing the beam energy from 1400 eV to 3500 eV reduces the time required for N_2^+ to reach the charge transfer cell from 10 μs to 6 μs . The radiative lifetimes of the N_2^+ A state are known to vary¹ from 14 μs in $v = 1$ to 6 μs in $v = 10$. Hence, the relative population of vibrationally excited N_2^+ A state levels participating in the charge transfer reaction will be slightly greater at the higher beam energies.

A second possible effect of beam energy is the velocity dependence of the charge-exchange process itself. An associated consideration here is that the range of scattering angles for product N_2^* molecules that are accepted into the dissociation region is beam energy dependent. Since the charge exchange processes observed here are all highly nonresonant (the energy defects are > 3

eV), and the collision velocity varies by only a factor of 1.5 from the highest beam energy (3600 eV) to the lowest (1400 eV), it seems unlikely that the charge-transfer reaction alone can produce the observed spectral changes.

The third, and in our opinion the most significant, effect arising from a change in ion beam energy, is the variation in flight time for the N_2^* between its point of formation in the charge transfer cell and its observed dissociation in the region between the slit and flag. If we attribute all changes in the fragment energy release spectra observed as a function of beam energy, to changes in N_2^* state populations produced by predissociation during this transit time, predissociation lifetimes of the N_2^* levels can be derived. These are given in Table 1 and their magnitudes should be valid within a factor of about 2. Most notable is the long lifetime of the groups F and B. Using these lifetimes and the observed relative intensity of each peak we can roughly estimate the population of individual states formed in charge transfer. These values turn out to be of the order of $5 \cdot 10^{-4}$ to 10^{-6} of the parent beam intensity. To deduce the fractional population on the neutral beam we have assumed a channel plate detection efficiency for coincidences of 1% and a geometrical detection efficiency of 18% (based on an isotopic distribution of the fragments in the center of the mass frame and the size of the detector and slit).

It remains for us to discuss the fine, oscillatory structure that appears superimposed on the gross vibrational features in the energy release spectra. It is tempting to attribute this structure to the predissociation of individual rotational levels in the electronic states discussed above. However, we have thus far not been able to model these features assuming reasonable rotational constants for these states ($1.0 - 1.2 \text{ cm}^{-1}$) and population of the levels in a Maxwell-Boltzman distribution. In a recent

study, we observed that the $H_2\ c^3\Pi_u$ state formed by nonresonant charge transfer of H_2^+ in Xe at keV energies yielded a rotational distribution in the H_2 product comparable to that of the H_2^+ reactant ($T_{rot} \sim 1400K$). However, other studies, for example the charge transfer of Ar^+ in HBr at 3 keV, have observed¹⁰ very high rotational excitation ($T_{rot} \sim 3000K$) in the product molecular ion. Consequently, we do not know what the rotational temperature of the N_2 product in the present reaction is, and for that matter, do not know if the product rotational distribution can even be characterized by a temperature. Nor do we know if the N_2^+ rotational distributions produced in the charge transfer process have been modified by differential predissociation rates during the flight into the dissociation region. In addition to these uncertainties regarding the rotational distribution(s), the incomplete resolution of the fine structure, and the extent to which the fine structure appears to overrun that of adjacent vibrational features greatly complicate its interpretation.

As an alternative explanation, we must also consider that within the very same energy range to which we have assigned the major predissociated levels, there exist a range of Rydberg states of the ion-pair type at larger internuclear separations, such as the radiatively identified b and b' states (see Figure 4 of Reference 1). The small vibrational spacings expected in these states is consistent with the observed overlaying oscillatory features. Consequently, we choose not to present even a qualitative analysis of the oscillatory structure here. It is clear nonetheless, that such structure is not an artifact introduced by the detector. For example, this structure does not appear in the spectra of fragments obtained using the supersonic nozzle, nor does it appear in the spectra of fragments from the

photodissociation or unimolecular dissociation processes we have observed with this detector in such species as H_2^+ , H_2 , NO , and O_2 .

CONCLUSIONS

By observing the spontaneous fragmentation of metastable N_2 molecules produced by charge transfer of N_2 in various gases, we have discovered several new Rydberg members of this molecule. The fact that the new states are all predominantly of the type $ns\sigma_g + N_2^+$ likely reflects the selectivity of the experiment on the basis of lifetime rather than a preference for populating this orbital in the charge exchange process. Absolute energies of these states are obtained by measuring the energy imparted to their neutral dissociation fragments, and branching among dissociation limits is observed. The precision at which the molecular energies are determined is solely governed by the unknown rotational populations.

We have not yet addressed the origin of the observed predissociations. To permit the observed long lifetimes, highly unfavourable conditions for the interaction of bound and continuum states must exist. This is not unexpected for Rydberg states since their configurations are clearly distinct from the repulsive states arising from the lowest four dissociation limits of N_2 .

ACKNOWLEDGEMENTS

It is a pleasure to thank Dr. D. L. Huestis for his enthusiastic interest in our work and for many fruitful discussions. This work was supported by NSF under grant number ATM-85-04152 and by the Aero Propulsion and Power Directorate, Wright Laboratory, (AFMC), Wright-Patterson AFB, Ohio, under contract F33615-85-C-2560.

REFERENCES

1. A. Lofthus and P. H. Krupenie, J. Phys.Chem. Ref. Data, 6, 113 (1977).
2. K. P. Huber and G. Herzberg, Molecular Spectra and Molecular Structure, Vol. 4, Constants of Diatomic Molecules (Van Nostrand Reinhold, New York, 1979).
3. H. Helm and P. C. Cosby, Bull. Am. Phys. Soc. 31, 936 (1986).
4. N. G. Utterback and B. Van Zyl, Phys. Rev. Lett. 20, 1021 (1968).
5. A. Salop, D. C. Lorents, and J. R. Peterson, J. Chem. Phys. 54, 1187 (1971).
6. Colutron, Model 101Q, Boulder, Co.
7. H. Helm, and P. C. Cosby, J. Chem. Phys. 86, 6813 (1987).
8. D. P. De Bruijn, J. Neuteboom, and J. Los, Chem. Phys. 85, 233 (1984).
9. Momentum transfer during the dissociative charge transfer reaction also played a major role in reducing the kinetic energy release resolution observed with this configuration, since the product N_2^* produced at the nozzle is no longer constained by the slit to a 4 mrad cone. Restricting the detected fragment coincidences to those for which the ratio $R_a/R_b - 1$, thus eliminating from consideration most dissociative charge transfer events that produced significant (>0.6 mrad) deviations of the N_2^* center of mass velocity vector from the beam axis, increased the apparent energy resolution, but did not recover the band-like structure that appears when the dissociation of only long-lived N_2^* species (formed in the charge transfer cell) is observed.
10. M. J. Haugh and K. D. Bayes, J. Chem. Phys. 75, 1472 (1971).
11. P. Cremashi, A. Chattapadhyay, P. V. Madhavan and J. L. Whitten, Chem. Phys. 109, 117 (1986).

TABLE 1. OBSERVED DISSOCIATION CHANNELS AND THEIR ASSIGNMENT

W (eV)	LIFETIME (ns)	COMMENTS	DISSOCIATION LIMIT	ION CORE	HYDROGEN	ENERGY (eV)	
						THIS WORK	PREVIOUS
A 440	0.6	a, b	$2D^{+2}D^{+}$	$A(v=0)$	$4s\sigma_g^3\pi_u$	14.97	(15.02) ^c
B 585	>2	a	$4S^{+2}D^{+}$	$A(v=0)$	$3s\sigma_g^3\pi_u$	12.73	(12.80) ^c
C 675	0.5	a	$2D^{+2}D^{+}$	$A(v=1)$	$4s\sigma_g^3\pi_u$	15.20	
D 820	1.3	a	$4S^{+2}D^{+}$	$A(v=1)$	$3s\sigma_g^3\pi_u$	12.96	
E 1050	~1	a	$4S^{+4}S$	d		10.81	(10.80) ^e
{ F 1320 F' 1400 }	{ 1.3 <1 }	{ f g }	{ $4S^{+2}P^{+}$ $4S^{+2}P^{+}$ }	{ $X(v=0)$ $X(v=0)$ }	{ $5s\sigma_g^3\pi_g$ $4d\pi_g^3\pi_g$ }	{ 14.66 14.74 }	{ (14.76) ^h (14.77) ^h }
G 1640	0.6	a, b	$4S^{+2}P^{+}$	$A(v=0)$	$4s\sigma_g^3\pi_u$	14.97	(15.02) ^c
H 1880	0.5	a, b	$4S^{+2}P^{+}$	$A(v=1)$	$4s\sigma_g^3\pi_u$	15.20	

a) removed by argon in source

b) branching to second dissociation limit

c) observed energy of $3\pi_u$ component (Reference 1)d) tentative identification: G^3A_g or $1^3\Sigma^+$ (see Figure 3 of Reference 1)e) energy of G^3A_g (Reference 1)

f) peak position at longest flighttime

g) peak position at shortest flighttime

h) calculated energy of Reference 11

FIGURE CAPTIONS

Figure 1. Schematic diagram for the experimental arrangement. A mass-selected N_2^+ ion beam, accelerated to several keV energy, is neutralized in the charge-exchange cell. Fast neutrals formed by charge transfer propagate through the aperture and slit and are intercepted by the beam flag. Coincident fragments produced by unimolecular dissociation of N_2 in the region between the slit and flag impinge on the PSD-C detector. In selected experiments, the N_2^+ beam is neutralized by gas introduced through the nozzle beam.

Figure 2. Center-of-mass kinetic energy release spectra observed from the unimolecular dissociation of N_2 . In the upper spectrum, the precursor N_2^+ ions were formed in a pure N_2 discharge, accelerated to 2 keV and neutralized in NO gas. The lower spectrum was obtained under identical conditions except that the precursor N_2^+ ions were formed in a mixture of 30% N_2 and 70% Ar. Features in the spectra are labeled by letters A - H.

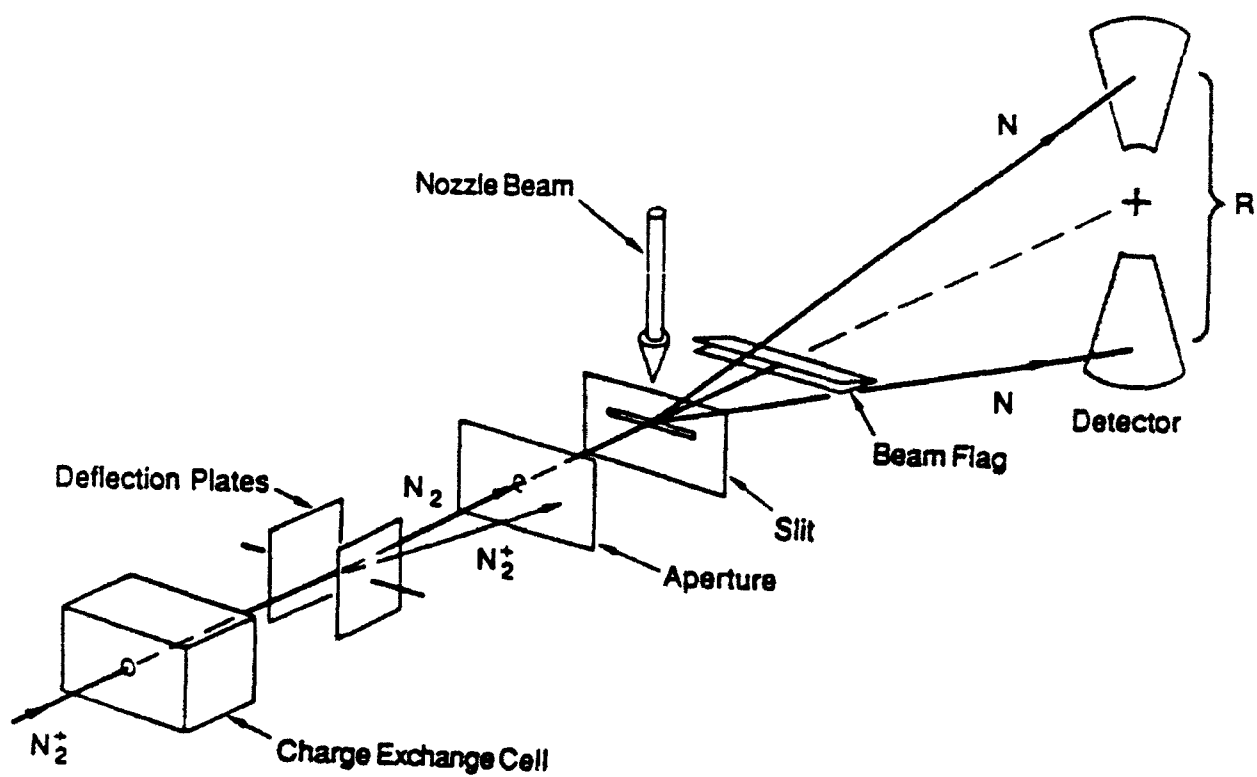
Figure 3. Center-of-mass kinetic energy release spectra for the unimolecular dissociation of N_2 formed by charge transfer of N_2^+ (N_2 discharge) at 3 keV in four different gases.

Figure 4. Center-of-mass kinetic energy release spectra for the unimolecular dissociation of N_2 formed by charge transfer of N_2^+ (N_2 discharge) at 2 keV in NO gas. The two spectra show the effect on the spectral features of the flag size used to intercept undissociated molecules.

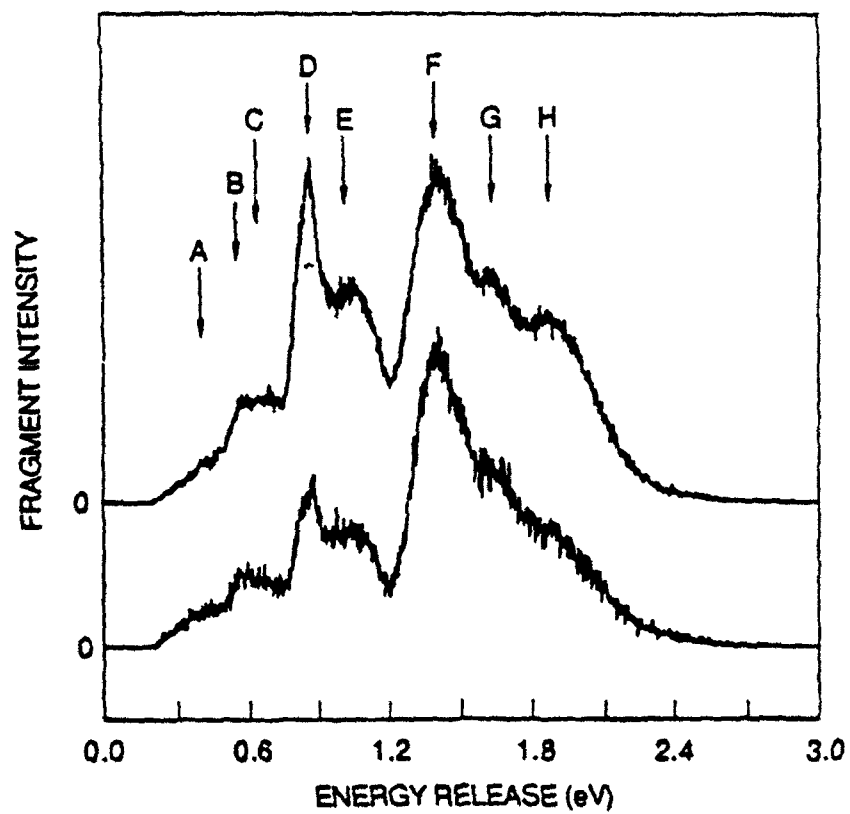
Figure 5. Center-of-mass kinetic energy release spectra for the unimolecular dissociation of N_2 formed by charge transfer of N_2^+ (N_2 discharge) at the three labeled acceleration voltages in NO gas using the small beam flag to intercept the undissociated neutral molecules.

Figure 6. Schematic diagram of the $ns\sigma_g$ Rydberg manifold converging to the $N_2^+ A^2\Pi_u$ core. Energy values indicated are taken from Reference 1.

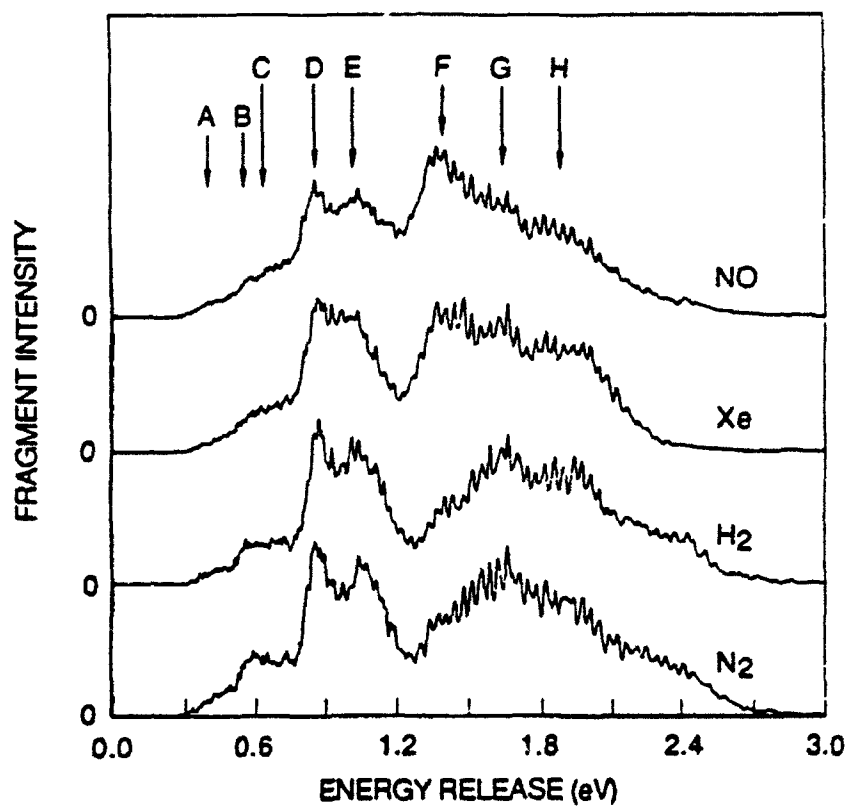
Figure 7. Energies of the predissociating levels observed in N_2 relative to the separated atom limits of $N + N$. These levels are labeled by letters A-H, corresponding to the features labeled in the kinetic energy release spectra. Known Rydberg levels of N_2 converging to the $N_2^+ X$ and A states are shown in this figure by solid lines. Expected, but previously unobserved levels converging to these cores are given by the dashed lines.



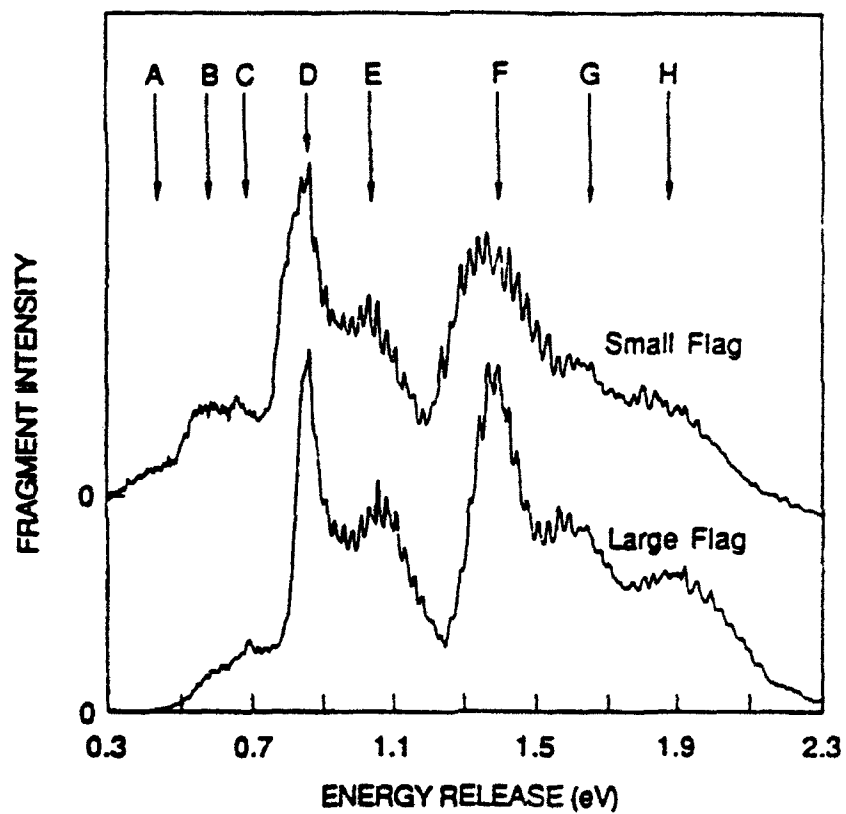
JA-330883-323F



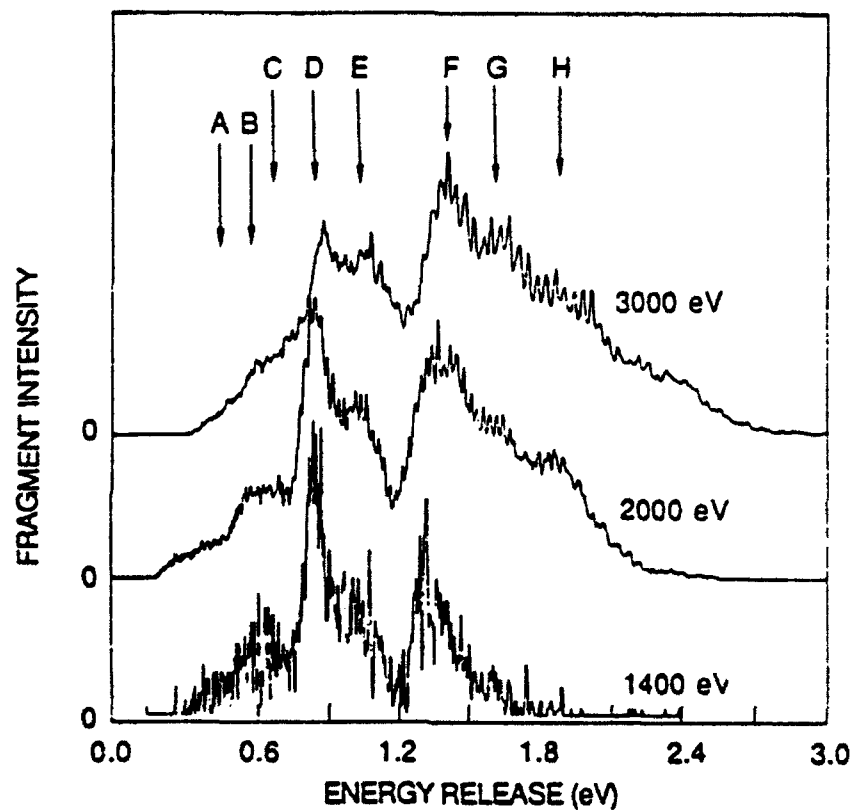
RA-3309583-113



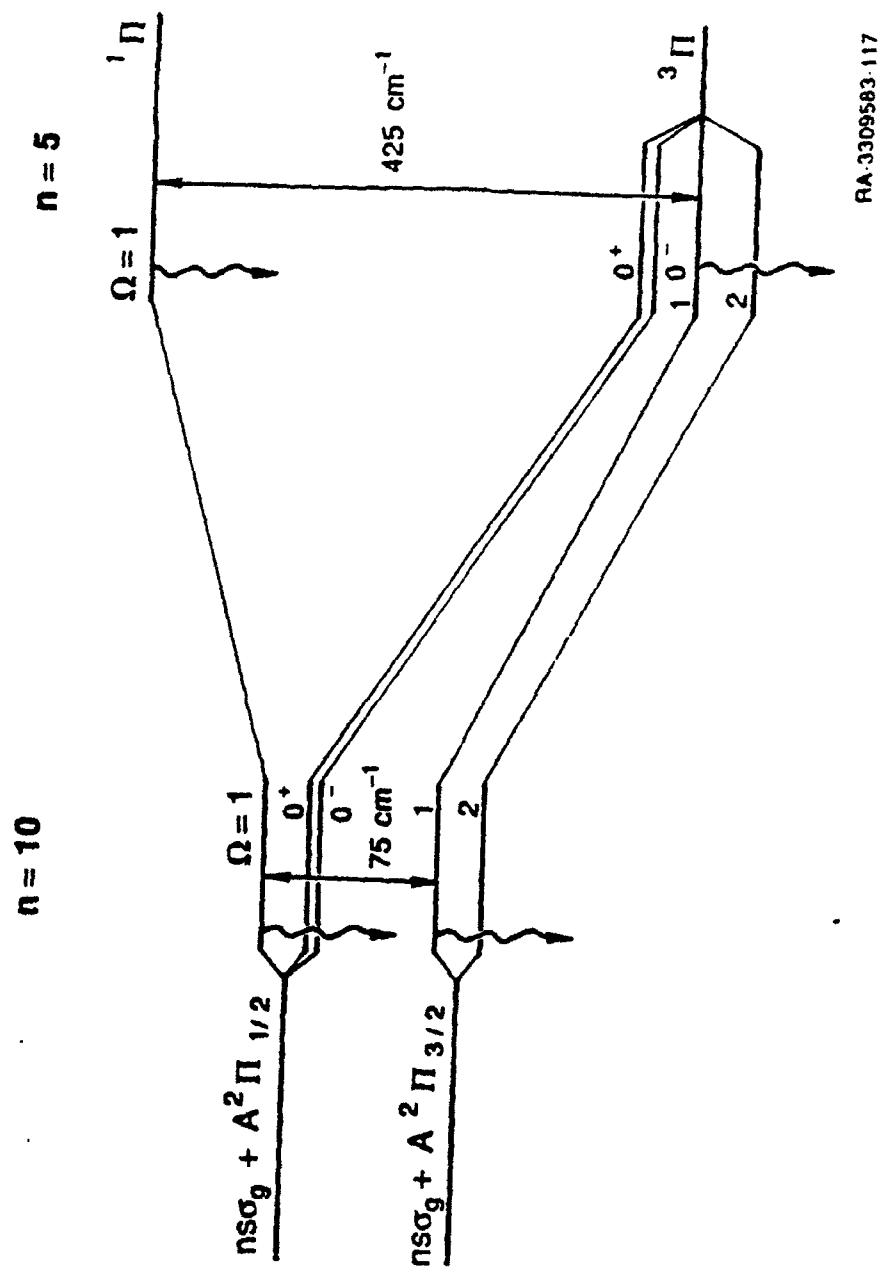
RA-3309583-114



RA-3309583-115

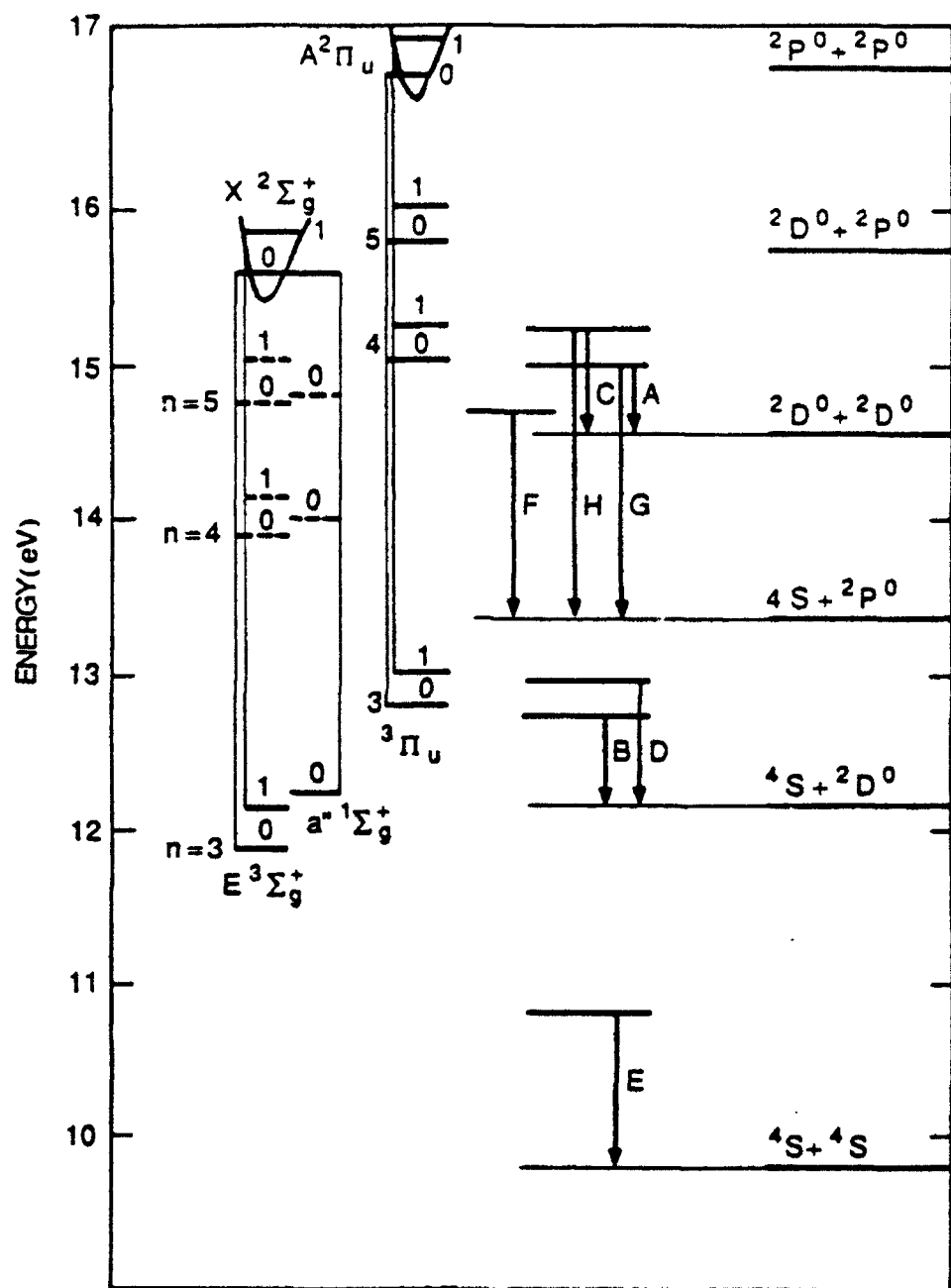


RA-3309583-116



RA-3309583-117

Fig. 6
Helm and Cosby



RA-330583-112

Appendix C

UNIMOLECULAR DISSOCIATION OF NO

UNIMOLECULAR DISSOCIATION OF NO

Philip C. Cosby and Hanspeter Helm

Molecular Physics Department
SRI International
Menlo Park, CA 94025

We have observed the spontaneous unimolecular dissociation of NO molecules formed by charge-transfer neutralization of NO^+ ions. The dissociations are observed 3 μs after formation of the neutral molecule. Analysis of the fragment kinetic energy releases that accompany the dissociations locates the energy of the predissociating levels. Preliminary identification suggests that the $L' \ ^2\Phi$ state is efficiently populated in the charge-transfer reaction and that a number of vibrational levels of the L' state are sufficiently perturbed by the $B' \ ^2\Delta$ to allow predissociation with lifetimes of $>10 \mu\text{s}$.

With the exception of the molecular species, the present experiments were performed in a manner identical to that employed in our previous study of N_2 (see Appendix B). Explicit account was taken of the heteronuclear character of NO in detection of the dissociation fragments. The NO^+ ions were produced by 180 eV electron-impact ionization of low pressure NO gas and were neutralized in NO gas at energies in the range of 2 - 4 keV. The fragmentation was observed under a variety of experimental conditions allowing variations in beam energy, distance from the charge transfer cell to the dissociation region, and detector geometry. No change in either fragment energy release or

dissociation rate was observed under these conditions, allowing us to establish a lower limit on the dissociation lifetime of the metastable levels as $>10\ \mu\text{s}$. Furthermore, neither collision-induced dissociation of the fast (keV) NO molecules nor dissociative autoionization was found to play a role in the observed dissociations. A dissociation rate of $6 \times 10^3\ \text{s}^{-1}\text{cm}^{-1}$ was observed from an NO beam of $8 \times 10^8\ \text{s}^{-1}$, suggesting that the dissociating levels account for more than 0.04% of the population in the NO beam.

A typical fragment energy release (W) spectrum observed from NO 3 μs after its production by charge transfer is shown at the top of Figure 1. This spectrum is the raw data acquired by the detector and includes not only the fragment energies produced by the molecule, but also W -dependent energy shifts and broadening due to the finite distance over which the fragments are collected. These apparatus effects, however, can be assessed using Monte-Carlo trajectory studies that explicitly incorporate the variety of apparatus geometries employed in the measurements. The simulation of the experimental spectrum is shown at the center of Figure 1. A satisfactory fit was achieved for all the spectra by assuming the predissociation of six vibrational levels, each with a rotational population distribution of 400 K. The appropriate level energies and intensities are shown at the bottom of Figure 1. A listing of the energy of these vibrational levels, their approximate relative intensity contributions to the dissociation, and the rotational constants employed in the fits is given in Table I. With the possible exception of the very weak feature at $W = 2.010\ \text{eV}$, the listed energies are expected to have a relative accuracy of $\pm 0.005\ \text{eV}$ and an absolute accuracy of $\pm 0.020\ \text{eV}$.

The fragment energy releases, W , in Table I specify the energy of the dissociating level above one of the dissociation limits in the NO molecule. The dissociation limit observed here is almost certainly the lowest NO dissociation limit $\text{N}(^4\text{S}) + \text{O}(^3\text{P})$. Levels $>1\ \text{eV}$ above any of the higher dissociation limits would lie in the ionization continuum and be subject to autoionization at a rate rapid compared to the slow dissociation observed here.

A very large number of NO electronic states, both Rydberg and valence, have bound levels in the region 1 - 2 eV above the lowest dissociation limit¹ and the situation is further complicated by numerous strong homogeneous Rydberg-valence perturbations.²⁻⁴ Nevertheless, the Rydberg states and valence state levels strongly perturbed by them are known to have radiative and/or predissociation lifetimes of order 10 ns,^{1,5} and can thus not directly participate in the observed dissociations. Bound valence states known¹ or expected⁶ to lie in this region are the B²Π, L'²Φ, B'²Δ, b⁴Σ⁻, G²Σ⁻, L²Π, and I²Σ⁺. Of these, only the L' state is without a dipole-allowed radiative cascade channel into a lower electronic state.

The L'²Φ is the lowest energy NO electronic state with Λ > 1, and thus has no radiative channels accessible below v = 7. As a result, this state has only recently been observed in the gas phase, using the technique of stimulated emission pumping from the B' state.⁷ The potential energy curve for the L' state derived by those measurements is shown in Figure. 2, together with that of the B' state. Energy levels in L' above v = 9 are obtained only by extrapolation and the extrapolated potential energy curve was used to estimate the rotational constants listed in Table I. The horizontal bars in this Figure represent the observed fragment energies and intensities from Table I. It can be seen that there is reasonable correspondence between the observed energy releases and specific vibrational levels in the L' state.

It remains for us to explain why dissociation of all levels in the L' state would not be observed, or perhaps more appropriately, why predissociation of any of the L' levels should occur, since only states with Λ ≤ 1 arise from N(⁴S) + O(³P). It is known⁷ that L'(v=9) heterogeneously perturbs the rotational levels of B'²Δ(v=1) with an Ω-dependent perturbation matrix element in the range of 4.3 - 0.3 cm⁻¹. This relatively weak interaction produces detectable (~1 cm⁻¹) shifts in the rotational levels only where the B' and L' levels are nearly degenerate in energy. However, a dissociation lifetime of order 10 μs implies an

equivalent level shift of only $5 \times 10^{-7} \text{ cm}^{-1}$! Levels separated in energy by as much as one vibrational interval could readily produce such a weak perturbation.

Granted an appropriate admixture of $^2\Delta$ character, the L' state could be predissociated by spin-orbit coupling to the continuum of the $a^4\Pi$ or another state to produce the unimolecular dissociation. Vibrational factors associated with both the L' - B' and B' - a interactions would establish the relative predissociation rates and thus the presence or absence of vibrational features in the fragment spectrum. It is not known whether the unobserved vibrational levels have substantially longer or shorter lifetimes than those levels that appear in the fragment spectrum. A quantitative treatment of the proposed predissociation mechanism is not appropriate at the present time. However, given both the agreement of fragment energy with L' vibrational level energy and with the onset of the B' - L' interaction, we are reasonably confident that the observed fragments arise from the L' state.

Due to its $(3\sigma_g)^2 (1\pi_u)^3 (1\pi_g^*)^2$ electron configuration,⁶ the L' state cannot be directly produced from the ground state NO^+ in a single electron transfer. However it could be formed from either the $\text{NO}^+ \text{ } ^2^3\Sigma^+$ or $w^3\Delta$ states. Such metastable excited states are known^{8,9} to account for more than 30% of the NO^+ ions formed by high energy electron impact. Moreover, the L' state can be formed in vertical, near-resonant transitions from $a(v \geq 7)$ or $w(v \geq 0)$, suggesting that its fractional population in the fast NO beam may be significant.

REFERENCES

1. K. P. Huber and G. Herzberg, *Molecular Spectra and Molecular Structure IV. Constants of Diatomic Molecules* (Van Nostrand Reinhold, N.Y., 1979).
2. A. Lagerqvist and E. Miescher, *Can. J. Phys.* **44**, 1525 (1966).
3. R. Gallusser and K. Dressler, *J. Chem. Phys.* **76**, 4311 (1982).
4. Ch. Jungen, *Can. J. Phys.* **44**, 3197 (1966).
5. K. Shibuya and F. Stuhl, *Chem. Phys.* **79**, 367 (1983).
6. H. H. Michels in *The Excited State in Chemical Physics*, J. W. McGowan, Ed. (Wiley, N.Y., 1980), Vol. II, Ch. 4.
7. M.-F. Taherian, P. C. Cosby, and T. G. Slanger, *J. Chem. Phys.* **83**, 3878 (1985).
8. R. F. Mathis, B. R. Turner, and J. A. Rutherford, *J. Chem. Phys.* **49**, 2051 (1968).
9. P. C. Cosby and H. Helm, *J. Chem. Phys.* **75**, 3882 (1981); P. C. Cosby and H. Helm, unpublished research.

Table 1.

Fragment energies observed in the unimolecular dissociation of NO. The fragmentation is observed $\sim 3 \mu\text{s}$ after formation of the molecule. Approximate relative intensities of the fragments and the rotational constants used in the spectral simulations are also given.

Fragment Energy (eV)	Fragment Relative Intensity	Rotational Constant (cm^{-1})
0.998	0.49	0.97317
1.090	1.00	0.95605
1.490	0.26	0.87695
1.624	0.36	0.83058
1.872	0.06	0.75265
2.010	0.02	0.69536

Figure Captions

- Figure 1 Fragment energy releases observed in the unimolecular dissociation of NO after a 3 μ s delay following charge transfer neutralization of NO⁺ in NO gas at 3 keV. The experimental spectrum is shown at top. The Monte Carlo simulation of the spectrum is shown at center. Energy levels and intensities used in the simulation are shown at bottom.
- Figure 2 Potential energy curves of the NO L' $^2\Phi$ and B' $^2\Delta$ states relative in energy to the N(4 S) + O(3 P) dissociation limit. Observed fragment energies and intensities are shown by the horizontal lines to the right in the figure.

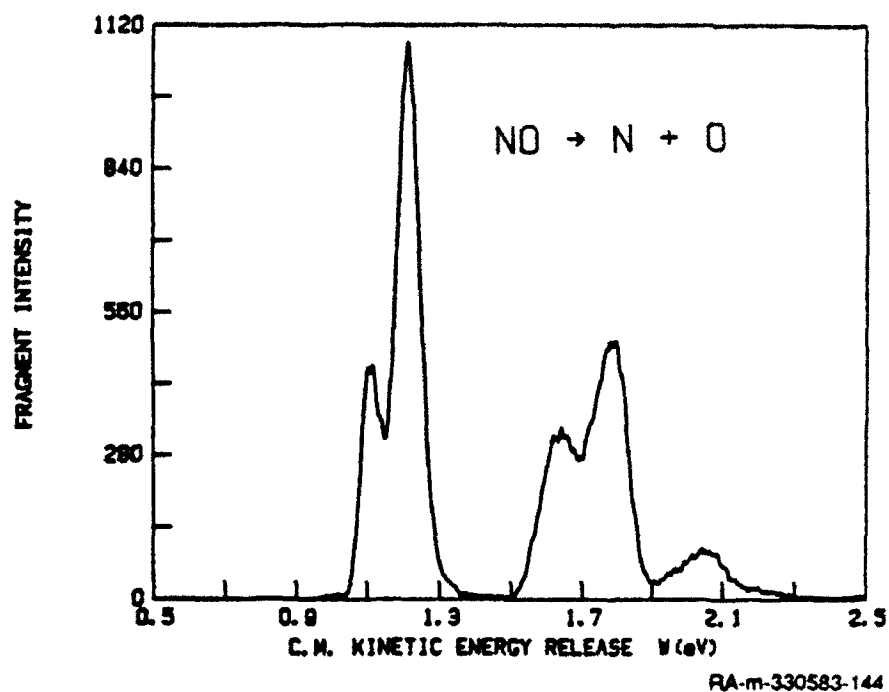


Figure E-1. Fragment energy releases observed in the unimolecular dissociation of NO.

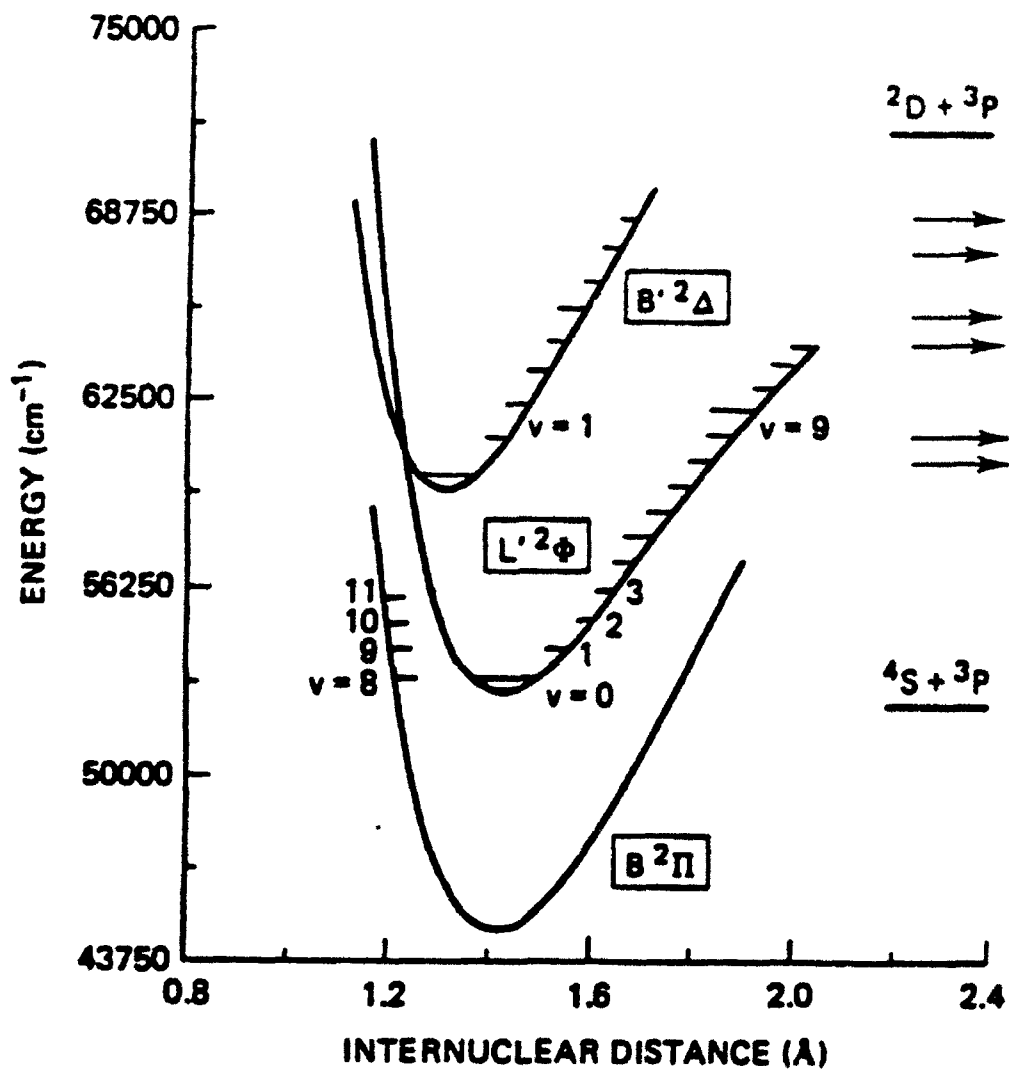


Figure E-2. Observed predissociation channels in NO and relevant potential energy curves. Observed fragment energies are indicated by the horizontal arrows.

Appendix D

ELECTRON-IMPACT DISSOCIATION OF CARBON MONOXIDE

ELECTRON-IMPACT DISSOCIATION OF CARBON MONOXIDE

P. C. Cosby

Molecular Physics Laboratory
SRI International
Menlo Park, CA 94025

ABSTRACT

The electron-impact dissociation of CO to form C and O atoms is observed in a crossed beam experiment at electron energies between the dissociation threshold (14 eV) and 198.5 eV. The center-of-mass energy released in the dissociation of individual molecules is explicitly measured using a position and time sensitive detector for the correlated neutral fragments. The observed energy release distribution is found to be highly structured, reflecting electron-impact excitation to Rydberg states converging to $\text{CO}^+(\text{X}^2\Sigma^+)$ which predissociate to ground state atoms. Little or no dissociation is observed from states above the first ionization limit. Total electron impact dissociation cross sections, exclusive of dissociative ionization contributions, and partial cross sections for the dissociative excitation of specific CO electronic states are presented.

MP 92-086
January 27, 1993

INTRODUCTION

The interaction of electrons with molecules is widely recognized as a critical process in the physics of ionized gases. Not only can excited molecular states or charged species be produced by the interaction, but the gas composition can be directly modified by electron induced dissociation. In this latter process,^{1,2} the electron excites an electronic state of the molecule that subsequently dissociates. The excitation step is believed to be well-described above threshold by theory,^{3,4} and has been the subject of numerous experiments.⁵ However, the fate of the molecule in this excited state is determined by the relative rates of the competing processes of dissociation, photoemission, and ionization, the quantitative calculation of which can be extremely difficult. Experimental characterization of the dissociation channel has also been difficult. With few exceptions,⁶⁻⁹ observations have relied upon the detection of highly excited fragments,¹⁰⁻¹⁴ which generally represent only a small subset of the accessible product channels. No technique has allowed a direct distinction between products arising from dissociative ionization, i.e. dissociation of the ionized molecule, and those from dissociation of the neutral molecule.

We report here a new technique for the quantitative observation of electron dissociation reactions. The reactant molecules are present as a fast neutral beam that is intersected by an electron beam. Therefore, the dissociation products are constrained to a narrow cone and can be detected through secondary emission at an electron multiplier. At keV energies, the secondary emission efficiency of the multiplier is relatively insensitive to electronic excitation of the fragments, allowing near-uniform detection sensitivity to either ground or excited state products. Position and time-sensitive detection at the multiplier of the two correlated products from a single dissociating molecule permits accurate definition of the center-of-mass translational energy release (W) in the dissociation and the angular distribution of the fragments. Charged particles produced by the electron interaction are collected by an electric field such that dissociative ionization cannot contribute to the correlated product signal.

We apply this technique to electron impact on carbon monoxide and observe for the first time the reaction:



where CO^* signifies a dissociative electronic state of the molecule. Since the excited state necessarily lies above a molecular dissociation limit, the fragments in (1b) are produced with translational energy, W , corresponding to the energetic difference between the dissociating state and the internal energy of the products at infinite separation. Explicit measurement of the translational energy release W allows identification of the intermediate CO^* and the atomic states of the products.

Total absolute cross sections for Reaction (1) are reported here for electron impact energies in the range of 13-200 eV. In addition, detailed product distributions are determined over much of this range, allowing the assignment of partial dissociation cross sections for the more important dissociative states in the CO molecule. Since the present experimental technique is new, it is discussed here in some detail. Application of this technique to the electron-impact dissociation of other molecules such as N_2 , O_2 , CO_2 , and NO_2 will be reported separately.

EXPERIMENT

A schematic representation of the major features of the dissociation apparatus is shown in Figure 1. A fast (3-5 keV) CO^+ ion beam is neutralized by resonant charge transfer in CO gas to produce a fast CO beam, which is collimated by a narrow slit and intercepted by the beam flag. Dissociation fragments produced in the region between the slit and the flag with sufficient transverse velocity to escape collection by the beam flag travel an extended distance (~ 1 m) where they are detected by a pair of position and time sensitive detectors. A weak (5 V/cm) transverse electric field, not shown in Fig. 1, in the region between the beam flag and the detector

prevents charged particles from arriving at the detector. The construction and functional description of the detector has been described elsewhere¹⁵ and will not be repeated here. The principle parts of the apparatus as they relate to the electron dissociation measurements are described below.

Neutral Beam

CO⁺ ions, produced from CO gas in an ion source, are accelerated to a selected energy in the range 3 - 5 keV, mass selected, collimated, and passed through a 10 cm long charge transfer cell containing CO gas. The pressure of CO gas in the cell was adjusted to produce approximately 10% attenuation of the ion beam. Charged particles exiting the cell are swept out of the beam by electrostatic deflection and collected. Neutrals leaving the cell are collimated by a 0.5 × 3 mm slit positioned 39 cm downstream of the charge transfer cell. Neutrals passing through the slit are intercepted by a 1.8 mm wide beam flag positioned 13.8 cm downstream of the slit. The function of the slit is threefold: (1) it produces a well defined neutral beam with an angular divergence of 1.2 mrad, (2) in combination with the beam flag, it masks the PSD-C from observing both fragments from a dissociation event occurring upstream of the slit, and (3) it preferentially passes the products of symmetric charge transfer, which are predominantly forward scattered with little angular divergence and greatly attenuates contributions from other scattering processes, such as collision induced dissociation and dissociative charge transfer.

Neutral Beam Flux. The neutral beam flux passing through the electron impact ionization region was monitored by displacing the beam flag and measuring the apparent current generated by the neutral beam in a Faraday cup centered on the PSD-C. The Faraday cup consisted of a stainless steel tube terminated by an insulated stainless steel collector. A potential difference of 80 VDC between the collector and the tube and a length/diameter ratio of 40 for the tube facilitated the consistent removal of the secondary electrons from the collector that were produced by the impact of the fast neutral beam. The neutral beam flux N is related to the measured current at the Faraday cup I_{fc} by the relation:

$$N = \frac{I_{fc}}{\eta}, \quad (2)$$

where η is the effective secondary emission coefficient. Absolute calibration of the neutral beam flux was made with a pyroelectric bolometer^{16,17} constructed from a 0.5" diameter \times 0.1" disk of Lead Zirconate-Titanate with silver electrodes deposited on the circular surfaces.¹⁸ The neutral beam was modulated at 5 Hz (by modulating the CO⁺ beam prior to charge transfer neutralization) and the pyroelectric signal, which is proportional to the power deposited by the fast beam, was detected by a lock-in amplifier. The absolute neutral beam flux was determined by comparison with the pyroelectric signal produced by an ion beam, whose flux was known from the measurement of its current with a calibrated electrometer:

$$N = \frac{IV_n}{eV_i}, \quad (3)$$

where N is the neutral beam flux, I is the current of the ion beam of equal energy, e is the electron charge and V_n and V_i are the bolometer outputs produced by the neutral and ion beam, respectively. Intercomparison of these two measurements of the neutral beam flux provides a direct measurement of the effective secondary emission coefficient at the Faraday cup for routine beam monitoring with an accuracy of approximately 6%. (For 3000 eV CO, $\eta = 0.31$). This coefficient was found to be stable to within this calibration accuracy over extended periods of time (months). Maintaining the entire detector region in a clean (ion pumped) high vacuum ($<1 \times 10^{-8}$ Torr) probably contributed to this stability.

Internal Energy Distribution in the Fast Beam. The composition of the neutral beam is determined by the state composition of the precursor ion beam and the neutralization conditions. The present measurements were made with CO⁺ ion beams produced by two different ion sources: a low pressure (Nier-type) electron impact ion source and a high pressure hollow cathode ion source, with research grade CO gas used in each. In the Nier-type source, 100 eV electron impact produces the ions in a vertical excitation process in thermal (400K), low pressure

(10^{-5} Torr) CO gas and these ions are extracted by a weak repeller field in the absence of collisions. Vertical ionization of CO $X(v=0)$ produces CO^+ in three electronic states: $X^2\Sigma^+$, $A^2\Pi$, and $B^2\Sigma^+$, for which the partial ionization cross sections (σ_A, σ_B) are known.¹⁹⁻²¹ The B state is extremely short-lived (55 ns)²² and radiatively cascades predominantly into the lower vibrational levels of the $X^2\Sigma^+$ before the ions leave the ion source. The A state is longer-lived, with radiative lifetimes²¹ (τ_{A+}) of 4.0-2.4 μ s in $v=0-6$, but almost completely radiates, predominantly into the X state, during the ≥ 7 μ s flight time (t) between the ion source and the charge transfer cell. Using the partial ionization cross sections and vibrational overlap integrals²³ and energies computed from the RKR potential energy curves of the CO ground state²⁴ and the CO^+ X, A, and B states,²² the population distribution of CO^+ $X(v)$ entering the charge transfer cell can be estimated with some confidence from:

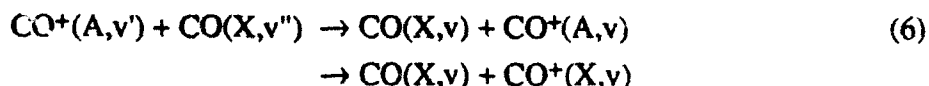
$$\begin{aligned}
 p(X^+) &= \frac{\sigma_T - \sigma_A - \sigma_B}{\sigma_T} q(X^+, X=0) + \\
 &\frac{\sigma_A}{\sigma_T} \sum_{A^+} \frac{q(A^+, x=0) q(A^+, X^+) v_{A^+ X^+}^3}{\sum_{X^+} q(A^+, X^+) v_{A^+ X^+}^3} \left(1 - e^{-t/\tau_{A^+}}\right) + \\
 &\frac{\sigma_B}{\sigma_T} \sum_{B^+} \frac{q(B^+, X=0) q(B^+, X^+) v_{B^+ X^+}^3}{\sum_{X^+} q(B^+, X^+) v_{B^+ X^+}^3}, \quad (4)
 \end{aligned}$$

where X^+ , A^+ , and B^+ refer to vibrational levels in the CO^+ states, σ_T is the cross section²⁵⁻²⁷ for the production of CO^+ from CO, σ_A and σ_B are the partial ionization cross sections, and $q(i,j)$ is the Franck-Condon factor and v_{ij} is the photon energy connecting the levels i and j . The usual assumption is made in (4) that the transition moments vary negligibly with internuclear distance. For a 3000 eV beam energy, Eqn. (4) yields an ion population distribution of 0.6328, 0.1445, 0.0805, 0.0512, and 0.0343 in $v=0-4$ of the CO^+ X state when the ions arrive at the charge transfer cell. In addition, 5.7% of the ion beam remains in the $A^2\Pi$ state, predominantly in its lowest vibrational levels due to their longer relative lifetimes.

Even at the relative high beam energies employed here (3-5 keV), the cross section for the symmetric, resonant charge transfer reaction in the neutralization cell



is rather large (approx 20 \AA^2);²⁸ hence the electron transfer takes place at large intermolecular separations with minimal perturbation of the electronic structure of the isolated molecules and little transfer of momentum. Calculations of this charge exchange reaction have shown that the selection of product states at these higher energies is dominated by the Franck Condon factors for ionization/recombination transitions in the isolated species.²⁸ In fact, this propensity is observed even in asymmetric charge transfer reactions.²⁹ For the case of CO^+/CO , the Franck Condon factors are nearly diagonal, leading to a nearly vibrationally adiabatic transfer of population from the fast ion beam to the fast neutral beam. Taking the vibrational overlaps explicitly into account, the predicted population distribution in $\text{CO } X^1\Sigma^+(\text{v}=0-3)$ is 0.565, 0.193, 0.091, and 0.054, accounting for >90% of the population. As mentioned above, approximately 5.7% of the ion beam arriving at the charge transfer cell populates the $A^2\Pi$ state. This state has both symmetric and asymmetric product channels



accessible to it. However, the Franck Condon factors for either of these channels are quite small relative to those from $\text{CO}^+(\text{X})$ reactants; hence the charge transfer cross sections for $\text{CO}^+(\text{A})$ are undoubtedly smaller than from $\text{CO}^+(\text{X})$, with the result that the contribution of this state to the product distribution in the fast neutral beam will be even smaller than its 5.7% concentration in the reactant ion beam and can be neglected.

The CO^+ ion beam produced by the hollow cathode ion source is subject to a large number of low energy collisions with relatively high pressure (0.2-1 Torr) CO gas within the

source volume. We would expect the electronic and vibrational excitation in these ions to be almost completely quenched by low energy charge exchange reactions prior to their extraction. This has indeed been found for other species³⁰ (H_3^+ , O_2^+) produced with this ion source. Charge transfer neutralization of a $\text{CO}^+(\text{X}, \text{v}=0)$ ion beam should produce a neutral $\text{CO}(\text{X})$ beam almost entirely (>90%) in its ground vibrational level.

The basis for the rotational distribution in the neutral beam is the thermal (300-400K) rotational distribution of the source gas. This distribution is expected to be largely unchanged by ionization or by radiative cascade among the ion states ($\Delta J = 0, \pm 1$) that accompanies beam production with the electron impact source. In the hollow cathode source, the rotational distribution will be a thermal distribution in the ion at the temperature of the bath (source) gas. Since the CO and CO^+ ground states have nearly the same rotational constants,²² the rotational population distribution of the ions produced by each source will be nearly identical. There is very little information on rotational propensities in the charge transfer reaction. Clearly, if the electron exchange occurs at sufficiently large intermolecular separations, the product rotational distributions will largely reproduce those of the reactant ion beam, i.e. differ by at most a few quanta from that of the thermal source gas. This is supported by the LIF study by Ding and Richter³¹ of the analogous N_2^+/N_2 reaction at 800 eV. Other studies have found that the degree of rotational excitation in the products scales with increasing energy defect in the neutralization reaction.³²

Species Composition of the Fast Beam. Contamination of the CO neutral beam by other atomic or molecular species can arise either in the ion source or in the charge transfer cell. Mass selection of the ion beam with unit mass resolution excludes the products of dissociative ionization or of ion molecule reactions in the ion source from entering the charge transfer cell. Unfortunately, the main contaminant of the CO source gas is N_2 , whose charged product N_2^+ has the same nominal mass as CO^+ at our level of resolution. The use of high purity CO source gas (total impurities < 0.003%) and frequent monitoring of the N^+ current produced by the ion source

insured that N_2^+ charge transfer products made negligible contributions to the neutral beam purity. (This species at the ppm level does, however, provide the dominant contribution to the background encountered in measuring the electron-impact dissociation products, as will be described below).

The second source of contamination is collisional dissociation or dissociative charge transfer of the CO^+ beam in the charge transfer cell. In general, these contributions will be small, reflecting the size of their cross sections ($< 1 \text{ \AA}^2$) in comparison with that for symmetric resonance exchange (20 \AA^2). In addition, significant scattering accompanies these processes with small cross sections, so many of these fragments are excluded by the slit entrance to the interaction region, with an acceptance of 1.3 mrad vertical and 5.1 mrad horizontal. By comparison, a dissociation occurring in the charge transfer cell with an energy release of $W=1$ eV will produce the fragments dispersed over 21 mrad. Nevertheless, it is important to confirm the beam purity. For this we use the electron beam to ionize the molecular beam and observe the ionization products. Fragments produced in the charge transfer cell will arrive at the electron interaction region with very nearly the same laboratory velocity as the CO^+ precursor and with an angular divergence established by the entrance slit (1.3 mrad in the vertical direction, 5.1 mrad horizontal, in the sense of Figure 1). By positioning a pair of vertical electrostatic deflector plates in the region between the electron beam and the beam flag, fast charged species produced by direct ionization of the molecular beam will be deflected by an amount inversely proportional to their mass. This deflection, projected over a distance of approximately 94 cm, is observed on one of the position sensitive anodes of the PSD-C. The integrated counts observed on the anode for one deflection voltage (175 v) following 50 eV electron impact on the CO beam is shown in Fig. 2. The abscissa in this figure gives the distance of ion impact vertically with respect to the projected point of impact of the neutral beam on the detector. The large peak is produced by CO^+ , formed by direct ionization of CO. The width of this peak reflects the angular divergence in the neutral beam (1.2 mrad) and the vertical slit width (0.05 cm). The position of the peak

(2.02 cm) on the detector reflects the specific deflection voltage chosen. If the molecular beam were contaminated by O atoms, for example, a peak of comparable width should be observed near 3.54 cm in this spectrum with a height reflecting the concentration (and relative ionization cross section) of this species. A series of such spectra obtained for a range of deflection voltages and at electron energies up to 200 eV showed no definitive evidence of contamination by either C or O, leading to the conclusion that CO constitutes $\geq 95\%$ of the molecular beam.

ELECTRON GUN

The rectangular electron beam utilized for the neutral beam dissociation and ionization measurements is produced in a simple pentode gun from a directly heated Thoria (ThO_2) coated irridium filament of rectangular (0.07×2.8 cm) geometry. The third lens, with an open area of 0.3×2.6 cm, provides the smallest geometric constraint to the electron beam, whose width is otherwise determined by the accelerating voltages applied to the first four lens elements. The fifth lens, with an open area of 0.95×3.8 cm, is maintained at ground potential and is covered with 95% transmission tungsten mesh to minimize field penetration into the electron beam-neutral beam interaction region. This lens defines one side of the interaction region, with an identical element terminating the 0.89 cm wide interaction region. A potential of 1.5 VDC is maintained between these two elements to minimize trapping of slow electrons or ions in this region. The nominal electron energy is selected by the potential difference between the filament and the entrance to the interaction region. Collection of the electrons that pass through the interaction region is accomplished by a two element, 1 cm deep Faraday cup. The potential of the cup, typically -20VDC with respect to the interaction region (lens 5) is adjusted to approximately 2 volts above the onset of the plateau for a constant current of collected electrons ($dI/dV = 0$). No magnetic field is used for collimation of the electron beam, to facilitate transmission of an ion beam through the gun to the detector. Electron currents at the Faraday cup range from 0.1 mA for a nominal 10 eV electron beam to 1 mA for nominal beam energies ≥ 50 eV. Retarding potential difference measurements at the Faraday cup show a triangular electron energy spread

with a full width at half maximum of 1.5 eV, independent of beam energy over the range of 15 - 200 eV. This width roughly corresponds to the voltage drop across the directly heated filament. The gun assembly is maintained at a vacuum of $\leq 3 \times 10^{-8}$ Torr during operation.

The explicit spatial overlap of the electron beam and the fast neutral beam is one of several critical elements required for a determination of the dissociation cross sections. To facilitate the measurement and optimization of this overlap, the entire electron gun assembly is mounted on a micrometer adjusted translation stage. For reference, consider an orthogonal x,y,z coordinate system with the neutral beam propagating along the y axis with its slit dimensions of 0.05×0.2 cm in the z,x plane. The electron beam propagates along the x axis with its narrow and long dimensions in the z,y plane and the gun assembly can be translated along the z-axis with a precision and reproducibility of $< 7 \times 10^{-4}$ cm. The relative overlap of the two beams is determined by observing the products of the electron impact interaction (dissociation or, more easily, ionization) as a function of electron gun translation. Figure 3a shows the number of CO^+ ions (the summation of the counts in the CO^+ peak in Fig. 2) formed by electron impact ionization of the CO beam at 40 eV as the electron gun position is translated over a distance of 0.6 cm. The 0.128 cm FWHM of the near-gaussian ionization signal represents the convolution of 0.07 cm wide neutral beam (at the electron beam, considering angular divergence) with the spatial distribution of the electron beam at this energy. As mentioned above, the spatial distribution of the electron beam is highly dependent on the accelerating voltage. Figure 3b shows the variation in the FWHM of the ionization products with nominal electron energy. These values are also a good representation of the effective electron beam width; explicit deconvolution of the 0.07 cm neutral beam width decreases these values by ≤ 0.007 cm. Calibration of the electron beam energy with respect to the nominal acceleration voltage was accomplished by comparing the apparent electron energy dependence of the measured cross sections for ionization of Ar and of CO in the first 20 eV above threshold with the reported

values.^{33,27} The mean correction thus obtained is 1.5 ± 1.5 eV with respect to the nominal acceleration voltage. This correction is incorporated in the data reported here.

In addition to providing a mechanism for defining the overlap of the electron and neutral beam, translation of the electron gun allows phase sensitive detection of the electron impact dissociation signal from various other dissociation processes that can occur in the fast beam. To appreciate how very minor effects can mask the dissociation signal, consider the relative densities of the electron beam, the neutral beam and the residual gas in the interaction region. For typical conditions of a neutral beam flux of $3 \times 10^{10} \text{ s}^{-1}$ for 3000 eV CO and a current of 0.5 mA for 20 eV electrons, their respective beam densities amount to only 1.4×10^5 molecules/cm³ and 3.6×10^7 electrons/cm³, respectively. These are quite small in comparison with the density of residual gas of $9.6 \times 10^8 \text{ cm}^{-3}$ in the interaction region at a pressure of 3×10^{-8} Torr. Thus the main product of electron impact will be the ionization and excitation of the residual gas, though these products are easily distinguished because they are translationally slow (the impact of slow metastables that drift from the electron beam region constitute the primary, but noncoincident, background at the PSD-C (see Fig. 2)). Similarly, collisions of the fast CO beam with the residual gas in the region between the slit and the beam flag can produce fast products. For example, collision induced dissociation with a cross section of order $1 \times 10^{-18} \text{ cm}^2$ can produce a product flux comparable to electron impact dissociation with a cross section of $1 \times 10^{-16} \text{ cm}^2$. Simple electrical modulation of the electron flux and phase sensitive detection of the dissociation products is one obvious approach to distinguishing the electron/neutral beam products. But this approach has a very serious drawback in that the residual gas rapidly adsorbs on all surfaces in the electron gun in the momentary absence of electron bombardment degassing. The repetitive adsorption/degassing cycle that accompanies modulation of the electron current serves to also modulate the neutral gas density within the electron interaction region (and thus a collision induced dissociation background) in phase with the electron beam. Translation of the electron gun assembly with the electron beam operating at constant current and continuously

striking the same surfaces, allows modulation of the electron beam /neutral beam interaction without affecting other variables.³⁴

Dissociation Fragment Detection

Another key element in the measurement of electron dissociation cross sections is the sensitive and exclusive detection of the dissociation fragments. This is accomplished by the position sensitive detector for correlated particles (PSD-C), which has been used previously for the observation of photodissociation^{15,30,35-37} and dissociative charge transfer^{32,38} products. This detector^{39,15} makes use of the fact that when a molecule dissociates, its fragments are imparted equal, but opposite, momenta with respect to its center of mass, which is travelling with the velocity of the molecule prior to dissociation. The components of the fragment momenta both parallel with and perpendicular to the center of mass velocity produce a spatial separation of the two fragments that is linearly proportional to the distance over which the fragment trajectories are allowed to propagate unimpeded. This is shown schematically by the Newton velocity diagram for the dissociation of CO in Figure 4. The function of the PSD-C, positioned a distance L from the point of dissociation, is to measure this separation of the two fragments resolved into its two components: R , the radial separation of the fragments in the direction perpendicular to the center of mass velocity (the beam direction) and the separation parallel to the beam, as manifested by the difference in the fragment arrival times Δt . The PSD-C detector explicitly measures these two quantities for each pair of fragments from which both the center-of-mass translational energy release with which the molecule ejected the fragments:

$$W = \frac{E_0}{L^2} \left[\frac{Mm}{(M+m)^2} \right] \left[R^2 + (v\Delta t)^2 \right] \left[1 + \frac{2(m-M)v\Delta t}{(M+m)L} \right] \quad (7)$$

is determined, as well as the center-of-mass angle (with respect to the beam direction) Θ at which they were ejected:

$$\Theta = \tan^{-1}(R/v\Delta t) \quad (8)$$

are calculated. In these equations, m and M are the masses of the light (C) and heavy (O) fragments, respectively, produced by the dissociating molecule of mass $m + M$, $E_0 = (M + m)v^2/2$ is the kinetic energy of the CO molecule (i.e. the kinetic energy of the CO^+ charge transfer precursor), v is its velocity, and L , R , and Δt are defined above. The accuracy of the detector is better than $100\text{ }\mu\text{m}$ in the determination of R and better than 1 ns for Δt . The beam energy is specified to within 10 eV . For cases, such as photodissociation with a well-defined laser beam, where the distance L can be precisely specified to within 0.2 cm for photodissociation events, W can be determined with an absolute accuracy of better than $\pm 0.020\text{ eV}$. For the present case of electron impact dissociation, the uncertainty in L , ΔL , is specified by the length of the electron beam, neutral beam interaction ($\Delta L = 2.6\text{ cm}$), producing a resolution in W of $\Delta W/W = 2\Delta L/L = 0.052$. If a molecule were to dissociate by some mechanism other than electron impact, such as spontaneous dissociation or collision induced dissociation, ΔL can be even larger, with a maximum value of $\Delta L = 18\text{ cm}$, as limited by the spacing between the beam defining slit and the beam terminating flag. The W resolution for such processes is substantially degraded: $\Delta W/W \leq 0.38$.

The correlation between fragment separation and arrival time difference exists only when both fragments arise from a single dissociating molecule. In fact, this constraint is easily satisfied at the detector. For a worst case event, where the fragments from 3000 eV CO are ejected with $W = 4\text{ eV}$ parallel to the beam, both fragments arrive within $\Delta t = 0.52\text{ }\mu\text{s}$. This interval is yet smaller for larger E_0 , smaller W , and other ejection angles. Count rates on either anode of the detector of several thousand per second can be maintained with negligible false coincidence events. Even when a false coincidence is detected, the lack of correlation between R and Δt produces a constant background that can easily be distinguished.

The fact that the two correlated fragments are detected allows effective discrimination against competing electron-impact dissociation processes such as dissociative ionization:





Application of a weak electric field in the region between the beam flag and the detector prevents the charged fragment from arriving at the detector. The neutral product of course can impact on one half of the detector, but is not interpreted as a correlated event.

Fragment Angular Distribution

As shown in Eq. (8), the angle of fragment ejection relative to the velocity vector of the beam is given by the ratio of the fragments' spatial and temporal separations. Since the molecules are (presumably) randomly oriented in the beam, spontaneous dissociation of the molecule produces a fragment pair for which Θ can assume any value between 0 and $\pi/2$. The electron beam provides an orientation reference between the center of mass distribution of the electron impact dissociation fragments and the laboratory direction defined by the neutral beam velocity. More specifically, the momentum transfer vector \mathbf{K} , the difference between the momenta of the incident and scattered electron that induced the electronic transition, provides the symmetry axis for the collision.^{40,41} At electron energies substantially above the transition threshold, the direction of \mathbf{K} is effectively orthogonal to the incident electron velocity. At threshold energies, \mathbf{K} can assume any direction with respect to the incident velocity; the actual distribution of angles is given by the differential cross section⁵, such as is measured by electron energy loss spectroscopy. The alignment of the molecular axis of a diatomic molecule with respect to \mathbf{K} is well defined by group theory for any pair of initial and final states in the molecule and can be described as either perpendicular ($1.5\sin^2\theta$) or parallel ($3\cos^2\theta$) with respect to \mathbf{K} and with cylindrical symmetry about \mathbf{K} . Presuming axial ejection (along the bond axis), this alignment also describes the molecular fragments.

For an orientation of the electron beam with respect to the active area of the PSD-C, such as is shown in Figure 1, the observation of the fragment angular distribution with cylindrical symmetry about the neutral beam direction gives little information with regard to fragment

alignment with respect to K . Indeed, for an electron induced perpendicular transition at high electron energies, most of the fragments would actually fall outside the active area of the PSD-C. On the other hand, with the electron beam direction oriented along the direction of the PSD-C active area (vertical in Fig. 1) a preferential collection of the fragments from this transition is expected. Measurements were made for the electron impact dissociation of CO for both orientations of the electron beam at 30 and 100 eV. In each case, the fragment distribution with Θ was characteristic of an isotropic distribution. A more sensitive test is a comparison of the total electron dissociation cross sections obtained from the two orientations, but these were found to be equal to within their nominal accuracy (20%).

A near-isotropic fragment distribution can certainly be rationalized for the case of CO since the energy distribution of the fragments very clearly demonstrates that the predominant source of dissociation is via the excitation to predissociated electronic states. These states live for more than one rotational period before dissociating such that discrete rotational levels within these states are well defined. In the case of photodissociation, the fragment angular distribution depends little on the electronic symmetry of the predissociated state, but rather on the change in rotational angular momentum that accompanies its excitation. Even when excited with linearly polarized light, the distributions^{42,43} accompanying photon induced $\Delta J = \pm 1$ transitions are much closer to being isotropic than either parallel or perpendicular, except at very low rotational quantum numbers, which constitute only a small fraction of the total thermal population. Since high electron energies approach the case of *unpolarized* light and particular rotational branches are not resolved by electron excitation, full randomization of predissociation fragment anisotropies is not unreasonable.

While predissociation provides a rationale for isotropic fragment distributions in CO, precisely the same results have been obtained for electron impact dissociation of other molecules, particularly O₂. In the case of O₂, fragments that can be uniquely attributed to direct dissociation in a Σ - Σ transition, exhibited no anisotropy in Θ in either orientations of the electron beam, nor

in the magnitudes of the collected fragment flux. In contrast, the anisotropies arising from a Σ - Σ transition have been well characterized by both experiment⁴⁴ and theory^{45,46} in the case of the dissociative ionization of H_2 . Given that none is observed with the present experimental arrangement, we must suspect that the electron velocity vectors are not orthogonal to the neutral beam velocity. While there is a geometric constraint along the narrow width of the beam that would limit linear electron trajectories to a maximum deviation from orthogonality of approximately 12° at beam intersection, the very long length of the electron beam along the neutral beam direction (2.6 cm) provides effectively no angular constraint in the plane of the neutral beam. In view of these findings, we interpret the collection of dissociation fragments as arising from an isotropic distribution in the center of mass frame of the molecule, but acknowledge the possibility of undetected anisotropies in assessing the absolute errors in the measurement.

Fragment Mass Ratio

The separation R of the fragments at the detector surface is the sum of the individually measured radial distances of the two fragments from the center of the detector: $R = R_a + R_b$, as illustrated in Fig. 4. These two radial distances allow distinction between the light and heavy mass particles to establish the proper sign of Δt in Eq. (7). Since the two fragments were ejected with equal momenta in the center-of-mass frame and the difference in the fragment arrival times at the detector is small relative to their flight time after dissociation,

$$\frac{R_m}{R_M} \sim \frac{M}{m}. \quad (10)$$

That is, the ratio of these distances is inversely proportional to the ratio of the fragment masses. Figure 5 shows the distance ratio observed for the fragments produced by electron impact dissociation of the fast neutral (CO) beam by 40 eV electrons. The dashed line in this figure denotes the mass ratio for C + O fragments. While the distance ratio distribution is rather broad,

reflecting both the angular divergence of the CO beam and the approximate nature of Eqn. (5), the distribution clearly confirms the expected products of reaction (1).

Quantitative Fragment Detection

A critical consideration in the quantitative measurement of electron impact dissociation is that not all dissociation products can be detected. This loss of fragments arises both in the projection of the fragments onto the active surface of the detector and in the detector's ability to generate a useful electrical signal registering the fragment impact. We account for these two sources of fragment loss by a collection efficiency term χ and a coincidence efficiency term ξ .

Collection Efficiency. The present fragment detection technique has a significant advantage in that the Jacobian for the transformation from the center of mass frame of the molecule to the laboratory frame of the detector is unity, provided the active area of the detector were sufficiently large to collect all fragments.³⁹ However, a practical implementation of this technique places several geometric constraints on the fragment trajectories that can actually strike the detector. These constraints, which arise from the beam flag and the finite active area of the detector, produce a collection efficiency that is an explicit function of beam energy E_0 , translational energy release W , and the center of mass fragment ejection angles Θ , defined above, and Φ , the radial angle in the plane orthogonal to the beam velocity: $\chi(E_0, W, \Theta, \Phi)$. Given explicit values for these variables and the physical dimensions of the apparatus, χ can be explicitly calculated for linear trajectories. In order to realistically reproduce the angular divergence of the fast neutral beam, the extended dimensions of the electron beam/neutral beam overlap region, and the radial asymmetry of the beam flag, Monte Carlo sampling is used to compute χ . For the experiments described here, E_0 is the selected value of the ion beam energy (3000 - 5000 eV), W is defined by the explicitly observed values for the dissociation fragments (Eqn. (7)), and Θ, Φ are drawn from an isotropic center of mass distribution, as discussed above. The values of χ for CO dissociation, computed as a function of W at two beam energies are shown in Figure 6.

Coincidence Efficiency. Fast neutrals striking an active area of the detector create secondary electrons that are amplified by the microchannel plates and provide both a fast timing signal and position dependent signal that must be detected and interpreted. The efficiency in converting a neutral impact into a detected electrical signal is an independent characteristic of each half of the detector. For the case of a molecular dissociation producing a flux of D fragment pairs striking an active region of the detector, the apparent flux of detected fragments on the two detector halves are:

$$\begin{aligned} C_1 &= D \cdot \rho_1 \\ C_2 &= D \cdot \rho_2 \end{aligned} \tag{11}$$

where ρ_1 and ρ_2 are the efficiencies on each half of the detector for converting fragment impacts to detected events. The apparent coincidence flux, where both fragments from the same molecule have produced detectable signals, is

$$C = D \cdot \rho_1 \cdot \rho_2. \tag{12}$$

Taking the ratio of the apparent coincidence flux to the apparent fragment flux on each half of the detector yields a direct measure of the individual efficiencies:

$$\begin{aligned} \rho_2 &= C/C_1 \\ \rho_1 &= C/C_2. \end{aligned} \tag{13}$$

This measurement can be made with any well defined source of dissociation events. In practice, we use molecular photodissociation as the source because of the ease with which a substantial flux of fragments can be generated and modulated. The coincidence efficiency $\xi = \rho_1 \cdot \rho_2$ is explicitly dependent on fragment velocity (which is effectively the same as that of the parent molecule). However, we operate at sufficiently high velocities that fragment mass, charge, and electronic excitation have little effect on ξ , which can generally be determined to within 5%

accuracy. For the fragment velocity appropriate for 3000 eV CO dissociation, ξ is measured to be 0.0442.

DISSOCIATION CROSS SECTION DETERMINATION

The cross section σ for electron impact dissociation occurring in a crossed molecular and ion beam is given⁴⁷ by the equation:

$$\sigma = \frac{R F}{N_e N_n M} \quad (14)$$

where R , N_e , and N_n are the flux of products, electrons, and neutral molecules, respectively, M is a velocity factor:

$$M = \frac{\sqrt{v_e^2 + v_n^2 - 2v_e v_n \cos \theta}}{v_e v_n \sin \theta}, \quad (15)$$

where v_e and v_n are the velocities of the electron and neutral beams and θ is their angle of intersection. For orthogonal beams where $v_e > v_n$, as in the present experiment, $M \sim v_n^{-1}$. The form factor F describing the overlap of the two beams is given by:

$$F = \frac{N_e N_n}{\int_{-\infty}^{\infty} n_e(z) n_n(z) dz}, \quad (16)$$

where $n_e(z)$ and $n_n(z)$ are the differential fluxes of the electron and neutral beams along the direction mutually orthogonal to both beams, z . Since the profile of the electron beam can be determined directly, as discussed above, and the neutral beam profile can be accurately calculated from the slit dimensions and measured angular divergence, the cross section could be calculated directly from Eqn. (14). However, small changes in the profile of the electron beam can introduce large errors in the cross section through the form factor F . DeFrance, et al.⁴⁸ and Müller, et al.³⁴ have shown that the ability to accurately translate the electron beam completely through the region of intersection allows the uncertainties introduced by F to be completely

avoided in the cross section measurement. From their derivation, if the total number of dissociation fragments N is accumulated as the position of the electron beam is moved at a constant velocity u along the z direction through the region of intersection of the two beams, then the dissociation cross section is given by:

$$\sigma = \frac{N u}{M N_e N_n} \sim \frac{N u v_n}{N_e N_n}, \quad (17)$$

provided the starting and ending positions of the electron beam are totally beyond the range of overlap. In terms of the experimental observables: the number of detected dissociation fragment pairs (N^*), the neutral current at the Faraday cup I_{fc} , and the electron beam current I_e :

$$\sigma = \frac{N^* u v_n \eta e}{\xi \chi I_e I_{fc}}, \quad (18)$$

where e is the electron charge and the other symbols have been defined above. In practice, the scan of the electron beam position is accomplished in a series of m discrete steps, with the N^* dissociation products accumulated for a selected time interval τ at each position z . In order to exclude electron-independent dissociation products from the accumulated total fragments, the (position independent) background dissociation flux N_{bkg} is accumulated during the course of the scan for a period of 5τ with the electron beam positioned at the scan starting position z_0 , ending position z_m , or alternately at z_0 and z_m after each five steps of the electron gun:

$$N^* = \sum_{k=0}^{m/5} \left(\sum_{i=5k}^{5k+4} N^*(z_k, \tau) - N^*_{bkg}(z_0, 5\tau) \right). \quad (19)$$

The significance of modulo 5 in the summation is only as a compromise between minimizing the rather significant period of time required to reposition the electron gun to its starting or ending location with the micrometer drive (1-2 sec) and maintaining an accurate sample of the dissociation background flux throughout the scan. Typically, $500 \leq m \leq 3000$, $1s \leq \tau \leq 3s$,

$|z_m - z_0| \geq 0.48$ cm and $u = |z_m - z_0|/m\tau \leq 9.8 \times 10^{-4}$ cm/s. A typical accumulation of N^* as a function of electron gun position is shown in Fig. 7 for CO interacting with 48.5 eV electrons. The data points in this figure are the values of the argument of the summation over k in Eqn. (19), i.e., after each background subtraction. The error bars in this Figure represent the statistical error associated with the background subtraction and they increase in both relative and absolute value with increasing scan distance after the electron beam has completely passed through the neutral beam. The value of N^* for the cross section calculation is determined from the onset of the linear region after the electron beam has passed completely through the neutral beam.

RESULTS AND DISCUSSION

CO DISSOCIATION CROSS SECTION

The total dissociation cross section measured for the reaction (1) is shown by the data points in Figure 8 and listed in Table I as a function of electron impact energy in the range of 13.5 - 198.5 eV. The cross section rises steeply from zero to a maximum of $7.6 \times 10^{-17} \text{ cm}^2$ at electron energies in the range of 40-50 eV, slowly decreasing at higher electron energies. A linear regression of the cross section determined at the four lowest electron energies yields an onset for the dissociation at 11.2 eV, which is fortuitously close to the CO dissociation energy²² $D_0^0 = 11.092 \text{ eV}$, considering the $\pm 1.5 \text{ eV}$ accuracy of the electron energy determination. The cross sections in this Figure presume an isotropic distribution of fragments with respect to the electron momentum transfer vector, which as discussed above, appears to be consistent with the present observations. The error bars given for the cross section values in the figure primarily reflect the statistical error in determining the apparent fragment flux N^* , with smaller contributions due to variations in electron flux and neutral flux during the determinations. Considering the root-mean-square contributions of the individual absolute uncertainties of each term in Eqn. (18) except χ yields an absolute uncertainty in the cross section of 11.7%. Cross sections remeasured after substantial periods of time (months) or with the fast neutral beam generated with the two different ion sources fall within this range of uncertainty. Cross sections measured with the two orthogonal orientations of the electron beam with respect to the detector fall within $\pm 20\%$ of each other, though statistical errors contribute appreciably to this range. If we also consider the 23% uncertainty in the fragment collection efficiency factor χ that can arise from undetected deviations from a purely isotropic fragment angular distribution, the rms estimate for the absolute uncertainty in the dissociation cross sections increases to 25.8%. Since variations in the measured cross section of this order are not specifically excluded by the present measurements, this value of 25.8% appears to be the more appropriate estimate of the true absolute

uncertainty of the dissociation cross section. Both the relative errors and the absolute errors in the measured cross section are listed in Table I. As indicated in Eqn. (1), this cross section refers only to the production of *two neutral* dissociation fragments and include no contribution from dissociative ionization products.

Other measurements of the CO total electron impact dissociation cross section are not available for comparison. However, Kanik, Trajmar, and Nickel⁴⁹ have recently reported total electronic state excitation cross sections for electron impact on CO at energies between 1 eV and 1 keV. These cross sections, shown by the solid line in Fig. 8, were deduced from the difference between the total electron scattering cross section and the sum of the integral cross sections for elastic scattering, vibrational excitation, and ionization at each electron energy. As can be seen from Fig. 9, the total excitation cross section is typically 4 to 5 times larger than the measured dissociation cross section. This cross section ratio is roughly the ratio of the energy difference between CO $X^1\Sigma^+(v=0)$ and the first ionization limit (14.0 eV) to the energy difference between the lowest dissociation limit of CO and the first ionization limit (2.9 eV), reflecting the fact that only electronic excitation to states above the dissociation limit can produce dissociation. Information on the identity of the dissociating CO states is given by the observed fragment energy distribution, discussed below.

FRAGMENT ENERGY DISTRIBUTION

Apart from providing a mechanism for detecting correlated dissociation fragment pairs, the PSD-C detector further labels each detected dissociation with the spatial and temporal separation of the two fragments, which via Eqn. (7) specifies the center-of-mass translational energy release (W) with which they are produced. In accumulating this spectrum, the value of W is calculated from the measured R and Δt of each detected dissociation fragment pair, assuming a fixed value for L corresponding to the distance from the center of the electron beam to the detector and presuming the fragment masses are 12 and 16. Based on this calculated value of W , the event is binned into the one of 1024 equally spaced W intervals in the range $0 \leq W \leq 6$

eV. The raw (uncorrected) fragment distribution observed for 58.5 eV electron impact on a 3000 eV fast neutral (CO) beam is shown in Figure 9 for W in the range of 0-3.5 eV. Essentially no fragmentation is observed at $W > 3.5$ eV. The spectrum was acquired at two positions of the electron beam: the upper trace with the electron beam intersecting the fast neutral beam and the lower trace with the electron beam positioned outside the region of overlap. The electron gun location was alternated between these two positions every 30s during the 9.5 hours required to acquire this spectrum. The upper spectrum includes both the electron impact dissociation products as well as those arising from other (background) dissociation processes. The lower trace has contributions from only the background dissociation processes. Given the collection and coincidence efficiencies of the detector, the observed background fragments represent a fractional dissociation of 6.7×10^{-8} of the neutral beam flux.

From the fragment energy distribution in this background spectrum and the distance ratio of these fragments at the detector R_a/R_b , we can identify the fragments arising from electron beam independent processes in this spectrum as being predominantly due to the unimolecular reaction:



occurring in the 18.3 cm region between the slit and the beam flag, with a small contribution due to collision induced dissociation of CO. This identification is supported by the distance ratio of the fragments, which is found to be centered about unity, and by the fragment energy distribution observed from spontaneous dissociation of N_2 , produced by charge transfer neutralization of N_2^+ in a variety of gasses.⁵⁰ Comparison of the fragment flux observed from a pure N_2 beam with the background flux observed here implies an N_2 contamination of the CO beam in the range of 1×10^{-3} to 1×10^{-4} . The spectrum in Fig. 9 was acquired from a CO beam produced with the electron-impact ion source and with the electron beam/neutral beam interaction region thoroughly degassed. Production of the CO beam using the hollow cathode ion source invariably

lead to an order of magnitude higher concentration of N_2 contamination. Poorer vacuum in the electron gun region produces a high contribution to the background dissociation from collision-induced dissociation of the fast neutral beam and yields a very broad, unstructured W spectrum in the background channel.

The fragment energy release spectrum characteristic of electron-impact dissociation alone is obtained by direct subtraction of the two spectra in Fig.9. The resulting difference spectrum, now binned into one-half as many intervals to reduce the statistical noise introduced by the subtraction, is shown in Fig. 10. This difference spectrum has also been divided by the collection efficiency function shown in Fig.6, to provide a better visual representation of the relative fragment intensities.⁵¹ As shown in Fig. 9, fragments are observed with $W > 0.23$ eV. However, the collection efficiency for these very low energy fragments depends on the alignment of the beam flag with the neutral beam to micron precision, which cannot in practice be achieved with a reasonable degree of reproducibility. For this reason, the spectrum shown in Fig. 10 is for $W \geq 0.3$ eV. Detailed fragment energy distributions were obtained at electron impact energies ranging from 28.5 - 98.5 eV. They show precisely the same features and relative intensities as in the 58.5 eV spectrum given in Fig. 10. Well defined distributions could only be obtained with the CO beam produced by the electron-impact ion source; the much higher background in beams generated from the hollow-cathode source precluded quantitative comparisons of the effect of (anticipated) different vibrational distributions in the CO beams.

It can be seen from Fig. 10 that the fragment intensity is grouped into regions (peaks) with specific values of W . The width of these peaks increases with increasing W , reflecting the resolution function of the apparatus, $\Delta W = .052W$. A quasi-discrete energy release spectrum is characteristic of the predissociation of bound energy states in the molecule as opposed to dissociation from nonbonding or antibonding (repulsive) states, that would give rise to a continuous range of energy release values. In either case, the energy release W specifies the energy of the dissociating molecular state relative to that of its dissociation products at infinite

separation. For a given state with an energy E_i relative to $\text{CO } X^1\Sigma^+(v=0)$ dissociating to ground state fragments $\text{C}(^3\text{P}) + \text{O}(^3\text{P})$, the translational energy release produced by dissociation of state i is:

$$W_i = E_i - D \quad (21)$$

where D is the CO dissociation energy²² ($D_0^0 = 11.092$ eV) if ground state fragments are produced, or an appropriately higher, discrete value if one or both of the atomic fragments is produced in an excited state. CO is rather unique in that its first ionization limit²² $\text{CO}^+ 2\Sigma^+$ lies only 2.906 eV above its lowest dissociation limit. The energetically accessible excited atomic products⁵² in this region are $\text{C}(^1\text{D})$, $\text{O}(^1\text{D})$, and $\text{C}(^1\text{S})$, with values of $D=12.356$, 13.059, and 13.776 eV, respectively.

The electronic states of CO lying above the first dissociation limit have been extensively studied using both inelastic electron scattering⁵³ (EELS) and by optical photoabsorption.⁵⁴⁻⁵⁸ Both techniques define the energies of excited states relative to the $\text{CO } X^1\Sigma^+(v=0)$, which can be compared to the W spectrum through Eqn. (21). Our spectrum, Fig. 10 (top) is compared with the EELS spectrum observed by Skerbele, Dillon, and Lassetre⁵³ from the forward scattered electrons produced by 45 eV electron impact on CO. This EELS spectrum is shown in Fig. 10 (center) and assumes the value of D for the production of ground state fragments. It can be seen that essentially all of the features in the EELS excitation spectrum have corresponding features in the fragment translational energy (dissociation) spectrum. This supports the presumption that ground state fragments are predominantly produced in the dissociation. If excited atomic products were produced, the EELS spectrum would be shifted lower in W by at least 1.2637 eV from its position in Fig. 10 and no such correspondence would be possible. This does not, however, exclude the production of excited fragments as a minor dissociation channel.

The EELS spectrum reflects only the excitation step in reaction (1), i.e., the excited state could radiate or autoionize rather than dissociate and still appear in the EELS spectrum, whereas

only dissociative channels can contribute to the fragment spectrum. The fact that the excitation spectrum continues to energies well above the ionization limit ($W = 2.9$ eV), whereas the dissociation spectrum abruptly terminates suggests that autoionization rather effectively competes with dissociation in states above this limit. At lower energies, the similarity between the excitation and dissociation spectrum suggests that predissociation effectively competes with radiation in nearly all of the CO excited states produced above the first dissociation limit. There is however one notable exception: the $C^1\Sigma^+(v=0)$ level, with a maximum at $W = 0.32$ eV, has no comparable analog in the fragment spectrum. This level appears as the lowest energy peak in the EELS spectrum. The energy of this state is just above the low energy cut-off of the fragment detector, yet little evidence is found for its contribution to the dissociation spectrum. This is consistent with the observation by Lee and Guest⁵⁴ that the fluorescence intensity from the $C^1\Sigma^+(v=0)$ level is much stronger than that from the $E^1\Pi$ state, the next higher energy feature in the scattering spectrum, even though the cross sections for photo-excitation of these two states are comparable. It is further consistent with the predissociation probability of zero that has been assigned to this state by Viala, et al.⁵⁵ based on the linewidth and pressure dependence of its optical absorption spectrum.

A detailed analysis of the states contributing to the dissociation spectrum must take into account the fact that each of the spectral peaks is an unresolved envelope of rotational levels and the overlap of the rotational envelopes of adjacent states. Recent high resolution absorption measurements have identified 53 vibrational bands lying above the lowest CO dissociation limit and extending nearly to the ionization limit and provide energies, rotational constants, and absorption oscillator strengths for nearly all of them.⁵⁶ Given these energies and rotational constants for these *optically* accessible states, and assuming a Boltzmann distribution for the rotational populations characterized by a single temperature T , the relative intensities of the individual states can be adjusted in a Monte Carlo simulation of the apparatus transmission function to approximate the observed dissociation spectrum. Early stages of the simulation made

it clear that a continuum dissociation background also must contribute to the experimental dissociation spectrum to account for the lack of resolution at the base of the peaks. With the present resolution it is impossible to uniquely determine the form of this continuum, but one that linearly decreases with W between the fragment intensity at 0.3 eV and that at $W = 3.3$ eV seems to be indicated. Such a continuum would represent 28% of the observed dissociation, which seems rather high considering that no prominent continua have been observed in either the EELS or photoabsorption measurements nor is one expected by theory^{59,60} near the dissociation threshold. Vibrational excitation in the CO beam may give more facile access here, particularly if the continuum dissociation products are not ground state atoms. Alternate explanations for the apparently wide base of the peaks would require a non-Boltzmann rotational distribution in the CO beam or predissociation lifetimes in excess of 10 ns. This latter possibility seems unlikely given the estimated lifetimes⁵⁶ for the electronic states, and while the former possibility cannot be excluded, neither can it be accurately modeled at the present experimental resolution.

The final simulated spectrum for $T = 700\text{K}$ is shown at the bottom of Figure 10, superimposed on this continuum. While this temperature is somewhat hotter than anticipated for the charge transfer, it provides a reasonable representation of the major features in the observed spectrum. The level positions, intensities and identifications used in the simulation are given in Table II. Also given in this table is the band index number, originally assigned to the features in the CO absorption spectrum by Letzelter, et al.,⁵⁷ which has found rather widespread use^{55,56,61} as a definitive label for the CO states above the dissociation limit. The stick spectrum locates the vibrational origins and relative intensities of these levels in Figure 10. The rotational constants used for the simulation were taken directly from Ref. 56; those for the six highest energy levels are assigned the rotational constants²² of $\text{CO}^+ X^2\Sigma^+$. The intensities in the table are expressed as partial dissociation cross sections in Mb, using 72% of the total cross section of Fig. 8 as attributable to predissociation. These cross sections are of course influenced by the specific vibrational distribution in the present CO beam, with estimated relative populations in $v''=0-3$ of

0.565, 0.193, 0.091, and 0.054, respectively. Apart from the uncertainty introduced by the approximate partitioning of the fragment distribution between predissociation and continuum contributions, the individual partial cross sections given in the Table are clearly only estimates in those regions where several states fall within the apparatus resolution. However, the summation of the individual contributions within the congested regions should give a realistic assessment of the dissociation magnitude.

The lower energy features in the fragment energy distribution are well separated and their partial dissociation cross sections may hold some quantitative significance. It should be noted in Table I that the variation in the partial dissociation cross section with vibration in the $C^1\Sigma^+$ and $E^1\Pi$ states does not resemble the estimated populations for these vibrational levels in the $CO\ X^1\Sigma^+$ state. Because of the diagonal nature of the Franck-Condon factors for the $C\leftarrow X$ and $E\leftarrow X$ transitions, as evidenced by their photoabsorption cross sections,⁵⁶ a close correspondence between the relative cross sections and vibrational populations would be expected if the relative rates for predissociation and radiation in the C and E states were independent of vibration. In fact, there is strong evidence for a strong vibrational dependence in the branching ratios. From photoabsorption measurements, Viala, et al.⁵⁵ have estimated dissociation probabilities of 0, 0.60, 1.0 for $C^1\Sigma^+(v=0,1,2)$ and 0.89, 0.98, 1.0 for $E^3\Pi(v=0,1,2)$. Lee and Guest⁵⁴ have obtained qualitative information for this same behavior from measurement of the photoabsorption and fluorescence cross sections of these states. Dividing the partial cross sections in Table I by the estimated beam population for the corresponding vibrational level and assuming a unit dissociation probability for the highest vibrational level in each state yields dissociation probabilities of 0, 0.4, 0.9, 1.0 for $C^1\Sigma^+(v=0-3)$ and 0.5, 0.5, 1.0 for $E^1\Pi(v=0-2)$, but their accuracies are predicated on weak dissociation features, viz. C(3) and E(2). These probabilities are qualitatively consistent with those of the optical measurements.

A second comparison which can be made is to average the partial cross sections, weighted by predissociation probability and ground state vibrational population, over the

vibrational contributions in the C and E states. This yields an estimate for the electron impact excitation cross sections for the C and E states of 17.2 Mb and 10.3 Mb, respectively. These compare quite well with the values of 19.9 Mb and 12.9 Mb that have been calculated for 60 eV electron impact excitation of the C and E states by Chung and Lin.³ James, et al.⁶² have recently determined the emission cross section of E(0) for electron impact at 20 and 200 eV, reporting cross sections of 0.535 and 0.417 Mb at these energies, respectively. Comparing the average of these two emission cross sections with the sum of the partial dissociation cross sections for E(v=0-2) (to account for the ground state population distribution) in Table I yields a dissociation probability for E(0) of 0.91. This compares very well with the dissociation probability of 0.89 obtained from the absorption study, but is considerably larger than the above estimate based on expected vibrational populations.

Of particular note in Figure 10 is that the rapid decrease in fragment intensity near $W = 3$ eV is represented almost exactly in the simulation. Since the level energies in Table II extend to within 0.083 eV of the ionization limit, the high degree with which the simulation reproduces the observed fragment distribution strongly supports the above contention that no significant dissociation is observed above this limit. This is further supported by the fact that members of the $ns\sigma$ Rydberg series converging to $\text{CO}^+ A^2\Pi$, identified by the asterisk in Table I, appear to be strongly excited by the electron impact, as evidenced by their relatively large partial dissociation cross sections. However, the higher members of this or other series are not observed above the ionization limit with comparable dissociation cross sections. Nevertheless, some dissociative processes do occur above this limit, as evidenced by the detection of translationally hot high Rydberg atoms^{10,13} and $\text{O}(^5\text{S})$ ¹² following electron impact excitation of CO.

The present simulation is deficient in that only optically accessible states have been included. Nineteen $^3\Sigma^+$ and $^3\Pi$ members of the $nl\sigma$ and $nl\pi$ Rydberg series converging to the $\text{CO}^+ X$ state have been identified by EELS.⁶³ The energies for most of these states correspond to $W > 1.2$ eV, where the fragment spectrum is quite blended, and could not necessarily be

distinguished from optically accessible states of comparable energy. However, the $v=0,1$ levels of the $3p\sigma$ Rydberg state should appear at $W = 0.323, 0.601$ eV, respectively, and be easily distinguishable, but are not observed in the experimental spectrum with an intensity comparable to the optically allowed states in this region. On the other hand, the experimental feature near $W = 1.2$ eV is significantly broader than can be simulated with the states in Table I alone. The breadth of this feature may indicate that predissociation of the $^3\Sigma^+ 3d\sigma$ ($v=0$), with an origin at $W = 1.243$ eV, is making an observable contribution to the dissociation.

The partial cross sections in Table II explicitly refer to 58.5 eV electron impact, but can be expected to scale with the electron energy dependence of the total cross section (Table I) over the electron energy range of 28.5 and 98.5 eV based on the observed product distributions. At lower electron energies, however, spin-exchange collisions become relatively more important;⁶² hence significant departures in the energy dependence of specific partial dissociation cross sections from that of the total cross section can be anticipated.

CONCLUSIONS

A new technique is presented for the measurement of electron impact dissociation that allows observation of all important product channels and explicitly distinguishes them from the products of dissociative ionization, a process that can be independently measured. Absolute cross sections for the electron impact dissociation of the CO molecule are reported for electron energies extending from the dissociation threshold to 198.5 eV. The magnitude of the cross section, which rises to 0.75 \AA^2 for electron energies near 50 eV, is small in comparison with other electron induced processes such as excitation and ionization. Nevertheless, the dissociation channel produces profound chemical changes by converting a relatively inert, strongly bound molecule into translationally hot atoms. Analysis of the fragment energies that accompany CO dissociation show that electron induced transitions into predissociated Rydberg states converging to the ground state of the ion is the predominant source of the dissociation and that $\text{C}(^3\text{P})$ and $\text{O}(^3\text{P})$ atoms, with kinetic energies in the range of 0-1.66 eV and 0-1.24 eV, respectively, are the predominant dissociation products.

The CO molecule is the second most abundant molecular species in the interstellar medium and in comets. However, a quantitative understanding of its abundance in terms of chemical models of these environments has yet to be achieved. The recent availability of accurate photodissociation cross sections has produced a significant advance toward this goal for the case of interstellar CO.⁶¹ Woods, et al.^{64,65} have found evidence for electron impact processes in recent observations of comet Halley, but have thus far included only ionization and dissociative recombination channels in their model. It is hoped that cross sections presented here will allow the useful inclusion of the electron impact dissociation channel to the models of these two media.

ACKNOWLEDGEMENT

This research was supported by the U. S. Air Force Wright Laboratory under contract No. F33615-85-R-2560. The author wishes to thank H. Helm, J. R. Peterson, and D. L. Huestis for a variety of assistance during the course of this work. The author further acknowledges F. Rostas, J. M. Ajello, and S. Trajmar for providing preprints of their work prior to publication.

REFERENCES

1. E. C. Zipf, "Dissociation of Molecules by Electron-Impact" in *Electron-Molecule Interactions and Their Applications*, L. G. Christophorou, ed (Academic, Orlando, 1984) Ch. 4.
2. R. N. Compton and J. N. Bardsley, "Dissociation of Molecules by Slow Electrons," in *Electron Molecule Collisions*, I. Shimamura and K. Takayanagi, ed. (Plenum, N.Y., 1984) Ch. 4.
3. S. Chung and C. C. Lin, Phys. Rev. A **9**, 1954 (1974).
4. L. Mu-Tao and V. McKoy, J. Phys. B **15**, 3971 (1982).
5. S. Trajmar and D. C. Cartwright, "Excitation of Molecules by Electron Impact" in *Electron-Molecule Interactions and Their Applications*, L. G. Christophorou, ed (Academic, Orlando, 1984) Ch. 2.
6. S. J. B. Corrigan, J. Chem. Phys. **43**, 4381 (1965).
7. H. F. Winters, J. Chem. Phys. **44**, 1472 (1966).
8. A. Niehaus, Z. Naturforschung **22a**, 690 (1967).
9. T. Nakano, H. Toyoda, and H. Sugai, Jap. J. Appl. Phys. **30**, 2908 (1991); *ibid.*, p. 2912.
10. K. C. Smyth, J. A. Schiavone, and R. S. Freund, J. Chem. Phys. **60**, 1358 (1974).
11. R. S. Freund, J. A. Schiavone, and D. F. Brader, J. Chem. Phys. **64**, 1122 (1976).
12. W. C. Wells, W. L. Borst, and E. C. Zipf, Phys. Rev. A **17**, 1357 (1978).
13. J. A. Schiavone, S. M. Tarr, and R. S. Freund, J. Chem. Phys. **70**, 4468 (1979).

14. Y. Hatano, Comments At. Mol. Phys. **13**, 259 (1983).
15. H. Helm and P. C. Cosby, J. Chem. Phys. **86**, 6813 (1987).
16. K. H. Berkner, B. R. Myers, and R. V. Pyle, Rev. Sci. Instrum. **39**, 1204 (1968).
17. M. W. Geis, K. A. Smith, and R. D. Rundel, J. Phys. E **8**, 1011 (1975).
18. Gulton Industries Type G1512.
19. J. F. M. Aarts and F. J. deHeer, Physica **49**, 425 (1970).
20. J. M. Ajello, J. Chem. Phys. **55**, 3158 (1971).
21. R. F. Holland and W. B. Maier, J. Chem. Phys. **56**, 5229 (1972).
22. K. P. Huber and G. Herzberg, *Molecular Spectra and Molecular Structure, IV. Constants of Diatomic Molecules* (Van Nostrand Reinhold, N.Y., 1979).
23. The potential curves and Franck-Condon factors were computed from molecular constants with the program RKR and FCF, kindly provided by D. L. Albritton and R. N. Zare.
24. G. Guelachvili, D. deVilleneuve, R. Farrenq, W. Urban, and J. Verges, J. Mol. Spectrosc. **98**, 64 (1983).
25. D. Rapp and P. Englander-Golden, J. Chem. Phys. **43**, 1464 (1965).
26. D. Rapp, P. Englander-Golden, and D. D. Briglia, J. Chem. Phys. **42**, 4081 (1965).
27. E. Hille and T. D. Märk, J. Chem. Phys. **69**, 4600 (1978).
28. M. R. Flannery, P. C. Cosby, and T. F. Moran, J. Chem. Phys. **59**, 5494 (1973).
29. A. Salop, D. C. Lorents, and J. R. Peterson, J. Chem. Phys. **54**, 1187 (1971).

30. P. C. Cosby and H. Helm, *Phys. Rev. Letters* **61**, 298 (1988).
31. A. Ding and K. Richter, *Z. Physik A* **307**, 31 (1982).
32. D. P. deBruijn, J. Neuteboom, and J. Los, *Chem. Phys.* **85**, 233 (1984).
33. R. C. Wetzel, F. A. Baiocchi, T. R. Hayes, and R. S. Freund, *Phys. Rev. A* **35**, 559 (1987).
34. A. Müller, K. Huber, K. Tinschert, R. Becker, and E. Salzborn, *J. Phys. B* **18**, 2993 (1985).
35. H. Helm and P. C. Cosby, *J. Chem. Phys.* **90**, 4208 (1989).
36. P. C. Cosby and H. Helm, *J. Chem. Phys.* **90**, 1434 (1989).
37. W. Koot, W. J. van der Zande, J. Los, S. R. Keiding, and N. Bjerre, *Phys. Rev. A* **39**, 590 (1989).
38. W. J. van der Zande, W. Koot, and J. Los, *J. Chem. Phys.* **91**, 4597 (1989).
39. D. P. deBruijn and J. Los, *Rev. Sci. Instrum.* **53**, 1020 (1982).
40. G. H. Dunn, *Phys. Rev. Lett.* **8**, 62 (1962).
41. R. N. Zare and D. R. Herschbach, *Proc. IEEE* **51**, 173 (1963).
42. C. Pernot, J. Durup, J. B. Ozenne, J. A. Beswick, P. C. Cosby, and J. T. Moseley, *J. Chem. Phys.* **71**, 2387 (1979).
43. R. N. Zare, *Ber. Bunsenges. Phys. Chem.* **86**, 422 (1982).
44. G. H. Dunn and L. J. Kieffer, *Phys. Rev.* **132**, 2109 (1963).
45. E. H. Kerner, *Phys. Rev.* **92**, 1441 (1953).
46. R. N. Zare, *J. Chem. Phys.* **47**, 204 (1967).

47. L. J. Kieffer and G. H. Dunn, *Rev. Mod. Phys.* **38**, 1 (1966).
48. P. Defrance, F. Brouillard, W. Claeys, and G. Van Wassenhove, *J. Phys. B* **14**, 103 (1981).
49. I. Kanik, S. Trajmar, and J. C. Nickel, *J. Geophys. Res.* (submitted for publication).
50. H. Helm and P. C. Cosby, to be published.
51. This procedure provides accurate relative intensities for continuous energy release distributions and accurate relative areas for the discrete structure in the spectrum.
52. C. E. Moore, *Nat. Stand. Ref. Data Ser., Nat. Bur. Stand. (US)* **34** (1970).
53. A. Skerbele, M. A. Dillon and E. W. Lassettre, *J. Chem. Phys.* **46**, 4162 (1967).
54. L. C. Lee and J. A. Guest, *J. Phys. B* **14**, 3415 (1981).
55. Y. P. Viala, C. Letzelter, M. Eidelsberg, and F. Rostas, *Astron. Astrophys.* **193**, 265 (1988).
56. M. Eldelsberg and F. Rostas, *Astron. Astrophys.* **235**, 472 (1990).
57. C. Letzelter, M. Eidelsberg, F. Rostas, J. Breton and B. Thieblemont, *Chem. Phys.* **114**, 273 (1987).
58. G. Stark, K. Yoshino, P. L. Smith, K. Ito, and W. H. Parkinson, *Ap. J.* **369**, 574 (1991).
59. D. L. Cooper and K. Kirby, *J. Chem. Phys.* **87**, 424 (1987).
60. K. Kirby and D. L. Cooper, *J. Chem. Phys.* **90**, 4895 (1989).
61. E. F. Van Dishoeck and J. H. Black, *Ap. J.* **334**, 771 (1988).
62. G. K. James, J. M. Ajello, I. Kanik, B. Franklin, and D. E. Schemansky, *J. Phys. B* (submitted for publication).

63. B. Wallbank, S. Daviel, J. Comer, and P. Hicks, *J. Phys. B* **16**, 3065 (1983).
64. T. N. Woods, P. D. Feldman, K. F. Dymond, and D. J. Sahnou, *Nature* **324**, 436 (1986).
65. T. N. Woods, P. D. Feldman, and K. F. Dymond, *Astron. Astrophys.* **187**, 380 (1987).

Table I

ELECTRON IMPACT DISSOCIATION CROSS SECTION OF CO

Electron Energy (eV)	Cross Section (Mb) ^a	Relative Error (Mb)	Absolute Error (Mb)
13.5	10.8	11.8	12.1
18.5	28.4	5.8	9.3
21.0	48.0	8.5	15.0
23.5	52.0	4.7	14.2
28.5	65.8	4.5	17.6
33.5	65.6	7.9	18.7
38.5	75.0	3.7	19.7
48.5	75.6	2.2	19.6
58.5	75.0	4.3	19.8
73.5	69.5	3.5	18.3
98.5	65.8	3.0	17.2
123.5	64.7	4.0	17.2
148.5	58.6	3.9	15.6
198.5	43.6	3.5	11.8

Table II

PARTIAL ELECTRON IMPACT DISSOCIATION CROSS SECTIONS OF CO

Band Index ^a	State ^a	W ^b (eV)	Partial Cross Section (Mb) ^c
39	E 3p π $^1\Pi(0)$	0.4122	3.02
38	C 3p σ $^1\Sigma^+(1)$	0.5543	1.24
37	E 3p π $^1\Pi(1)$	0.6804	1.02
.	C 3p σ $^1\Sigma^+(2)$	0.8161	1.38
36	E 3p π $^1\Pi(2)$	0.9372	0.94
35	C 3p σ $^1\Sigma^+(3)$	1.0724	0.93
34	V 3s σ $^3\Pi(0)^*$	1.1556	0.76
33	F 3d σ $^1\Sigma^+(0)$	1.2586	3.45
.	G 3s σ $^3\Pi(1)^*$	1.3706	0.73
32	G 3d π $^1\Pi(0)$	1.4180	0.09
31	J 4s σ $^1\Sigma^+(0)$	1.4712	2.19
30	F 3d σ $^1\Sigma^+(1)$	1.5097	0.09
29	W 3s σ $^3\Pi(2)^*$	1.5765	0.58
28	W 3s σ $^1\Pi(0)^*$	1.6380	1.61
27	K 4p σ $^1\Sigma^+(0)$	1.6687	0.90
26	L' 3d π $^1\Pi(1)$	1.6882	0.96
25	L 4p π $^1\Pi(0)$	1.6956	0.59
24	J 4s σ $^1\Sigma^+(1)$	1.7477	0.22
23	H 3s σ $^3\Pi(3)^*$	1.8026	0.04
22	W 3s σ $^1\Pi(1)^*$	1.8574	2.76
21	H 4p σ $^1\Sigma^+(1)$	1.9419	2.62
20	L 4p π $^1\Pi(1)$	1.9602	0.46
19	4d σ $^1\Sigma^+(0)$	1.9937	1.25
18	W 3s σ $^1\Pi(2)^*$	2.0650	2.33
17	I' 5s σ $^1\Sigma^+(0)$	2.0786	2.41
16	$^1\Sigma^+(2)$	2.1425	0.48
15C	5p σ $^1\Sigma^+(0)$	2.1795	1.09
15B	5p π $^1\Pi(0)?$	2.1995	1.09
15A	5p π $^1\Pi(0)?$	2.2077	0.35
14	$^1\Pi(2)$	2.2222	0.35
13	$^1\Pi(2)$	2.2425	0.74
12	W 3s σ $^1\Pi(3)^*$	2.2834	1.42
11	$^1\Sigma^+(1)$	2.3006	0.45
10	5d σ $^1\Sigma^+(0)$	2.3280	0.77
9C	5s σ $^1\Sigma^+(1)$	2.3660	0.29
9B	6s σ $^1\Sigma^+(0)$	2.3796	0.29
9A	$^1\Pi(2)$	2.4080	1.05
8B	6p σ $^1\Sigma(0)$	2.4273	0.57
7D	$^1\Sigma^+(2)$	2.4615	0.56
7C	5p π $^1\Pi(1)$	2.4650	0.56
7B	5p σ $^1\Sigma^+(1)$	2.4654	0.56
7A	$^1\Pi(0)$	2.4758	0.56
6		2.5226	1.51
5		2.5704	0.76
4		2.5902	1.18
3		2.6586	1.45
2		2.7180	2.01
1		2.8229	2.75

^aReference 56.^bBand origin of Ref. 56 referenced to ground state C + O.^c1 Mb = 1×10^{-18} cm²

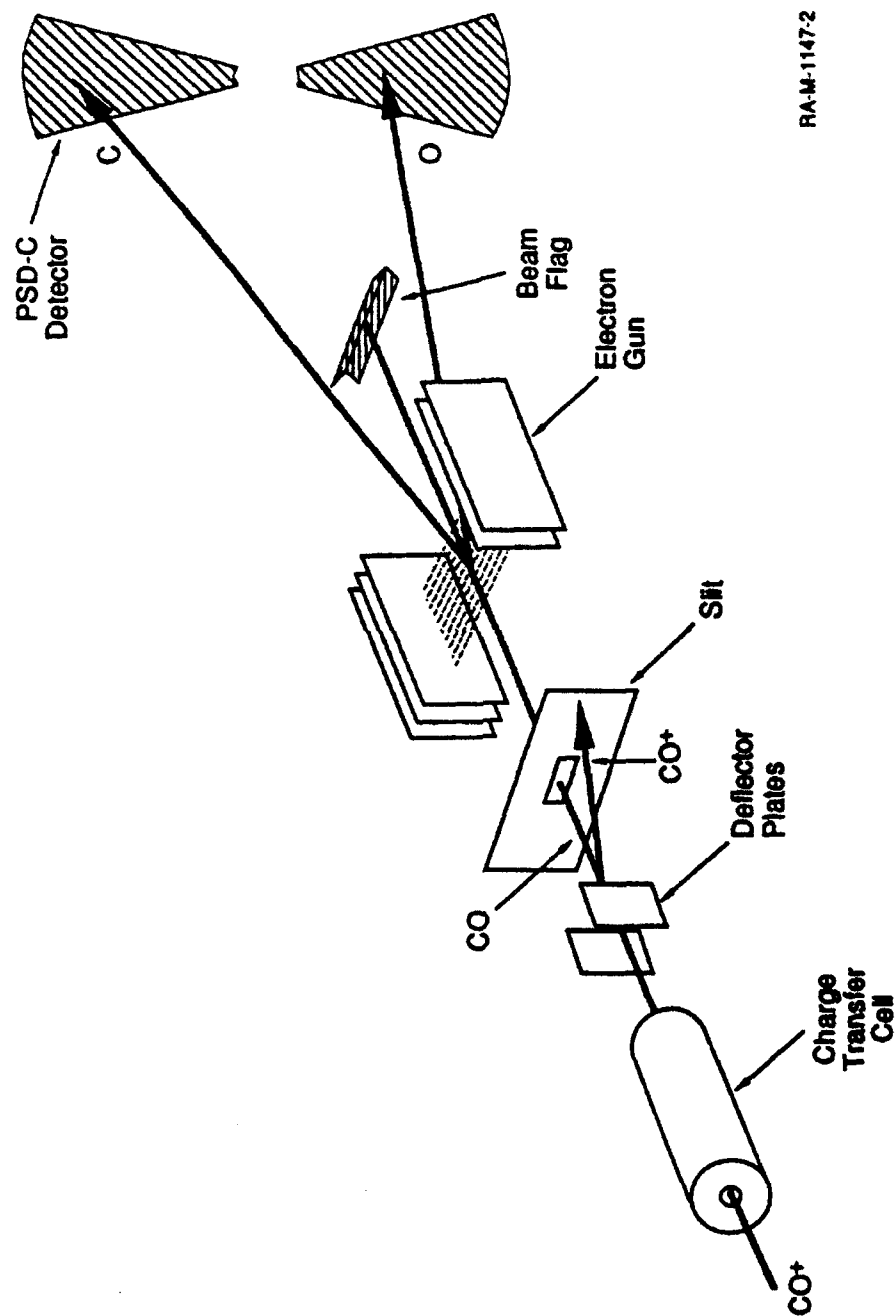
FIGURE CAPTIONS

- Figure 1. Schematic diagram of the electron-impact dissociation apparatus. A fast (keV) CO beam, produced by charge transfer neutralization of CO^+ , is intersected by an electron beam. The correlated fragments C and O from dissociation of individual CO molecules are spatially and temporally detected at the position sensitive detector for correlated fragments (PSD-C). Undissociated molecules are intercepted by the beam flag. The bolometer, Faraday cup, and charged particle deflection plates in the region downstream of the electron beam are not shown.
- Figure 2. Composition of the CO beam. The relative flux of noncoincident events detected on one anode of the PSD-C is shown as a function of radial distance from the CO beam following 50 eV electron impact and deflection of the charged fragments. The expected location of O^+ produced from the ionization of O contaminants in the beam is indicated by the arrow. The underlying background in the spectrum is due to slow metastables produced by electron impact on the residual gas in the electron gun that drift unimpeded to the PSD-C.
- Figure 3. Characteristics of the electron beam. The upper spectrum shows the apparent flux of CO^+ ionization products arriving at the PSD-C as the electron gun is translated a distance of 0.6 cm across the 0.07 cm wide CO beam. The peak essentially reflects the spatial distribution in the electron beam along the direction of translation. The lower figure shows the variation in this spatial distribution with electron beam energy, expressed in terms of its full width at half maximum.

- Figure 4. Newton velocity diagram showing the mapping of the CO center of mass energy release onto the position sensitive detector as a radial (R) and temporal (Δt) separation of the C and O fragments.
- Figure 5. Distribution of the ratio of radial distances at the detector for the correlated neutral products of 38.5 eV electron impact on CO. The mass ratio of C and O fragments is shown by the dashed line.
- Figure 6. The geometric collection efficiency χ of the detector for the CO dissociation products as a function of center of mass energy release W for beam energies of 3000 eV and 5000 eV. The efficiencies refer to an isotropic distribution of the fragments in the center of mass frame.
- Figure 7. Accumulation of C + O electron-impact dissociation products (N^*) as the electron gun is translated across the CO beam at a constant velocity. The data points refer to N^* evaluated after 5 successive positions of the electron gun. The electron beam energy is 48.5 eV. The error bars refer to the statistical error in N^* .
- Figure 8. The total cross section, in units of 10^{-18} cm^2 , for the reaction $\text{CO} + e \rightarrow \text{C} + \text{O} + e$ as a function of incident electron energy is shown by the open squares. The error bars refer to relative errors in the measurement. The solid line connects the values of Ref. 49 for the total electronic excitation cross section of CO and is scaled here by a factor of 5.

Figure 9. Center of mass energy release W observed for electron impact dissociation of CO. The upper spectrum is observed with 58.5 eV electron beam intersecting the CO beam. The lower spectrum, observed with no overlap of the electron and neutral beams, is primarily due to spontaneous dissociation of an N_2^+ contaminant in the CO beam. The spectra are uncorrected for collection efficiency.

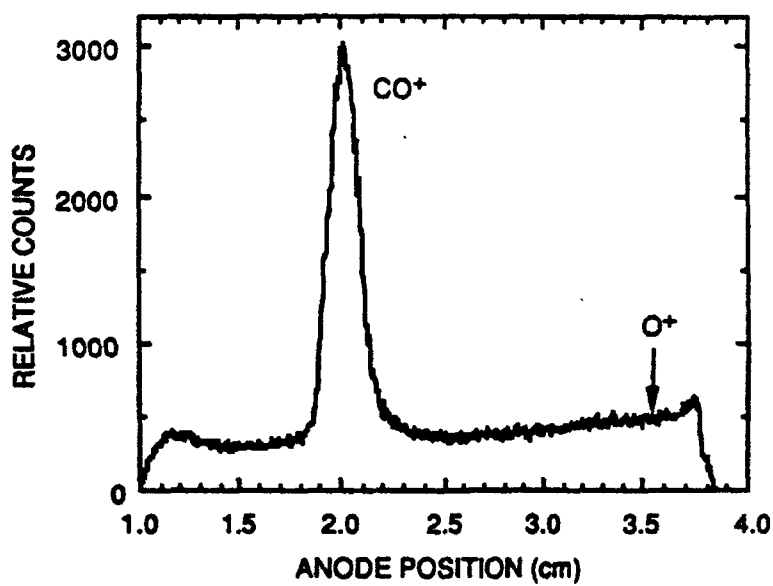
Figure 10. Center of mass energy release in the electron impact dissociation of CO. The upper spectrum is the center of mass energy release (W) observed for 58.5 eV electron impact on CO. Amplitudes in the spectrum have been corrected for geometric collection efficiency. The center spectrum is the electron energy loss spectrum of Ref. 53 for forward scattered electrons, shifted by 11.092 eV to reference the energy loss to the lowest dissociation limit of CO. Features in this spectrum locate the energies of CO states excited by 45 eV electron impact. The lower spectrum is a simulation of fragment energy release expected from predissociation of known electronic states of CO. Vertical lines at the bottom of the spectrum locate the origins of the electronic states included in the simulation. The dashed line locates the energy of the $CO+X^2\Sigma^+$ state relative to the lowest CO dissociation limit.



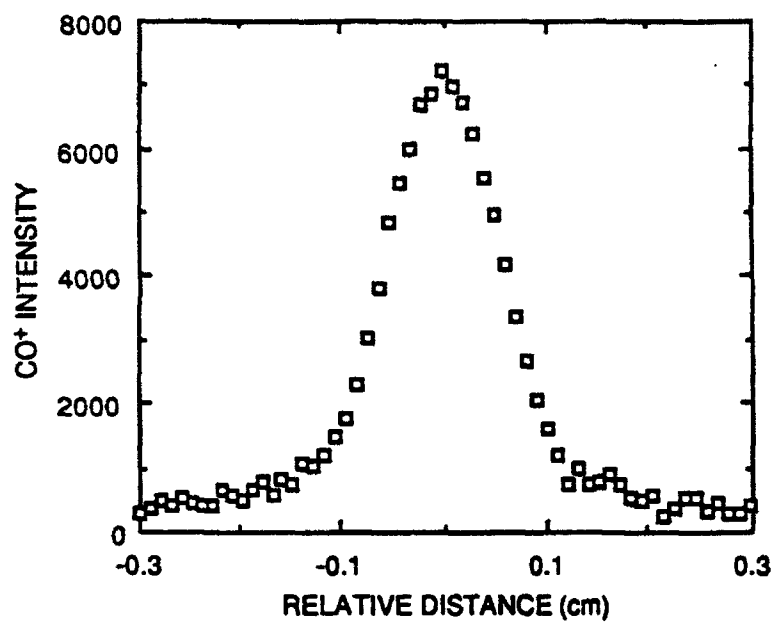
RA-M-1147-2

Fig. 1
Cosby
J. Chem. Phys.

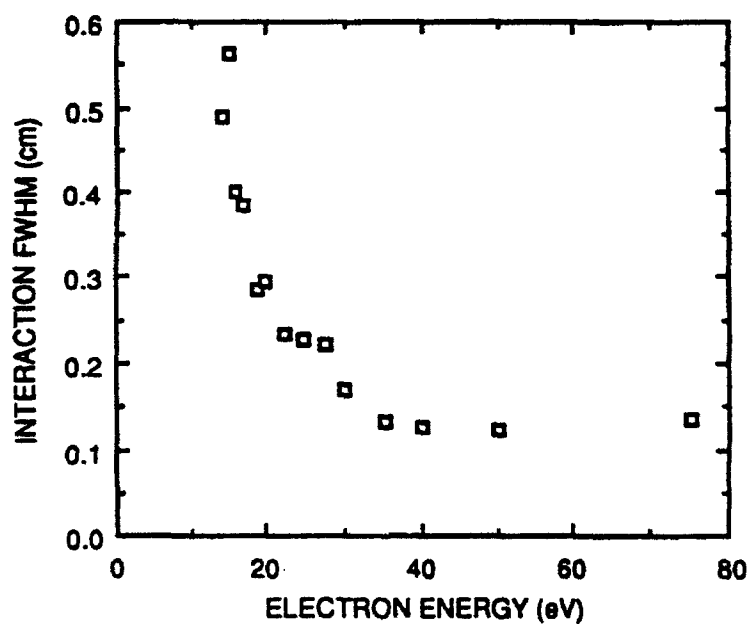
Fig. 1



CAM-1147-1

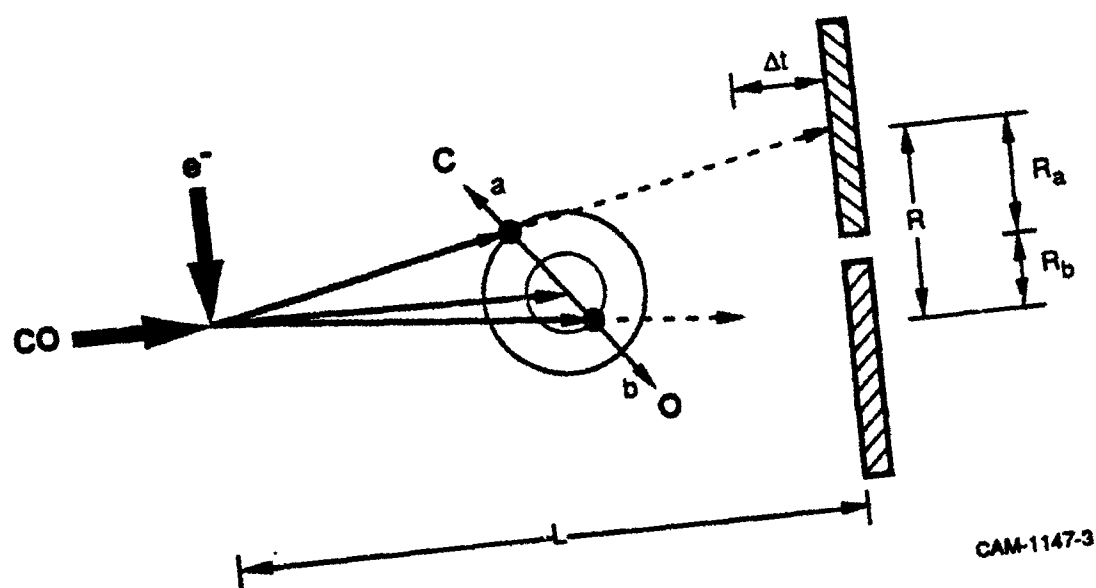


(a)



(b)

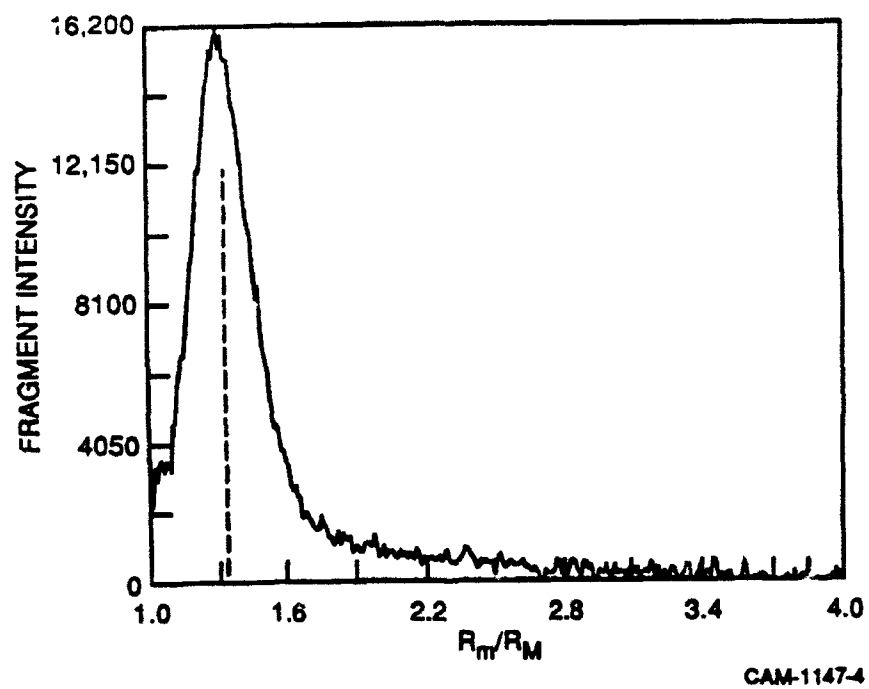
CAM-1147-2



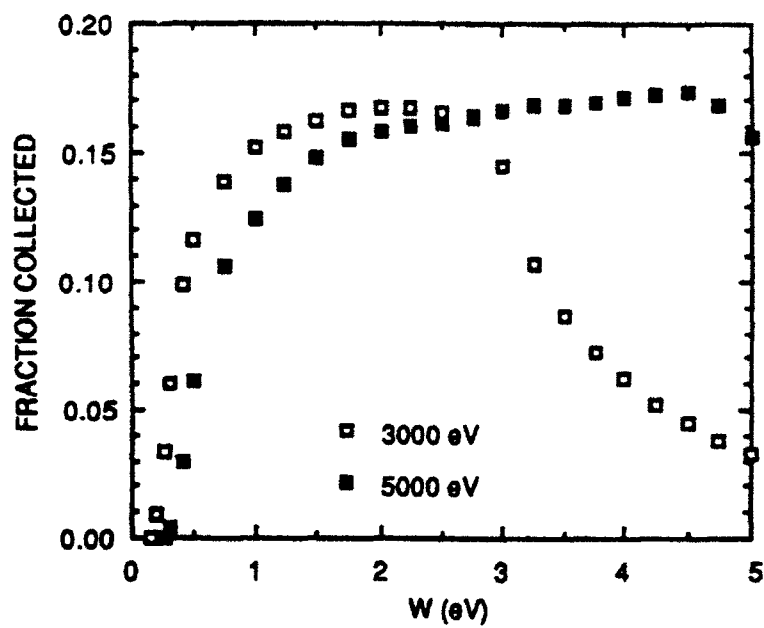
CAM-1147-3

11/

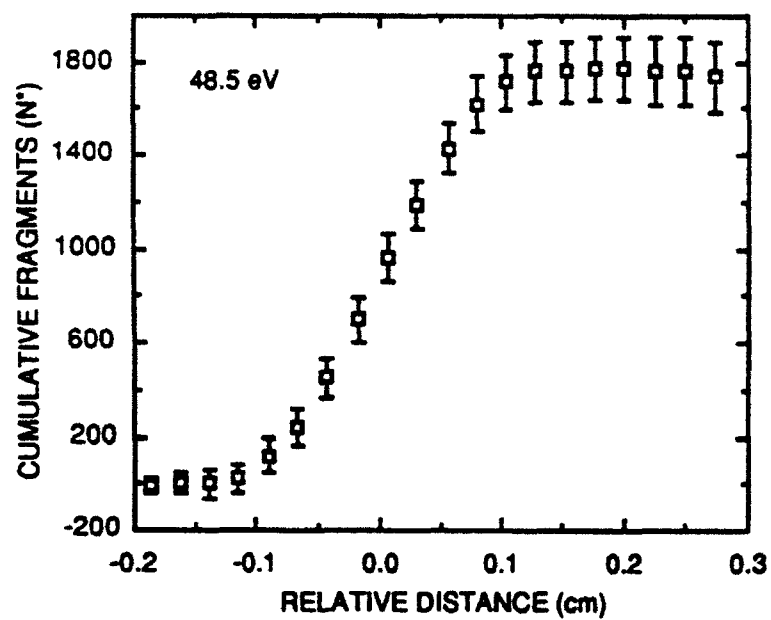
Fig. 4
Cosby
J. Chem. Phys.



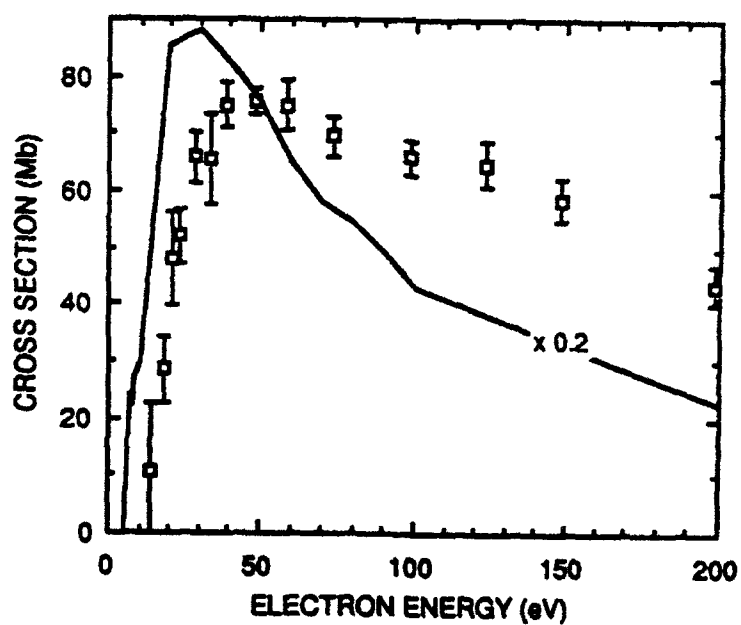
SP



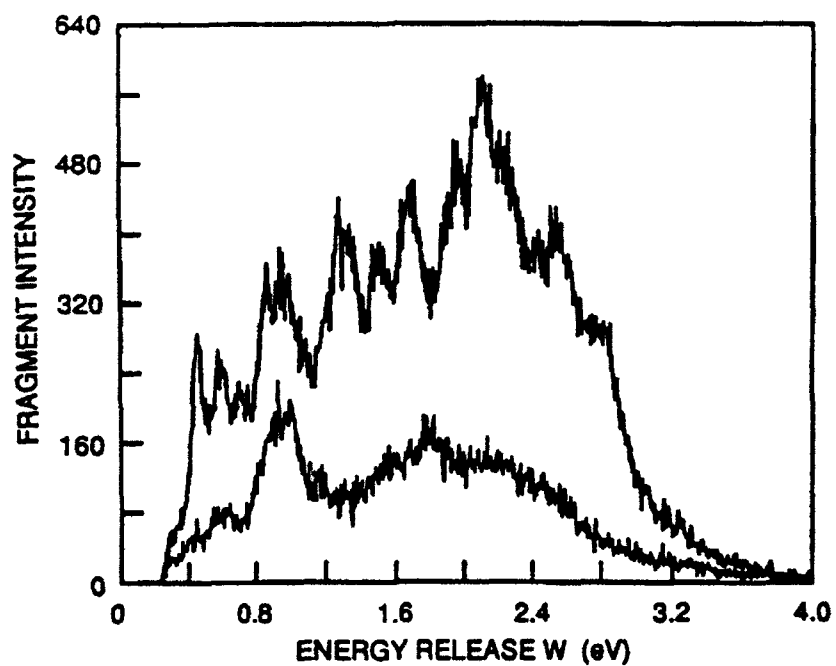
CAM-1147-3



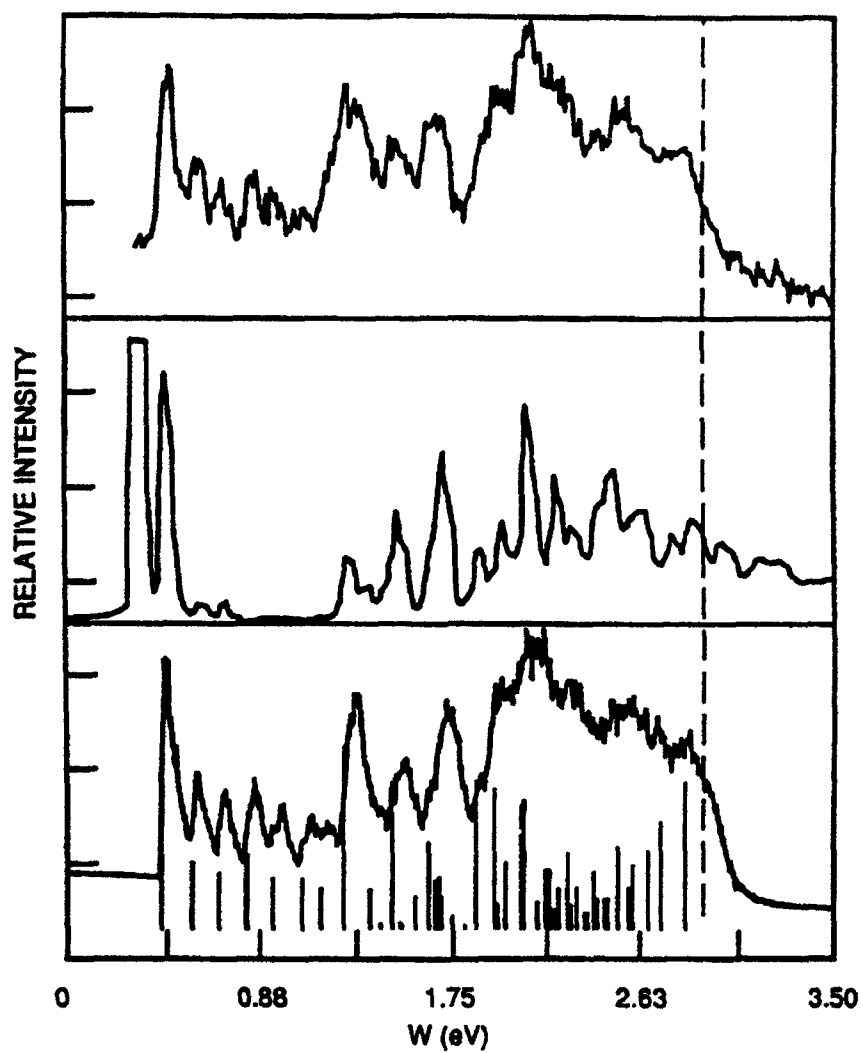
CAM-1147-6



CAM-1147-7



CAM-1147-8



CAM-1147-9

Appendix E

PHOTODISSOCIATION MEASUREMENT OF ROVIBRATIONAL ENERGIES AND POPULATIONS OF MOLECULES IN FAST BEAMS

Photodissociation measurement of rovibrational energies and populations of molecules in fast beams

Hanspeter Helm and Philip C. Cosby

Molecular Physics Department, SRI International, Menlo Park, California 94025

(Received 11 February 1987; accepted 10 March 1987)

Using as examples H_2 and H_2^+ , we show that position- and time-sensitive detection of the two correlated photofragments can be used to determine the rovibrational energies and populations of molecules in a fast beam by observing the product distribution from bound-free photodissociation.

I. INTRODUCTION

Fast beams of ionic and neutral molecules are increasingly used in spectroscopy,¹ electron-impact ionization,² dissociation,³ and photoionization⁴ studies. Specifically, in the case where absolute dissociation or dissociative recombination cross sections are to be measured, the internal energy content of the molecules is of major significance for the interpretation of the results. Low-pressure ion sources commonly deliver molecular ions in strong nonequilibrium populations. When the molecular ion M^+ is formed by electron impact on the corresponding molecule M , it is generally assumed that, for electron energies substantially above threshold, the vibrational distribution in M^+ can be estimated by the Franck-Condon factors for a vertical ionization transition⁵ (corrected for radiative cascade from excited electronic states of the ion) with a rotational population characteristic of the equilibrium gas temperature of M , as is observed in photoionization. However, when M^+ is produced from the dissociative ionization of a larger molecule, there can be little *a priori* knowledge of its rovibrational distribution. Indeed, evidence indicates that such ions can be extremely hot.⁶ Clearly a commonly usable tool to assess the rovibrational energy content of molecules in fast beams would be of great benefit.

In the current paper we explore such a scheme which is based on bound-free photodissociation. When viewed from the standpoint of wavelength dependence, the bound-free photodissociation process appears to contain little potential for determining discrete molecular structure. In spectroscopic studies the bound-free process often accompanies the acclaimed fingerprint of discrete molecular transitions as weak, nearly structureless background. We will show below that bound-free photodissociation offers itself as a useful tool to determine bond energies and molecular state populations when we experimentally examine the distribution of continuum energies generated in bound-free absorption.

In a Born-Oppenheimer picture of a diatomic molecule, the cross section for photodissociation of a bound level specified by the vibrational quantum number v and rotational quantum number N is given by⁷

$$\sigma_{v,N}(\nu) = (4\pi\mu)^2 (\epsilon/2\mu)^{1/2} \nu / (3\hbar^3 c) Q_{v,N}^2, \quad (1)$$

where

$$Q_{v,N} = \int_0^\infty \chi_{v,N}(r) \chi_{\epsilon,N}(r) Q_\epsilon(r) dr. \quad (2)$$

Here μ is the reduced mass of the molecule, ϵ the continuum energy of the dissociating fragments, ν the photon frequency, and Q_ϵ the transition moment. The quantity ϵ is related to the photon energy $h\nu$ by the relation

$$\epsilon = h\nu - D_{v,N}, \quad (3)$$

with $D_{v,N}$ being the dissociation energy of the photodissociated level with respect to the dissociation limit to which the continuum energy is referenced. In Eq. (2), $\chi_{v,N}$ is the normalized bound state wave function and $\chi_{\epsilon,N}$ is the continuum wavefunction normalized at large R to a unit modulus sine function. In Eq. (1) several simplifications have been introduced in addition to the standard Born-Oppenheimer picture; the cross section σ is averaged over the angle between the photon polarization and an isotropic distribution of orientations of the molecular axis, and it has been assumed that the continuum wave function varies only slowly with N , such that the continuum wave functions $\chi_{\epsilon,N \pm 1}$, which are accessed in P - and R -branch type transitions, be set equal to $\chi_{\epsilon,N}$, which is accessed in the Q branch. Equation (1) describes the cross section as a function of wavelength for a single molecular energy level with quantum numbers v,N . In general, this cross section is a slowly varying function on the scale of the photon energy; it is characterized by slow oscillations (in general, on the scale of hundreds of inverse centimeters), which reflect the varying overlap of the bound state wave function with the continuum state. In the case of a conventional absorption experiment, the total cross section is measured. It is given by the weighted sum of individual $\sigma_{v,N}$ partial cross sections,

$$\sigma(\nu) = \sum_v \sum_N p_{v,N} \sigma_{v,N}(\nu), \quad (4)$$

where the weight $p_{v,N}$ is the rovibrational population of each initial level. The summed cross section is even less structured on the wavelength scale since the oscillations of individual $\sigma_{v,N}$'s are out of phase in photon energy as are the bound state vibrational wave functions in internuclear distance.

In terms of the above discussion it may appear that bound-free photodissociation bears little potential for obtaining precise information on the level structure of molecules. The bound-free photodissociation process in a di-

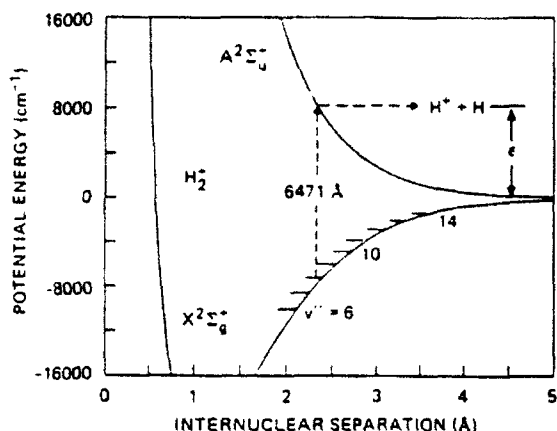


FIG. 1. Photodissociation of H_2^+ at visible wavelengths. The potential energy curves of H_2^+ in the region of its lowest dissociation limit [$H^+ + H(1s)$] are shown. The vertical dashed arrow represents the electronic transition into the continuum from one rovibrational level ($v=8, N=0$) of the $X^2\Sigma_g^+$ state when pumped by photons at 6471 Å. The transition produces fragments with a discrete release of translational energy ϵ .

atomic molecule, however, inherently contains very precise information, equivalent to that obtainable in photoelectron spectroscopy.⁸ This potential is recognized when we rewrite Eq. (4) in terms of the energy distribution of the flux Φ of photodissociation fragments produced by discrete energy photons of intensity $I(\nu)$:

$$d\Phi(\epsilon, \nu)/d\epsilon = I(\nu) h\nu p_{v,N} \sigma_{v,N}. \quad (5)$$

Since the energy balance (3) has to be obeyed, the distribution of photofragment kinetic energies $d\Phi(\epsilon)/d\epsilon$ will also be discrete when a monochromatic light source is used for the excitation. In this case, the energy distribution appears as an image of the bond energies of the dissociated levels, shifted into the continuum by the photon energy. Figure 1 shows, as an example, the energy balance for photodissociation of a single molecular level of H_2^+ . The distribution of intensities in the energy distribution of the photofragments reflects the respective (v, N) population, weighted by the partial cross section $\sigma_{v,N}$. The energetic width of the discrete continuum energies generated in the bound-free transition is solely determined by the lifetime of the lower molecular state that is excited to the continuum and the bandwidth of the photon source.

The recognition of this application of bound-free photodissociation is by no means new. Vibrational resolution in bound-free photodissociation was first achieved by Ozenne *et al.*⁹ and by Van Asselt *et al.*¹⁰ Their experiments were followed by a series of others¹¹⁻¹⁵ which demonstrated both the capabilities of bound-free photofragment spectroscopy, as well as its limitations. These limitations were imposed by the finite resolution of conventional electrostatic or magnetic analyzers with which the photofragment kinetic energies or momenta were determined in the laboratory frame, and by the unavoidable energy spread and angular divergence in the molecular beam. More recently, a position-sensitive detector for the two correlated particles (PSD-C) that are produced in the dissociation of a diatomic molecule was devel-

oped at FOM^{16,17} and applied in photodissociation of metastable neutral molecular hydrogen.¹⁸ A main advantage of the correlated two-particle detection scheme is that no compromise of resolution is associated with spatial filtering of the fragment laboratory distribution, such as that which occurs when the fragments enter a conventional energy analyzer. The PSD-C scheme allows the detection of very nearly all fragments with a sensitivity that is, to first order, independent of the kinetic energy release and the ejection angle in the center-of-mass frame, and establishes the dissociation energy and angle for each detected fragment pair.

The underlying principle of the PSD-C technique is understood with the help of the velocity diagram in Fig. 2. The mutual separation in space and time of the two fragments that arise from a single photodissociation event is related to the center-of-mass energy release ϵ and angle θ by the equations (written here for the homonuclear case)

$$\epsilon = E_0/(4L^2)[(v_0\tau)^2 + R^2], \quad (6)$$

$$\theta = \arctan[R/(v_0\tau)], \quad (7)$$

where $v_0 = (2E_0/M)^{1/2}$ is the velocity of the parent molecule of mass M and kinetic energy E_0 . The spatial separation of the fragments R is measured in a plane perpendicular to the parent beam propagation located at a distance L from the photodissociation region. The two fragments of the parent molecule cross this plane in a time interval τ . Since only arrival time differences between the coincident fragments have to be measured, the laser and the molecular beam can be operated continuously. The position and time-sensitive detector permits both quantities, R and τ , to be determined with high accuracy. In our current apparatus, we achieve a resolution for ϵ at the level of 10 to 20 meV for values of ϵ in the range of eV. This is sufficient to resolve rotational and

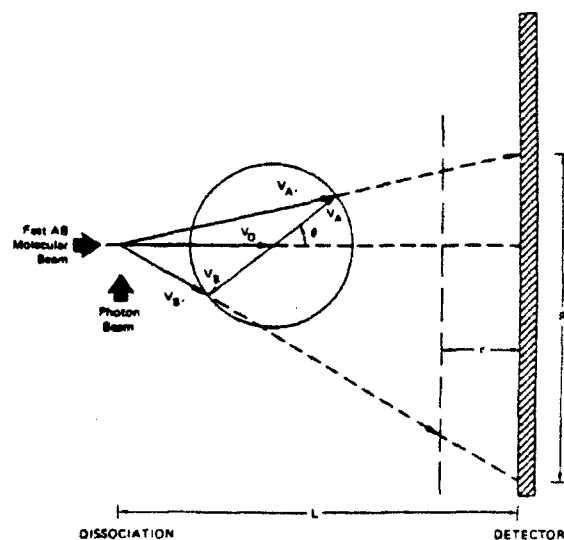


FIG. 2. Velocity vector (Newton) diagram for the photodissociation of a homonuclear molecule (AB). The laboratory velocity vectors are drawn at $\sim 3\%$ of their actual relative magnitudes. Projection of the fragments, represented by the dashed arrows, onto the PSD-C detector yields the experimental observables: the separations of the correlated fragments in both distance R and in arrival time τ .

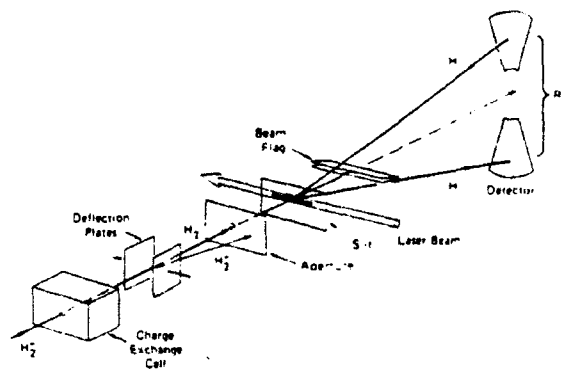


FIG. 3. Schematic diagram of the photodissociation apparatus. For the case of H_2^+ photodissociation, no gas is added to the charge transfer cell and the ions are allowed to pass undeflected through the aperture.

vibrational structure in the distribution function (5) of a hydrogenic molecule. The resolution achieved here is by no means the ultimately achievable one. We estimate that with the proper choice of beam energy and flight distance L , a resolution of below 1 meV should be obtainable with current position-sensitive detectors.

In the following, we first describe the fast-beam apparatus, followed by a description of the position and time-sensitive detector, which we built at SRI, and finally, the application of this detector to diagnose fast beams of both H_2^+ and neutral molecular hydrogen in the $c^3\Pi_u^-$ state formed by charge exchange of H_2^+ . The latter case in particular demonstrates the capability of the method to explore, in addition to the level structure of the bound molecule, quasiscrete structure in the continuum which modifies the bound-free photodissociation intensity.

II. EXPERIMENTAL

A. Fast-beam apparatus

A schematic drawing of the fast beam apparatus is shown in Fig. 3. Ions from a low pressure, hot filament ion source¹⁹ are extracted at energies of several keV, mass selected in a Wien filter, and, in the case of the neutral beam study, neutralized in a charge exchange cell before entering the detector chamber through a 1.5 mm aperture. A distance 200 mm into the detector chamber the beam passes through a narrow (0.3 mm) slit. Adjacent to the slit, the fast beam is crossed at right angles by the intracavity beam of a cw-argon or -krypton ion laser. Typically, 30 W of radiation are available for photodissociation over the ~ 2 mm laser beam diameter. At 3 keV beam energy, the residence time of hydrogen molecules in the laser beam is of the order of 4 ns. Hence the excitation probability for a molecule with cross section $\sigma = 10^{-18} \text{ cm}^2$ is of the order of 10^{-5} . At beam current of 10^9 molecules/s, this would result in a photodissociation rate of 10^4 s^{-1} .

These fragments spread along the parent beam direction in a cone within which the intensity distribution is governed by the angular distribution of fragments in the center-of-mass (c.m.) frame. For a given initial molecular level, the laboratory frame opening angle of this cone is defined by

those fragments that dissociate at 90° with respect to the beam line, the opening half-angle of the cone being $\arctan(\epsilon/E_0)^{1/2}$. For the present experiments the polarization of the laser was chosen perpendicular to the parent beam direction. Since the dominant photodissociation processes investigated here are characterized by a parallel transition moment, this choice of orientation in the laser polarization results in the most effective detection of photofragments by a detector aligned parallel to the laser polarization.

B. Detector

The front face of our position and time sensitive detector is placed $L = 1043 \text{ mm}$ from the dissociation region. The detector consists of two pairs of 5 cm diam microchannel plates which are shielded from the beam except for two opposing sectors of opening angle of 15° , permitting the separate detection of a photofragment pair that falls within the sector area. The sectors extend from 7 to 35 mm measured radially from the parent beam line allowing fragment pair separations which fall within the range $15 \text{ mm} < R < 70 \text{ mm}$ to be monitored. For fragment energies $\epsilon < 1.13 \times 10^{-3} E_0$, approximately 17% of the fragments formed in a parallel transition fall within the open area of the detector and can be recorded. The remaining 83% of the photofragments fall outside the 15° sector angle, and photofragments with energies $\epsilon < 5.17 \times 10^{-5} E_0$ fall entirely inside the dead area at the center of the detector.

The detector and its associated electronics permit measurement of the spatial separation of photofragments with a precision of typically $100 \mu\text{m}$ by measuring on a multianode structure the position of the electron cloud emitted by the microchannel plates, using the charge division method.^{16,17} A cross section of the detector is shown in Fig. 4(a). The multianode structure is generated by photolithography of a copper-clad printed circuit board using the computer generated layout that is shown in Fig. 4(b). The active detection areas are confined to the two circular portions above which the two pairs of microchannel plates are mounted. Each area consists of 35 concentric ring segments with electrical connections extending to the edge of the board where they are interconnected with the resistors and capacitors as required for the charge division method. The resistor/capacitor chain was built from $10 \text{ k}\Omega$ monolithic resistors and 4.7 nF ($\pm 0.5\%$) ceramic chip capacitors which are electrically contacted on the board with Cu-Be springs. The charge deposited on an anode array is amplified by a charge-sensitive preamplifier (Canberra 2004)-linear amplifier (Canberra 2012) combination connected to each end of that anode's RC chain.

Situated between the end face of the microchannel plates and the anode are two grids (33% transmission) that pick up the transit of each electron cloud produced by a fragment. The $\sim 1 \text{ ns}$ transit time of the cloud from the end face of the final microchannel plate to the anode (a distance of 5 mm) produces a voltage pulse on the respective grid with a typical rise time of 400 ps.

The voltage pulse from each timing grid is amplified by a preamplifier (Comlinear E103) and detected by a constant-

fraction discriminator (Tennelec TC-455). After a fixed cable delay time, these pulses provide the start and stop inputs to a time-to-amplitude converter (Canberra 2143) to establish the value of τ for the fragment pair. The four charge pulses and the TAC output pulse are digitized by five analog-to-digital converters (Canberra 8077) and input to a micro-computer (PDP-11/73) through a CAMAC interface. The entire process from the impact of the fragment pair on the detector to storage in computer memory of the radial positions of the two fragments and their arrival time difference requires $\sim 40 \mu\text{s}$.

The dead area in the center of the detector is shielded from the photodissociation region by a V-shaped beam flag, which serves as a beam stop for the parent molecular beam. The size of this flag must be chosen sufficiently large that nearly all the undissociated molecules are collected, but not so large that its shadow from the dissociation region falls on an active area of the detector. In connection with the slit, the beam flag significantly reduces the background of fragments that arise from unimolecular and collision-induced dissociation of beam molecules. Since the pressure in the detector chamber is of the order of 10^{-9} Torr, collision-induced dissociation in the region between the slit and the flag contributes only a minor background.

C. Detector accuracy

A extensive discussion of the uncertainties inherent in the use of the position and time-sensitive detection technique to measure the energy and angle of the dissociation event has been presented in two papers published by the FOM group.^{16,17} Briefly, the limiting factors for the precision are set by the linearity of the capacitor chains for the charge division, and the linearity of the amplifiers and analog-to-digital converters used to measure the output of the capacitor chain. We note here an additional source of error inherent in all position-sensitive detection schemes that are based on the measurement of a purely radial coordinate (rather than a two-dimensional measurement). This error is associated with the fact that the anode strips are curved. Hence a cylindrically symmetric electron charge cloud whose diameter is larger than the width of an individual strip will be divided among the strips in an asymmetric way; the strips at shorter R will receive more charge than those at larger R , thereby shifting the measured center of the charge cloud to shorter distance. Although this position error could be eliminated by keeping the size of the electron cloud small compared to the anode strip widths (1 mm), such a procedure would eliminate the obvious improvement in position resolution that is achieved by having the cloud distributed over a number of anode strips.

For strip radii that are large compared to the electron cloud diameter, the error in the distance measurement is fairly small. At small radial distance, however, the absolute error in R can become quite substantial. For a cloud diameter of 10 mm and a position 20 mm from the detector center, the apparent R value determined from the charge distribution on the anode would underestimate the true radial distance by 3%. We have incorporated this position correction

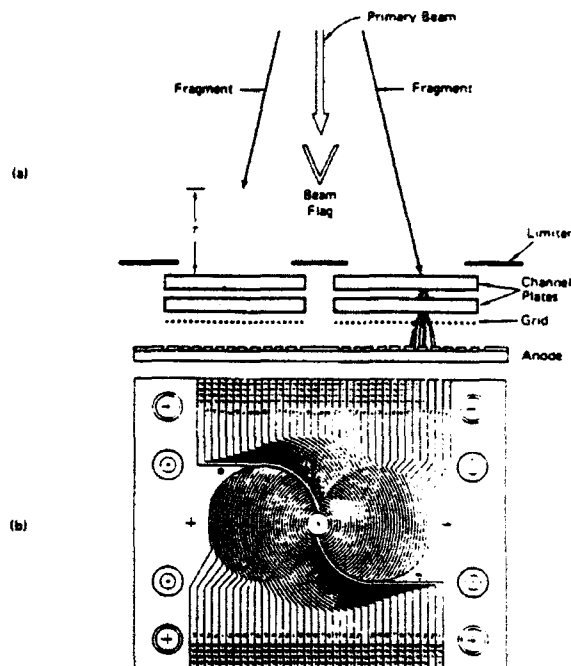


FIG. 4. Schematic diagram for the position sensitive detector for correlated fragments (PSD-C). The upper figure (a) shows a cross sectional view of the detector. The lower figure (b) is a negative photograph of the anode board. Dark areas in this figure denote the absence of copper on the surface of the board. Overall dimensions of the board are 100 mm \times 129 mm. The resistors and capacitors for charge division position measurement on the two sets of anode rings are mounted on the pads shown on the upper and lower edges of the board.

into the data acquisition software, such that true radial positions are calculated from the charges measured at the detector anodes. The unknown parameter required for determining the magnitude of the corrections is the diameter of the electron cloud. This is established by observing the changes in the radial positions of discrete features in the photofragment spectrum as a function of molecular beam energy.

In the case of molecular ion photodissociation, a limiting factor in the resolution appears in a position sensitive detection scheme from residual electric and magnetic fields that can influence the propagation path of the charged photofragment. This effect was readily noted in our experiments on H_2^+ and was partially eliminated by mounting a shielded deflection plate below the beam flag (see Fig. 3). With this arrangement, protons travelling below the beam flag could be prevented from reaching the lower detector half, such that coincidences were only recorded for dissociation events where the charged fragment was ejected above and the neutral fragment below the flag. In this case a deflection of the charged particle path due to external fields results only in a slight falsification of the absolute value of R but not (to first order) in a loss of resolution. In the present studies of H_2^+ and H_2 photodissociation, a position resolution of 100–200 μm and a position accuracy of $<250 \mu\text{m}$ was observed over the central 80% of the detector.

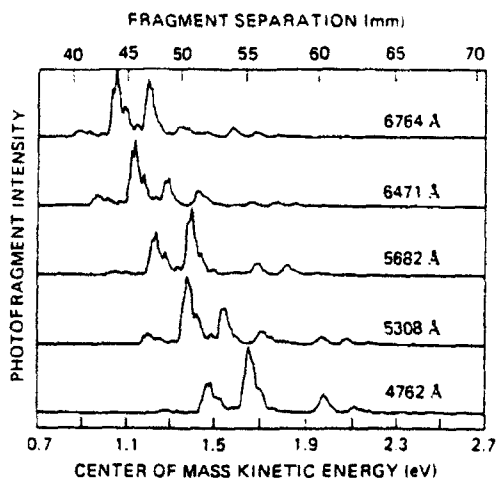


FIG. 5. Observed center-of-mass energy releases (ϵ) in eV from the photodissociation of H_2^+ at five discrete wavelengths of the krypton ion laser. The scale at the top of this figure gives the measured radial separation R (mm) of those fragment pairs arriving at the detector with $\tau = 0$, i.e., those fragments produced by dissociation of the H_2^+ with $\Theta = 90^\circ$.

III. RESULTS

A. Photodissociation of H_2^+

Photodissociation of H_2^+ has been studied extensively by a number of laboratories.^{9,10,20-26} At wavelengths extending from the infrared to the near ultraviolet, the photodissociation involves an electronic transition from the $X^2\Sigma_g^+$ ground electronic state of H_2^+ to the continuum of the repulsive $A^2\Sigma_u^+$ state. The potential energy curves for these states are shown in Fig. 1. Since the A state is well isolated from higher electronic states in the region of its dissociation limit, this process represents a classic example of a bound-free photodissociation. At the wavelengths studied here (7525–4579 Å), X state vibrational levels extending from $v'' = 4$ to the highest level ($v'' = 18$), can participate in the photodissociation.

The H_2^+ ions for this study were produced in a column¹⁸ (hot-filament) discharge ion source using pure hydrogen gas at pressures in the range of 50–200 mTorr and discharge voltages in the range of 70–250 V. Under these conditions, production of H_2^+ accounted for > 90% of the positive ions. The ions were extracted from the source, accelerated to a kinetic energy in the range of 1000–3000 eV, and mass selected by a Wien filter before intersecting the intracavity beam of a line-selected Ar^+ or Kr^+ ion laser. The electric vector of the ion laser was constrained by four sets of windows at Brewster's angle to lie perpendicular to the ion beam and parallel to the open segments of the PSD-C detector.

The photofragment spectra for H_2^+ at $E_0 = 2807$ eV observed by the PSD-C detector at five lines of the Kr^+ laser are shown in Fig. 5. The accumulation time for each spectrum in this figure was 5 to 20 min, depending on the laser power available at each wavelength. The lower abscissa in this figure is the energy release in the photodissociation ϵ calculated from the measured values of R and τ using Eq.

(6). The upper abscissa gives the equivalent values of R measured by the detector for fragments arriving with $\tau = 0$. In this case, the fragment kinetic energy ϵ is directly related to the measured separation of the photofragments at the detector R . It can be seen that as the photon energy is changed, the photofragments cover different portions of the detector, with R values ranging from 20 to 60 mm. A similar, but opposite effect is observed when the beam energy E_0 is varied.

The apparent randomness of the fragment distributions in Fig. 5 is reconciled when the photon energy $h\nu$ is subtracted from the fragment energy ϵ and the data replotted (Fig. 6). On the energy scale $\epsilon - h\nu$, the energies of the absorbing levels in the $\text{H}_2^+ X^2\Sigma_g^+$ are readily identified. At the top of Fig. 6 is shown the energy²⁶ of the lowest rotational level $N = 0$, relative to the ground state dissociation limit, of the vibrational levels involved at these wavelengths. It is apparent from this figure that each vibrational feature consists of a number of incompletely resolved peaks. The energies of these peaks correspond to rotational energy levels within each ground state vibrational level. This assignment is supported by the 3:1 intensity alternation that is characteristic of the statistical weights of the odd and even rotational levels in a homonuclear molecule of nuclear spin 1/2.

The detection of photofragments using the PSD-C technique has the advantage that all dissociating levels that produce fragments within the physical limits of the detector are observed simultaneously. Fluctuations in the intensity of the parent beam or of the laser produce equal contributions to the statistical noise in each of the spectral features. Furthermore, the Jacobian for the transformation from the coordinate frame of the dissociating molecule to the frame of the detector is unity¹⁶; there is no amplification of the statistical noise as a function of ϵ , or equivalently, as a function of lower state energy level. This is in marked contrast to the case where the fragments are detected solely by dispersal of their laboratory energies or momenta.^{9-15,23-26}

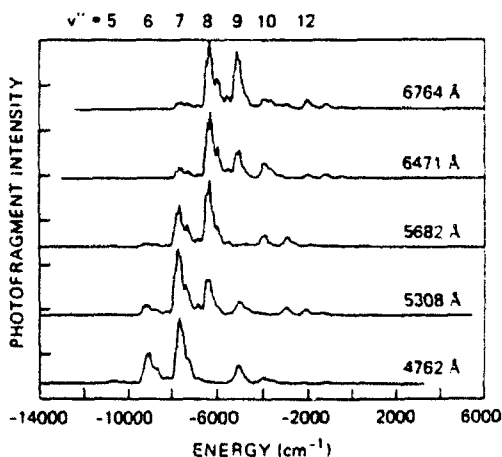


FIG. 6. The experimental data of Fig. 5 after subtraction of the photon energy from the observed energy releases to yield the energy of the lower state levels relative to the dissociation limit. The known energies of the vibrational levels in the rotationless $\text{H}_2^+ X^2\Sigma_g^+$ potential energy curve are given at the top of this figure.

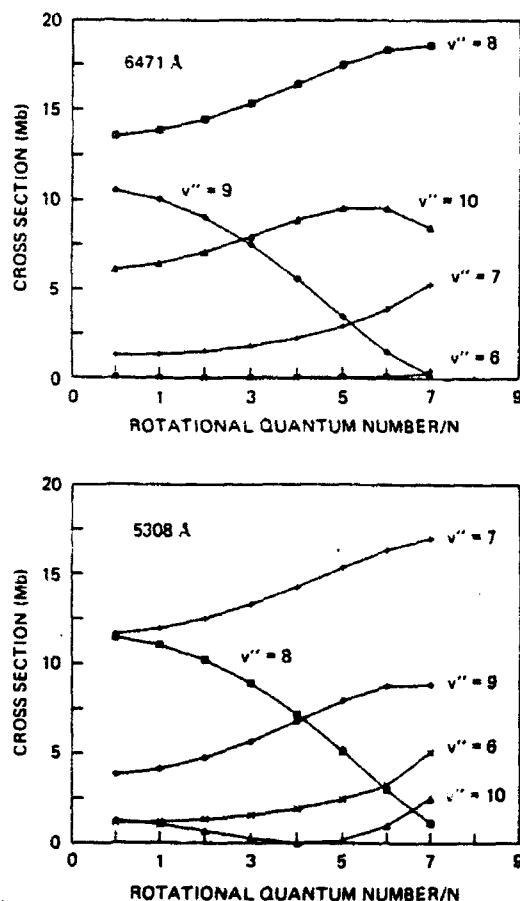


FIG. 7. Partial photodissociation cross sections, in units of 10^{-18} cm^2 , for $\text{H}_2^+ A-X$ calculated as a function of rotational quantum number N for vibration levels $v = 6-10$. Those cross sections for excitation at 6471 Å are shown in the upper figure while those for excitation at 5308 Å are shown in the lower figure.

Given the vibrational and rotational resolution in the photofragment spectra, the PSD-C technique seems to offer a good way to probe the population distribution among the internal states of a beam of molecules. However, to relate photofragment intensities to initial state populations, explicit account must be taken of the rotational and vibrational dependence of the photodissociation cross section [Eq. (4)]. These partial cross sections, $\sigma_{v,N}$ were calculated with the computer program of Sando²⁸ using the potential energy curves for the X and A states of H_2^+ given by Wind²⁹ and Peek.³⁰ The cross sections at two of the relevant wavelengths are shown in Fig. 7 as a function of rotational quantum number N for $v'' = 6-10$. In addition to the strong dependence on wavelength and vibrational quantum number mentioned earlier, it can be seen that the cross section for a given vibrational level can vary by an order of magnitude for rotational levels between $N = 0$ and $N = 7$.

In order to derive the state distribution of the ion beam from the photofragment spectra, the spectra were simulated by representing each lower state vibrational and rotational level by a Gaussian line shape at the photofragment energy $\epsilon = h\nu - E(v,N)$, where $h\nu$ is the photon energy corre-

sponding to the particular laser wavelength and $E(v,N)$ are the energy levels of the X state given by Kuriyan and Pritchard.²⁷ The amplitude of each Gaussian at a particular exciting wavelength λ was given by

$$A(\lambda, v, N) = \sigma_{v,N} p(v) (2T_l + 1) (2N + 1) \exp(-F/kT_l), \quad (8)$$

where T_l is the total nuclear spin of ortho ($T_l = 1$) or para ($T_l = 0$) hydrogen, $p(v)$ is the fractional population in vibrational level v , and N is the rotational quantum number. The term F in Eq. (8) represents the rotational energy of the equilibrated species, H_2^+ or H_2 , that is appropriate to the formation of ions in the source. The H_2^+ are initially created by electron impact in the discharge and would, in the absence of collisions, be expected to retain the rotational population distribution of the parent H_2 molecules.³¹ The path taken by the nascent ions and their acceleration characteristics between the point of formation within the source and their extraction into a collision-free environment of the beam are not well defined. However, the H_2^+ formed in pure H_2 are subject to rapid two-body conversion³² into H_3^+ . This rate constant ($k \sim 2 \times 10^{-9} \text{ cm}^3 \text{ s}^{-1}$) is at least as fast as that of any collisional processes leading to vibrational or rotational relaxation. Since $[\text{H}_2^+]/[\text{H}_3^+] > 10$ under the source conditions used here, it is reasonable to expect that the nascent rotational distribution of H_2^+ will be retained by the ion beam, i.e., the ion beam will be described by a rotational distribution that is characteristic of the H_2 source gas temperature.

The photofragment spectra were simulated for a given choice of Gaussian linewidth by varying $p(v)$ and source gas temperature T in Eq. (7). A best fit was observed for a Gaussian linewidth (FWHM) of 18 meV, a hydrogen gas temperature of 1400 K, and the H_2^+ vibrational populations (Franck-Condon factors) of Dunn.³ The observed PSD-C photofragment spectrum at $\lambda = 6471 \text{ Å}$ and the simulation for this wavelength are shown in Fig. 8. The ratios of the low N rotational components, which are partially resolved in the more intense vibrational peaks, are quite sensitive to the choice of rotational temperature and could not be reproduced if the temperature were varied by $> 100 \text{ K}$ from the mean value of 1400 K.

It is clear from the fit to the photofragment spectra that the relative population of H_2^+ in vibrational levels $5 < v'' < 14$ is within 10% of that predicted³ for direct ionization. This is in contrast to previous reports of a depopulation of the higher vibrational levels in H_2^+ beams produced by monoplasmatron¹⁰ and duoplasmatron²⁴ ion sources. Such depopulation has been attributed¹⁰ to collisional dissociation of the vibrationally excited ions; the calculations of Peek³³ predict the cross section for collisional dissociation of H_2^+ ($v'' > 7$) to be more than an order of magnitude larger than that for H_2^+ ($v'' = 0$). Such processes are presumably of minor importance in the present work where production of H^+ in the source is $< 10\%$ of the total ion current.

It should be noted that the peaks in the PSD-C spectrum are not expected to be Gaussian on the energy scale shown in Fig. 8, but should exhibit more tailing toward small values of ϵ . Position measurement errors have a Gaussian distribution

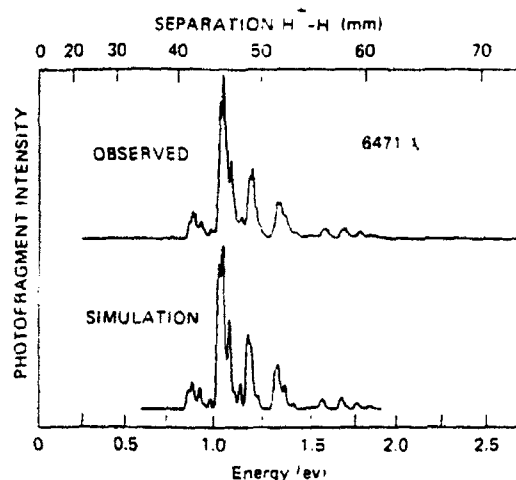


FIG. 8. Photofragment energy release spectrum from the photodissociation of H_2^+ at 6471 Å. The experimental spectrum is shown in the upper portion of this figure. The simulated spectrum is shown in the lower portion. The simulation assumed formation of the H_2^+ by direct ionization of H_2 at a rotational temperature at 1400 K, with each photodissociated energy level represented by a Gaussian peak of 18 meV FWHM.

on an R scale (not R^2) and timing errors in observing this parallel electronic transition will bias the spread in the R spectrum toward smaller values of R for the choice of laser polarization used here. However, a sample Monte Carlo simulation of the photodissociation observed with the PSD-C detector showed that the apparent lower state populations are not significantly distorted by the use of Gaussian peak shapes.

B. Photodissociation of H_2 $c^3\Pi_u$

To test the sensitivity and properties of our two-particle detector, a neutral system has several advantages over an ionic species. For one, the flight path of the neutral photodissociation products is unaffected by residual electric and magnetic fields. Secondly, the energy of a neutral fast beam can be varied in a rather precise fashion by controlling the potential of the charge exchange cell, thereby eliminating uncertainties in the absolute beam energy which enters the measured separation energy through Eq. (6). To form the fast neutral beam we chose xenon as a charge transfer target because it was a permanent gas compatible with our charge exchange cell. The formation of the long lived c state of H_2 in the reaction



is endothermic by about 8 eV and proceeds with relatively small cross section when compared to the efficiency in an alkali target. From the observed photodissociation signal of $H_2 c^3\Pi_u$ we calculate that approximately 0.15% of the neutral beam was formed in the c state when 10% of the ions were neutralized in xenon.

In the visible wavelength range, transitions from the c state access the electronic states of the $3s, 3d$ complex of H_2 . As shown in Fig. 9 two of these states, the $h^3\Sigma_g^+$ and $i^3\Pi_g$, dissociate into $H(2l) + H(1s)$ while the two others, the

$g^3\Sigma_g^+$ and $j^3\Delta_g$ states correlate to the $H(3l) + H(1s)$ dissociation limit. The photodissociation of the c state at wavelengths between 5600 and 6600 Å proceeds via four mechanisms which have been discussed in detail recently.¹⁸ For the current experiments, only two of these processes have to be considered: Bound-free photodissociation via the i state and predissociation of bound levels in the j and g states.

The current photodissociation studies of the c state were performed at the three krypton ion laser wavelengths, 5683.46, 6472.67, and 6766.28 Å. At these photon energies no discrete transitions were observed in previous¹⁸ photodissociation experiments of the c state, but a very small background from bound-free photodissociation appeared in the spectra. This background was attributed¹⁸ to transitions from high vibrational levels in the c state to the repulsive wall of the i and h states. Due to the higher transition moment expected for transitions $3d-2p$ than for $3s-2p$, the dominant contribution to bound-free photodissociation is expected from the i state. In Fig. 10 we show the variation of the calculated photodissociation cross section for selected c -state vibrational levels through the $i^3\Pi_g$ state. It may be noted that these cross sections vary far less with v than did those presented in the previous section for the photodissociation of H_2^+ . The reason for this behavior is that at the wave-

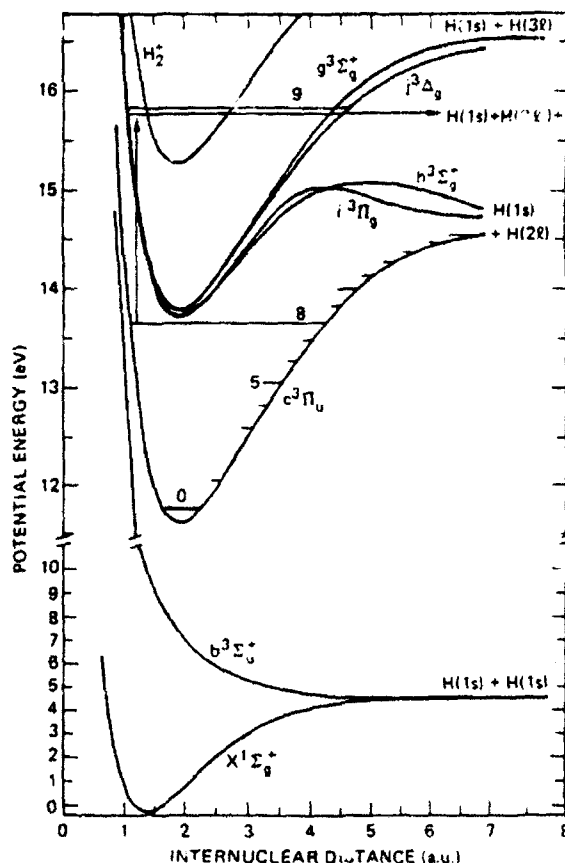


FIG. 9. The potential energy curves of H_2 relevant to photodissociation of the $c^3\Pi_u$ state. The ground electronic states of H_2 and H_2^+ are shown for reference.

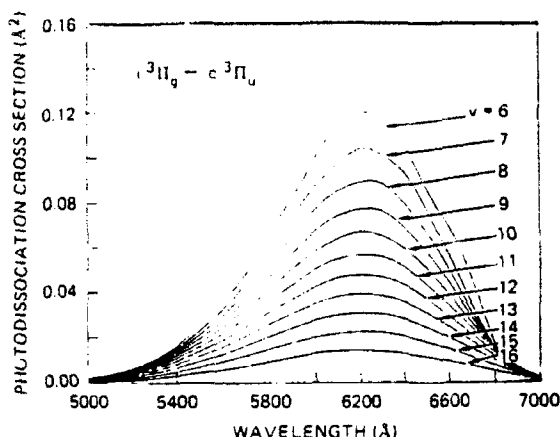


FIG. 10. Calculated cross section, in units of 10^{-16} cm^2 , as a function of exciting wavelength for the photodissociation of H_2 in the $c^3\Pi_u$ ($v = 6-16$) state through the (unperturbed) continuum of the $i^3\Pi_g$ state.

lengths considered here the dominant contributions to bound-free transitions come from near the left-hand turning point of the c -state vibrational levels where the difference potential between the c and the i state varies little with internuclear separation. For the same reason, the rotational dependence of the bound-free cross section for this process is found to be minor at the wavelengths shown in Fig. 10.

The bound-free photodissociation process is, however, complicated due to the presence of the two *gerade* $n = 3$ states, g and j , which modify the i -state continuum. At internuclear separations shorter than R_e , all $n = 3$ states have potential energy curves which are nearly degenerate. Due to this degeneracy and due to the very large l -uncoupling, the bound $3d$ states interact strongly with the continuum of the i state and this interaction leads to the very rapid predissociation of those bound levels in the j and g states that lie above the potential barriers in the i and h states. A previous experimental and theoretical study¹⁸ of this predissociation showed that the predissociation proceeds on time scales of the order of 1×10^{-14} s causing the natural width of the j state levels to be of the order of 50 cm^{-1} for rotational levels $N = 2$. The widths increase with N , as expected for predissociation by rotational coupling.

The presence of predissociated levels in the j and g states thus modifies the wavelength dependence of the bound-free photodissociation via the i state through the interaction of the bound and continuum channels. Due to the strength of this interaction the influence of the coupling extends over a wide energy range; the i -state continuum wave function carries j and g state character at energies well separated from the resonance positions in the j and g states. In accordance with the Beutler-Fano picture,³⁴ this interaction will lead to a wavelength-dependent enhancement (or suppression) of the bound-free contribution for a given lower state level. These interference effects are very much evident in the photodissociation spectra discussed below.

The photofragment spectra of H_2 obtained with the PSD-C detector for photodissociation at 6471 and 5682 Å are given in Fig. 11. Again we have subtracted the photon

energy from the measured separation energy ϵ . The peak positions apparent from the figure display the energy location of the respective c -state levels. At the bottom of the figure we have indicated the rovibrational energy positions for the c state which we calculated using the potential energy curve given by Kolos and Rychlewski.³⁵ The absolute accuracy of our measurement is considered to be of the order of 100 cm^{-1} and within that uncertainty the measured level positions match those predicted from the potential energy curve.

The observed variation of intensity with both v and N was at first unexpected, but as pointed out above, can be understood quantitatively from the interaction of the i state continuum with the bound levels in the j and g states. We divide our discussion of the observed intensity pattern into three parts. First, we discuss the pattern expected in the case of photodissociation via the pure i state, then we discuss the observed enhancement of certain v, N combinations. Finally we explain the enhanced photofragment intensity which appears near the dissociation limit in the case of photodissociation at 6471 Å.

In the lower part of Fig. 11, we have simulated the expected appearance of pure i state photodissociation at 6471 Å. For this simulation we have first calculated the rovibrational population of the H_2 c state by assuming the rovibrational populations in the H_2^+ precursor that were established in the preceding section, and that the redistribution of internal energy in the charge transfer reaction is governed by the Franck-Condon factors for the $\text{H}_2^+ X^2\Sigma_g^+(v') \rightarrow \text{H}_2 c^3\Pi_u(v'')$ transitions, as is appropriate for a nonre-

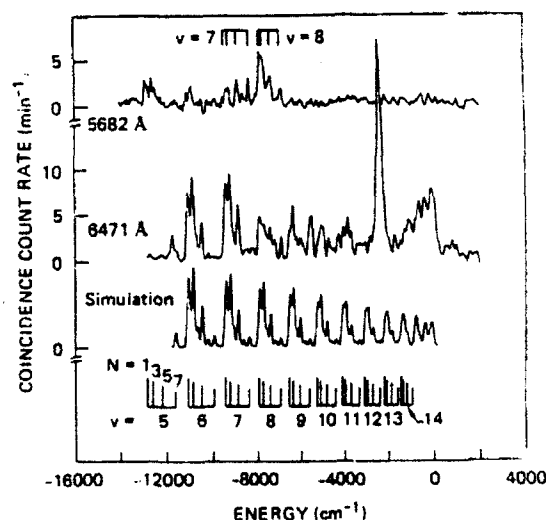


FIG. 11. Photofragment energy release spectra for the photodissociation of H_2 at 5682 and 6471 Å. The experimental spectra are shown in the upper half of the figure; the energy of the exciting photons has been subtracted from the observed energy releases to obtain the dissociation energies of the lower state levels involved in the photodissociation. The lines in the lower portion of the figure indicate the known dissociation energies of rotational levels $N = 1, 3, 5$, and 7 in vibrational levels $v = 5-14$ of the metastable $\text{H}_2 c^3\Pi_u$ state. The spectrum labeled "simulation" assumes photodissociation of the c state via an unperturbed i state at 6471 Å. The tick marks at the top of the figure denote the expected locations of some perturbations in the 5682 Å spectrum (see the text).

sonant process at high energy,¹⁶ and $\Delta N = 0$ rotational transitions. This distribution was folded with the calculated partial cross sections from Fig. 10 and an experimental Gaussian peak width of 150 cm^{-1} . A very similar pattern is predicted for photodissociation through the pure i state at 5682 Å , albeit with a reduced intensity since the photodissociation cross section is typically a factor of 3 smaller at this wavelength. This and the lower laser power available explain the smaller signal-to-noise ratio for the spectrum obtained at 5682 Å .

Comparing the predicted and observed spectrum at 6471 Å we see that the two spectra agree in general trends, but the experimental spectrum shows significantly enhanced photodissociation from $v = 12$, $N = 7$ and near the dissociation limit. In addition the intensities for $N = 7$ levels are enhanced for $V = 8, 9$. In the spectrum obtained at 5682 Å a very pronounced enhancement appears for the higher N levels in $v = 7$ and all N 's in $v = 8$, with the $v = 10$ and higher vibrational levels being absent or reduced.

As we indicated above in general terms, the enhancement of specific (v, N) levels can be attributed to the presence of bound but rapidly predissociated levels in the j and g states which are, at given laser wavelength, more or less distant from the continuum energy in the i state that is accessed from the discrete levels in the c state. In the absence of experimental information on the exact energy location of the high-lying bound j -state levels, we have used the theoretical potential energy curve of Rychlewski³⁷ to calculate the bound rovibrational levels in the j state. The results from such a calculation have to be treated with some care since l -uncoupling is not taken into account when considering the pure j state. Comparing the calculated energies for the j state with those known precisely from bound-bound spectroscopy³⁸ at energies below the dissociation limit $H(1s) + H(2l)$, we find that for $N = 5$, the calculations underestimate the energy of the j state levels by about 50 cm^{-1} . The magnitude of the level shift due to l -uncoupling is roughly linear in N . The magnitude of the shifts are likely to be very similar in the energy region above the barrier of the i and h states since the dominant uncoupling interaction is weighted with R^{-1} and the states are near degenerate for all energies at short R .

The uncertainty about the precise level position stops us at this point from attempting a detailed interpretation of the observed enhancement. Nevertheless the bound-bound line positions in H_2 are so well separated in energy that we are able to identify the j state levels which are responsible for the enhancement of the photodissociation cross section from specific c -state levels. In particular, we find that the $(\Delta v = 1) P(5)$ and $P(7)$ transitions from $v = 7$ lie within 100 cm^{-1} of the photon energy at 5682 Å . Likewise, the $(\Delta v = 1) Q(2)$, $Q(3)$, and $Q(4)$ transitions from $v = 8$ lie within 20 cm^{-1} of the energy at 5682 Å . In agreement with our predictions above, the photodissociation spectrum at 5682 Å shows the peaks originating from $v = 7$, $N = 5$ and 7 and $v = 8$, $N = 2, 3, 4$ greatly enhanced. By contrast the Q branches from $v = 9$ lie more than 250 cm^{-1} from the laser energy and are in fact absent in the photodissociation spectrum at 5682 Å . Similarly, the $(\Delta v = 0) P(7)$ transition from $v = 12$ is calculated to lie within 100 cm^{-1} of the laser

energy at 6471 Å . As can be seen from Fig. 11 this c -state level is very dramatically enhanced. On the basis of the calculations we would predict a similar enhancement of the $N = 7$ level from $v = 13$. This level is, however, conspicuously absent in the spectrum. While care must be taken in this comparison due to our scant knowledge of the j state energy levels, we want to point out that both enhancement and suppression are expected as a result of the bound-state-continuum interaction.¹⁴

Finally, we must mention the observed enhancement in the photodissociation cross section for the highest vibrational levels of the c state at 6471 Å . This enhancement was not observed at the two other wavelengths investigated, 5682 and 6764 Å . The enhancement is associated with the proximity of the photon energy at 6471 Å (15450 cm^{-1}) with the separation of the dissociation limits $H(n = 3) + H$ and $H(n = 2) + H$ (15234 cm^{-1}). As a result the bound-bound transitions among the highest vibrational levels in the c and j states fall into near resonance with the photon energy at 6471 Å . Specifically, the $(14, 15)$ and $(16, 16)$ bands are predicted³⁷ to lie within 5 cm^{-1} of the photon energy and the $(13, 14)$, $(15, 15)$, $(15, 16)$, and $(17, 17)$ bands are predicted to lie within 100 cm^{-1} . The rapid predissociation that was observed for the intermediate vibrational levels of the j state¹⁸ is expected to be active also for the highest levels. Hence these transitions will contribute to the photodissociation signal in the same manner as the (v, N) selective enhancement that occurs at intermediate vibrational levels. Obviously the transitions to the highest vibrational levels to the g state will fall into the same energy range as those to the j state and they will also contribute to the observed pileup of photodissociation intensity near the dissociation limit of the c state.

IV. SUMMARY

We have demonstrated that a position-sensitive detector for correlated particles provides sufficiently high resolution to resolve both vibrational and rotational contributions in the photofragment energy release spectrum of a bound-free photodissociation process. At the current level of resolution, the discrete rotational contribution to the photodissociation can be resolved only in hydrides. However, substantial improvement in the position-sensitive detection should be readily achievable with current technology, which would allow rotational resolution in the photodissociation of all but the heaviest molecules.

Having achieved rotational resolution, some caution is required to extract the rovibrational population distribution from the photofragment energy release spectrum. There appear to be three general cases where accurate distributions can be determined with a reasonable degree of experimental effort:

(a) When the bound-free photodissociation process is well defined, as in the case of H_2^+ , where the initial and final electronic states of the molecule are well characterized and the continuum is not modified by perturbations, accurate population distributions can be established from photofragment spectra obtained at only a few widely spaced wavelengths.

(b) When the initial state is well characterized, but the final state is not, the lower state population distribution can be established if the photofragment spectra are observed at wavelength intervals that are chosen such that each oscillation in the partial photodissociation cross section $\sigma(v, N)$ is probed (see e.g., Ref. 13).

(c) Finally, the case arises as in H_2 , where the continuum of the final state is significantly modified by perturbations. Generally the width of such perturbations are narrow compared to the oscillations in the partial photodissociation cross sections for excitation into the pure continuum. Photofragment energy release spectra obtained with a continuously tunable wavelength source should provide sufficient information to extract the lower state population distribution.

ACKNOWLEDGMENTS

It is a pleasure to acknowledge very helpful discussions with members of the FOM laboratory on the operation of their detector. We also wish to thank I. C. Adams for assistance in the design and the precision machining of the detector parts. This research was supported with funds from the National Science Foundation under Grant Nos. PHY 84011517 and ATM 8504152, and by the Aero Propulsion Laboratory, Air Force Wright Aeronautical Laboratories, Aeronautical Systems Division (AFSC), United States Air Force, Wright-Patterson AFB, Ohio under Contract No. F33615-85-C-2560.

¹H. Helm, in *Electronic and Atomic Collisions*, edited by J. Eichler, I. V. Hertel, and N. Stolterfoht (North-Holland, Amsterdam, 1984), p. 275.

²P. B. Armentrout, S. M. Tarr, A. Dori, and R. S. Freund, *J. Chem. Phys.* **75**, 2786 (1981).

³G. H. Dunn and B. van Zyl, *Phys. Rev.* **154**, 40 (1967).

⁴R. Kachru and H. Helm, *Phys. Rev. Lett.* **55**, 1575 (1985).

⁵G. Dunn, *J. Chem. Phys.* **44**, 2592 (1966).

⁶H. Helm, P. C. Cosby, M. M. Graff, and J. T. Moseley, *Phys. Rev. A* **25**, 304 (1982).

⁷G. H. Dunn, *Phys. Rev.* **172**, 1 (1968).

⁸J. Berkowitz, *Photoabsorption, Photoionization and Photoelectron Spectroscopy* (Academic, New York, 1979).

⁹J. -B. Ozenne, D. Pham, and J. Durup, *Chem. Phys. Lett.* **17**, 422 (1972).

¹⁰N. P. F. B. Van Asselt, J. G. Maas, and J. Los, *Chem. Phys. Lett.* **24**, 555 (1974); *Chem. Phys.* **5**, 429 (1974); *J. Chem. Phys.* **11**, 253 (1975).

¹¹J. T. Moseley, R. P. Saxon, B. A. Huber, P. C. Cosby, R. Abouaf, and M. Tadjeddine, *J. Chem. Phys.* **67**, 1659 (1977).

¹²R. Abouaf, B. A. Huber, P. C. Cosby, R. P. Saxon, and J. T. Moseley, *J. Chem. Phys.* **68**, 2406 (1978).

¹³F. J. Griesman, J. T. Moseley, R. P. Saxon, and P. C. Cosby, *Chem. Phys.* **51**, 169 (1980).

¹⁴J. T. Moseley, J. -B. Ozenne, and P. C. Cosby, *J. Chem. Phys.* **74**, 337 (1981).

¹⁵H. Helm, and R. Möller, *Phys. Rev.* **27**, 2493 (1983).

¹⁶D. P. de Bruijn and J. Los, *Rev. Sci. Instrum.* **53**, 1020 (1982).

¹⁷D. P. de Bruijn, J. Neuteboom, and J. Los, *Chem. Phys.* **85**, 233 (1984).

¹⁸H. Helm, D. P. de Bruijn, and J. Los, *Phys. Rev. Lett.* **53**, 1642 (1984); D. P. de Bruijn and H. Helm, *Phys. Rev. A* **34**, 3855 (1986).

¹⁹Coultron, model 101Q, Boulder, CO.

²⁰H. G. Dehmelt and K. B. Jefferts, *Phys. Rev.* **125**, 1318 (1962).

²¹K. B. Jefferts, *Phys. Rev. Lett.* **20**, 39 (1968).

²²F. von Busch and G. H. Dunn, *Phys. Rev. A* **5**, 1726 (1972).

²³J. -B. Ozenne, J. Durup, R. W. Odom, C. Pernot, A. Tabche-Fouhaille, and M. Tadjeddine, *Chem. Phys.* **16**, 75 (1976).

²⁴P. J. Novak, H. H. Holsboer, H. Heubers, R. W. Wijngaerts Van Resandt, and J. Los, *Int. J. Mass Spectrom. Ion Phys.* **34**, 375 (1980).

²⁵A. K. Edwards, R. Kutina, N. Cue, D. S. Gemmel, K. Inglis, E. P. Kanter, and B. J. Zabransky, *Phys. Rev. A* **23**, 2724 (1981).

²⁶R. E. Kutina, A. K. Edwards, R. S. Pandolfi, and J. Berkowitz, *J. Chem. Phys.* **80**, 4112 (1984).

²⁷M. Kuriyan and H. O. Pritchard, *Can. J. Chem.* **55**, 3420 (1977).

²⁸P. S. Herman and K. M. Sando, *J. Chem. Phys.* **68**, 1153 (1978).

²⁹H. Wind, *J. Chem. Phys.* **42**, 2371 (1965).

³⁰J. M. Peek, *J. Chem. Phys.* **43**, 3004 (1965).

³¹J. Allison, T. Koudow, and R. N. Zare, *Chem. Phys. Lett.* **64**, 202 (1979).

³²B. G. Reuben and L. Friedman, *J. Chem. Phys.* **37**, 1636 (1962).

³³J. M. Peek, *Phys. Rev.* **140** (1965).

³⁴H. Fano, *Phys. Rev. A* **2**, 353 (1970).

³⁵W. Kolos and J. Rychlewski, *J. Mol. Spectrosc.* **66**, 428 (1977).

³⁶L. Tomcho and M. J. Haugh, *J. Chem. Phys.* **56**, 6089 (1972).

³⁷J. Rychlewski, *J. Mol. Spectrosc.* **104**, 253 (1984).

³⁸S. Keiding and N. Bjerre (private communication).

Appendix F

ELECTRON-IMPACT DISSOCIATION OF NITROGEN

ELECTRON-IMPACT DISSOCIATION OF NITROGEN

P. C. Cosby

**Molecular Physics Laboratory
SRI International
Menlo Park, CA 94025**

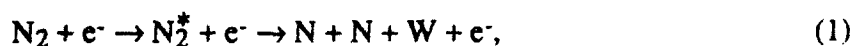
ABSTRACT

The electron-impact dissociation of N_2 to form two nitrogen atoms is observed in a crossed beam experiment at electron energies between 18.5 eV and 148.5 eV. Detection of the correlated dissociation fragments with a time and position sensitive detector permits detection of both ground and excited state fragments, but excludes interference from dissociative ionization products. The observed translational energy releases in the N_2 dissociation are consistent with predissociation to $N(^2D) + N(^4S)$ fragments as the primary dissociation mechanism. Absolute cross sections for the electron impact dissociation are measured and compared with previous measurements. Recommended values of this cross section are given for electron-impact energies between 10 eV and 200 eV.

**MP 92-275R
January 27, 1993**

INTRODUCTION

The nitrogen molecule comprises a significant fraction of the earth's atmosphere and the atmospheres of Titan and Triton. Within these environments, N_2 is subject to significant bombardment both by energetic electrons, as is characteristic of aurorae, and by lower energy photoelectrons produced in the normal atmosphere.¹ Ionization,²⁻⁴ dissociative ionization,⁵⁻⁷ excitation,⁸ and dissociation⁹⁻¹² of the N_2 can result from electron impact. Laboratory studies have produced a rather complete set of quantitative data¹³ for these processes, with the exception of electron impact dissociation. In the electron-impact dissociation reaction



electron impact produces an electronically excited state of N_2 that subsequently dissociates into atoms with the release of translational energy, represented here by W . While the overall cross section for this reaction is known,^{8,13} little information is available concerning the electronic states and translational energies of the products which determine their subsequent reactions.¹⁴

Electron energy loss studies¹⁵⁻¹⁸ have shown that discrete (bound) levels of N_2^* are produced in the first step of Reaction (1); thus dissociation of N_2 must primarily occur through predissociation. Only three electronic states of the atoms, 4S , 2D , and 2P , are energetically accessible below the ionization limit of the molecule, but an *a priori* prediction of the branching among these in the predissociation is greatly complicated by strong Rydberg-valence interactions¹⁹ among the N_2^* levels, as evidenced by experimental measurements in a small fraction of the relevant levels.²⁰ Measurements have been made of the concentrations of $N(^2D)$ and $N(^2P)$ in the upper atmosphere,^{15,16} but many processes other than reaction (1) contribute to these observations.

The present measurements observe Reaction (1) in a crossed beam arrangement in which an electron beam intersects a fast beam of N_2 . The spatial and temporal separations of

the correlated pair of atomic products formed in the dissociation of a single N_2 molecule are explicitly measured to provide a direct measurement of the translational energy release W in Reaction (1). The measured translational energy release, in combination with the known energies of N_2^+ , also determines the electronic states of the dissociation products. Detection of charged products is explicitly excluded in the experiment, allowing the electron impact dissociation products of N_2 to be detected without contamination from dissociative ionization processes. Quantitative product detection further allows an independent measurement of the cross section for reaction (1) over the electron energy range of 18.5 eV to 148.5 eV.

EXPERIMENT

The experimental apparatus and measurement procedures have been described in detail for the electron-impact dissociation of CO_2^{23} and will be considered only briefly here. A fast (3-5 keV), collimated beam of N_2 molecules is created by near-resonant charge transfer neutralization of an N_2^+ beam and intersected at right angles by an electron beam within an interaction region defined by a narrow slit and a beam flag. Undissociated molecules are collected by the beam flag. If an N_2 molecule dissociates within this region and its fragments are produced with sufficient transverse velocity to escape collection by the beam flag, the correlated pair of fragments is detected by a position sensitive detector (PSD-C) which measures their radial (R) and temporal (Δt) separations.²⁴ This measurement specifies the center-of-mass translational energy released in the dissociation (W), i.e. the difference in energy between the dissociating molecular state and its atomic products at infinite separation:²⁵

$$W = \frac{E_0}{4L^2} \left[R^2 + \left(\frac{2E_0\Delta t}{M} \right)^2 \right] \quad (2)$$

Here, the translational energy of the fast N_2 beam, E_0 , is taken to be the energy of the N_2^+ precursor in the charge transfer, L is the distance between the point of dissociation of the N_2 molecule and the PSD-C, and M is the mass of the N_2 molecule.. These are taken to be constants

describing all dissociating N₂ molecules. The measurement further specifies the angular distribution of the fragments in the planes orthogonal to the detector. The fast N₂ beam flux is measured by a pyroelectric bolometer and the absolute collection efficiency of the PSD-C for dissociation fragments is calibrated. All charged particles are collected by a weak electric field in the region between the beam flag and the PSD-C; hence dissociative ionization products do not contribute to the present measurements.

As described previously,²³ the electron beam has a rectangular geometry and an energy spread of ~1.5 eV FWHM. Energy calibration of the electrons is made from the observed threshold for the ionization of Ar²⁶ and has an estimated accuracy of ± 1 eV. Overlap between the electron and neutral beams is controlled by physically translating the electron gun and electron collector as a unit. This capability allows distinction to be made between neutral fragments created by spontaneous or collisional dissociation of the N₂ in the region between the slit and the beam flag, and electron impact dissociation of N₂ within the electron beam. The gun translation further allows an accurate dissociation cross section to be measured without a specific determination of the form factor describing the overlap of the electron and neutral beams.

With the electron gun and the neutral beam aligned, overlap of the beams takes place within a $\Delta L = 2.6$ cm interval along the neutral beam flight path. Since it is not known *a priori* where along this interval a particular N₂ molecule dissociates to produce a detected pair of fragments, the value of W implied by Eqn. (2) can deviate from the true magnitude of the translational energy release by the factor

$$\frac{\Delta W}{W} = \frac{2\Delta L}{L} = 0.052. \quad (3)$$

This factor represents the effective translational energy resolution achieved by the PSD-C for the electron-impact dissociation fragments. Pressures within the interaction region were maintained at $<2 \times 10^{-8}$ Torr during the measurements.

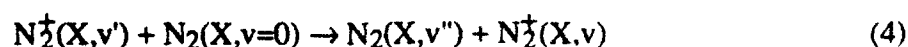
Two orientations of the electron beam velocity vector with respect to the PSD-C in combination with the fragment angular distribution observed by the PSD-C are required to define the full angular distribution of the electron-impact dissociation fragments. In the present measurements, these distributions are found to be isotropic within the center-of-mass frame of the N_2 at electron-impact energies ≥ 28.5 eV. At lower electron energies, the flux of fragments dispersed in both energy release and angle was too small for a detailed angular distribution to be determined. In interpreting the present data, we presume that this distribution remains isotropic at lower electron energies.

The state distribution of the fast N_2 beam at the time of electron impact is primarily dependent on the distribution in the N_2^+ precursor. Measurements were made for the N_2^+ produced in two different ion sources: a hollow cathode discharge source²⁷ (HC) and an electron-impact ionization source²⁸ (EI). The EI source was operated with low pressure ($\sim 10^{-4}$ Torr) N_2 gas and 100 eV ionization energy. Electron impact on N_2 at this energy populates three electronic states of N_2^+ : $X^2\Sigma_g^+$, $A^2\Pi_u$, and $B^2\Sigma_u^+$ with relative abundances of 0.5, 0.4, and 0.1 respectively.⁴ The B state is short-lived¹³ and radiates primarily into the $X^2\Sigma_g^+$ state inside the ion source volume. However, the A state is relatively long lived, with vibrationally-dependent lifetimes²⁹ ranging from 16.0 μ s in $v=0$ to 7.6 μ s in $v=7$, and radiates into the X state throughout the 6.4 μ s flight time between the ion source and the charge transfer cell. The population distribution in the N_2^+ beam at the time of charge transfer is estimated²³ using the ionization Franck-Condon factors for the initial vibrational distribution in each of the N_2^+ electronic states and Einstein A factors for the radiative decay into the ion ground state, both taken from the recent evaluation of Gilmore et al.²⁹ These predict 76% of the ion population in the $X^2\Sigma_g^+$ state, 80.6% of which is in $v=0$, 13.9% in $v=1$, and the remainder in higher levels. The remaining 24% of the ion beam resides in the A state, 93% of which is distributed among $0 \leq v \leq 3$.

In the hollow cathode discharge in N_2 gas at pressures in the range of 0.5 - 1.0 Torr, the nascent ionization products are subject to numerous low energy ion molecule reactions before

leaving the source. Successive charge transfer reactions, in particular, lead to a net electronic and vibrational relaxation of the molecular ions into their ground state. This has been verified experimentally^{28,30} in the case of O_2^+ and H_3^+ production and is expected to also be the case for N_2^+ . It is anticipated that >90% of $N_2^+(HC)$ populates the $X^2\Sigma_g^+(v=0)$ level.

The product distributions formed in the charge-transfer neutralization of N_2^+ at keV energies in N_2 gas are governed by the Franck-Condon factors for the ionization/recombination transitions in the exchange and by a propensity to retain thermoneutrality in the reaction for production of the forward scattered products. For the symmetric charge exchange reaction:



the partial cross sections have been calculated^{31,32} for specific values of v' and v'' . These predict that neutralization of $N_2^+(HC)$ will produce a fast N_2 beam with ~90% of its population in $X^1\Sigma_g^+(v=0)$. For the case of $N_2^+(EI)$, reaction (4) is expected to yield significant populations in both $v=0$ and $v=1$ of $X^1\Sigma_g^+$. However, this distribution is augmented by both symmetric and asymmetric charge transfer channels from the large fraction of $N_2^+(A)$ in the beam, which will undoubtedly yield a higher degree of vibrational excitation, extending at least to $v''=5$, in the product N_2 beam. However, the contribution of this vibrational excitation to the final beam depends critically on the relative charge transfer cross sections of $N_2^+(X)$ and $N_2^+(A)$ with N_2 , since $\leq 10\%$ of the N_2^+ beam is actually neutralized under the conditions of the experiment. A smaller relative charge transfer cross section for $N_2^+(A)$ in N_2 was indicated by the experimental measurements of Flannery et al.³¹ This is consistent with the fact that Reaction (4) involves the capture of an electron into the $3\sigma_g$ orbital of the N_2^+ core, whereas neutralization of $N_2^+(A)$ involves capture into the $1\pi_u$ orbital. Preferential capture into the $3\sigma_g$ orbital of O_2^+ is found to dominate in $O_2^+ + Cs$ reactions.³³ Thus, vibrational populations in $v''>1$ of the N_2 beam formed from $N_2^+(EI)$ should not exceed 24% of the beam, and will likely comprise a substantially smaller fraction of the beam population.

RESULTS

Fragment Energy Distributions

Dissociation of N_2 is found to occur not only as a result of electron-impact excitation, but also from the unimolecular dissociation of excited states populated during production of the fast N_2 beam. Representative distributions of fragment translational energy release (W) observed for a 3000 eV N_2 beam are shown in Fig. 1. In accumulating these distributions, the value of W was calculated from Eqn. (2) given the observed values of R and Δt of each detected dissociation fragment pair, assuming a fixed value for L corresponding to the distance from the center of the electron beam to the detector, and assuming an N_2 beam energy E_0 equal to the acceleration potential of the N_2^+ precursor. Based on this calculated value of W and the position of the electron beam relative to the N_2 beam, the event is binned into one of two sets of 1024 equally-spaced W intervals in the range $0 \leq W \leq 5.0$ eV. The histograms represented by the solid lines in Fig. 1 were obtained with the electron beam intersecting the N_2 beam, while those represented by discrete points were observed when the electron beam was positioned such that no intersection of electrons with the N_2 beam was possible. These distributions are uncorrected for the collection efficiency of the apparatus, which produces the apparent cut off in fragment intensity near $W = 0.2$ eV. They reflect N_2 dissociation products that were formed somewhere within the 18 cm long interaction region defined by the slit and the beam flag (see Fig. 1 of Ref. 23), i.e., to dissociations that occurred during the interval 2.7 - 4.0 μs after the charge transfer formation of the N_2 . The distributions are also not corrected for resolution, Eqn. (3), which for $\Delta L = 18$ cm is significantly degraded for dissociation processes that occur throughout this region ($\Delta W/W = 0.37$). The upper distributions in Fig. 1 are obtained from an N_2 beam formed from $N_2^+(EI)$ with a total accumulation time of 4.6 hours, equally divided between electron beam intersection and nonintersection using a 1.1 mA beam of 48.5 eV electrons and an N_2 beam flux of 4×10^9 s $^{-1}$ in the interaction region. The lower set of distributions in Fig. 1 were observed with the N_2 beam

formed from $N_2^+(HC)$. These spectra were acquired over a longer time interval and at a lower electron energy (30 eV) and current, but are scaled in the figure to the same product of N_2 beam flux and accumulation time as is appropriate for the upper distributions.

Spontaneous Dissociation Fragments. Dissociation of N_2 in the absence of electron beam interaction represents a rather substantial background to observing the N_2 electron impact dissociation products, indicated by the small intensity difference between the solid lines and the dots in Fig. 1. Under the conditions of the present measurements, the background dissociation represented $> 95\%$ of the observed fragmentation. This background is independent of pressure within the interaction region, suggesting that it arises from unimolecular dissociation of electronically excited N_2^* molecules in the beam. The structure in the W distribution of this background, reflecting the energetic locations of the dissociating N_2^* electronic states relative to their separated atoms, appears quite similar for both $N_2^+(EI)$ and $N_2^+(HC)$ precursors, qualitatively suggesting that essentially the same dissociating N_2^* states are formed. However, the relative intensities of specific features are substantially greater when the N_2^+ is produced by electron impact, presumably reflecting an increased cross section for their charge transfer formation from the $A^2\Pi_u$ state. Furthermore, the overall intensity of spontaneous dissociation is greater in the N_2 beam formed from the $N_2^+(EI)$ precursor, representing a fractional decay of 5×10^{-6} of the N_2 beam flux within the interaction region, compared with a fractional decay of 2×10^{-6} for N_2 formed from $N_2^+(HC)$. Explicit identification of the dissociating N_2^* states solely on the basis of these W distributions is difficult because of the very poor resolution, $\Delta W/W \sim 0.37$, that accompanies the very long region over which products are collected, and is beyond the scope of the present paper. However, fragments produced in the region near $W = 2$ eV have been optically identified as arising from predissociation of the metastable $a''^1\Sigma_g^+(v=0)$ level.³⁴ Given the known lifetime³⁵ of this state (3.49 ± 0.10 μ s) and the range of flight times between the charge transfer cell and the interaction region, we can estimate the concentration of $a''^1\Sigma_g^+(v=0)$ in the nascent N_2 beam to be approximately 10 ppm from the observed flux of fragments. Such a

small population would be consistent with the fact that a'' formation by charge transfer in N_2 is approximately 12 eV nonresonant. Lifetimes of the other states contributing to the spontaneous background dissociation are not known, but the formation of these states would also be highly nonresonant; hence it is reasonable to assume that their fractional concentration in the N_2 beam is also quite small.

Electron-Impact Dissociation Fragments. Despite the relatively high flux of spontaneous dissociation fragments, the W distribution of the electron-impact dissociation process, Eqn. (1), can be obtained from a direct subtraction of the nonintersecting W distribution from the distribution obtained with the electron beam intersecting the N_2 beam. These distributions, now corrected for the collection efficiency of the apparatus and binned into one-fifteenth fewer W intervals to minimize the statistical error introduced by the subtractions, are shown in Figure 2. The statistical error associated with each binned intensity is represented by its error bar in the figure. Fragment intensities within each bin are connected by a solid line to assist a visual identification of the fragment intensity in adjacent W bins. It should be noted that the size of each bin in the distribution exceeds the nominal resolution of the apparatus for energy releases $W < 1.2$ eV, as indicated by Eqn. (3). The true collection efficiency for fragments produced with $W < 0.5$ eV is strongly dependent on the precise alignment of the beam collection flag with the N_2 beam. Error bars given for those points in the distribution at these low values of W may therefore not fully reflect the actual magnitudes of the errors. Because of the relatively large spontaneous dissociation background, the statistical errors throughout the distribution are quite large. Nevertheless, a clear pattern of structure appears in the distributions that is reproducible and varies little with changes in electron-impact energy, or with the choice of bin size. This is indicated by the three distributions shown in Fig. 2.

The top and center distributions in Fig. 2 are observed for an N_2 beam produced from $N_2^+(HC)$ with electron impact energies of 28.5 eV and 48.5 eV, respectively. The bottom distribution is obtained at an electron impact energy of 48.5 eV for the N_2 beam produced from

$N_2^+(EI)$. It can be seen that for each of these distributions, the highest fragment intensities are produced in two peaks centered near $W \sim 0.8$ eV and $W \sim 1.1$ eV. Substantial fragmentation also occurs at lower energy releases and for energy releases $W < 2.4$ eV. At higher values of W , the fragmentation intensity is much smaller, despite the fact that the sensitivity of the apparatus is quite uniform for fragments produced with energy releases in the range $1 \text{ eV} \leq W \leq 3 \text{ eV}$. The fragment distributions shown for the two electron energies in Fig. 2 are also characteristic of those observed at higher electron impact energies. At electron energies below ~ 25 eV, it was not possible to obtain a statistically significant distribution of fragment flux dispersed among a useful number of W bins, due to the decrease in both electron beam intensity and dissociation probability with decreasing electron energy.

As noted above, fragmentation in the range of $0.5 \leq W \leq 1.2$ eV groups into at least two peaks which are quite narrow. Such a distribution is characteristic of the predissociation of discrete energy levels in the N_2 , rather than the result of an electron-impact excitation to a dissociative continuum. Predissociation is also found to characterize the fragment energy distributions observed in the electron-impact dissociation of the isoelectronic CO molecule.²³ Despite the rather large error bars, the $W \sim 1.1$ eV peak is clearly narrower than that centered near $W \sim 0.8$ eV and has a peak intensity comparable to or smaller than the $W \sim 0.8$ eV peak for the N_2 beam formed from $N_2^+(HC)$. There is also a suggestion of subsidiary structure in the $W \sim 0.8$ eV peak. The variation in fragmentation intensity with W is more regular at the higher energy releases. However, the degradation in energy resolution with increasing energy does not allow a clear distinction between the production of these fragments by continuum dissociation or by the predissociation of several N_2 energy levels. At fragment energy releases below $W \sim 0.5$ eV, the fragment distributions are less reproducible, for the reasons given above and show no clear evidence of structure. The data do indicate, however, that the flux of fragments in this region is consistently higher from beams produced from the neutralization of $N_2^+(HC)$ than from

$N_2^+(EI)$, although in each case, these low energy fragments represent a relatively small fraction of the total dissociation products.

Dissociation Cross Section

The total dissociation cross section σ_{dis} is obtained from the relation

$$\sigma_{dis} = \frac{N^* u v_n \eta e}{\xi \chi I_e I_{fc}} \quad (7)$$

as discussed in Ref. 23. Here, I_{fc}/η is the N_2 beam flux, I_e is the electron beam current, v_n is the velocity of the N_2 beam, taken here to be the velocity of the N_2^+ precursor, e is the electron charge, ξ is the coincidence efficiency of the PSD-C, and χ is the collection efficiency of the PSD-C, i.e., the fraction of the total cm distribution of the dissociation fragments that is viewed by the detector, and N^* is the total accumulated number of electron impact dissociation pairs as the electron beam is slowly translated completely across the N_2 beam at a constant velocity u . Each of these terms is separately measured with the exception of the PSD-C collection efficiency χ , which is an explicit function of the N_2 beam energy, fragment energy release W , and the center of mass angles Θ and Φ defining the ejection of the fragments orthogonal to the plane of the PSD-C and within the plane of the PSD-C, respectively. Only Θ is explicitly measured by the PSD-C for each dissociation event, whereas the Φ distribution must be inferred from a comparison of the total apparent cross sections measured at two different orientations of the electron beam with respect to the active axis of the PSD-C. Thus χ makes the single largest contribution to the uncertainty in σ_{dis} . Finally, an error is introduced into the cross sections by the present inability to observe fragments produced with $W < 0.3$ eV. As can be seen in Fig. 2, there is appreciable fragment flux at values of W just above this limit, particularly when the N_2 beam is formed from $N_2^+(HC)$. However, as discussed in the next section, there is no reason to believe that very low energy releases would dominate the electron-impact dissociation for this molecule. For the present measurements, we approximate this unobserved flux by extrapolating the average fragment intensity observed for the interval $0.3 \leq W \leq 0.5$ eV to $W=0$. This introduces

an increase in fragment flux beyond that actually observed of roughly 5%. The total absolute uncertainty in the dissociation cross section, taken as the rms sum of the uncertainties in Eqn. (7), is $\pm 28\%$.

The absolute cross section for electron-impact dissociation of N_2 , reaction (1), was measured over the electron energy range of 18.5 to 148.5 eV using an N_2 beam formed from $N_2^+(HC)$. The measured values, in units of megabarns ($1 \text{ Mb} = 1 \times 10^{-18} \text{ cm}^2 = 0.01 \text{ \AA}^2$) are shown by the solid points in Figure 3 and are given in Table I as a function of electron impact energy. The estimated absolute errors in these values are given in Table I and are represented by the bars in Fig. 3. Dissociation cross sections were also measured at several electron-impact energies using an N_2 beam formed from the $N_2^+(EI)$ precursor. No detectable systematic difference in the cross section values from those given in Table I was observed.

The dissociation cross section of N_2 has also been determined by Winters⁹ from measurements of the effective pumping speed within a constant volume of N_2 gas that is produced by the adsorption of the N-atom dissociation products on nickel and molybdenum surfaces following electron impact. This measurement included not only electron-impact dissociation, Reaction (1), but also dissociative ionization:



However, the cross section for Reaction (5) has been independently measured by several groups^{5,6,13} as a function of electron energy. If we subtract this dissociative ionization cross section, using the recommended values of Itikawa et al.,¹³ from the dissociation cross section of Winters, the cross section for Reaction (1) is obtained. These values are shown by the open circles in Figure 3 and are also listed in Table I. The error limits given in Figure 3 are the absolute errors of $+10\%/-20\%$ estimated by Winters (but shown in the figure as $\pm 20\%$), and do not include the small additional errors associated with the dissociative ionization cross section. A comparison of the solid and open circles in Fig. 3 shows that the present measurements lie

uniformly below the implied measurements of Winters. However, it is also seen in this figure that with few exceptions, both sets of measurements overlap within their stated error limits. One exception is the cross section at an electron impact energy of 18.5 eV, where the present measurement has a value of roughly 32% that of the interpolated value of Winters. However, in this region, the cross section changes rapidly with electron energy, hence systematic errors in the electron energy of the two data sets (± 1 eV in the present measurements) will appear as a difference in cross section magnitude. Also, the angular distribution of fragments could not be explicitly determined in the present measurements at this low electron energy; rather it was assumed that it remained constant from observations at higher energies. This introduces an increased uncertainty because molecular alignment will likely be enhanced as the excitation threshold is approached. Since the dissociation cross section for N_2 obtained in the present measurements and the value of this cross section implied by the measurements of Winters are reasonably consistent within their state error limits, the best estimate for the dissociation cross section of N_2 would be obtained from an average of the two sets of measurements.

Neither the present measurements nor the measurements of Winters gives a good definition of the variation of the dissociation cross section with electron energy in the immediate region of the dissociation threshold. However, detailed relative cross sections in this region have been reported by Winters, Horne, and Donaldson,³⁶ who also used a surface adsorption measurement technique, and also by Niehaus.¹⁰ The latter work utilized a pair of modulated electron beams and mass spectrometer detection to observe the neutral products of electron impact dissociation. A significant variation of this method has recently been used³⁷ to determine the electron impact dissociation cross section of CH_3 . The sensitivity of Winters et al.'s experiment to variations in the fragment angular distribution near threshold should be minimal, but that of Niehaus is unclear. Nevertheless, Zipf³⁸ has noted that the relative cross sections of Winters et al. and Niehaus are in good agreement, suggesting that these relative cross sections are reliable.

An improved representation of the cross section for electron-impact dissociation of N_2 can be obtained by taking a weighted average of the present absolute cross section values and those of Winters⁹ and extrapolating this average to threshold electron impact energies using the relative pumping speed measurements of Winters, Horne, and Donaldson.³⁶ Derived values for this cross section are given in Table II for electron energies between 10 eV and 200 eV and are shown by the solid line in Figure 3.

DISCUSSION

Because of the importance of N_2 in the earth's atmosphere, where it is subject to electron impact by ambient photoelectrons and auroral electrons, the excitation and dissociation of N_2 has received considerable attention. Excitation processes have been particularly well characterized over the past 30 years using the technique of electron energy loss spectroscopy. Although discrepancies exist in the excitation cross sections of particular electronic states which are being addressed even at the present time,³⁹ the identification and relative importance of most N_2 electronic states excited by electron impact is reasonably well understood. The ultimate fate of these excited states, however, is considerably less clear. Despite a rather substantial bond dissociation energy⁴⁰ of 9.7537 ± 0.0011 eV, most of the electronic states in N_2 lie above the lowest dissociation limit $N(^4S) + N(^4S)$. Thus, the possible decay channels of the excited states includes not only radiative cascade to lower states, but also predissociation to atoms and, above 15.580732 ± 0.000009 eV, ionization.⁴¹ The problem is more complex yet, when one considers that for 50 eV electron impact, at least 80% of the electronic excitation to states above the first dissociation limit populates the bound states $b^1\Pi_u$, $b'^1\Sigma_u^+$, $c^1\Pi_u$, $c'^1\Sigma_u^+$, $o^1\Pi_u$, $e^1\Pi_u$, and $e'^1\Sigma_u^+$ states.⁸ All vibrational levels of these states lie above the second N_2 dissociation limit, $N(^2D) + N(^4S)$ at 12.1373 eV, and many of their levels also lie above the third limit, $N(^2P) + N(^4S)$ at 13.329 eV. Thus predissociation to two or three dissociation limits can compete with allowed optical fluorescence into the ground $X^1\Sigma_g^+$ state or the $a^1\Pi_g$ state. In addition, the b and b' valence states are strongly mixed with the c , c' , o , e , and e' Rydberg states.¹⁹ This mixing

produces large irregularities in the spacings of the rovibrational levels and in transition intensities. Furthermore, it produces irregularities in both predissociation rates and product branching ratios since the mixing implicitly modifies the coupling to the dissociation continua.

Dissociation of N_2 has been considered in detail by Zipf and McLaughlin.¹¹ They measured the cross sections for the emission of photons from these states as a function of electron energy. By subtracting the emission cross sections from the excitation cross sections derived from electron scattering data,¹⁵ they arrived at state specific dissociation cross sections and predissociation branching ratios (η_{dis} , the ratio of the predissociation cross section to the excitation cross section) for individual vibrational levels in the N_2 states. Their data, summarized by electronic state for 200 eV electron impact, is given in Table III. More recently, Ajello et al.¹² have measured the emission cross sections at higher resolution utilizing the recent reevaluation⁴² of the Lyman- α cross section which serves as the vuv emission standard in both their and earlier work. They also derive cross sections for the predissociation of individual vibrational levels by subtracting the measured emission cross sections from electron impact excitation⁸ cross sections. Their results for the N_2 states, as summarized by James et al.⁴³ for 100 eV electron impact, are also given in Table III, as are the excitation cross sections for these states at 50 eV given by Trajmar et al.⁸ A comparison of the measurements in Table III shows first that there is considerable variation in the values of the excitation cross sections assumed for the various states. This variation is even more pronounced when one considers that the cross sections for each of these states should decrease as the electron energy increases from 100 eV to 200 eV. Despite this variation, there is a remarkable degree of consistency in the implied predissociation branching ratios (η_{dis}) for most of the states. The exception is the implied branching ratio for the c' state, which Zipf and McLaughlin find to be ~28% predissociated, while Ajello et al. find no evidence of predissociation, implying < 10% predissociation considering the nominal accuracy of the emission cross sections. As pointed out by Ajello et al.,

this disagreement would be even greater (55% vs <10%) if the Zipf and McLaughlin emission cross sections were rescaled to the new value for the Lyman- α standard.

Apart from the seven perturbed electronic states, excitation of several other electronic states that lie above the lowest dissociation limit is known to accompany electron impact on N_2 . In particular, the $a^1\Pi_g$, $w^1\Delta_u$, $C^3\Pi_u$, $E^3\Sigma_g^+$, $a''^1\Sigma_g^+$, $G^3\Pi_u$, and $F^3\Pi_u$ states have measurable excitation cross sections.⁸ The C state however, does not dissociate for levels that are significantly populated by electron impact,⁴⁴ and the strongly populated levels in both the a'' and E states are relatively long-lived.^{35,45} Both the a and w states are known to dissociate⁴⁴ in those levels, $v>6$ and $v>4$ respectively, that lie above the $N(^4S) + N(^4S)$ limit. Ajello and Shemansky⁴⁶ estimate that dissociation of the a state amounts to 13% of its excitation cross section and give values for the dissociation cross section of this state of 1.54, 0.77, and 0.39 Mb at electron energies of 50, 100, and 200 eV, respectively. The excitation cross section of the w state is large for threshold electron energies, but decreases rapidly with higher electron energies.⁸ Its contributions to dissociation would be negligible at the higher electron energies. Emission has never been detected from either the G or F states, hence dissociation of these states is probable. Total excitation cross sections⁸ for these states are 1.7 Mb and 1.0 Mb, respectively, at 60 eV.

Predissociation of a rovibrational level produces a discrete release of translational energy to the fragment atoms which must be accounted for in describing electron energy deposition in N_2 . Furthermore, both the translational energy and the electronic state of the dissociation fragment can affect its subsequent reactions. The magnitude of the translational energy release depends only on the energy of the predissociated level above the relevant dissociation limit of the molecule. As discussed above, there are only three possible dissociation limits that can be populated from the b, b', c, c', e, and e' states. If fragments are formed at each of these limits, then one predissociated level can produce as many as three discrete translational energy releases which are widely separated in energy. Relative to the translational energy release for the

production of ground state atoms $N(^4S) + N(^4S)$, the translational energy release for production of $N(^2D) + N(^4S)$ would be 2.384 eV lower, while that for production of $N(^2P) + N(^4S)$ would be 3.576 eV lower, given the known⁴⁷ energy separations of the atomic states.

The fragment energy release distributions observed in the present work from electron impact dissociation of N_2 provide a direct measure of the dissociation products from the ensemble of electronic states and rovibrational levels formed in the electron impact. Given that the relative predissociation cross sections for the dominant electronic states excited by electron impact are known (Table III), the distribution of fragment energy release accompanying their predissociation should be predictable with only a presumption as to which of the three possible dissociation limits are populated. Predicted fragment energy release distributions are shown in Fig. 4 together with observed distribution for 50 eV electron impact. The predicted distributions represent the partial dissociation cross sections for 100 eV electron impact of Ajello et al.¹² and James et al.⁴³ for the c' , c , b' , b , and o states, and of Ajello and Shemansky⁴⁶ for the a state. The partial dissociation cross sections for the e and e' states are the 200 eV partial excitation cross sections of Zipf and McLaughlin¹¹ and those for the G and F states are the 50 eV integral excitation cross sections of Trajmar et al.⁸ distributed over vibrational envelopes characteristic of the $N_2^+ X^2\Sigma_g^+$ and $A^2\Pi_u$ states, respectively. The energy of each point in the distribution represents a vibrational energy above the specified dissociation limit. An explicit consideration of rotational structure would smear these points to higher energy by 0.04 to 0.08 eV whereas apparatus resolution would broaden the rotational distribution by Eqn. (3). The center distribution presumes that all predissociation, with the exception of the a state, produces $N(^2D) + N(^4S)$, while the bottom distribution is for production of $N(^2P) + N(^4S)$. In all cases, only the lowest dissociation limit is accessible in the predissociation of the a state. The $N(^4S) + N(^4S)$ and $N(^2D) + N(^2D)$ distributions are not shown. The former can be obtained by shifting all points in the center distribution, with the exception of those for state a , by +2.746 eV. The latter can be obtained by shifting the value of W for all points in the bottom distribution, also with the

exception of a, by -1.191 eV. Very few of the known predissociated levels lie above the $N(^2D) + N(^2D)$ limit.

A comparison of the experimental fragment energy distribution with the calculated distributions shows a strikingly good agreement with that calculated for $N(^2D) + N(^4S)$ production. In particular, the two peaks in the experimental distribution match quite precisely with the production of fragments to this limit from $c(v=0)$ and $c(v=1)$, shown as the open squares in the center distribution with $W = 0.797$ eV and $W = 1.071$ eV, respectively. This association is made more compelling by the fact that vibrational excitation in the N_2 beam produced an enhanced intensity in the $W \sim 1.1$ eV peak, as was shown in Fig. 2. Furthermore a broadening of the lower W peak correlates with significant predissociation expected from $v=2,3,4$ of the b state. Finally, the sharp decrease in the experimental fragment intensity for $W > 2.4$ eV is also matched by the relative predissociation cross sections, where the contribution here is largely from very high vibrational levels of the b' state.

The very good overall agreement between the center distribution and the experimental spectrum in Fig. 4 provides a clear indication that production of $N(^2D) + N(^4S)$ is the dominant dissociation channel in N_2 dissociation. Furthermore the experimental spectrum specifically excludes any significant production of $N(^4S) + N(^4S)$ dissociation products, except those arising from high vibrational levels of the a state. Of the remaining electronic states, the lowest energy level lies 2.746 eV above this dissociation limit. It can be seen from the experimental spectrum that very few fragments are produced at this or higher values of W . Finally, the experimental distribution clearly allows production of $N(^2P) + N(^4S)$ as a minor dissociation channel in the predissociation. As can be seen in Fig. 4, production of fragments at this limit will primarily contribute to the fragment energy distribution in the region near $W = 1$ eV and would not be distinctly resolved as a minor contribution to the experimental spectrum. Information on the relative contributions of the 2D and 2P predissociation channels could in principle be determined from a quantitative simulation of the experimental fragment distributions. However, such a

simulation is not attempted here. Rotationally resolved photofragment energy release studies have demonstrated that branching of the predissociation products between the 2D and 2P limits can be quite complex, as expected from the strong Rydberg-valence couplings, and must be considered on a level by level basis.²⁰ In particular, branching between these limits was shown to vary with rotational level for the $e'(v=0)$ state and with rotational level and parity for the $e(v=0)$ state. In contrast, the $b'(v=16,17)$ levels were found to exclusively (>95%) predissociate to the $^2D + ^4S$ limit, even though they lie more than 1 eV above the $^2P + ^4S$ dissociation limit. These b' levels correspond to the solid circles in the center distribution at $W = 2.091$ eV and 2.167 eV, respectively. Similar product branching determinations are in progress for the other N_2 states.³⁴

Another conclusion from the comparison in Fig. 4 is that predissociation of bound N_2 states, as implied by the absence of significant continua in electron energy loss excitation spectra, makes the dominant contribution to the electron impact dissociation of N_2 . Predissociation is consistent with the observed lack of sensitivity of the dissociation cross section to anticipated changes in the vibrational distribution within the N_2 beam. Furthermore, the overall pattern of predissociation among the N_2 states derived by Ajello et al.¹² and by James et al.⁴³ appears to be in rather good agreement with the observed fragment energy distributions. One might therefore expect that the sum of the partial dissociation cross sections of Ajello et al. and James et al. would approach the total dissociation cross sections determined in the present work and by Winters.⁹ As shown in Table III, the sum of the dissociation cross sections for the $b, b', c, c', o,$ and a states is 46.7 Mb with an absolute uncertainty of order 25%. Excitation and complete dissociation of the $e, e', G,$ and F states would account for an additional ~ 6 Mb for the dissociation cross section to give a nominal total of 53 ± 18 Mb, where the error limits allow a factor of two uncertainty in the contributions of the latter states. The total dissociation cross section implied by the present measurements (Table I) is 85 ± 24 Mb. Thus these two sets of measurements are consistent within their nominal absolute uncertainties. However, the total

dissociation cross section of Winters, $145 \pm 15/-29$ Mb, clearly is inconsistent with the summed partial dissociation cross sections, even allowing for an additional error contribution from uncertainty in the dissociative ionization correction. If we presume that both the Winters cross section and the summed partial dissociation cross sections are accurate within the stated limits, this would imply that dissociation channels, beyond those considered in Fig. 4, must contribute an additional >45 Mb to the dissociation, i.e., an increase of roughly a factor of two in both density and magnitude over the partial cross sections shown in Fig. 4. Although such a possibility cannot be excluded entirely, it does not seem reasonable given the good overall agreement shown in Fig. 4. More likely the discrepancies reflect the combined systematic errors in all three absolute cross sections. This would support the suggestion in the previous section that a weighted average of the total dissociation cross section determined by Winters and that determined in the present work will likely provide the most accurate measure for N_2 dissociation.

SUMMARY

Absolute dissociation cross sections and translational energy release distributions are measured for electron impact on N_2 in a fast molecular beam. The dissociation is observed without contamination of the products by the dissociative ionization channel. A comparison of the observed fragment distributions with the known energies and partial dissociation cross sections of excited levels of N_2 indicates that predissociation to form $N(^2D) + N(^4S)$ products is the dominant dissociation mechanism. Production of $N(^4S) + N(^4S)$ and $N(^2P) + N(^4S)$ as minor dissociation channels cannot be excluded on the basis of the present measurements.

Absolute cross sections measured in the present experiment are found to be consistent with those previously determined by Winters. A combination of the present values with previous measurements of the absolute and relative dissociation cross sections yields a set of recommended values for the N_2 dissociation cross section over the electron energy range from 10 eV to 200 eV. Given the vast differences in technique among the various measurements, the recommended values (Table II) should be considered highly reliable within their stated absolute uncertainties.

ACKNOWLEDGMENTS

This research was supported by the U. S. Air Force Wright Laboratory under contract No. F33615-85-R-2560.

REFERENCES

1. J. L. Fox and G. A. Victor, *Planet. Space Sci.* **36**, 329 (1988); D. F. Strobel, R. R. Meier, M. E. Summers, and D. J. Strickland, *Geophys. Res. Letters* **18**, 689 (1991).
2. D. Rapp and P. Englander-Golden, *J. Chem. Phys.* **43**, 1464 (1965).
3. P. B. Armentrout, S. M. Tarr, A. Dori, and R. S. Freund, *J. Chem. Phys.* **75**, 2786 (1981).
4. J. P. Doering and L. Goembel, *J. Geophys. Res.* **96**, 16025 (1991).
5. D. Rapp, P. Englander-Golden, and D. D. Briglia, *J. Chem. Phys.* **43**, 4081 (1965).
6. A. Crowe and G. W. McConkey, *J. Phys. B* **6**, 2108 (1973).
7. K. Kollmann, *Int. J. Mass Spectrom. Ion Phys.* **17**, 261 (1975).
8. S. Trajmar, D. F. Register, and A. Chutjian, *Phys. Reports* **97**, 219 (1983).
9. H. F. Winters, *J. Chem. Phys.* **44**, 1472 (1966).
10. A. Niehaus, *Z. Naturforsch.* **22a**, 690 (1967).
11. E. C. Zipf and R. W. McLaughlin, *Planet. Space Sci.* **26**, 449 (1978).
12. J. M. Ajello, G. K. James, B. O. Franklin, and D. E. Shemansky, *Phys. Rev. A* **40**, 3524 (1989).
13. Y. Itikawa, M. Hayashi, A. Ichimura, K. Onda, D. Sakimoto, K. Takayanagi, M. Nakamura, H. Nishimura, and T. Takayanagi, *J. Phys. Chem. Ref. Data* **15**, 985 (1986).
14. S. Solomon, *Planet. Space Sci.* **31**, 135 (1983).

15. J. Geiger and B. Schröder, *J. Chem. Phys.* **50**, 7 (1969).
16. G. Joyez, R. I. Hall, J. Reinhardt, and J. Mazeau, *J. Elect. Spectrosc. Rel. Phenom.* **2**, 183 (1973).
17. A. Chutjian, D. C. Cartwright, and S. Trajmar, *Phys. Rev. A* **16**, 1052 (1977).
18. P. Hammond, G. C. King, J. Jureta, and F. H. Read, *J. Phys. B* **20**, 4255 (1987).
19. D. Stahel, M. Leoni, and K. Dressler, *J. Chem. Phys.* **79**, 2541 (1983).
20. H. Helm and P. C. Cosby, *J. Chem. Phys.* **90**, 4208 (1989).
21. E. C. Zipf, P. J. Espy, and C. F. Boyle, *J. Geophys. Res.* **85**, 687 (1980).
22. D. W. Rusch and J.-C. Gerard, *J. Geophys. Res.* **85**, 1285 (1980).
23. P. C. Cosby, *J. Chem. Phys.* (submitted for publication).
24. H. Helm and P. C. Cosby, *J. Chem. Phys.* **86**, 6813 (1987).
25. D. P. deBruijn and J. Los, *Rev. Sci. Instrum.* **53**, 1020 (1982).
26. R. C. Wetzol, F. A. Baiocchi, T. R. Hayes, and R. S. Freund, *Phys. Rev. A* **35**, 559 (1987).
27. H. Helm, *Phys. Rev. A* **38**, 3425 (1988).
28. C. W. Walter, P. C. Cosby, and J. R. Peterson, *J. Chem. Phys.* **98**, xxxx (1993).
29. F. R. Gilmore, R. R. Laher, and P. J. Espy, *J. Phys. Chem. Ref. Data* **21**, 1005 (1992).
30. P. C. Cosby and H. Helm, *Phys. Rev. Letters* **61**, 298 (1988).
31. M. R. Flannery, P. C. Cosby, and T. F. Moran, *J. Chem. Phys.* **59**, 5494 (1973).
32. M. R. Flannery and T. F. Moran, *J. Phys. B* **9**, L509 (1976).

33. W. J. van der Zande, W. Koot, J. R. Peterson, and J. Los, Chem. Phys. Letters **140**, 175 (1987).
34. C. W. Walter, P. C. Cosby, and H. Helm, Bull. Am. Phys. Soc. **37**, 1099 (1992)
35. A. W. Kam and F. M. Pipkin, Phys. Rev. A **43**, 3279 (1991).
36. H. F. Winters, D. E. Horne, and E. E. Donaldson, J. Chem. Phys. **41**, 2766 (1964).
37. T. Nakano, H. Toyoda, and H. Sugai, Jap. J. Appl. Phys. **30**, 2908 (1991); *ibid.*, p. 2912.
38. E. C. Zipf, "Dissociation of Molecules by Electron Impact" in *Electron-Molecule Interactions and their Applications*, L. G. Christophorou, ed. (Academic Press, Orlando, 1984) V. I, Ch. 4.
39. J. M. Ratliff, G. K. James, S. Trajmar, J. M. Ajello, and D. E. Shemansky, J. Geophys. Res. **96**, 17559 (1991).
40. Y. Roncin, F. Launay, and M. Larzilliere, Phys. Rev. Letters **53**, 159 (1984).
41. K. P. Huber and Ch. Jungen, J. Chem. Phys. **92**, 850 (1990).
42. D. E. Shemansky, J. M. Ajello, and D. T. Hall, Ap. J. **296**, 765 (1985).
43. G. K. James, J. M. Ajello, B. Franklin, and D. E. Shemansky, J. Phys. B **23**, 2055 (1990).
44. A. Lofthus and P. H. Krupenie, J. Phys. Chem. Ref. Data **6**, 113 (1977).
45. R. S. Freund, J. Chem. Phys. **50**, 3734 (1969).
46. J. M. Ajello and D. E. Shemansky, J. Geophys. Res. **90**, 9845 (1985).
47. C. E. Moore, Nat. Stand. Ref. Data Ser., Nat. Bur. Stand. (U.S.) **34** (Sept. 1970).

Table I.

Cross sections (σ_{dis}) measured for the electron-impact dissociation of N_2 . The dissociative ionization cross section from Ref. 13 has been subtracted from the measured cross section of Ref. 9 to arrive at the values labelled Winters. Cross section units are $1 \text{ Mb} = 1 \times 10^{-18} \text{ cm}^2$.

Electron Energy (eV)	Dissociation Cross Section (Mb)		
	Present Measurements		Winters
	σ_{dis}	Uncertainty	σ_{dis}
18.5	17.4	11.4	54.2
23.5	66.5	22.0	98.5
28.5	80.7	24.7	121.3
38.5	86.5	29.0	139.9
48.5	101.7	29.5	143.3
73.5	95.5	25.2	146.0
88.5	84.0	25.1	150.2
148.5	90.2	27.2	127.2

Table II.

Recommended cross section for the electron-impact dissociation of N₂.
Cross section units are 1 Mb = 1×10^{-18} cm².

Electron Energy (eV)	Estimated Cross Section (Mb)	Probable Absolute Uncertainty (Mb)
10	0	-
12	1	-
14	4	-
16	20	-
18	36	18
20	52	20
25	87	17
30	104	22
40	115	26
50	123	21
60	123	24
80	120	30
100	116	30
125	110	22
150	104	18
175	99	-
200	95	-

Table III.

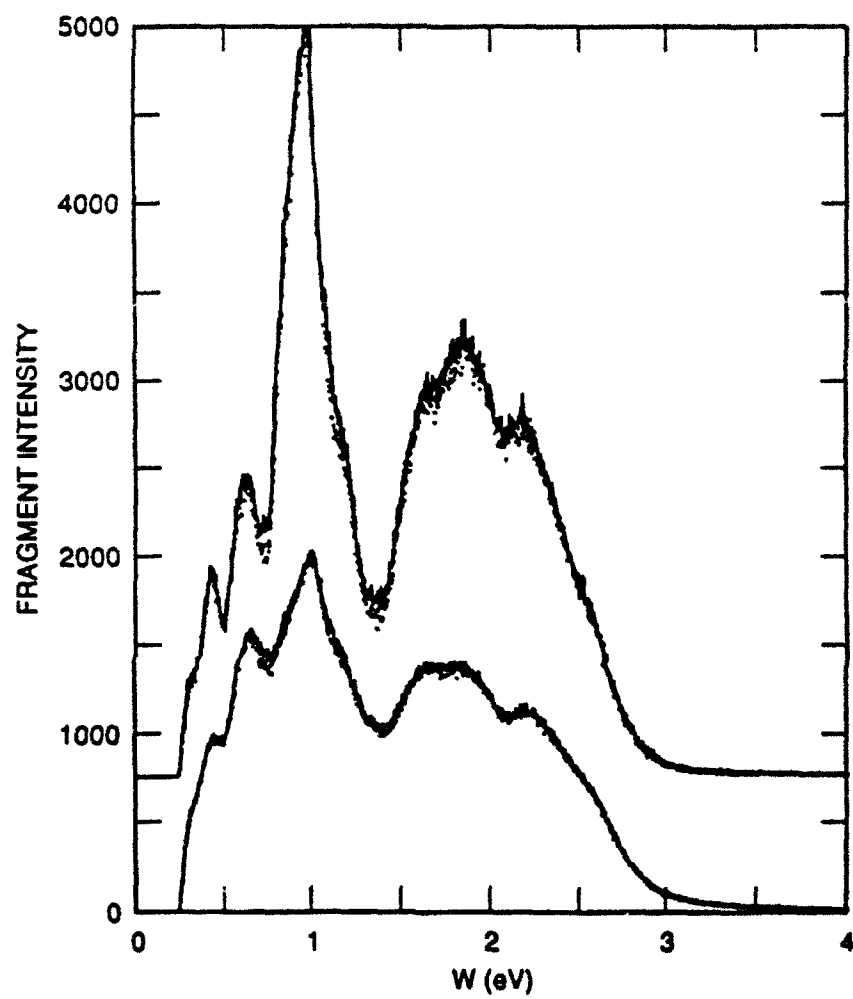
Partial excitation cross sections and dissociation fractions (η_{dis}) for the electronic states of N_2 .

State	Excitation Cross Section (Mb)			η_{dis}	
	Ref. 11 200 eV	Ref. 43 100 eV	Ref. 8 50 eV	Ref. 11 200 eV	Ref. 43 100 eV
$a^1\Pi_g$	-	6.2 ^a	2.9	-	0.12 ^a
$w^1\Delta_u$	-	-	0.7	-	-
$b^1\Pi_u$	20.7	12.1	17.8 ^b	0.97	0.95
$b'^1\Sigma_u^+$	17.1	12.8	10.3 ^b	0.83	0.84
$c^1\Pi_u$	12.0	16.1	8.7 ^b	>0.99	1.0
$c'^1\Sigma_u^+$	23.8	12.1	12.5 ^b	0.29	0.0
$o^1\Pi_u$	4.8	7.5	2.1 ^b	>0.99	1.0
$e^1\Pi_u$	2.0	-	-	>0.99	-
$e'^1\Sigma_u^+$	0.6	-	-	>0.99	-
$G^3\Pi_u$	-	-	2.3 ^b	-	-
$F^3\Pi_u$	-	-	1.2 ^b	-	-

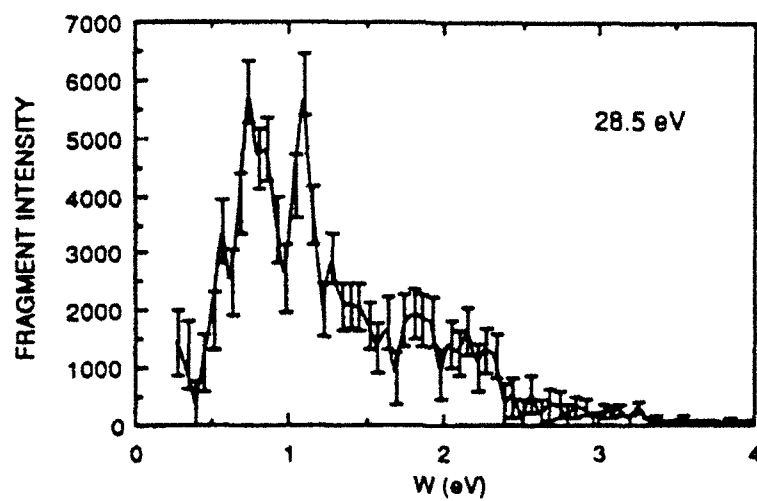
^a Reference 46^b Average of cross section values given at 40 eV and 60 eV.

FIGURE CAPTIONS

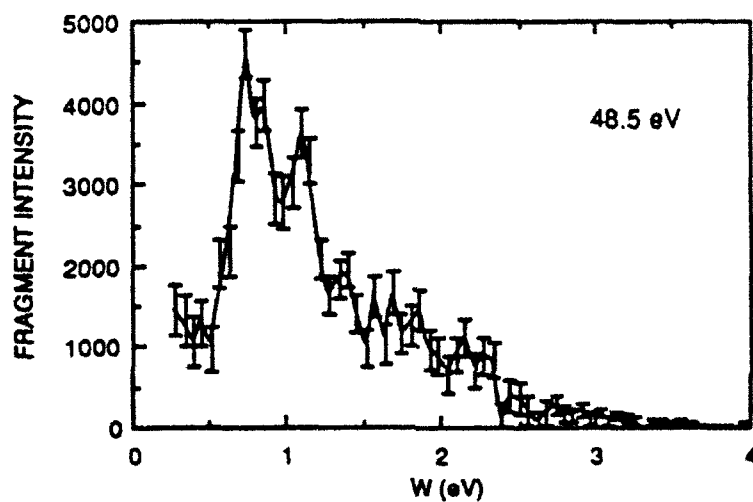
- Figure 1. Distribution of translational energy releases W observed for the dissociation of N_2 . The spectra are uncorrected for the variation in the collection efficiency of the apparatus with W . Distributions in the lower part of the figure are observed for an N_2 beam produced from neutralization of N_2^+ formed in the hollow cathode ion source. A low pressure electron-impact source was used to generate the precursor N_2^+ for the distributions in the upper part of the figure. Fragment distributions observed with the electron beam intersecting the N_2 beam are shown by the solid lines, while those observed with no intersection between the electron and N_2 beams are given by the points.
- Figure 2. Translational energy release distributions produced by electron-impact dissociation of N_2 . The distributions have been corrected for collection efficiency, but not for the variation in resolution with W [see Eqn. (3)]. Distributions at the top and center of the figure are observed for electron impact energies of 28.5 eV and 48.5 eV, respectively. The distribution at the bottom of the figure is observed for 48.5 eV electron impact on an N_2 beam with enhanced vibrational excitation. Statistical errors of the points in the three distributions are represented by the error bars. The solid lines are included only as a guide to interconnect discrete points in the distributions.
- Figure 3. Cross sections for electron-impact dissociation of N_2 [Reaction (1)]. Present measurements are given by the filled circles together with error bars indicating the estimated absolute uncertainty. The previous measurements of Ref. 9, corrected for dissociative ionization, are given by the open circles. The solid line connects the recommended values for the cross section listed in Table II.
- Figure 4. Observed and predicted translational energy release distributions in the electron impact dissociation of N_2 . The upper distribution is the translational energy release distribution observed for 48.5 eV electron impact. Distributions at the center and bottom of the figure are the partial dissociation cross sections for the vibrational levels of 10 predissociated electronic states of N_2 (see text and Table III) plotted as a function of energy relative to the $N(^2D) + N(^4S)$ dissociation limit (center) or the $N(^2P) + N(^4S)$ dissociation limit. The close correspondence between the top and center distributions indicates that $N(^2D) + N(^4S)$ are the dominant N_2 dissociation products.



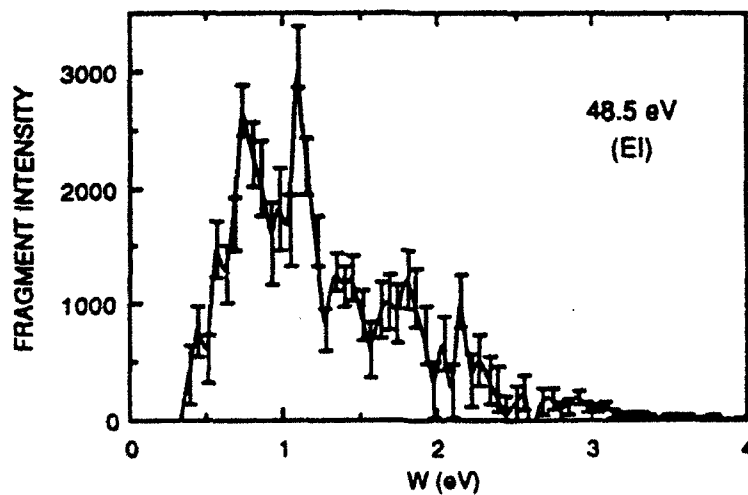
CAM-1147-18



(a)

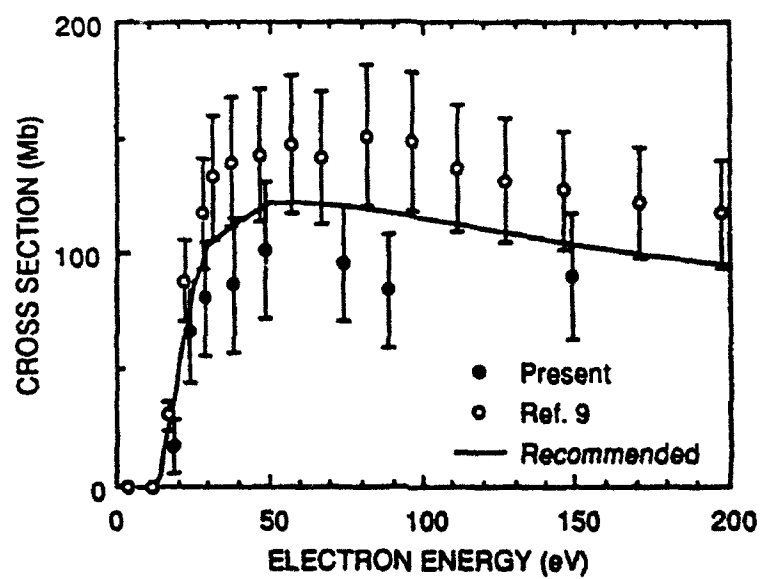


(b)

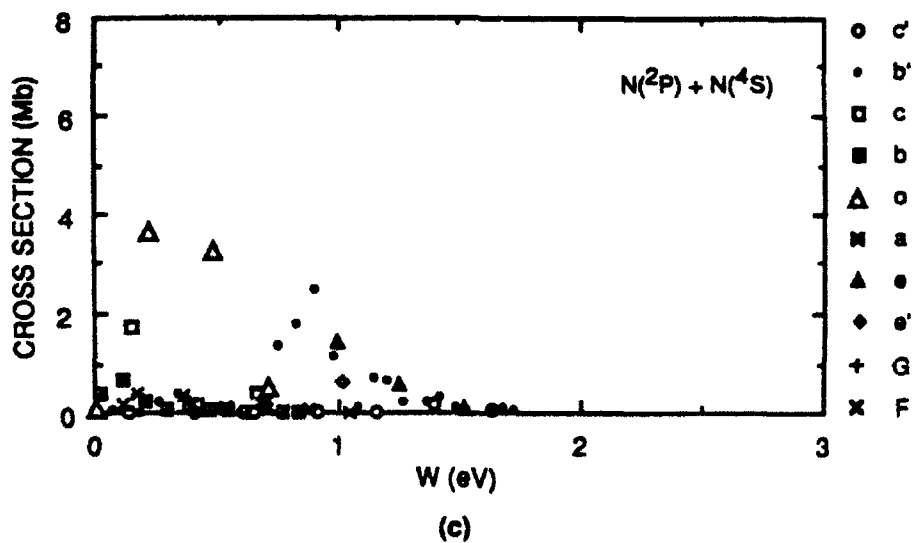
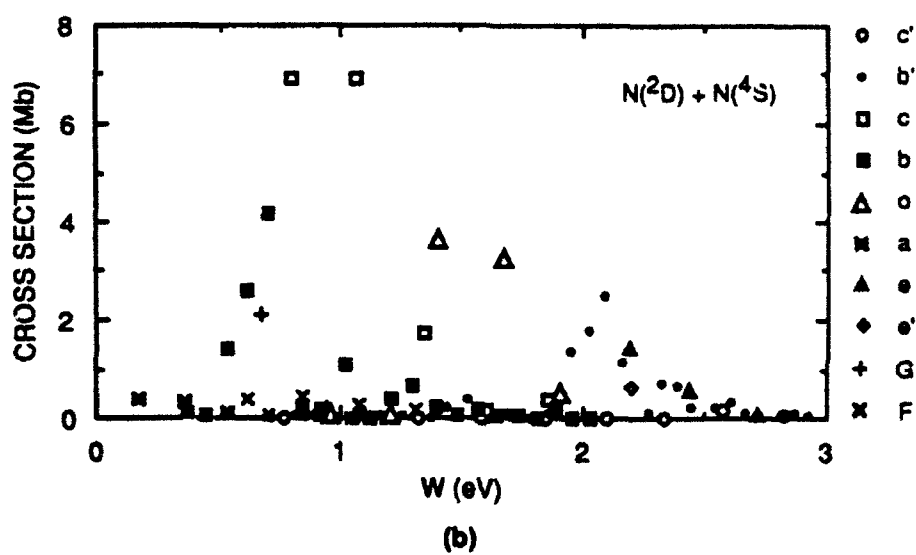
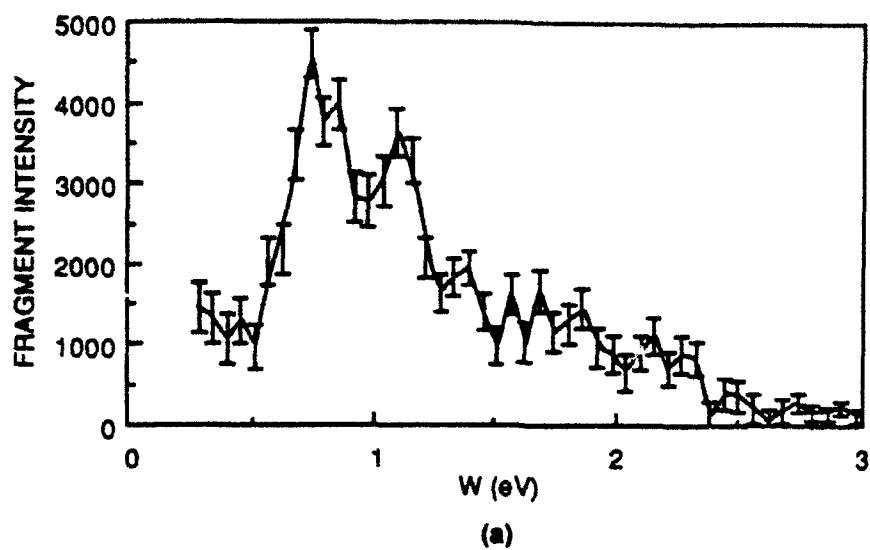


(c)

CAM-1147-17



CAM-1147-18



CM-1147-19

Appendix G

ELECTRON-IMPACT DISSOCIATION OF OXYGEN

ELECTRON-IMPACT DISSOCIATION OF OXYGEN

P. C. Cosby

Molecular Physics Laboratory
SRI International
Menlo Park, CA 94025

ABSTRACT

The electron-impact dissociation of O_2 to form two oxygen atoms is observed in a crossed beam experiment at electron energies between 13.5 eV and 198.5 eV. Detection of the correlated dissociation fragments with a time and position sensitive detector permits detection of both ground and excited state fragments, but excludes interference from dissociative ionization products. The observed translational energy releases in the O_2 dissociation are consistent with production of $O(^1D) + O(^3P)$ fragments following electron impact excitation to the $B^3\Sigma_u^-$, $B'^3\Sigma_u^-$, and $2^3\Pi_u$ states, and production of $O(^3P) + O(^3P)$ fragments from excitation to the (unresolved) $c^1\Sigma_u^-$, $A'^3\Delta_u$, and $A^3\Sigma_u^+$ states. Absolute cross sections for the electron impact dissociation of O_2 are measured.

MP 92-261R

January 28, 1993

INTRODUCTION

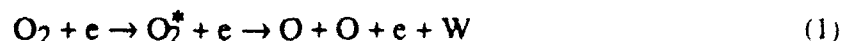
The O_2 molecule is an important constituent of the atmosphere and other gaseous media. The importance of obtaining an understanding of its response to electron impact, such as occurs in aurora and discharges, has prompted a large number of experimental and theoretical investigations of this species. Total electron impact cross sections are well known as are those for ionization, elastic scattering, rotational and vibrational excitation, and for the excitation to several of the electronic states in this species. However, dissociation cross sections must be inferred from the cross sections measured for excitation to specific electronic states. Compilations of cross sections for electron impact processes in O_2 are available from several sources.¹⁻³

The O_2 molecule provides perhaps the best case for inferring dissociation cross sections from excitation cross sections since all of its electronic states that are accessible from a thermal population in the ground $X^3\Sigma_g^-$ state with electric dipole allowed transitions lie above the first dissociation limit and appear to dissociate. Optical emission in the Schumann-Runge bands is observed in O_2 discharges at high pressure,⁴ but the fraction of emitted light is small because all levels of the upper state of this system, $B^3\Sigma_u^-$, are found to rapidly predissociate.⁵⁻⁷ At lower pressures, only optical emission from highly excited atomic O, O^+ , and O^{++} states is observed⁸⁻¹⁰ and highly excited neutral fragments formed by electron impact on O_2 have been detected using nonoptical techniques.¹¹⁻¹³ In general, the processes forming highly excited fragments represent only a small subset of the overall O_2 dissociation, and frequently their formation is through dissociation processes in the O_2^+ ion.

Direct detection of the dominant O_2 dissociation fragments has historically been difficult. Formation of O atom products in the ground 3P state and in the lower excited states, 1D and 1S , accounts for all of the accessible dissociation limits below the ionization limit of the molecule. The 1D and 1S excited states are long-lived, with radiative lifetimes of 148 s and 0.8 s, respectively. These excited states can be monitored by their red and green line emission in the

upper atmosphere, but are subject to rapid collisional quenching or reaction in most laboratory environments. Nevertheless a few laboratory measurements of ^1S , ^1D , and ^3P production following photodissociation of O_2 have been made.¹⁴⁻¹⁷ In addition, there has been one unpublished measurement using chemi-ionization to detect O atom production following electron impact dissociation of O_2 .¹⁸

The approach in the present experiment is to study the reaction:



in a crossed beam experiment. The O_2 beam is formed with several keV of translational energy such that the O-atom dissociation fragments can be detected by secondary electron emission at an electron multiplier detector. At high impact velocities, the secondary emission efficiencies of individual atomic states are roughly the same; hence fragments produced at the lower dissociation limits can be detected. The high velocity of the molecules further serves to constrain the spatial dispersion of the fragments such that all of the fragments, or at least a known fraction of them, can be detected. The fragments are detected in multiple coincidence with respect to their spatial and temporal separations, allowing a discrete pair of atomic fragments to be directly associated with the dissociation of a single molecule and to obtain an explicit measurement of the translational energy release W . Charged dissociation products are explicitly excluded from detection; hence products of electron-impact dissociation O_2 , reaction (1), are observed without contributions from dissociative ionization processes in the present work.

EXPERIMENT

The experimental apparatus and measurement procedures have been described in detail for the electron-impact dissociation of CO ¹⁹ and will be considered only briefly here. A fast (3-5 keV), collimated beam of O_2 molecules is created by near-resonant charge transfer neutralization of an O_2^+ beam and intersected at right angles by an electron beam within an interaction region

defined by a narrow slit and a beam flag. Undissociated molecules are collected by the beam flag. If an O₂ molecule dissociates within this region and its fragments are produced with sufficient transverse velocity to escape collection by the beam flag, the correlated pair of fragments is detected by a position sensitive detector (PSD-C) which measures their radial (R) and temporal (Δt) separations.²⁰ This measurement specifies the center-of-mass translational energy released in the dissociation (W), i.e. the difference in energy between the dissociating molecular state and its atomic products at infinite separation:

$$W = \frac{E_0}{4L^2} [R^2 + (\frac{2E_0\Delta t}{M})^2], \quad (2)$$

Here, the translational energy of the fast O₂ beam, E_0 , is taken to be the energy of the O₂⁺ precursor in the charge transfer, M is the mass of O₂, and L is the distance between the point of dissociation of the O₂ molecule and the PSD-C. Both of these are taken to be constants describing all dissociating O₂ molecules. The measurement further specifies the angular distribution of the fragments in the planes orthogonal to the detector. The fast O₂ beam flux is measured by a pyroelectric bolometer and the absolute collection efficiency of PSD-C for dissociation fragments is calibrated. All charged particles are collected by a weak electric field in the region between the beam flag and the PSD-C; hence dissociative ionization products do not contribute to the present measurements.

As described previously,¹⁹ the electron beam has a rectangular geometry and an energy spread of ~ 1.5 eV FWHM. Energy calibration of the electrons is made from the observed threshold for the ionization of Ar²¹ and has an estimated accuracy of ± 1 eV. Overlap between the electron and neutral beams is controlled by physically translating the electron gun and electron collector as a unit. This capability allows distinction to be made between neutral fragments created by spontaneous or collisional dissociation of the O₂, and electron impact dissociation of O₂. The gun translation further allows an accurate dissociation cross section to be measured without a specific determination of the form factor describing the overlap of the electron and neutral beams.

With the electron gun and the neutral beam aligned, overlap of the beams takes place within a $\Delta L = 2.6$ cm interval along the neutral beam flight path. Since it is not known *a priori* where along this interval a particular O_2 molecule dissociates to produce a detected pair of fragments, the value of W implied by Eqn. (2) can deviate from the true magnitude of the translational energy release by the factor

$$\frac{\Delta W}{W} = \frac{2\Delta L}{L} = 0.052. \quad (3)$$

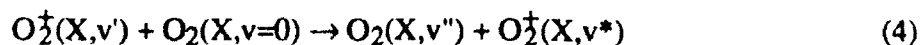
This factor represents the effective translational energy resolution achieved by the PSD-C for the electron-impact dissociation fragments. Pressures in the interaction region were maintained at $<2 \times 10^{-8}$ Torr in the present measurements.

Two orientations of the electron beam velocity vector with respect to the PSD-C in combination with the fragment angular distribution observed by the PSD-C are required to define the full angular distribution of the electron-impact dissociation fragments. In the present measurements, these distributions are found to be isotropic within the center-of-mass frame of the O_2 at electron-impact energies >25 eV. At lower electron energies, the flux of fragments dispersed in both energy release and angle was too small for a detailed angular distribution to be determined. In interpreting the present data, we presume that this distribution remains isotropic at lower electron energies.

The internal state distribution of the O_2 beam is determined by the composition in the O_2^+ reactant beam and by the gas used for the neutralization. In order to achieve a substantial difference in populations, the O_2^+ ions used in the present work were created by two different ion sources. A Nier-type source produced O_2^+ by 100 eV electron impact (EI) on O_2 gas. Following the $>5\mu s$ transit time between the ion source and the charge transfer neutralization region, the $O_2^+(EI)$ beam consists of ions in two electronic states: $X^2\Pi_g$ and $a^4\Pi_u$. The vibrational distribution of the ions in these states is explicitly measured by observing with the PSD-C the dissociative charge transfer (DCT) products of O_2^+ following neutralization in Cs vapor. The

observed vibrational distribution in the $X^2\Pi_g$ state, given in Table I of Walter et al.,²² has 93% of the population distributed among $v=0-4$ of the $X^2\Pi_g$ state. The vibrational distribution observed for the $a^4\Pi_u$ state agrees with that reported by van der Zande et al.²³ and by Grieman et al.,²⁴ with 92% of the $a^4\Pi_u$ state population distributed among $v=0-8$. The estimated distribution of population between the X and a states is 0.47 and 0.53, respectively.²² A second ion source²⁵ produced O_2^+ with a hollow cathode (HC) discharge in 0.5-1 Torr of O_2 gas. These $O_2^+(HC)$ ions are found to populate only $X^2\Pi_g(v=0)$ as evidenced by their Cs DCT translational energy release spectrum.²⁶

Charge transfer neutralization from the initial ion state distribution determines the final population distribution in the O_2 beam. The present measurements were made using O_2 , furan, or Ar as the neutralizing gas. These have ionization potentials of 12.06 eV, 8.88 eV, and 15.76 eV, respectively. Pressures in the charge transfer cell were adjusted in each case such that the transmitted O_2^+ beam current was attenuated by approximately 10%. Under these conditions, both O_2 and furan produced an O_2 beam with comparable efficiency, but Ar provided a substantially lower neutral beam flux. At keV energies, the product state distribution produced by the charge transfer of a particular initial ion state is determined by both the vibrational overlap integrals in the ionization and recombination steps and the magnitude of the energy defect in the reaction. For the case of O_2^+ , these requirements conflict such that the transfer of population between specific vibrational levels in the ion and the neutral is not adiabatic. Partial charge transfer cross sections have been calculated²⁷ for the production of specific product states in the reaction



at 2210 eV. They predict that even from $v'=0$, significant populations will be created in $v''=0-2$ of the products, with 90% of the product population distributed in $v'' \leq 4$. This should be an appropriate estimate for the fast O_2 beam population distribution produced by charge transfer in O_2 of 3000 eV $O_2^+(HC)$. A similar distribution is also expected from the calculated cross sections

for the neutralization of the $X^2\Pi_g$ component of $O_2^+(EI)$, despite the incidence of vibrational excitation in the reactant ion. However, neutralization of the large population of $a^4\Pi_u$ state in the $O_2^+(EI)$ beam with O_2 has near-resonant product channels leading to the production of high vibrational levels in O_2 , more than 4 eV above the ground vibrational level.²⁸ There is no reliable way to estimate the O_2 beam state distribution produced by neutralization in furan or Ar. Empirically, it is found here that electron-impact dissociation cross sections measured for the O_2 beam produced from $O_2^+(HC)$ were comparable for each of the three charge transfer gases, suggesting comparable vibrational distributions. In contrast, O_2 beams produced from $O_2^+(EI)$ yielded significantly smaller cross sections, suggesting a higher degree of vibrational excitation.

RESULTS

Fragment Energy Release

The distribution of translational energy releases produced by dissociation of a 3000 eV O_2 beam formed in the charge-transfer neutralization of $O_2^+(EI)$ in O_2 is shown in Fig. 1. The spectra are uncorrected for the collection efficiency of the apparatus, which produces the apparent cut off in the fragment intensity near $W = 0.2$ eV and produces some attenuation of the fragment intensity for $W < 1$ eV and $W > 4$ eV. The upper spectrum in this Figure is obtained with a 1.1 mA beam of 50 eV electrons intersecting the O_2 beam with a flux of $5 \times 10^9 \text{ s}^{-1}$, while the lower spectrum is obtained under the same conditions, but with the electron gun repositioned such that there is negligible overlap between the electron and neutral beams. The total accumulation time of the two spectra was 9.7 hours with a 50% duty cycle for intersecting and nonintersecting beams. The two spectra are histograms of the apparent value of W implied by Eqn (2) from measured values of R and Δt for each pair of correlated dissociation fragments; fragments observed during beam intersection are binned separately from those observed during nonintersection.

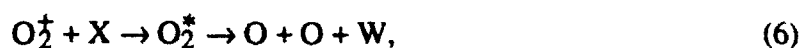
The lower spectrum thus represents the dissociation background to the electron impact dissociation studies and consists of a structured energy releases in the region $1 \text{ eV} \leq W \leq 2.2 \text{ eV}$

superimposed on a continuum of energy releases that decreases in intensity with increasing W . Studies of this spectrum as a function of residual gas pressure in the interaction region show an increase in the overall continuum intensity with increasing gas pressure in the range of 10^{-8} to 10^{-7} Torr, suggesting that the continuum arises from collision induced dissociation of the O_2 beam:



This continuum contribution was found to be somewhat stronger when furan was used as the neutralizing gas than when O_2 was used.

In contrast, the structured region of the spectrum is effectively unchanged by either gas pressure changes or the choice of O_2 or furan as the neutralizing gas. The energy release near 1.8 eV is more prominent in beams produced from $O_2^+(EI)$ than from $O_2^+(HC)$, but the lower energy features are essentially invariant with the state composition of the O_2^+ beam. These findings suggest that the structured components in the energy release spectrum of the background dissociation arise from dissociative charge transfer of O_2^+ :



where the O_2^* produced in the charge transfer must survive transit between the charge transfer cell and the entrance to the interaction region (the slit) before dissociating, a time period of roughly 3 μ s. From the broad appearance of the energy releases and the large energy defect (~ 7 eV) required for the charge transfer reaction to produce an O_2 state lying >1 eV above the lowest dissociation limit, we estimate that the spectrum arises from a very small concentration (~ 1 ppm) of O_2^* in the fast beam with a dissociation lifetime of order 10 μ s. This is discussed in more detail elsewhere.²⁹ It should be noted that fragments produced by collisional dissociation or spontaneous dissociation are collected from essentially the entire distance between the slit and the beam flag, not just within the region of electron beam neutral beam overlap. Thus the resolution (and

accuracy) of translational energy releases is substantially degraded, with $\Delta W/W \sim 0.34$ for the products of reactions (5) and (6).

The translational energy release spectrum for electron-impact dissociation of O_2 , reaction (1), is given by a direct subtraction of the two spectra in Fig. 1. The results of such subtractions, now corrected for PSD-C collection efficiency and binned into fewer channels, are shown in Fig. 2 for electron beam energies of 28.5, 38.5, and 148.5 eV. The spectra, which are not corrected for resolution, Eqn. (3), are measured using an O_2 beam produced from $O_2^+(HC)$ neutralized in O_2 . The error bars given for the fragment intensity at each W represent the statistical error associated with the subtraction and the calculated collection efficiency. Over most of the spectrum, the collection efficiency is quite flat (see Fig. 6 of Ref. 19). However, at $W < 0.5$ eV, the true collection efficiency is strongly dependent on the precise alignment of the beam flag with the O_2 beam; hence the actual uncertainties in this region can be significantly larger than implied by the error bars. Detailed W spectra of the dissociation fragments were obtained over the electron energy range of 20-200 eV. Below 20 eV, the combination of small dissociation cross sections and small electron beam currents produced W spectra with statistical errors comparable to the binned fragment intensity and were of no utility.

The fragment energy release spectra shown in Fig. 2 exhibit several characteristics. At all electron energies, most of the O_2 dissociations produce a value of W in the range $1 \leq W \leq 2.5$ eV. We identify this as W region II for later discussion. At electron energies < 70 eV, a significant number of fragments are also produced with $W < 1$ eV. The precise variation of fragment intensity with W in this region is somewhat uncertain, as mentioned above. However, it is quite clear, as shown in Fig. 2, that the number of fragments produced within this region is much smaller for higher electron energies. We designate this as region I. Finally, fragments are produced in the region $2.5 \leq W \leq 4$ eV, designated as region III. These are somewhat more prominent at the lower electron impact energies. At all electron energies, negligible fragmentation is observed with $W > 4$ eV.

Total Dissociation Cross Section

The total dissociation cross section σ_{dis} is obtained from the relation

$$\sigma_{\text{dis}} = \frac{N^* u v_n \eta e}{\xi \chi I_e I_c}, \quad (7)$$

as discussed in Ref. 19. Here, I_c/η is the O_2 beam flux, I_e is the electron beam current, v_n is the velocity of the O_2 beam, taken here to be the velocity of the O_2^+ precursor, e is the electron charge, ξ is the coincidence efficiency of the PSD-C, and χ is the collection efficiency of the PSD-C, i.e. the fraction of the total cm distribution of the dissociation fragments that is viewed by the detector, N^* is the total accumulated number of electron impact dissociation pairs as the electron beam is slowly translated completely across the O_2 beam at a constant velocity u . Each of these terms is separately measured with the exception of the PSD-C collection efficiency χ , which is an explicit function of the O_2 beam energy, fragment energy release W , and the center of mass angles Θ and Φ defining the ejection of the fragments orthogonal to the plane of the PSD-C and within the plane of the PSD-C, respectively. Only Θ is explicitly measured by the PSD-C for each dissociation event, whereas the Φ distribution must be inferred from a comparison of the total apparent cross sections measured at two different orientations of the electron beam with respect to the active axis of the PSD-C. Thus χ makes the single largest contribution to the uncertainty in σ_{dis} . Finally, an error is introduced into the cross sections by the present inability to observe fragments produced with $W < 0.3$ eV. As can be seen in Fig. 2, there is appreciable fragment flux at values of W just above this limit, particularly at the lower electron impact energies. However, as discussed in the next section, there is no reason to believe that very low energy releases would dominate the electron-impact dissociation for this molecule. For the present measurements, we approximate this unobserved flux by extrapolating the average fragment intensity observed for the interval $0.3 \leq W \leq 0.5$ eV to $W=0$. This introduces an increase in fragment flux beyond that actually observed ranging from 5% at the higher energies to 14% at the lowest energies. The total absolute uncertainty in the dissociation cross section, taken as the rms sum of the uncertainties in Eqn. (7), is $\pm 34\%$.

Total dissociation cross sections were measured for the O_2 beam produced from $O_2^+(HC)$ neutralized in O_2 or furan and for $O_2^+(EI)$ neutralized in all three charge transfer gases. Cross sections for O_2 formed by the $O_2^+(HC)$ precursor were found to be equal to within $\sim 15\%$ regardless of the neutralizing gas, whereas those for the $O_2^+(EI)$ precursor were systematically $\sim 30\%$ smaller. This difference presumably reflects a higher degree of vibrational excitation in the O_2 produced from $O_2^+(EI)$. The cross sections measured from the $O_2^+(HC)$ precursor are given as a function of electron impact energy in Table I and shown as the solid circles in Fig. 3 in units of $1 \text{ Mb} = 1 \times 10^{-18} \text{ cm}^2 = 0.01 \text{ \AA}^2$. The magnitude of the error bars in Fig. 3 reflects only the relative uncertainty in the measured cross sections; the absolute uncertainty is $\pm 34\%$.

DISCUSSION

Fragment Energy Release

Representative potential energy curve of O_2 are shown in Fig. 4, which also shows the ground electronic state of O_2^+ . Electron impact on O_2 $X^3\Sigma_g^-$ produces an electronic excitation in the molecule, as indicated in reaction (7). The O_2 molecule has a great many electronic states, 18 arise from just the lowest dissociation asymptote $^3P + ^3P$. Considering the possibility of spin-exchange in the collision, excitation of the $X^3\Sigma_g^-$ ground state gives access not only to other triplet states as in an electric dipole absorption, but also to the singlet and quintet manifolds as well. A careful consideration of selection rules³⁰ finds that essentially all of the excited states are accessible to electron impact excitation, though not with equal probabilities.

In the Born approximation, the differential cross section for electron impact excitation is given approximately by:

$$\sigma \sim \sigma_0 \left[\int_0^\infty \psi_i \psi_f dr \right]^2 \quad (8)$$

where σ_0 is the cross section for the excitation of a specific electronic final state from the initial state, here $X^3\Sigma_g^-$, for an electron of specific incident and scattered momenta, and the ψ are the

wavefunctions describing the nuclear motion along the internuclear coordinate r in the initial and final electronic states. The term in on the right hand side of the Eqn. (8) is simply the Franck-Condon factor for excitation between these states. Thus, states accessible to electron impact excitation must lie within a vertical region, shown in Fig. 4 by shading for an initial vibrational level $v=0$. If the final state is a continuum state or a predissociated bound state, the projection of the probability density described by this factor onto the energy coordinate relative to a specific pair of dissociation fragments should closely approximate the distribution of fragments in translational energy release W such as observed in the present experiment.

The lowest excited states of O_2 , $a^1\Delta_g$ and $b^1\Sigma_g^+$ have potential energy curves³² similar to those of the ground state and thus cannot be excited into a dissociative region with significant probability in a vertical transition, but rather produce only electronic excitation³³⁻³⁶ upon electron impact. The first dissociative regions accessed in vertical transitions are the repulsive walls of the so called "6 eV" states, $c^1\Sigma_u^-$, $A'^3\Delta_u$, and $A^3\Sigma_u^+$, which adiabatically dissociate to ground state fragments. The three states have similar potential energy curves³² and lie close in energy; hence only the $c^1\Sigma_u^-$ is shown in the figure. Vertical excitation to the 6 eV states,³⁴⁻³⁷ should give rise to production of $O(^3P) + O(^3P)$ with a kinetic energy distribution labeled I, given to the right of the figure, that extends from $W = 0$ to $W > 2$ eV. The next higher energy dissociation process is to the repulsive wall of the $B^3\Sigma_u^-$ state with correlates to $O(^1D) + O(^3P)$ fragments. Excitation in this Schumann-Runge (SR) continuum³⁸⁻⁴⁰ is expected to produce a fragment energy distribution labelled II which is peaked near $W \sim 1.7$ eV with a relatively sharp cutoff at higher W due to the avoided crossing of this state in the vertical region with the $^3\Sigma_u^-$ Rydberg state.⁴¹ Also accessible in this region are the repulsive curves arising from the ground state limit, of which the $1^3\Pi_u$ is shown in the figure.^{39,42} Adiabatic dissociation of these states will produce a form for the W spectrum similar to that of the B state, but shifted to higher kinetic energies by the 1D - 3P energy separation (1.967 eV). Finally, excitation is possible to Rydberg states formed on the $O_2^* X^2\Pi_g$ core.⁴³ Two of these, the $B'^3\Sigma_u^-$ and $2^3\Pi_u$ are accessible in dipole allowed transitions from the

ground state and are shown in the figure.⁴⁴ In addition, the $d^1\Pi_g$ and $C^3\Pi_g$ Rydbergs lie in the vertical region at a potential energy near 1 eV on the scale of the figure.⁴⁵⁻⁴⁸ These have been characterized by translational spectroscopy⁴⁹ and multiphoton ionization^{50,51} studies. All of these states are predissociated. For the B' and $2^3\Pi_u$, this is manifested by a substantial broadening of the transitions in the optical absorption spectrum.⁵² For the $1,3\Pi_g$, the fragmentation has been explicitly observed to the $^1D + ^1D$, $^1D + ^3P$, and $^3P + ^3P$ dissociation limits.⁴⁹ Dissociation products of the $B'^3\Sigma_u^-$ and $2^3\Pi_u$ states are not known. Dissociation to $^1D + ^3P$ has been assumed in Fig 4, as suggested by photodissociation studies,^{14,15} giving rise to the discrete energy releases labeled III.

The electron energy dependence of the differential cross section for excitation to the various electronic states in O_2 is given quite precisely by electron energy loss spectroscopy (EELS), which measures the energy and intensity of electrons inelastically scattered from a monochromatic electron beam. The difference in energy between the incident and scattered electrons is equal to the vertical excitation energy between the initial $O_2 X^3\Sigma_g^-(v=0)$ state and the final excited state. This differs from the translational energy release W measured here for dissociative states by the energy of the dissociation limit relative to $X^3\Sigma_g^-(v=0)$. The O_2 EELS spectrum observed by Wakiya⁵³ for electrons scattered by 15° following 50 eV electron impact is shown at the bottom of Fig. 5. This spectrum has an energy resolution comparable to that of the translational energy release spectra measured in the present work. A constant value of 7.083 eV has been subtracted from the observed EELS energy losses to place the energy scale of the spectrum in this figure relative to the $O(^1D) + O(^3P)$ dissociation limit, i.e. the zero of potential energy in Fig. 4. At 50 eV electron impact energy, the spectrum is dominated by dipole allowed transitions: excitation of the SR continuum $B'^3\Sigma_u^- \leftarrow X^3\Sigma_g^-$ occurs for energy losses between 0 and 2.2 eV and should produce fragmentation corresponding to region II in Fig. 4, and excitation of the $B'^3\Sigma_u^-$ and $2^3\Pi_u$ Rydberg states at energy losses near 3 eV, corresponding to region III in Fig. 4. The small undulations at the top of the SR feature have been assigned to excitation of the $^3\Pi_g$

Rydberg state.⁴⁰ Excitation to the 6 eV states, region I in Fig. 4, also contribute weakly to the EELS spectrum, but at energies below the energy zero on the scale of Fig. 5. While the relative intensities in the EELS spectrum are those obtained at a 15° scattering angle, they roughly reflect the relative excitation cross sections integrated over all scattering angles.

The fragment translational energy release spectrum obtained in the present work following 48.5 eV electron impact is shown at the top of Fig. 5. The similarity between the fragment energy spectrum and the EELS spectrum is strikingly good, both in terms of the cutoff for the SR feature near 2 eV and the appearance of fragments following predissociation of the $B'^3\Sigma_u^-$ and $2^3\Pi_u$ Rydberg states. In fact, the appearance of these fragments near 3 eV provides definitive evidence for predissociation of these states to the $^1D + ^3P$ dissociation limit; their positions in the spectrum would be shifted by ~2eV to higher or lower energy if other dissociation products were formed. Production of fragments at this limit has also been found following photoexcitation to these states.^{14,15}

The main deviation between the fragment and EELS spectra occurs for $W < 1\text{eV}$, where there is substantially more intensity than would be suggested by the excitation spectrum. However, excitation of the 6 eV states necessarily must produce ground state fragments. These correspond to region I of Fig. 4 and will contribute to the fragment intensity within the $W < 1\text{eV}$ region. Further justification for attributing the significant fragment intensity in this region to dissociation of the 6 eV states comes from the electron energy dependence of these fragments shown in Fig. 3. Substantially fewer fragments appear in this region for electron impact energies $> 70\text{ eV}$. Waikya⁵³ has reported integral excitation cross sections for the 6 eV group of states and for the SR continuum at several electron impact energies. The ratio of his cross sections $\sigma_{6\text{eV}}/\sigma_{\text{SR}}$ decrease from 0.105 at 20 eV to 0.021 at 100 eV. The relative decrease in the excitation cross section is consistent with the relative decrease in low W fragment intensity with increasing electron impact energy.

A second disagreement between the excitation spectrum and the fragment spectrum is the relatively high fragment flux in the region $2.2 \text{ eV} \leq W \leq 2.7 \text{ eV}$ between the high energy side of the SR feature and the B' fragments. An obvious source for such fragments would be from SR continuum dissociation accessed from vibrationally excited O₂ molecules in the fast beam. The EELS spectrum was obtained with an O₂ target gas equilibrated at room temperature; hence essentially all molecules are in the $v=0$ initial state. In contrast, we expect a distribution of vibrational levels, $0 \leq v \leq 4$ to be populated in the fast O₂ beam by charge transfer. However, if the effect of such vibrational excitation on the bound-free Franck-Condon factors is explicitly modeled using the empirical potential energy curves of Allison et al.,⁴² it is found to produce relatively little broadening in the fragment energy release spectrum. Although vibrational excitation expands the range of internuclear distances over which vertical excitation can take place, the main effect of this is to increase the relative fragment flux from dissociation in the SR continuum near $W \sim 1.8 \text{ eV}$, rather than to substantially broaden the feature to higher values of W . This is due to the inflection in the B state potential curve from an avoided crossing; its form has been empirically defined by Allison et al. to reproduce the optical absorption spectrum. In fact, there is some evidence of a weak peak in the fragment spectrum near 1.8 eV , which may be the manifestation of O₂ vibrational excitation. Another effect of vibrational excitation may be to weaken the features at $W \sim 3 \text{ eV}$ attributed to B', $2^3\Pi_u$ predissociation relative to the SR feature at $W \sim 1.7 \text{ eV}$. However, the energy releases of the predissociation features cannot be broadened by vibrational excitation. It therefore seems likely that the fragments in the region above the expected SR cutoff arise from dissociation of the 6 eV states, which are expected to produce fragments in excess of $W = 2.2 \text{ eV}$ even from an initial $v=0$ state, as indicated by distribution I in Fig. 4.

Another measure of the effects of O₂ vibrational excitation comes from the work of Stone, Lawrence, and Seitel.¹⁸ These authors reported the time of flight spectrum of O atom fragments produced following the dissociation of thermal O₂ molecules with a pulsed, 80 eV electron beam. Chemi-ionization of the O atoms in a samarium vapor cell allowed detection of ground state

atoms.¹⁴ Their time-of-flight spectrum, now transformed onto an energy release scale, is shown at the center of Figure 5. Horizontal error bars given in the figure indicate the rapid degradation in energy resolution with increasing energy release that accompanies a constant uncertainty in fragment flight time. In general, the fragment energy distribution compares favorably to that observed at $W < 1$ eV in the present measurements for electron impact energies between 48.5 eV and 98.5 eV. This gives support to attributing much of the fragment intensity in this region to dissociation of the 6 eV states, rather than to the effects of vibrational excitation. Their spectrum appears to decrease faster in intensity for $W > 2$ eV than the present measurements, however it is not clear that this can be attributed to the absence of vibrational excitation of $O_2 X$ in their measurements or to the decrease in peak fragment intensity that must accompany the degradation in energy resolution. This latter effect is most certainly responsible for the lack of any discernible feature in their spectrum near $W = 3$ eV from Rydberg state predissociation.

Total Dissociation Cross Section

There have been two theoretical calculations of the cross sections for electron-impact dissociation of O_2 . Chung and Lin⁵⁴ used the Born-Ochkur approximation to calculate the contribution to the electron-impact dissociation cross section arising from $B^3\Sigma_u^- \leftarrow X^3\Sigma_g^-$ excitation at electron energies between 10 eV and 1000 eV. Their results are given as the solid line in Figure 3. The calculations compare quite well with the measured cross sections, certainly within the absolute uncertainty of the measurements. However, only dissociation through the Schumann-Runge continuum has been considered in the calculations; hence they represent only a lower limit to the total dissociation cross section.

Calculations of the electron impact cross section over the electron impact energy range from threshold to 25 eV have been reported by Garrett et al.⁵⁵ using an impact parameter approach. These calculations considered only excitation in dipole-allowed transitions to the $B^3\Sigma_u^-$, $B^3\Sigma_u^+$, and $1^3\Pi_u$ states, shown in Fig. 4. The sum of these calculated cross sections as a function of electron energy are given by the dashed line in Fig. 3. Since excitation of the 6 eV states, in

particular, has been neglected, the calculated cross section also represents a lower limit to the total dissociation cross section. Nevertheless, the calculated cross section is substantially larger than the present measurements.

Experimental cross sections for electron-impact excitation to several dissociated states of O_2 have also been reported. These have been derived from differential EELS cross section measurements that have been converted to integral inelastic scattering cross sections and normalized to absolute elastic scattering cross section measurements. Trajmar, Williams, and Kuppermann³⁵ report the excitation cross sections at two electron impact energies to the 6 eV states, the SR continuum, and to the $B', 2^3\Pi_u$ Rydberg states. The sum of these cross sections are given by the two crosses in Figure 3. Wakiya⁵³ has reported the cross sections for excitation to these same states at 5 electron energies between 20 and 100 eV. The sum of his cross sections are given by the open circles in this figure, together with error bars indicating his estimated uncertainties. The open circles given at electron energies of 150 eV and 200 eV are Wakiya's cross sections for excitation to the SR continuum alone; it accounts for 85% of the summed cross section at 100 eV and should provide an even closer approximation to the total cross section at these higher energies. There is some disagreement between the two sets of measurements as to the electron energy dependence of the cross section between 20 eV and 50 eV, but in general the overall magnitudes of the cross section in this region is consistent. There appears to be strikingly good agreement between the Wakiya measurements and the total cross section calculated by Garrett et al. However, some of this agreement is fortuitous. Excitation to the B' state contributes 35% of the calculated total cross section at 20 eV, whereas excitation to the B' and higher states contributes only 13% to the total cross section of Wakiya⁵³ and 15% to the total cross section of Trajmar et al.³⁵

A comparison between the present cross sections, the solid circles in Fig. 3, and the experimental excitation cross sections from EELS finds the excitation cross sections to be uniformly larger than the present dissociation measurements over most of the electron energy

range. Nevertheless, both sets of measurements overlap within their mutual uncertainties for electron energies >25 eV, but at lower energies the disagreement is significant. There is the possibility that some fraction of the states excited in the EELS experiments do not dissociate, however this is unlikely given the present knowledge of the excited states in O_2 . A more likely reason for the smaller dissociation cross sections is that they are measured for O_2 with a vibrational population distributed among $v=0-4$. Garrett et al.⁵⁵ have calculated the effects of vibrational excitation on the excitation cross sections. They find that the cross section for $B \leftarrow X(v)$ at 20 eV decreases by roughly 18% between $v=0$ and $v=2$ and will presumably decrease further for excitation from higher vibrational levels. A decrease in the dissociation cross section with the enhanced vibrational excitation that is produced in the O_2 beam formed from $O_2^+(EI)$ neutralized in O_2 is also found in the present measurements.

Kanik et al.⁵⁶ have recently compiled a set of recommended electron scattering cross sections for O_2 . By subtracting measured values of the cross sections for elastic scattering and ionization from the total scattering cross section, they obtain a measure of the total cross section for electronic excitation over the electron energy range from 1 eV to 400 eV. Of particular interest here is that this implied electronic excitation cross section has a maximum value at 30 eV of 249 Mb. This value is nearly a factor of two greater than even the largest estimates for the cross sections given in Figure 3 and a factor of four greater than the present measurement of the dissociation cross section. The difference would imply a substantial reservoir for electron impact excitation other than dissociation or ionization, but this seems unlikely given the present knowledge of this molecule.

Partial Dissociation Cross Sections

The fragment translational energy release spectra measured in the present work allow some resolution of the total dissociation cross sections into partial cross sections. Determining the relative contributions of the 6 eV states and the SR continuum to the dissociation requires an assumption as to the explicit form of individual energy release contributions from these two

sources of fragments; hence we avoid making such a determination here. On the other hand, there is a fairly clear distinction between the fragments arising from the $B', 2^3\Pi_u$ and higher Rydberg states and those from the lower energy states. If we attribute the fragment flux with $W > 2.7$ eV to dissociation from these higher states, their implied dissociation cross sections are those given in Table I. It can be seen that they range from 6.3 Mb at electron energies near 30 eV to 2.5 Mb near 100 eV. The ratio of these partial cross sections to those reported by Wakiya⁵³ is roughly 0.4 over this energy range. This ratio is even smaller than the ratio of the total cross sections, 0.58. The smaller ratio may indicate that product channels other than $O(^1D) + O(^3P)$ are also populated in the predissociation, e.g. $O(^1D) + O(^1D)$ or $O(^1S) + O(^3P)$ which could be obscured in translational energy release spectrum by direct dissociation products (fragments I and II in Fig. 4). On the other hand, the smaller ratio may merely reflect a greater sensitivity of these bound-bound transitions to vibrational excitation in the initial state.

The calculations of Garrett et al.⁵⁵ yield a large cross section for excitation into the B' state, 46 Mb at 20 eV. This value far exceeds the experimental estimates of Wakiya⁵³ (<15.7 Mb) and of Trajmar et al.³⁵ (1.5 Mb) as well as that obtained from an extrapolation of the present estimates for the partial dissociation cross section to this lower electron energy. Garrett et al. assume that tunnelling represents the only dissociation path in the B' state and conclude that radiation rather than dissociation will be the dominant decay process in its lowest vibrational levels. This conclusion contrasts sharply with both the present measurements and with previous photoexcitation studies.^{14,15} Detailed studies of the absorption bands to the three vibrational levels of the B' state find asymmetric rotational lineshapes with a half-width-at-half maximum > 5.6 cm⁻¹ in these levels,⁵² implying a rapid predissociation of all levels.⁵² The discrepancy between the calculations of Garrett et al and experimental observations seems to arise from the use of a purely adiabatic description of the B' state. Recent calculations⁵⁷ find that the diabatic character of this state, formed from an avoided crossing of valence and Rydberg $^3\Sigma_u^-$ states, must be explicitly considered to be consistent with optical absorption measurements.

CONCLUSIONS

Absolute dissociation cross sections and translational energy release spectra are measured for electron impact on O_2 in a fast molecular beam. The translational energy release distributions are found to be consistent with the major contributions to O_2 dissociation arising from optically allowed electronic excitation to the $B^3\Sigma_u^-$, $B'^3\Sigma_u^-$ and $2^3\Pi_u$ states, each dissociating to form $O(^1D)$ + $O(^3P)$ atoms. Additional contributions appear in the fragment distributions that are consistent with dissociation of the "6 eV" states, $c^1\Sigma_u^-$, $A'^3\Delta_u$, and $A^3\Sigma_u^+$, to $O(^3P)$ + $O(^3P)$ atoms. Production of energy releases $W > 4$ eV was found to be negligible at all electron impact energies, suggesting that O_2 states formed at or above the lowest ionization limit either autoionize or dissociate to $O(^1S)$ + $O(^3P)$ or higher limits.

The total dissociation cross section is found to maximize at a value of 66 Mb for electron energies near 33 eV. However, the cross section refers to excitation from a vibrationally excited distribution $X^3\Sigma_g^-(v=0-4)$ in the fast molecular beam. Such excitation is endemic to the fast O_2 beam production via resonant or near-resonant charge transfer neutralization of O_2^+ due to the displacement in equilibrium internuclear separations of the ion and neutral ground electronic states. Tests using an O_2 beam with yet higher vibrational excitation yielded a cross section 30% smaller than this value. The measured dissociation cross section is smaller than previous measurements of the excitation cross sections to the primary dissociating excited states in O_2 . While there are substantial uncertainties in *both* the dissociation and the excitation cross sections, it seems most likely that the smaller dissociation cross section can be attributed to this vibrational excitation.

ACKNOWLEDGMENTS

This research was supported by the U. S. Air Force Wright Laboratory under contract No. F33615-85-R-2560. The author wishes to thank H. Helm and J. R. Peterson for a variety of assistance during the course of this work.

REFERENCES

1. A. V. Phelps, "Tabulations of Collision Cross Sections and Calculated Transport and Reaction Coefficients for Electron Collisions with O₂", JILA Information Center Report No. 28 (1985).
2. B. Eliasson and U. Kogelschatz, J. Phys. B **19**, 1241 (1986); "Basic Data for Modelling of Electrical Discharges in Gases: Oxygen", Brown Boveri Research Report KLR 86-11C (Baden, Switzerland, Brown Boveri Research Center, 1986).
3. Y. Itikawa, A. Ichimura, K. Ondaz, K. Sakimoto, K. Takayanagi, Y. Hatano, M. Hayashi, H. Nishimura, and S. Tsurubuchi, J. Phys. Chem. Ref. Data **18**, 23 (1989).
4. D. M. Creek and R. W. Nicholls, Proc. R. Soc. Lond. A **341**, 517 (1975).
5. B. R. Lewis, L. Berzins, J. H. Carver, and S. T. Gibson, J. Quant. Spectrosc. Radiat. Transfer **36**, 187 (1986).
6. A. S. -C. Cheung, K. Yoshino, J. R. Esmond, S. S. -L. Chiu, D. E. Freeman, and W. H. Parkinson, J. Chem. Phys. **92**, 842 (1990).
7. P. C. Cosby, H. Park, R. A. Copeland, and T. G. Slanger, J. Chem. Phys. (submitted for publication).
8. M. J. Mumma and E. C. Zipf, J. Chem. Phys. **55**, 1661 (1971).
9. J. M. Ajello and B. Franklin, J. Chem. Phys. **82**, 2519 (1985).

10. M. B. Schulman, F. A. Sharpton, S. Chung, C. C. Lin and L. W. Anderson, Phys. Rev. A **32**, 2100 (1985).
11. R. S. Freund, J. Chem. Phys. **54**, 3125 (1971).
12. S. Ohshima, T. Kondow, T. Fukuyama, and K. Kuchitsu, Chem. Phys. **135**, 267 (1989).
13. N. J. Mason and W. R. Newell, J. Phys. B **23**, 4641 (1990).
14. E. J. Stone, G. M. Lawrence, and C. E. Fairchild, J. Chem. Phys. **65**, 5083 (1976).
15. L. C. Lee, T. G. Slanger, G. Black, and R. L. Sharpless, J. Chem. Phys. **67**, 5602 (1977).
16. Y. Matsumi and M. Kawasaki, J. Chem. Phys. **93**, 2481 (1990).
17. Y. -L. Huang and R. J. Gordon, J. Chem. Phys. **94**, 2640 (1991).
18. E. J. Stone, G. M. Lawrence, and S. C. Seitel, "Time-of-Flight Spectrum of Ground State Atoms from Dissociation of O₂", *Electronic and Atomic Collisions: Abstracts of Papers of the IXth International Conference on the Physics of Electronic and Atomic Collisions*, J. S. Risley and R. Geballe, Ed. (University of Washington Press, Seattle, 1975) pp. 816-817.
19. P. C. Cosby, "Electron-Impact Dissociation of Carbon Monoxide", J. Chem. Phys. (submitted for publication).
20. H. Helm and P. C. Cosby, J. Chem. Phys. **86**, 6813 (1987).
21. R. C. Wetzel, F. A. Baiocchi, T. R. Hayes, and R. S. Freund, Phys. Rev. A **35**, 559 (1987).
22. C. W. Walter, P. C. Cosby, and J. R. Peterson, J. Chem. Phys. **98**, xxxx (1993).
23. W. J. van der Zande, W. Koot, J. R. Peterson, and J. Los, Chem. Phys. **126**, 169 (1989).
24. F. J. Grieman, J. T. Moseley, R. P. Saxon, and P. C. Cosby, Chem. Phys. **51**, 169 (1980).

25. H. Helm, Phys. Rev. A **38**, 3425 (1988).
26. W. J. van der Zande (private communication, 1991).
27. T. F. Moran, M. R. Flannery, and P. C. Cosby, J. Chem. Phys. **61**, 1261 (1974).
28. P. C. Cosby and H. Helm, J. Chem. Phys. **90**, 1434 (1989).
29. P. C. Cosby and H. Helm, "Product State Distributions in the Charge Transfer of $O_2^+(a^4\Pi_u)$ in O_2 and NO " (in preparation).
30. W. A. Goddard, D. L. Huestis, D. C. Cartwright, and S. Trajmar, Chem. Phys. Lett. **11**, 329 (1971).
31. E. N. Lassettre and M. E. Krasnow, J. Chem. Phys. **40**, 1248 (1964).
32. T. G. Slanger and P. C. Cosby, J. Phys. Chem. **92**, 267 (1988).
33. S. A. Lawton and A. V. Phelps, J. Chem. Phys. **69**, 1055 (1978).
34. A. Konishi, K. Wakiya, M. Yamamoto, and H. Suzuki, J. Phys. Soc. Japan **29**, 526 (1970).
35. S. Trajmar, W. Williams, and A. Kuppermann, J. Chem. Phys. **56**, 3759 (1972).
36. K. Wakiya, J. Phys. B **11**, 3931 (1978).
37. D. Teillet-Billy, L. Malegat, J. P. Gauyacq, R. Abouaf, and C. Benoit, J. Phys. B **22**, 1095 (1989).
38. J. Geiger and B. Schröder, J. Chem. Phys. **49**, 740 (1968).
39. D. C. Cartwright, N. A. Fiamengo, W. Williams, and S. Trajmar, J. Phys. B **9**, L419 (1976).
40. R. H. Huebner, R. J. Celotta, S. R. Mielczarek, and C. E. Kuyatt, J. Chem. Phys. **63**, 241 (1975).

41. A. C. Allison, S. L. Guberman, and A. Dalgarno, *J. Geophys. Res.* **91**, 10193 (1986).
42. A. C. Allison, S. L. Guberman, and A. Dalgarno, *J. Geophys. Res.* **87**, 923 (1982).
43. S. Chung, C. C. Lin, and E. T. P. Lee, *J. Phys. B* **21**, 1155 (1988).
44. R. J. Buenker, S. D. Peyerimhoff and M. Peric, *Chem. Phys. Lett.* **42**, 383 (1976).
45. S. Trajmar, D. C. Cartwright, and R. I. Hall, *J. Chem. Phys.* **65**, 5275 (1976).
46. D. Spence, *J. Chem. Phys.* **74**, 3898 (1981).
47. T. A. York and J. Comer, *J. Phys. B* **16**, 3627 (1983).
48. R. P. Saxon and B. Liu, *J. Chem. Phys.* **73**, 876 (1980).
49. W. J. van der Zande, W. Koot, J. R. Peterson and J. Los, *Chem. Phys. Lett.* **140**, 175 (1987).
50. A. Sur, C. V. Ramana, W. A. Chupka, and S. D. Colson, *J. Chem. Phys.* **84**, 69 (1986).
51. A. Sur, R. S. Friedman, and P. J. Miller, *J. Chem. Phys.* **94**, 1705 (1991).
52. B. R. Lewis, S. T. Gibson, M. Emami, and J. H. Carver, *J. Quant. Spectrosc. Rad. Transfer* **40**, 1 (1988).
53. K. Wakiya, *J. Phys. B* **11**, 3913 (1978).
54. S. Chung and C. C. Lin, *Phys. Rev. A* **21**, 1075 (1980).
55. B. C. Garrett, L. T. Redmon, C. W. McCurdy, and M. J. Redmon, *Phys. Rev. A* **32**, 3366 (1985).
56. I. Kanik, S. Trajmar, and J. C. Nickel, "Total Electron Scattering and Electronic State Excitation Cross Sections for O₂, CO, and CH₄", *J. Geophys. Res.* (submitted for publication).

57. Y. Li, M. Honigmann, K. Bhanuprakash, G. Hirsch, R. J. Buenker, M. A. Dillon, and M. Kimura, *J. Chem. Phys.* **96**, 8314 (1992).

Table I

Cross sections measured for the electron impact dissociation of O₂. Units are 1 Mb = 1×10^{-18} cm². Partial dissociation cross sections for the production of fragments with translational energy releases $W > 2.7$ eV are also given.

Electron Energy (eV)	Total Dissociation Cross Section			Partial Dissociation Cross Section	
	(Mb)	Relative Uncertainty (Mb)	Absolute Uncertainty (Mb)	W > 2.7 eV (Mb)	Absolute Uncertainty (Mb)
13.5	22.0	9.7	12.2	-	-
18.5	52.9	5.3	18.8	-	-
21.0	56.5	8.7	21.1	-	-
23.5	52.5	5.0	18.5	-	-
28.5	58.7	5.2	20.6	4.9	1.7
33.5	66.3	7.7	23.8	5.6	2.0
38.5	61.0	3.4	21.0	5.2	1.8
48.5	53.4	2.9	18.4	4.6	1.6
58.5	44.4	4.5	15.8	3.9	1.4
73.5	36.6	4.2	13.1	3.2	1.4
98.5	33.1	5.6	13.6	3.0	1.2
148.5	29.6	5.0	11.2	2.8	1.1
198.5	29.1	4.4	10.8	2.9	1.1

FIGURE CAPTIONS

- Figure 1. Distribution of translational energy releases W observed for the dissociation of O_2 . The spectra are uncorrected for the variation in the collection efficiency of the apparatus with W . The upper spectrum is obtained with a 48.5 eV electron beam intersecting the fast O_2 beam. The lower spectrum is observed with the electron gun positioned such that the electron beam and O_2 beam do not intersect. These spectra were obtained for O_2 produced by charge-transfer neutralization of $O_2^+(EI)$ to enhance the spontaneous dissociation structure. Direct subtraction of the two spectra gives the translational energy released in the electron-impact dissociation of O_2 .
- Figure 2. Translational energy release distributions produced by electron-impact dissociation of O_2 at three electron energies. The distributions have been corrected for collection efficiency, but not for the variation in energy resolution with W (see Eqn. (3)).
- Figure 3. Dissociation cross sections and excitation cross sections for electron impact on O_2 . The present measurements of the total dissociation cross section are given as a function of electron energy by the solid points with error bars reflecting the relative uncertainties of the individual measurements. The solid line labelled CL and the dashed line labelled GRMR are calculations of excitation cross sections to dissociative states by Ref. 54 and 55, respectively. The crosses labelled TWK and open circles labelled Wakiya are experimental estimates of the excitation cross sections to dissociative states in O_2 using electron energy loss spectroscopy by Ref. 35 and 53, respectively, where the error bars represent the absolute uncertainties of Ref. 53.
- Figure 4. Potential energy curves of O_2 relevant to electron-impact dissociation. Potential energy is relative to the $O(^1D) + O(^3P)$ separated atoms. The vertical excitation region from $O_2 X^3\Sigma_g^-(v=0)$ is indicated by the shaded region. Estimated translational energy release distributions from dissociative states in three regions: I for dissociation to ground state atoms; II and III for production of $O(^1D) + O(^3P)$, are shown to the right of the figure. Tic marks along the energy release distributions are in increments of 1 eV in W . The ground electronic state of O_2^+ and the first ionization limit are also shown in the figure.
- Figure 5. Three energy distributions of O_2 referenced to a common energy scale. The upper distribution is the translational energy release observed in the present work following 48.5 eV electron impact dissociation of a fast O_2 molecular beam. The center distribution is the translational energy release distribution obtained by transforming the $O(^3P)$ arrival time distribution observed by Ref. 18 following 80 eV electron impact on thermal O_2 . The bottom distribution is the scattered electron intensity at 15° as a function of energy loss observed by Ref. 53 following 50 eV electron impact on thermal O_2 . A value of 7.083 eV has been subtracted from the observed energy loss to reference it to the $O(^1D) + O(^3P)$ dissociation limit. The ordinates of each distribution are linear, but the numerical labels are arbitrary.

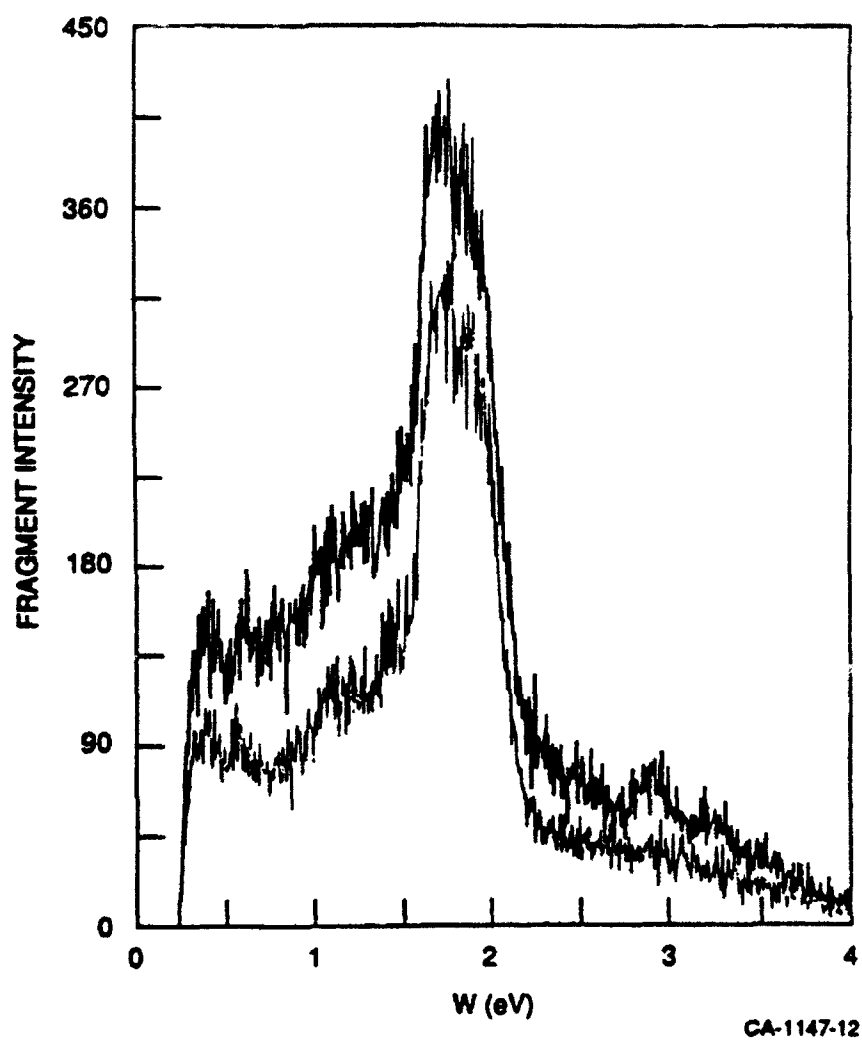
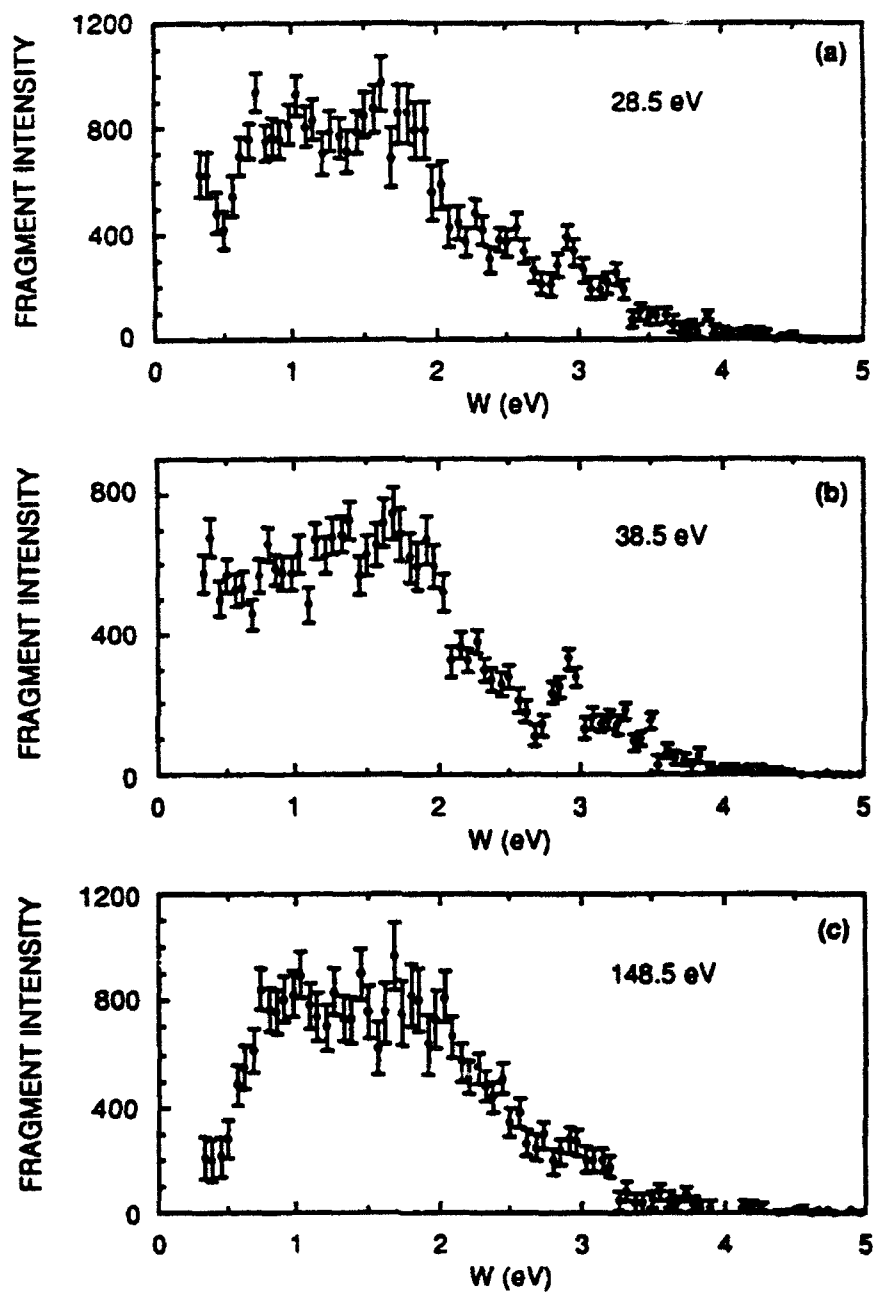


Figure 1



CAM-1147-13

Figure 2

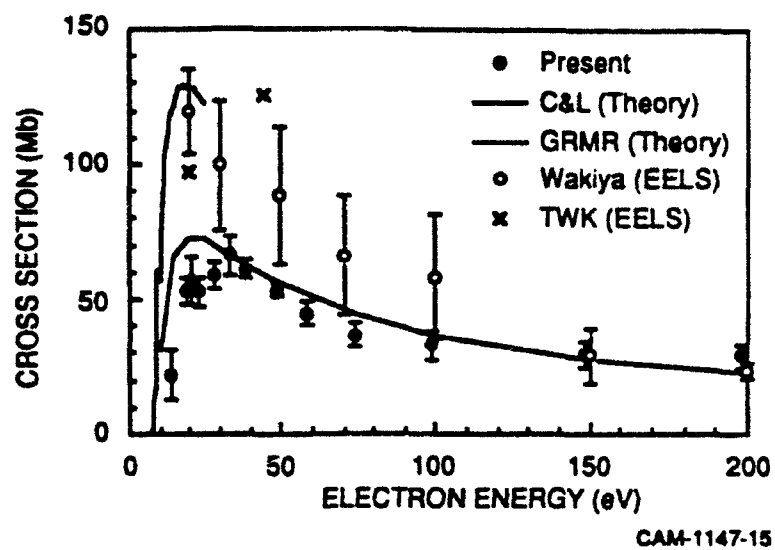
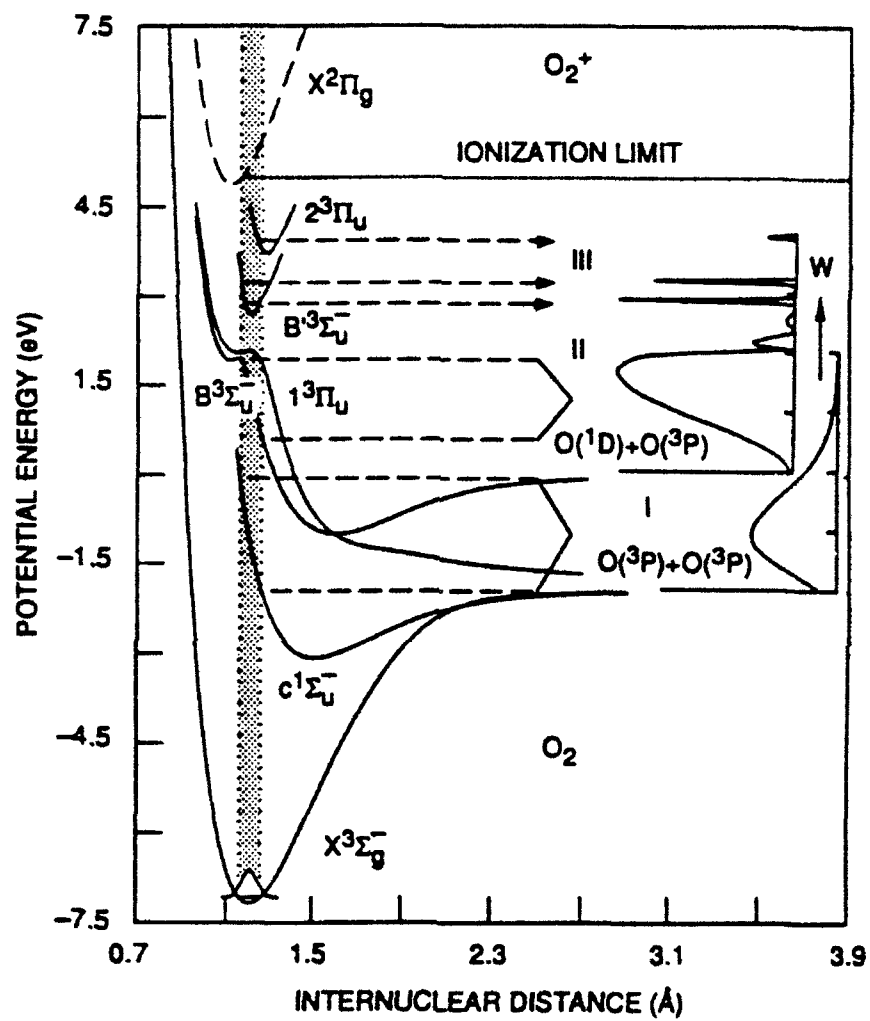
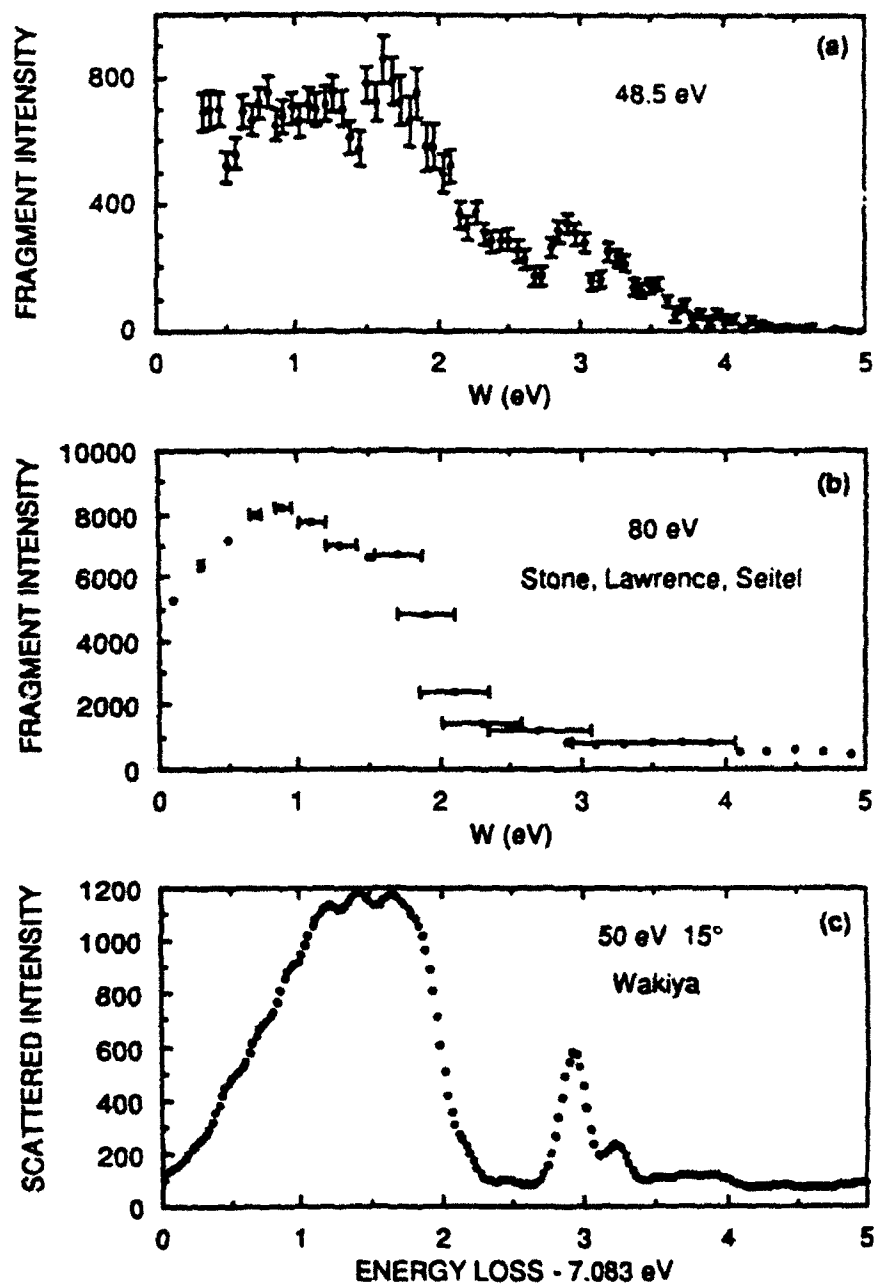


Figure 3



CA-1147-11

Figure 4



CAM-1147-14

Figure 5